A 15-YEAR CLIMATOLOGY OF AEROSOL OPTICAL AND PHYSICAL PROPERTIES AND NEAR-REAL TIME MEASUREMENTS OF WATER-SOLUBLE IONS IN $PM_{2.5}$ AND THEIR PRECURSOR GASES IN THE ATMOSPHERE OVER THE EASTERN MEDITERRANEAN

THESIS SUBMITTED TO

THE GRADUATE SCHOOL OF MARINE SCIENCES

OF

MIDDLE EAST TECHNICAL UNIVERSITY

BY

ERSİN TUTSAK

IN PARTIAL FULFILLMENT OF THE REQUIREMENTS

FOR THE DEGREE OF DOCTOR OF PHILOSOPHY

IN

OCEANOGRAPHY

JUNE 2018

Approval of the thesis:

A 15-YEAR CLIMATOLOGY OF AEROSOL OPTICAL AND PHYSICAL PROPERTIES AND NEAR-REAL TIME MEASUREMENTS OF WATER-SOLUBLE IONS IN $PM_{2.5}$ AND THEIR PRECURSOR GASES IN THE ATMOSPHERE OVER THE EASTERN MEDITERRANEAN

Submitted by **ERSİN TUTSAK** in partial fulfillment of the requirements for the degree of Doctor of Philosophy in Oceanography Department, Middle East Technical University by,

Assoc. Prof. Dr. Barış Salihoğlu ____________________

Director, Graduate School of **Marine Sciences**

Prof. Dr. Süleyman Tuğrul ____________________

Head of Department, **Oceanography**

Assoc. Prof. Dr. Mustafa Koçak ____________________

Supervisor, **Oceanography Department**, METU

Examining Committee Members:

Assoc. Prof. Dr. Barış Salihoğlu ____________________

Oceanography Department, METU

Assoc. Prof. Dr. Mustafa Koçak ____________________

Oceanography Department, METU

Prof. Dr. Nikolaos Mihalopoulos ____________________

Department of Chemistry, University of Crete, Greece

Assoc. Prof. Dr Malcolm Nimmo ____________________

Faculty of Science and Engineering, University Of Plymouth, United Kingdom

Assoc. Prof. Dr. Fatih Hüseyinoğlu ____________________

Marine School, Girne American University, TRNC.

Date: ____________________

I hereby declare that all information in this document has been obtained and presented in accordance with academic rules and ethical conduct. I also declare that, as required by these rules and conduct, I have fully cited and referenced all material and results that are not original to this work.

Name, Last Name : ERSİN TUTSAK

Signature :

ABSTRACT

Tutsak, Ersin

Ph.D. in Oceanography

Supervisor: Associated Prof. Dr. Mustafa Koçak

Middle East Technical University, 148 pages

Long-term aerosol optical and micro physical properties obtained from AERONET sun/sky radiometer situated at the rural coastal site of Eastern Mediterranean between January 2000 and December 2014 were analyzed. Moreover, concentrations of SO_4^{2-}, NH_4^+, NO_3^- (in $PM_{2.5}$) and their precursor gases (SO_2, NH_3 and HNO_3) were measured with a near real-time Ambient Ion Monitor-Ion Chromatography instrument in winter and summer of 2015. Air flow arriving at 1 km and 4 from Eastern Europe and Western Europe showed a negative trend from 2000 to 2014, decreasing about 0.2 % per year. In contrast, air flow arriving at 1 km (4km) from North Africa and Turkey demonstrated a positive trend throughout the study period, increasing 0.15 (0.40) % and 0.29 (0.15) % per year, respectively. The arithmetic mean AOT decreased 2.5 times from 440 nm (0.30) to 1020 nm (0.12), indicating the dominance of fine particles. AOT and α illustrated a large short-term variability, varying up to couple of fold from day to day. The lowest AOT values were chiefly found in winter owing to the removal of particles by rain. Enhanced AOT values at 440 nm were detected in spring with low $\alpha_{440\text{-}870}$ primarily due to mineral dust intrusions from North Africa and the Middle East. High AOT at 440 nm and $\alpha_{440\text{-}870}$ were principally characterized in summer because of high gas-to particle conversion, sluggish air masses and absence of rain. Elevated AOT with relatively lower α (0.7) and fine mode fraction (47 %) were observed when the air flow originated from North Africa (SAH) and the Middle East (MID). Regarding the relationship between AOT and Water Vapor (WV) as a function of α, three classes of aerosol were identified, namely, non-hygroscopic, moderately hygroscopic and hygroscopic. Potential source contribution function (PSCF) exhibited that non-hygroscopic particles were associated with mineral dust dominated aerosol population, originating from North Africa and the Middle East. Moderately hygroscopic particles were a mixture of mineral dust and anthropic aerosols due mainly to arrival of the dust after travelling over industrialized and populated sites (such as Spain, France and Italy). On the other hand, any particular potential source area couldn't be defined for hygroscopic particles, showing nearly mesoscale formation of secondary aerosols under the prevailing summer conditions.

Imaginary part of the refractive index, single scattering albedo, absorption angstrom exponent for dust, mixed and pollution events showed distinct difference. The imaginary part of refractive index for dust event fluctuated from 2.5 x 10^{-3} to 2.0 x 10^{-3} between 870 and 1020 nm and for wavelengths between 675 nm and 440 nm the imaginary part of refractive index augmented from 4.3 x 10^{-3} to 11.0 x 10^{-3}. Although similar spectral behavior was observed, the imaginary part of the refractive index at 440 nm for mixed event was 2.2 times lesser than that of mineral dust event. For pollution event, the imaginary part of refractive index slightly increased from 5.0 x 10^{-3} at 440 nm to 6.3 x 10^{-3} at 1020 nm. Aerosol type were classified into three groups namely dust, mixed and anthropic according to extinction angstrom exponent. The comparison of the microphysical properties of the three aerosol type revealed that categorization of the aerosol type based on extinction angstrom exponent was insufficient. The classification of aerosol type by applying cluster analysis to optical properties presented relatively better results. The aerosol absorption optical thickness at 440 nm and the imaginary part of the refractive index were statistically larger for Period II (2005-2009) compared to Period I (2000-2004) and III (20010-2014) due to the to the higher influence of dust intrusion from desert areas during Period II.

Of the water-soluble ions in $PM_{2.5}$, sulfate and ammonium were the prevailing species. Arithmetic mean sulfate and ammonium concentrations were respectively 2814 ng m^{-3} and 1371 µg m^{-3}. Aerosol nitrate arithmetic mean was 495 ng m^{-3}. Among the precursor gases, ammonia exhibited the highest concentration with a value of 3330 ng m^{-3}. Sulfur dioxide and nitric acid concentrations were 879 ng m^{-3} and 346 ng m^{-3}, respectively. Regarding arithmetic means of gas-to-particle conversion ratios for sulfate (0.62), ammonium (0.38) and nitrate (0.50), it might be suggested that the concentrations of these species were mainly influenced by non-local sources. Taking into account this study and historic off-line measurements, there was a decreasing trend for sulfate, nitrate and their precursor gases in the Eastern Mediterranean

Keywords: Aerosol optical and physical properties, hygroscopic behavior, SSA, AAOT, refractive index, aerosol type, SO_4^{2-}, NH_4^+, NO_3^-, SO_2, NH_3, HNO_3, Eastern Mediterranean

ÖZ

Tutsak, Ersin

Doktora, Oşinografi

Tez Yöneticisi: Doç. Dr. Mustafa Koçak

Orta Doğu Teknik Üniversitesi, 148 Sayfa.

Doğu Akdenizin kırsal kıyı bölgesinde konumlandırılmış AERONET güneş/gökyüzü radyometresinden Ocak 2000 ve Aralık 2014 tarihleri arasında elde edilen uzun dönemli aerosol optik ve mikro fiziksel özellikler analiz edildi. Ayrıca, 2015 yaz ve kış dönemlerinde SO_4^{2-}, NH_4^+, NO_3^- ($PM_{2.5}$ parçacık boyutunda) iyonlarıyla bunların öncül gazlarının derişimlerinin ölçümleri Ambient Ion Monitor-Ion Chromatography (Ortam İyonları İzleme - İyon Kromatografisi) enstrümanıyla nerdeyse gerçek zamanlı olarak gerçekleştirildi. Doğu Avrupa ve Batı Avrupa üzerinden istasyona 1 km ve 4 km irtifada gelen hava akımlarının 2000 ile 2014 yılları arasında yıl başına % 0.2 düşüşle ifade edilen bir negatif eğilim gösterdiği tespit edildi. Buna karşılık olarak, 1 km (4 km) irtifada Kuzey Afrika ve Türkiye üzerinden gelen hava akımlarının çalışma dönemi boyunca sırasıyla senelik % 0.15 (0.40) ve % 0.29 (0.15) artış gösteren bir pozitif eğilim gösterdiği ortaya koyuldu. AOK aritmetik ortalaması 440 nm'den (0.30) 1020 nm'ye (0.12) 2.5 kat azalarak ince parçacıkların baskınlığını gösterdi. AOK ve α değerlerinin kısa dönemli ölçekte büyük bir değişkenlik gösterdiği, günlük değişkenliğin birkaç katı bulduğu tespit edildi. Parçacıkların yağışla yıkanması sebebiyle en düşük AOT değerleri ağırlıklı olarak kışın gözlemlendi. 440 nm'de yüksek AOT değerleri ile düşük $\alpha_{440-870}$ değerleri, Kuzey Afrika ve Orta Doğu menşeli toz olaylarına bağlı olarak ilkbahar döneminde tespit edildi. 440 nm'de yüksek AOT ve $\alpha_{440-870}$, gaz-partikül dönüşümü, hareketsiz hava kütleleri ve yağışın olmayışı sebeyile esas olarak yaz döneminde karakterize edildi. Yüksek AOK'ye eşlik eden göreceli olarak düşük α (0.7) ve ince mod fraksiyonu (% 47) hava akışı Kuzey Afrika (SAH) ve Orta Doğu (MID) bölgelerinden kaynaklandığında gözlemlendi. α'nın bir fonksiyonu olarak AOK ile su buharı (SB) arasındaki ilişkiyle ilgili olarak üç aerosol sınıfı tanımlandı, su sevmez (non-higroscopic), orta derecede su sever ve su sevmez (higroscopic). Potansiyel Kaynak Katkı Fonksiyonu (PKKF) su sevmez parçacıkların Kuzey Afrika ve Orta Doğu kökenli mineral tozun baskın olduğu aerosol popülasyonlarıyla ilişkili olduğunu gösterdi. Orta derecede su sever parçacıkların mineral toz ve insan kaynaklı aerosollerin bir karışımı olup, mineral tozun endüstriyel ve yüksek nüfuslu bölgelerin (örneğin, İspanya, Fransa ve İtalya) üzerinden hareket etmesine bağlı olduğu bulundu. Öte yandan, su sever parçacıklar için herhangi bir özel potansiyel kaynak bölgesinin belirlenememesi, ikincil aerosollerin hakim yaz koşulları altında orta ölçekte oluşturulduğunu gösterdi.

Kırılma indisinin hayali kısmı, tekil saçılım albedosu ve absorpsiyon angstrom katsayısı toz, karışık köken ve kirlilik olayları için belirgin farklar gösterdi. Kırılma indisinin hayali kısmı toz olayları için 870 ve 1020 nm dalga boyları arasında 2.5 x 10^{-3} ila 2.0 x 10^{-3} arasında dalgalanma gösterirken, 675 nm ve 440 nm dalga boyları arasında kırılma indisinin hayali kısmı 4.3 x 10^{-3} ‘ten 11.0 x 10^{-3} ‘e yükseldi. Benzer spektral davranışlar gözlendiği halde, 440 nm’de kırılma indisinin hayali kısmı karışık kökenli aerosol olayında mineral toz olaylarına göre 2.2 kat daha az bulundu. Kirlilik olaylarında kırılma indisinin imajiner kısmı 1020 nm’de 5.0 x 10^{-3} ‘den 440 nm’de 6.3 x 10^{-3} ‘e hafif bir artış gösterdi. Aerosol türleri sönümlenme angstrom katsayılarına göre toz, karışık kökenli ve insan kökenli olmak üzere üç gruba ayrıldı. Üç aerosol türünün mikrofiziksel özelliklerinin kıyaslanmasında sönümlenme angstrom katsayısı esas alınarak yapılan aerosol türü sınıflandırmasının yetersiz olduğunu ortaya koydu. Optik özelliklere yığın analizi uygulanarak yapılan aerosol türü sınıflandırması nispeten daha iyi sonuçlar verdi.

440 nm’de aerosol optik kalınlık ve kırılma indisinin hayali kısmı Periyot II’de (2005-2009) çöl bölgelerinden kaynaklanan toz olaylarının daha etkili olmasına bağlı olarak Periyot I’e (2000-2004) ve Periyot III’e (2010-2014) kıyasla istatiksel olarak daha yüksek bulundu. $PM_{2.5}$’da bulunan suda çözünebilir iyonlar arasında sülfat ve amonyumun baskın türler olduğu görüldü. Sülfat ve amonyum derişimlerinin aritmetik ortalaması sırasıyla 2814 ng m^{-3} ve 1371 µg m^{-3} olarak tespit edildi. Aerosoldaki nitratın aritmetik ortalaması 495 ng m^{-3} bulundu. Öncül gazlar arasında amonyak 3330 ng m^{-3} ile en yüksek derişim gösterdi. Sülfür dioksit ve nitrik asit derişimleri sırasıyla 879 ng m^{-3} ve 346 ng m^{-3} bulundu. Sülfat, amonyum ve nitrat gazdan parçacığa dönüşüm oranlarının aritmetik oranlarına ilişkin olarak bu türlerin esas olarak yöresel olmayan kaynaklardan etkilendiği öne sürülebilir. Bu çalışma ve önceki off-line ölçümler dikkate alındığında, sülfat, nitrat ve bunların öncül gazlarının Doğu Akdeniz’de bir azalma eğilimi gösterdiği ortaya konmuştur.

Anahtar: Aerosol optik ve fiziksel özelikler, higroskopik özellik, SSA, AAOT, kırılma indeksi, SO_4^{2-}, NH_4^+, NO_3^-, SO_2, NH_3, HNO_3, Doğu Akdeniz.

To my lovely wife GÜL
And
My beautiful twin daughters Nefes and Birce
And
My family.

ACKNOWLEDGEMENTS

I am deeply grateful to my supervisor Assoc. Prof. Dr. Mustafa KOÇAK for his patience, guidance and support in the every stage of this work. Without his expertise, this study would never been completed.

I am very grateful to Prof. Dr. Nikolaos Mihalopoulos, Assoc. Prof. Dr. Malcolm Nimmo, Assoc. Prof. Dr. M. Fatih Hüseyinoğlu and Assoc. Prof. Dr. Barış Salihoğlu for their valuable contribution.

I would to like to thank Pınar KALEGERİ for her assist in near real time Ambient Ion Monitor-Ion Chromatography measurements and also her friendship.

Special thanks to the AERONET groups who kindly provided their data. This study was also supported by the DEKOSIM (Center for Marine Ecosystem and Climate Research) Project (BAP-08-11-DPT.2012K120880) funded by Ministry of Development of Turkey. Furthermore, the work presented here is supported in part by this TUBİTAK project (113Y104) and BAP-08-11-2014-021 by METU.

Satellite aerosol optical thickness, aerosol index, and active fires values used in this study were produced with the Giovanni online data system, developed and maintained by the NASA GES DISC. We also acknowledge the MODIS and OMI mission scientists and associated NASA personnel for the production of the data used in this research effort. We also thank NCAR/NCEP for providing the reanalysis datasets.

I should also like to express my gratitude to my team member, Gültekin Yılmaz and the many persons who directly or indirectly have contributed to this work.

TABLE OF CONTENTS

LIST OF TABLES

LIST OF FIGURES

CHAPTER I

1. INTRODUCTION

1.1. Aim of the Study

Aerosols play a crucial role in various geophysical and geochemical processes. Figure 1.1 illustrates the influence of aerosols on the global processes. Atmospheric particles can alter the earth's radiation and hence climate directly by scattering and absorbing both incoming solar radiation and re-emitted radiation from the surface of the Earth to the atmosphere (Haywood and Shine, 1997). Aerosols can play a critical role in the hydrological cycle (Rosenfeld *et al.*, 2008). Atmospheric particles serve as ice nuclei (IN) or cloud condensation nuclei (CNN) and hence they can influence the concentration and size distribution of cloud droplets; alter the distribution of rainfall and their radiative properties (Levin *et al.*, 2005; Huang *et al.*, 2006).They may act as reaction surfaces in the atmosphere. Field and laboratory studies have demonstrated that chemical reactions can occur between mineral dust and inorganic/organic species (such as nitric acid, sulfur dioxide, sulfuric acid, oxalic acid and ozone) depending on the mineralogical composition (Arimoto, 2001; Usher *et al.*, 2003; Kruger *et al.*, 2004). Atmospheric inputs (from wet and dry modes) may have negative and positive impact on marine environments. They supply macro and micro nutrients, such as P and Fe respectively, which might play a significant role in LNLC (Low Nutrient Low Chlorophyll) and HNLC (High Nutrient Low Chlorophyll) regions of the world oceans. Inhibition has been observed for specific phytoplankton species due to soluble copper associated with mineral dust particles (Paytan *et al.*, 2009). On the other hand, remarkable increase (up to 5 fold) in chlorophyll and primary production has been monitored during micro-cosm dust addition experiments (Herut *et al.*, 2005).

The Mediterranean Sea is bordered on its southern and eastern shores by desert regions including Sahara and Middle East deserts. These regions act as a source of mineral dust aerosols which are transported in the form of episodic pulses. Long range transport of mineral dust from the Sahara to the Eastern Mediterranean has been mainly observed during spring with the eastward passage of a frontal low pressure system, whereas mineral dust transport from the Middle East has been primarily monitored in the autumn (Kubilay *et al.*, 2000). On the other hand, the northern shore of the Mediterranean is surrounded by semi-industrialized and industrialized regions, which act as a continuous source of anthropogenic aerosols. The Mediterranean atmosphere is influenced by different pollutant sources from Western and Eastern Europe (Lelieveld *et al*., 2002). Therefore, one of the highest atmospheric deposition, aerosol optical thickness and radiative forcing in the world have been detected over the Mediterranean region (Kubilay *et al*., 2003; Barnaba and Gobbi, 2004; Vrekoussis *et al*., 2005; Papadimas *et al*., 2009; Koçak *et al*., 2010).

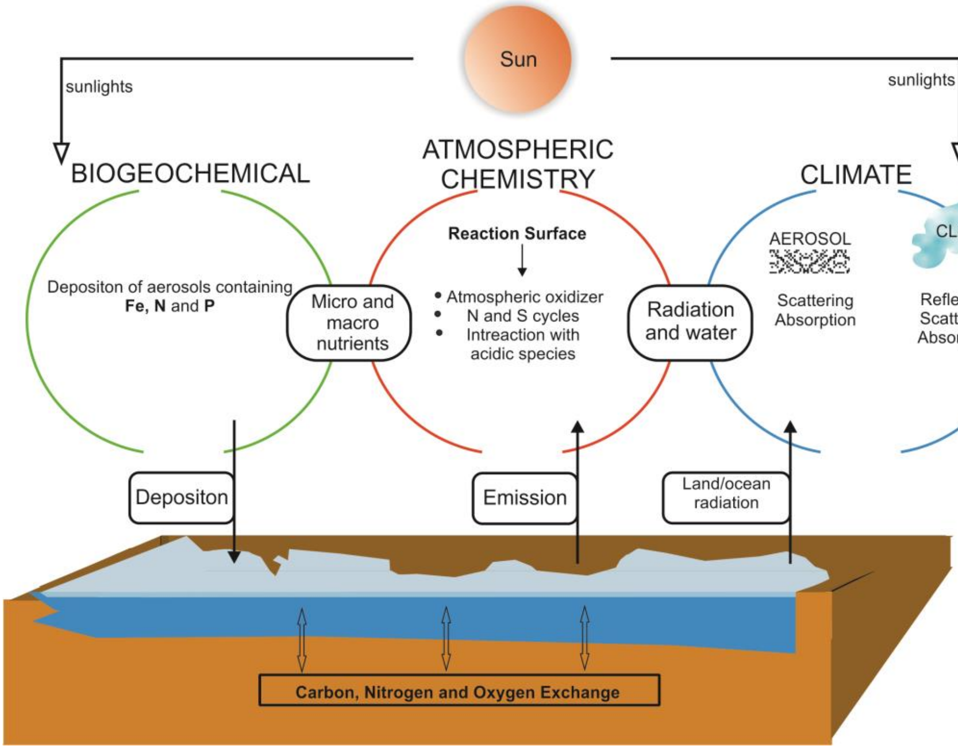

Figure 1.1 Impact of aerosols on global processes (inspired from Arimoto, 2001 and Shao *et al*., 2011).

Aerosol burden in the atmosphere and its radiative effects are spatially and temporally inhomogeneous and should be observed globally. The lack of detailed information of the optical and microphysical properties of aerosol leads to the large uncertainties in radiative forcing calculations (Charlson *et al*., 1992, Tegen *et al*., 1996, Hansen *et al*., 2000, Ramanathan *et al*., 2001). Thus, optical and microphysical properties of aerosol types are vital for better understanding aerosol radiative forcing and impact on climate change. For instance, mineral dust plays a significant role in radiative process (Miller and Tegen 1998). Optical properties of mineral dust can exhibit significant spatial variability according to its mineral and chemical composition (Sokolik and Toon 1990). Taking into account literature, aerosol optical and micro physical properties have not been well studied in the Eastern Mediterranean. The current study aims to explore the optical properties of the aerosol burden in the atmospheric column over the Eastern Mediterranean. This will be achieved by using a

15-year long dataset from the AERONET sun/sky radiometer. The unique contribution of the present study will be to (i) explore the climatology of the aerosol optical properties regarding their spectral behavior, (ii) assess the influence of meteorological parameters on the seasonal variability in aerosol optical properties, (iii) clarify the hygroscopic state of aerosols and source regions, (iv) classify aerosol types according to aerosol optical properties namely, aerosol optical thickness, aerosol absorption optical thickness, angstrom exponent, absorption angstrom exponent, single scattering albedo and refractive index, (v) evaluate the effect of climatological change on the aerosol optical thickness and angstrom exponent. Furthermore, this study aims to define, for the first time near-real time sulfate, ammonium and nitrate in $PM_{2.5}$ and their precursor gases concentrations in winter and summer as well as gas-to-particle conversions in the atmosphere over the Eastern Mediterranean.

1.2. Atmospheric Aerosols

An aerosol is described as a suspension of solid or liquid particles in a gaseous phase. Atmospheric particles originate from numerous sources namely, natural (e.g. mineral dust, sea salt, volcanic particles) and anthropogenic (e.g. fossil fuel combustion). Consequently, aerosols are composite mixture of insoluble and soluble constituents. This composite mixture can be categorized into five main classes: i) mineral dust, ii) sea salt, iii) sulfates, iv) nitrates and v) carbonaceous.

Figure 1.2 illustrates the size, generation and removal of atmospheric particles. As can be deduced from Figure 1.2, the particle size varies from a few nanometers to 100 micrometers. In general, the size of aerosols is divided into two groups: (i) coarse (d > 2.5 μm) and (ii) fine (d < 2.5 μm). This reflects two main formation mechanisms primary and secondary (Fine *et al.*, 2008, Koçak *et al.*, 2007 and Koulouri *et al.*, 2008). The size distribution of aerosols is mostly effected by the formation mechanisms.

Primary aerosol generation is a mechanical mechanism and such particles are ejected from the break up and suspension of bulk material (sea salt, soil dust and biological material) by the wind. Aerosols in this category are generally associated with particles of diameter exceeding 2.5 μm (coarse mode). Secondary aerosol formation involves a gas-to-particle conversion. Therefore, secondary aerosols are produced by transformation of gaseous constituents to liquid and solid with aerosols in this class being mainly associated with particles of diameter smaller than 2.5 μm (fine mode). Newly formed aerosols show a peak around 0.01 μm diameter and they are referred to as Aitken nuclei or transient nuclei owing to their short lifetime. These aerosols quickly coagulate to form bigger particles that typically fall in the size range between 0.1 and 1 μm diameter and this size group is referred to as the 'accumulation mode' since particle removal mechanisms are least efficient in this size (Seinfield and Pandis, 1998).

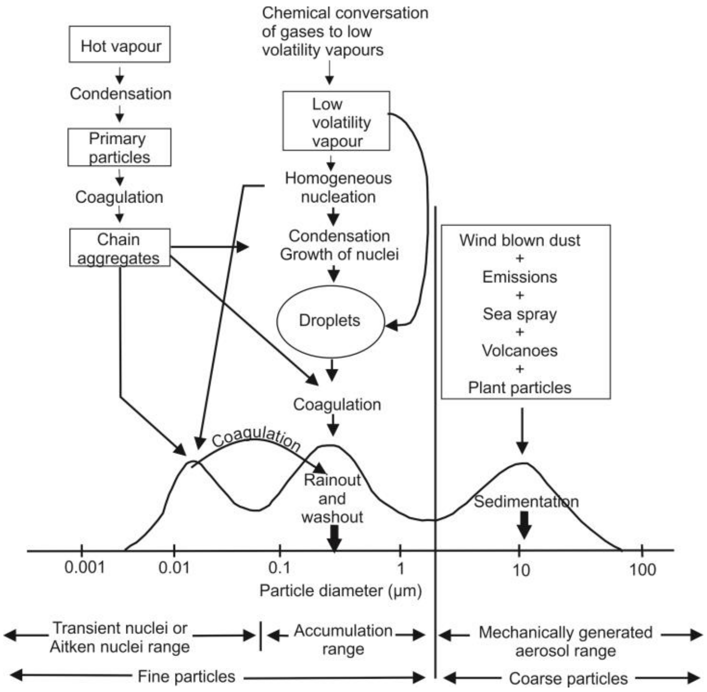

Figure 1.2 Schematic representation of three modes and of processes involved in generation and removal of atmospheric particles (modified from Seinfield and Pandis, 1998).

i) Mineral Dust: Mineral dust is emitted directly from soils in the source regions by winds. They are mainly affiliated with coarse particles, varying from few to tens of micrometers; however, they are partly associated with fine particles (Duce, 1995). Mineral dust particles (~ 1500 Tg y^{-1}) are one of the main components of Earth's atmospheric aerosols, comprising about half of the total aerosol burden (Seinfeld and Pandis, 2006).

ii) Sea Salt: Sea salt particles comprise of sodium, chloride and sulfates. Sea salt particles are produced at the sea surface by the bursting of air bubbles resulting from air induced by wind (Blanchard and Cipriano, 1983), representing 25 % of the aerosol burden.

iii) Sulfates: Sulfates are emitted by a variety of natural and anthropogenic sources. Burning of coal, petroleum products, smelting of non-ferrous ores, manufacture of sulfuric acid, the conversion of pulp into paper, and refuse incinerators are man-made sources of sulfate. The natural sources include biogenic and non-biogenic particles. The biogenic sulfate particles originate from biogenic emissions from oceans, plants, wetlands and soils and biomass burning whilst non-biogenic sulfate arise from sea salt/ mineral dust (as $CaSO_4$) and volcanic eruptions (Saltzman *et al*., 1986; Savoie *et al*., 1994; Mihalopoulos *et al*., 1997; Kouvarakis and Mihalopoulos, 2002; Kubilay *et al*., 2002).

iv) Nitrates: Natural sources of nitrate contain lightning, biological material and nitrification-denitrification processes but anthropogenic sources include combustion of fossil fuels, fertilizers, motor vehicles and nitric acid production (Prospero *et al*., 1996).

v) Carbonaceous Particles: These particles comprise of two main components: Organic material and black carbon. Black carbon is emitted during the combustion process and is therefore solely primary. Whereas, organic matter directly arises from sources or it may be formed by atmospheric reactions involving gaseous organic precursors (Seinfeld and Pandis, 1998)

1.3. Precursors of Aerosol SO_4^{2-}, NO_3^- and NH_4^+

SO_2 (g): Sulfur dioxide plays a central role in aerosol sulfate formation. On a global scale, 85 % of the sulfur dioxide has been attributed to anthropogenic sources such as the burning of fossil fuel (industry, thermic power plants), incineration, sulfuric acid production, pulp and paper industry, metal industry and vehicles (Whelpdale *et al*., 1996). Natural sources consist of volcanic emissions, vegetation and biological activities, accounting for 15 % of the total sulfur dioxide production. Anthropogenic sulfur dioxide emissions on a global scale between 1850 and 2005 are given in Figure 1.4. In the first 50 year, sulfur dioxide emissions dramatically increased by about 10 times, attaining 20,000 Gg levels. This increase was mainly attributed to the burning of coal (Smith *et al*., 2011). Up to the1950s, sulfur dioxide emissions increased at a steady pace, reaching 58,000 Gg. By the 1980s, sulfur dioxide emissions reached a peak with a value of 127,000 Gg and remained almost constant until 1990s. From 1990s to 2000s, emissions denoted a substantial decrease due to sulfur removal technology yet there was a noticeable enhancement by 2005 as result of emissions from developing countries such as China.

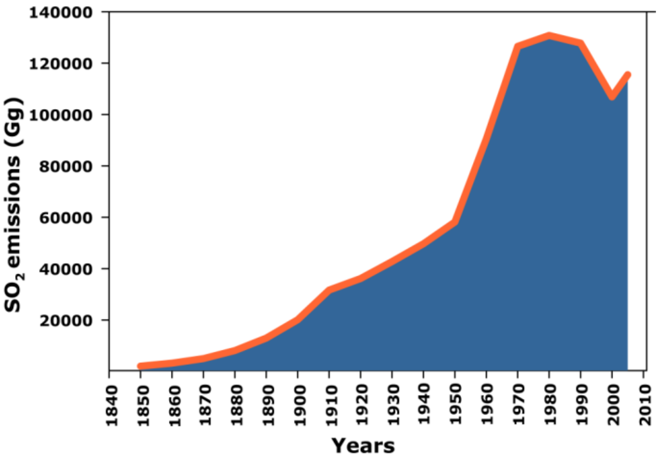

Figure 1.3 Anthropogenic sulfur dioxide emissions on a global scale between 1850 and 2005 (reconstructed from Smith *et al*., 2011).

Oxidation of sulfur dioxide to sulfate occurs throughout both homogeneous and heterogeneous reactions (Seinfield and Pandis, 1998, Finlayson-Pitts and Pitts, 1999). Hydroxyl radicals are the most significant oxidant in the homogeneous gas phase reactions. These reactions can be summarized as follow:

$$SO_2 + OH + M \rightarrow HSO_3\,(g) + M\ [1.1]$$

$$HSO_3(g) + O_2 \rightarrow SO_3\,(g) + HO_2\ [1.2, fast]$$

$$SO_3(g) + H_2O + M \rightarrow H_2SO_4\,(g) + M\ [1.3, fast]$$

The lifetime of sulfur dioxide in homogeneous reactions ranges from 1 to 2 weeks. Nonetheless, in the presence of water gas-to-particle conversion is accelerated owing to aqueous phase chemistry (Seinfield and Pandis, 1998, Finlayson-Pitts and Pitts, 1999). Heterogeneous oxidation reactions occur within clouds or fog droplets since sulfur dioxide has a very high solubility in water. These reactions are given below:

$$SO_2\,(g) + H_2O(aq) \rightarrow SO_2 \cdot H_2O\ [1.4]$$

$$SO_2 \cdot H_2O \leftrightarrow HSO_3^- + H^+\ [1.5]$$

$$H_2O_2(g) \leftrightarrow H_2O_2(aq)[1.6]$$

$$HSO_3^- + H_2O_2(aq) + H^+ \leftrightarrow SO_4^{2-} + 2H^+ + H_2O[1.7]$$

HNO_3 (g): Nitric acid is produced by the oxidation of NO_x. Precursors NO and NO_2 (referred to as NO_x) have crucial function in aerosol nitrate formation. Sources of NO_x

are traffic, fossil-fuel combustion, biomass-burning, soil emissions and lightning. Nitric acid is formed throughout day and night time reactions of NO_x. In the presence of ozone, NO (g) is rapidly oxidized to NO_2 (g) (Seinfield and Pandis, 1998, Finlayson-Pitts and Pitts, 1999).

$$NO\ (g) + \ O_3(g) \rightarrow \ NO_2(g) + \ O_2\ (g) \text{ [1.8]}$$

Nitric acid is yielded via OH oxidation of NO_2 (g) during day time reactions (Seinfield and Pandis, 1998, Finlayson-Pitts and Pitts, 1999).

$$NO_2\ (g) + \ OH\ (g) + \ M \rightarrow \ HNO_3\ (g) + \ M \ \text{ [1.9]}$$

In the night time, nitric acid is yielded throughout the following reactions (Seinfield and Pandis, 1998, Finlayson-Pitts and Pitts, 1999):

$$NO_2\ (g) + \ O_3(g) \rightarrow \ NO_3(g) + \ O_2\ (g) \text{ [1.10]}$$

$$NO_2\ (g) + NO_3(g) + \ M \ \rightarrow \ N_2O_5\ (g) + \ M \text{ [1.11]}$$

$$N_2O_5\ (g) + H_2O\ (surface) \rightarrow 2HNO_3(g) \ \ \text{ [1.11]}$$

NH_3 (g): Ammonia is emitted from variety of sources including agricultural practices, livestock husbandry, manure/storage/application, traffic, biomass-burning, waste/sewage management, industrial manufacturing, natural soils and vegetation (Bouwman *et al*., 1997; Paulot *et al*., 2014; Van Damme *et al*., 2014). Ammonia plays an important role neutralizing acidic inorganic (e.g. sulfuric and nitric acid) and organic species (such as oxalic acid) (Behara and Sharma, 2010; Updyke *et al*., 2012). During the neutralization reactions between alkaline ammonia and acidic sulfuric/nitric acid these salts are produced: NH_4HSO_4, $(NH_4)_2SO4$ and NH_4NO_3.

1.4. Long Range Transport

The Mediterranean Sea is bordered on its southern and eastern shores by desert regions including the Sahara and Middle Eastern deserts. These regions act as a source of mineral dust aerosols which are transported in the form of episodic pulses. Long range transport of mineral dust from the Sahara to the Eastern Mediterranean has been mainly observed during spring with the eastward passage of a frontal low pressure system, whereas mineral dust aerosols originated from the Middle East have been chiefly monitored in the autumn (Kubilay *et al*., 2000). In contrast, the northern shore of the Mediterranean is enclosed by industrialized and semi-industrialized regions, which act as a continuous source of anthropogenic dominated aerosols, dispersed to the regional atmosphere all year around (Dulac *et al*., 1987; Kubilay and Saydam, 1995). Long range transport of aerosols plays a crucial role in the aerosol burden at a receptor site. To understand and locate the possible sources of Mediterranean aerosols, back trajectory analysis has been applied by researchers (Dayan, 1986; Dulac *et al*., 1987; Kubilay and Saydam, 1995; Luria *et al*., 1996; Mihalopoulos *et al*., 1997; Kubilay *et al*., 2000, 2002, 2005; Rodriguez *et al*., 2001, 2002; Lelieveld *et al*., 2002; Toledano *et al*., 2009; Gerasopoulos *et al*., 2011).

Lelieveld *et al*. (2002) have shown that the Mediterranean atmosphere in summer is influenced by different pollutant sources as a result of long range transport. The study emphasized that the atmosphere within the boundary layer was loaded with pollutants emitted from both Western and Eastern Europe, whereas in the middle and upper troposphere Asian and to a lesser extent North American pollutants are transported from the west to the region.

Long range transport from desert regions to the Mediterranean has also been debated in numerous studies (Moulin *et al*., 1998; Kubilay *et al*., 2000). Long range transport from North Africa to the eastern Mediterranean occurs predominantly during spring and is usually associated with eastward passage of a frontal low pressure system whereas dust intrusions from the Middle East to the Eastern Mediterranean takes place typically in autumn (Kubilay *et al*., 2000). In contrast, transport from North Africa to the western and central Mediterranean are observed mainly during summer (Moulin *et al*., 1998).

1.5. Influence of Aerosols on Global Processes

1.5.1. Influence of Aerosols on Climate

Atmospheric particles exhibit extensively different optical properties than atmospheric gases and they may can scatter and absorb solar radiation. As a result of these features, aerosols modify the radiative budget of the atmosphere and also may indirectly affect the radiative budget by acting as cloud condensation nuclei (CCN).

1.5.1.1. Radiative Properties of Aerosols

As it is well documented, the influence of aerosols on the climate depends on their geographic distribution (see section 4.1), optical properties and ability to act as a cloud condensation nuclei (CCN) (Lohmann and Feichter, 2005, Dusek *et al*., 2006). Vital quantities related to optical and CCN properties can be gives as: (i) particle size distribution, (ii) scattering (single scattering albedo) and absorption (absorption aerosol optical thickness) and (iii) chemical composition and mixing state (absorption angstrom exponent, refractive index) (Holben *et al*., 2001; Dubovik *et al*., 2002).

Figure 1.4 demonstrates particle size distribution (PSD) , angstrom exponent (AE) and single scattering albedo (SSA) for key aerosol types namely: (i) Urban/Industrial (Goddard Space Flight Center (GSFC), Creteil/Paris, Mexico City), (ii) Biomass Burning (Amazonian Forest, South American Cerrado, African Savannah, Boreal Forest) and (iii) Desert Dust (Bahrain/Persian Gulf, Solar Village/Saudi Arabia, Cape Verde/Sal Island), (iv) Mixed Aerosol (Maldives) and (v) Oceanic Aerosol (Lanai/Hawaii). Based on Figure 1.4, the following summary can be made:

(a) Urban/Industrial and Mixed Aerosol Type: SSA value (0.98 at 440 nm) observed at GSFC denotes that aerosol over this site is almost non-absorbing and this low absorbing character is attributed to dominance of water-soluble atmospheric particles (Dubovik *et al*., 2002 and references therein). On the other hand, aerosol population at Mexico City (SSA = 0.90 at 440 nm) and Maldives (SSA = 0.91 at 440 nm) illustrate absorbing properties. The aerosol absorption at Creteil/Paris is intermediate (SSA = 0.94 at 440 nm). PSD shows peak around 0.12 μm and total volume of fine particles is larger than that of coarse (C_{vf}/C_{vc} ~ 3, Dubovik *et al.*, 2002) for GSFC and Creteil/Paris. In contrast, PSD at Mexico City and Maldives is significantly influenced by coarse particle (C_{vf}/C_{vc} ~ 1), mainly being between 1.5-5 μm.

(b) Biomass Aerosol Type: In general, biomass burning aerosols lead to low SSA since it contains remarkable amount of black carbon owing to combustion processes (Giles *et al*., 2012). As can be seen from the figure, SSA exhibits great variability from one biomass burning site to another. The lowest SSA (0.88 at 440 nm or highest absorption) is detected over African Savanna whilst the highest SSA values are observed at Amazon and Boreal forests with value of 0.94 at 440 nm. The intermediate SSA value (0.91 at 440 nm) is found at South American Cerrado. PSD for all biomass burning sites is predominated by fine particles, varying within the accumulation mode (from 0.1 to 0.3 μm).

(c) Desert Aerosol Type: The SSA for desert aerosol type increases with increasing wavelength (λ) because it is mainly consists of coarse particles containing iron oxides (Dubovik *et al*., 2002). SSA value is around 0.92 (at 440 nm) for all desert sampling sites (Bahrain/Persian Gulf, Solar Village/Saudi Arabia, Cape Verde/Sal Island). While PSD is dominated by coarse particles (chiefly between 1.9 and 2.54 µm), PSD exhibits bimodal distribution (Dubovik *et al*., 2002).

(d) Oceanic Aerosol Type: SSA for Lanai/Hawaii is 0.98 at 440 nm, implying low absorption characteristic of oceanic atmospheric particles (Dubovik *et al*., 2002). Although PSD is significantly affected by coarse particles (C_{vf}/C_{vc} ~ 0.5; Dubovik *et al*., 2002), the low absorption suggests sea-salt and water-soluble particles.

Single scattering albedo (SSA) and corresponding aerosol absorption optical thickness (AAOT) for (i) Urban/Industrial (Goddard Space Flight Center (GSFC), Creteil/Paris, Mexico City), (ii) Biomass Burning (Amazonian Forest, South American Cerrado, African Savannah, Boreal Forest) and (iii) Desert Dust (Bahrain/Persian Gulf, Solar Village/Saudi Arabia, Cape Verde/Sal Island), (iv) Mixed Aerosol (Maldives) are demonstrated in Figure 1.5. The highest AAOT is observed at South American Cerrado (~0.08 at 440 nm), however, the lowest AAOT is found at GSFC with a value of ~0.007 at 440 nm. The former might be attributed to absorbing particles such as black carbon whereas; the later might be resulted from water-soluble particles (Dubovik *et al*., 2002; Giles *et al*., 2012). As can be deduced from the diagram, AAOT for Urban/Industrial and biomass burning aerosol types decreases monotonously with increasing wavelength nonetheless there is a sharp decrease in AAOT with increasing wavelength for desert type aerosol (Russell *et al*., 2010). This drastic diminish is likely due to the particle size distribution of desert dust which is principally dominated by coarse particles.

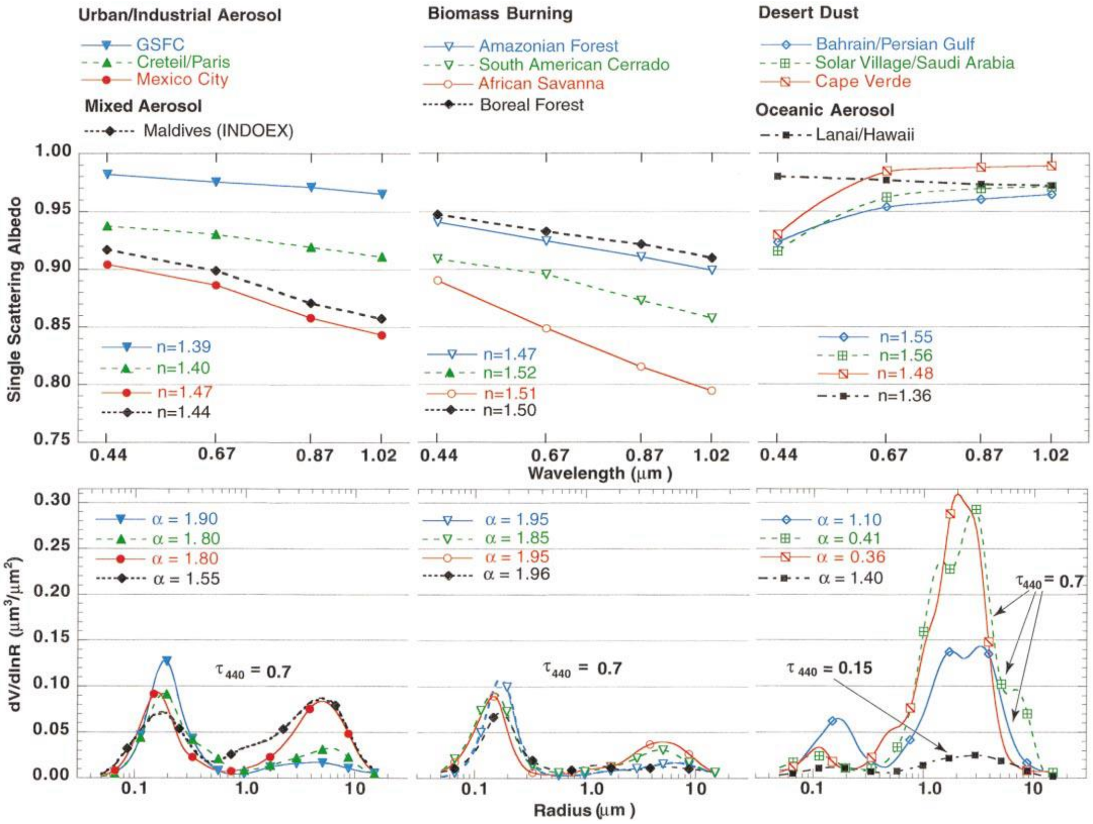

Figure 1.4 The averaged optical properties of different types of tropospheric aerosol retrieved from the worldwide AERONET network of ground-based radiometers. Taken from Dubovik *et al.*, (2002).

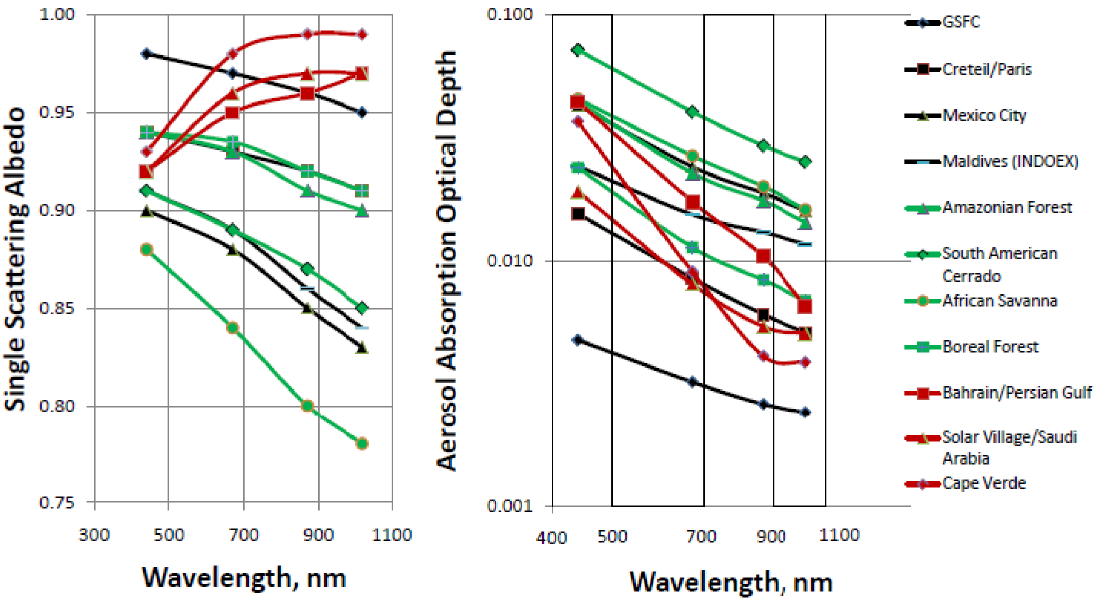

Figure 1.5 Spectra Of AERONET-derived Single Scattering Albedo (SSA) from Dubovik *et al.*, 2002 with corresponding Aerosol Absorption Optical Depth (AAOD) Black: Urban/Industrial or Mixed; Green: Biomass Burning; Red-Brown: Desert Dust. Taken from Russell *et al.*, 2010.

1.5.1.2. Global Distribution of Aerosols

Global spatio-temporal variability in **A**erosol **O**ptical **D**epth (AOD) retrieved by **M**ultiangle **I**maging **S**pectro **R**adiometer (MISR) sensor at spatial resolution of 0.5°×0.5° is given in Figure 1.6 (Mehta *et al.*, 2016). AOD values lower than 0.1 exhibits clear sky whilst values around 1 shows very high aerosol burden in the atmospheric column.

High AOD values are related to distinct processes in different regions and seasons of the year. Annual AOD map clearly exhibits remarkable difference between Northern and Southern Hemispheres, former having much more higher values mainly due to deserts and industrialized and populated countries.

Desert areas of the world are the chief source of mineral dust. The largest and most persistent sources (see Figure 1.7, for example Sahara Desert) have been identified in the Northern Hemisphere principally in a broad dust belt that extends from the west coast of North Africa over the Middle East, central and south Asia to China (Prospero *et al*., 2002; Washington *et al*., 2003). These studies have clearly revealed the dominance of the Sahara and demonstrated other key source regions including the Middle East, Taklamakan, south Asia, central Australia, the Ethosha and Mkgadikgadi basins of southern Africa, the Salar de Uyuni (Bolivia), and the Great Basin (United States).

Image particularly exhibits high AOD values (up to 1) over the desert regions of the world. Over North Africa and Equatorial Atlantic high annual AOD (0.3-1) are found whilst highest and lowest values are detected in JJA and DJF, respectively. Elevated AOD values over South Africa are clear in JJA due to biomass burning (Eck *et al*., 2009, 2013; Mehta *et al*., 2016). Similarly, high AOD values are obvious over the Middle East chiefly owing to deserts with a maximum in JJA period (Smirnov *et al*., 2002; Eck *et al*., 2008; Mehta *et al*., 2016). However, it worth mentioning that, aerosol burden in this region is also impacted by manmade activities such as vehicles, petroleum industry and shipping (Mehta *et al*., 2016).

Low AOD values are observed over Europe and Russia whilst higher aerosol burdens are found over Mediterranean particularly in MAM and JJA period because of (i) dust transport from Sahara and Middle East desert, (ii) increase in secondary aerosol and (iii) enhanced biomass burning (Kubilay et and Saydam, 1995; Mihalopoulos *et al*., 1997; Moulin *et al*., 1998; Kubilay *et al*., 2000; Sciare *et al*., 2008;

Koçak *et al*., 2005, 2012). Moderate to high AOD values (0.3-0.9) are particularly found over Eastern China and India and adjoining Arabian Sea (Eck *et al*., 2008, 2010; Giles *et al*., 2011; Mehta *et al*., 2016) whereas low AOD values (<0.2) are observed over the Pacific Ocean . Enhanced AOD values over Pacific in MAM period are related to anthropogenic and dust particles transported mostly from the Asian mainland (Smirnov et al., 1995; Mehta et al., 2016). AOD over Eastern China and India reaches its maximum in JJA season. In general, low AOD values are detected over South America. Relatively higher values are clear over desert regions such as Atacama and Amazon forest. High values over Amazon in SON season are as a result of deforestation and biomass burning (Schafer et al., 2002, 2008; Eck et al., 2003). The annual AOD values over North America remain less than 0.2 however; higher values are clear in MAM and JJA seasons since AOD burden is influenced by both natural and manmade sources (Holben et al., 2001; Eck et al., 2010; Schafer et al., 2014; Mehta et al., 2016) .

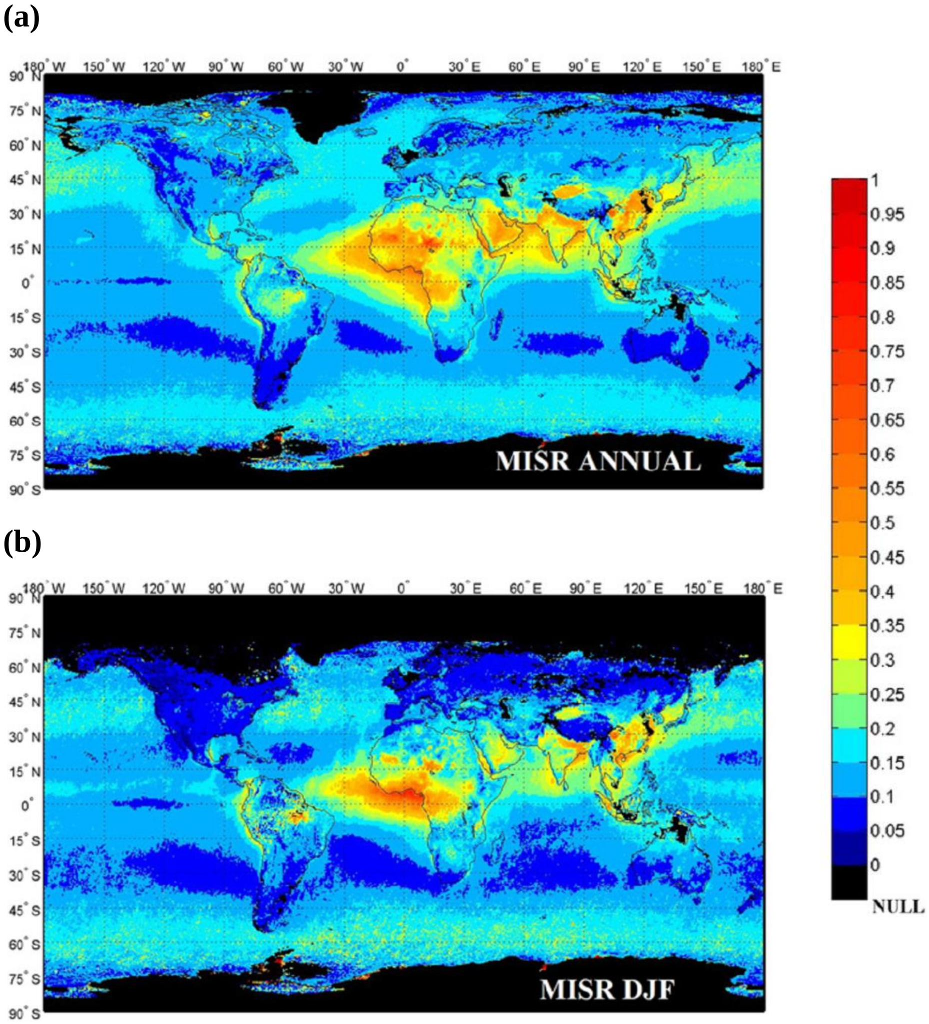

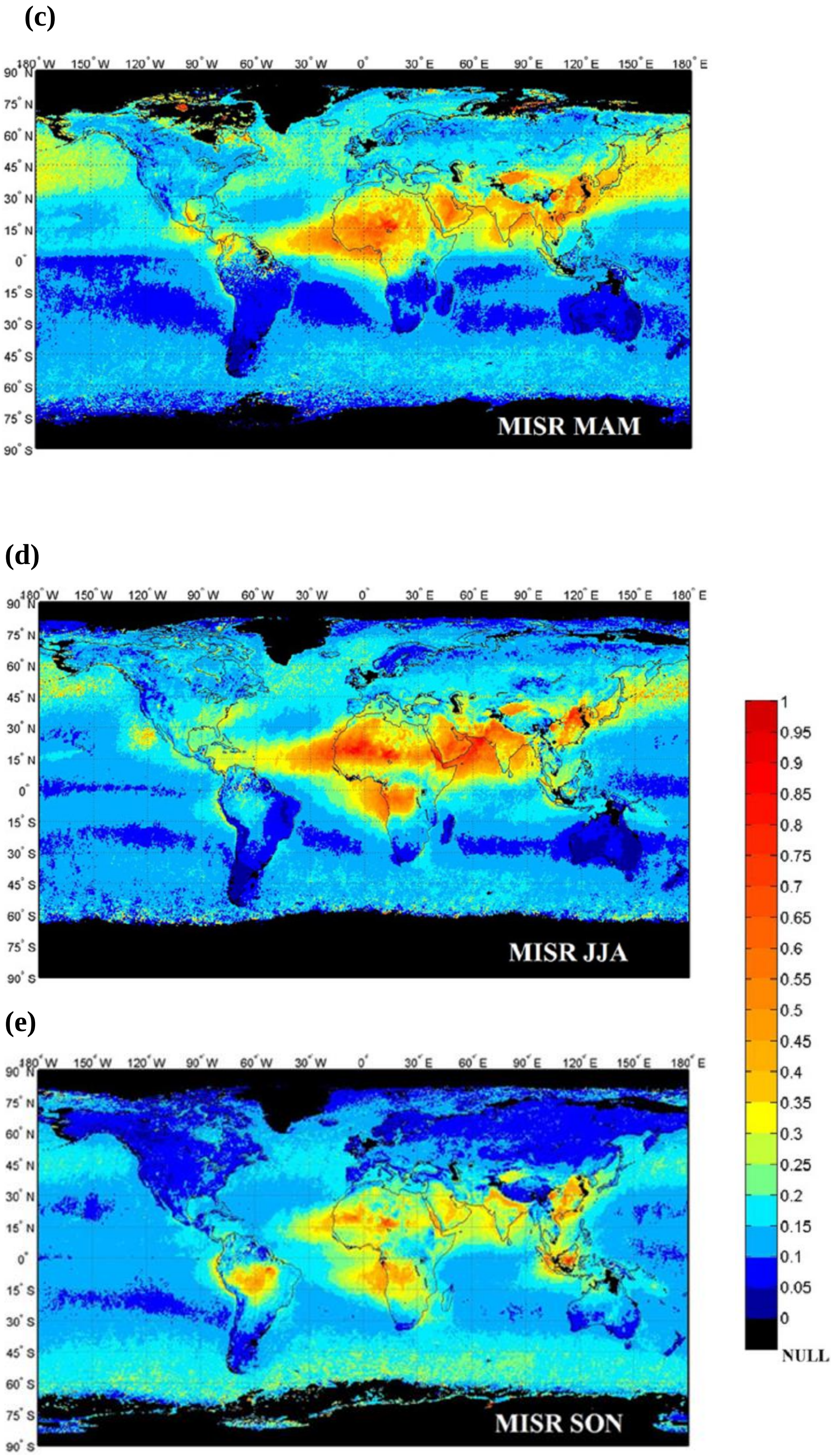

Figure 1.6 Annual and seasonal variations of aerosol optical depth from Multiangle Imaging Spectroradiometer (MISR), **(a)** annual, **(b)** winter (DJF), **(c)** spring (MAM), **(d)** summer (JJA) and **(e)** autumn (SON). Taken from Mehta et al., 2016.

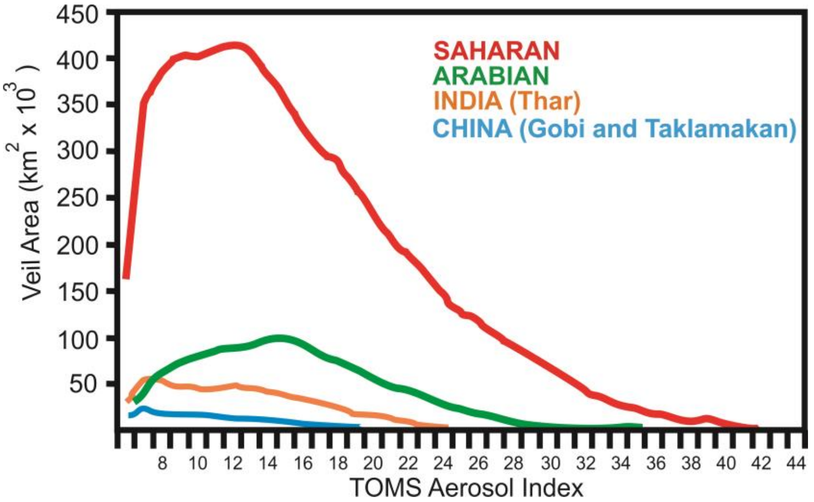

Figure 1.7 Area average TOMS AI values for the main dust regions. Modified from Washington *et al*., 2003.

Ground-based sky radiance sun photometer measurements (see section 4.1) also supports the above findings (see Figure 4.1). One of the lowest AOT with a value of 0.02 are observed at Mauna-Lao (Yoon *et al*., 2012) since it is above the planetary boundary layer (altitude of 3397 m). The aerosol exponent (1.2) suggests contribution of stratospheric aerosols to the columnar AOT over the site. AOT (0.4) and α (0.3) values at Capoverde/Sal Island, Dakar (rural coastal), Banizoumbou (rural/semi-arid) and Solar Village (rural) reflect heavy influence of mineral dust on aerosol burden (Holben *et al.*, 2001, Yoon *et al*., 2012, Gama *et al*., 2015). The highest AOT values are detected over the urban sites in Asia, namely, Taihu (~ 0.9, Xia *et al*., 2007) and Beijing (~ 0.7, Yoon *et al.*, 2012). It has been stated that these two Asian sites are under the heavy pressure of regional pollution (Xin *et al*., 2007).

1.5.1.3. Impact of Aerosols on Radiative Forcing

Figure 1.8 illustrates (produced from IPCC 2013; Dobbie *et al*., 2003; Papadimas *et al*., 2012) global radiative forcing of aerosols along with Green House Gaseous (GHGs). The IPCC (2001) report denoted that the largest uncertainties in the estimation of direct and indirect radiative forcing from aerosols are related to the insufficient knowledge of the high spatial and temporal variability of aerosol concentrations, of their microphysical, chemical and radiative properties. As can be deduced from the diagram, aerosol radiative forcing was still associated with a remarkably high uncertainty whereas GHGs forcing was affiliated with low uncertainty.

Sulfate aerosols are efficient at scattering incoming solar radiation back to outer space since they are associated with submicron particles. Owing to their small size they have minute influence on outgoing terrestrial radiation. The net direct forcing of sulfate particles is one of cooling, ranging from -0.2 to -0.6 W m^{-2}. Nitrate and organic aerosols could also found in the fine particle size range (Cabada *et al.*, 2004, Peltier *et al.*, 2007 and Koçak *et al.*, 2007). These aerosols decrease the amount of incoming solar energy; the direct effect being one of cooling. The direct radiative forcing of nitrate (-0.11 W m^{-2}) was estimated to be four times lesser than that of sulfate. Corresponding, radiative effects were -0.09 and -0.03 W m^{-2} for primary organic and secondary organic aerosols, varying between -0.6/-0.03 and -0.27/0.2 W m^{-2}. Biomass burning particles denoted cancellation between cooling and warming giving value of 0 W m^{-2} and its radiative forcing fluctuated from -0.2 to 0.2 W m^{-2}. On a global basis, sea salt radiative forcing was estimated to be around -0.15 W m^{-2}.

Mineral dust also alters the Earth's radiation budget by means of scattering and absorbing of both incoming solar radiation and outgoing terrestrial radiation (e.g., Sokolik and Toon, 1996). Regarding concentration, vertical distribution in the atmospheric column, particle size and mineralogy as well as albedo and temperature of the underlying surface, the direct radiative forcing of mineral dust could be either warming or cooling (Tegen and Lacis 1996). Mineral dust illustrated direct radiative forcing of -0.1 W m^{-2}, showing cooling and warming effect around -0.3 and 0.1 W m^{-2}, respectively.

Since it is an efficient absorber of solar radiation, black carbon is one of the most important constituent of positive forcing (warming) (Jacobson, 2000, Peng *et al.*, 2016). The direct radiative forcing of black carbon ranged between 0.05 and 0.8 W m^{-2} with a mean value of 0.4.

Taking in to account the global direct forcing resulted from atmospheric particles (-0.35 W m^{-2}), roughly 10 % of the global warming caused by GHGs (2.83 W m^{-2}) is abolished by the aerosols however, if one consider both direct (-0.35 W m^{-2}) and indirect (-0.45 W m^{-2}) forcing of aerosols, the cancellation of warming would reach 28 %.

Figure 1.6 also shows total radiative forcing over the Mediterranean. Radiative forcing of aerosols in the Mediterranean is dramatically different than that of estimated for Globe. It is assessed to be -2.4 W m^{-2}, being 3 times larger than that of estimated for Globe. This value would abolish 85 % of the warming effect stemmed from GHGs.

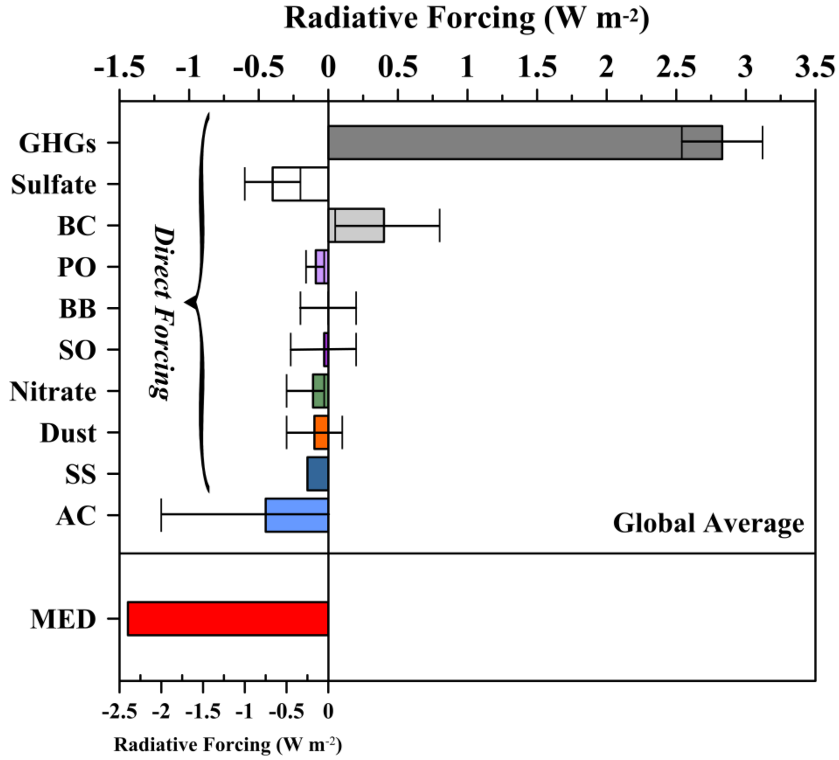

Figure 1.8 Comparison of aerosol forcing owning to various species with that of greenhouse gas forcing (GHG: Greenhouse gases, BC: Black carbon, BB: Biomass burning, SO: Secondary Organic, AC: Aerosol cloud, derived from IPCC, 2013; SS: Sea salt from Dobbie *et al*., 2003; Mediterranean taken from Papadimas *et al*., 2012)

1.5.2. Influence of Aerosols on Atmospheric Chemistry

During the transport of aerosols, they serve as media upon which chemical reactions can occur. Studies carried by different researchers have shown the relationship between atmospheric particles with trace, nitrogen and organic gases (Mamane and Gottlied, 1989, 1992; Dentener *et al*., 1996; Usher *et al*., 2003a,b; Krueger *et al*., 2004; Falkovich *et al*., 2004). Consequently, aerosols play a significant role in the removed mechanism of numerous atmospheric chemical species. Furthermore, reactions of aerosols in the atmosphere lead to a change in the physical and chemical properties of the atmospheric particles, including their optical properties and contribution to cloud condensation nuclei (Arimoto, 2001).

1.5.3 Influence of Aerosols on Biogeochemical Cycles

Aerosols transported in the atmosphere can deposit on land and oceanic surfaces, both near and far from their sources, which have important influences on biogeochemical cycles. Atmospheric deposition (wet and dry) of aerosols and gases can enhance primary productivity by suppling macronutrients as well as trace metals in areas of the ocean where primary production is nutrient limiting (Paerl, 1985; Seitzinger and Sanders, 1999; Paerl *et al*., 1999). For example, atmospheric deposition stimulates marine productivity in the oligotrophic Red Sea and the Mediterranean Sea, providing bioavailable N and P (Chen *et al.*, 2007; Herut *et al.*, 1999). Furthermore, atmospheric deposition of Fe into HNLC (High Nutrient Low Chlorophyll) regions may affect biotic process, strengthening primary production (Ussher *et al.*, 2004) or changing phytoplankton community structure (Baker *et al*., 2003).

1.6. Ground Based Real Time Measurements

1.6.1. Ground Based Sky Radiance Sun Photometer Measurements

Every object in nature emits electromagnetic energy and solar radiation is defined as electromagnetic energy emitted by the sun. The solar radiation on the top of the terrestrial atmosphere is called extraterrestrial solar radiation which is found over a wide spectrum ranging from ultraviolet to infrared rays and 97 percent of the total energy of extraterrestrial solar radiation is confined to short wavelengths (the spectral range 290 to 3000 nm). Part of the incoming solar radiation is absorbed, scattered and reflected by gas molecules, aerosols, water vapor and clouds while penetrating through the atmosphere. The solar radiation can be measured by radiometers. A radiometer absorbs solar radiation, converts it into heat and measures the resulting amount of heat relating to the level of solar radiation. Spectral measurements of direct solar radiation are used in atmosphere science to govern optical depth in the atmosphere (World Meteorological Organization, 2008)

AOT ground measurements have been performed for many years, by calculating the intensity decreased of sunlight between the top of the atmosphere (TOA) and at ground level. The radiance at TOA can be estimated from models, or measured by satellites or radiometers. Calculating AOT from measurements of the direct solar irradiance made by a radiometer is based on the Beer-Lambert law. The sun/sky spectral radiometers, namely CIMEL™ Sun Photometers are widely used in order to calculate AOT from measurements of the direct solar radiation at ground level. A wide range of these instruments have been deployed within the Aerosol Robotic Network (AERONET; Holben *et al*., 1998). Space AOT measurement can also done by satellite instruments, which provide a larger spatial coverage than AERONET. However, most AOT satellites are polar-orbiting and have low temporal resolution. Satellite algorithms for AOT works the same way used in sun photometers. Nevertheless, they have more difficulties since the light travel through the atmosphere twice. Satellite AOT retrieval algorithms apply complex methods to attempt to eliminate the noise produced by the land surface reflectance (e.g. Levy *et al*., 2010). The resulting measurements have a lower accuracy than sun photometric measurements, but satellite retrievals can cover the whole globe at resolutions fluctuating from 1 to 100 km.

1.6.2. Ambient Ion Monitor-Ion Chromatography (AIM-IC)

Traditionally, aerosol soluble ion composition is determined by offline analytical methods. In general, atmospheric particles are collected on filters such as polycarbonate, Teflon, quartz, glass fiber and cellulose nitrate drawing air through a filter by means of a vacuum pump. The samples must be extracted before analyses. Then, the ion chemical composition of the samples is commonly achieved by using ion chromatography.

During such sampling or sample storage, chemical and physical changes may occur (Schaap *et al*., 2004). The aforementioned changes may lead to positive and negative sampling errors (artifacts). Errors may arise from gas-particle and particle-particle interactions, gas absorption by the sampling media or collected particles and evaporation of collected species. For instance, retention of SO_2 and HNO_3 on filter substrate causes a positive bias (Tsai and Perng, 1998; Pakkenen *et al*., 1999; Schaap *et al*., 2002). Semi-volatile water-soluble ion species such as NH_4Cl and NH_4NO_3 can be lost due to changes in temperature and relative humidity. The loss of nitrate can also occur from chemical reactions between NH_4NO_3 and H_2SO_4/HCl (Appel and Tokiwa, 1981). In order to minimize positive and negative artifacts, filters in combination with denuders have been applied (Shaw *et al*., 1982, Klockow *et al*., 1989 and Koutrakis *et al*., 1993). This type of sampling configuration employs gas denuder upstream and downstream of a filter to collect reactive gases and volatilized species, respectively.

Ion chromatography based near real time measurements has been developed to minimize sampling errors and improve temporal resolution for better comprehension of the atmospheric chemistry and physics of the aerosols. Particle-Into-Liquid-Sampler coupled to ion chromatography (PILS-IC) was developed in the beginning of 2000 (Weber *et al*., 2001). On one hand, PILS-IC is capable of carry out rapid, automated online measurements of ionic composition in $PM_{2.5}$ however, it is incapable of detecting precursor gases. Gas/Particle Ion Chromatography (GPIC, Ullah *et al*., 2006) has been utilized to determine ionic composition of $PM_{2.5}$ and precursor gases. This instrument is capable of measuring ions and precursor gases such as chloride, nitrate, sulfate, ammonium, hydrochloric acid, nitric acid, sulfuric acid and ammonia. However, GPIC is not able to detect cations such as sodium, potassium, magnesium and calcium. Furthermore, gas and particle measurements cannot be carried out simultaneously since they staggered by 20 minutes. Monitor for AeRosols and Gases (MARGA, Applikon Analytical BV) has dual ion chromatography and it is capable of measuring anions and cations (ten Brink *et al*., 2007).

Ambient Ion Monitor – Ion Chromatography (AIM-IC) is an instrument capable of carry out continuous, near real time, hourly simultaneous measurements of ions (Na^+, NH_4^+, K^+, Mg^{2+}, Ca^{2+}, Cl^+, NO_2^-, NO_3^-, SO_4^{2-}) in $PM_{2.5}$ and precursor gases (HCl, HONO, HNO_3, H_2SO_4, NH_3). The AIM-IC comprises of AIM 9000D air sampler /URG Corp., Chapel Hill, NC) and ICS-5000 (Thermo-Dionex). It has high accuracy and precision (Markovic *et al*., 2012).

CHAPTER II

2. MATERIAL AND METOD

2.1. Study site and climatology of the region

The Erdemli atmospheric sampling site is located on the coastline of the **E**astern **M**editerranean (EM), Erdemli, Turkey (36.57°N and 34.26°E, Figure 2.1). The study site is surrounded by cultivated land and greenhouses having a distance of 10-50 km away from major pollutants sources, thus, the site is classified as rural according to the criteria proposed by Putaud *et al.*, (2004). Depending on regional atmospheric dynamics, the Erdemli aerosol population is mainly influenced by three aerosol sources namely; (i) anthropogenic particles from industrialized and semi-industrialized regions situated to the North, (ii) mineral dust from the Sahara and Middle East Deserts located to the South and (iii) sea salt from the Mediterranean Sea (Kubilay *et al*., 2000, Koçak *et al*., 2004; Koçak *et al*., 2007).

Climatically, the weather pattern of the Mediterranean region is characterized by mild, relatively wet winters and hot, dry summers (Lionello *et al*., 2006). Monthly average atmospheric temperatures and rainfall for a 15-year period (2000-2014) at the Erdemli site are illustrated in Fig. 3.5h, i. The temperature presents a strong seasonal cycle with a winter minimum and a summer maximum. The average monthly temperature commences to increase in April and reaches its maximum in August (28.5 °C) and then decreases to its minimum in January (9.8 °C). The site receives on annual average 549 mm of rain with a strong seasonal pattern. The majority of rainfall (304 mm) is observed in winter whereas very low amounts of rainfall (11mm) are observed in summer. It is clear that the character of the sampling site is the representative of Mediterranean climate in terms of both temperature and precipitation.

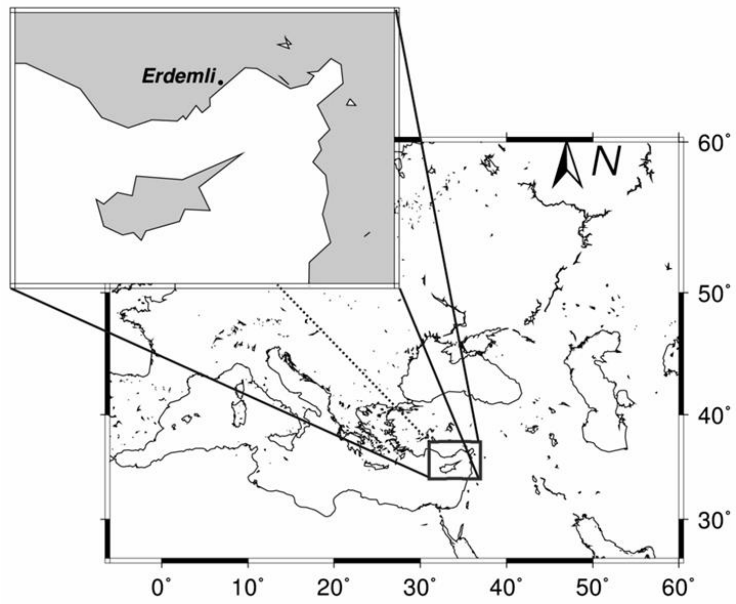

Figure 2.1 Location of sampling site (Erdemli) at the Southeastern coastal area of Turkey.

2.2. AERONET Measurements

AErosol **RO**bit **NET**work (AERONET) is a federated network of ground-based sun-sky radiometers operating worldwide since the middle of the 1990's. AERONET uses a CIMEL (CE318, Cimel Electronique of France) sun and sky radiometer and this instrument operates at more than 840 sites located all over the world. CE318 (see Figure 2.2) is a multi-channel, automatic sun-and-sky scanning radiometer that measures the direct solar irradiance and sky radiance at the Earth's surface. It consists of three main components namely: (a) instrument itself (sensor head, scanning motors and robotic arm), (b) control box (software for controlling predetermined scanning, sampling strategies, and for acquiring data) and (c) computer (data collection and transmission). The instrument has a main stem containing the azimuth motor. On the top of the motor there is a robot arm consisting of the zenith motor on one side and the sensor head on the other side. The collimators are attached to the sensor head. Two silicon detectors, one for each of the collimators are placed in the sensor head. Between the collimator windows and the detectors is a filter wheel, consisting of eight narrowband interference filters (at 340, 380, 440, 500, 675, 870, 1020, and 1640 nm) mounted along the circumference. The two collimators differ in the size of apertures whereas; they have the same field of view (1.2 degree). They are physically part of a single unit that is attached to the sensor head, larger collimator (10 times as large as the sun-viewing collimator) providing the necessary dynamic range to observe the sky.

Figure 2.2 AERONET CIMEL (CE318, Cimel Electronique of France) at IMS-METU, Erdemli.

AERONET provides aerosol columnar properties such as **A**erosol **O**ptical **T**hickness (AOT), perceptible **W**ater **V**apour (WV) and inversion aerosol products. More detailed descriptions are given in Holben *et al*. (1998). To summarize, the sun-sky radiometer makes direct Sun measurements every 15 minutes at 340, 380, 440, 500, 675, 870, 940 and 1020 nm. Except for 940 nm (used for retrieving WV), these measurements are then applied to calculate AOT (see equation 2.1), with an accuracy of ~ 0.01 for the wavelengths longer than 440 nm and ~ 0.02 for shorter wavelengths (Eck *et al*., 1999). AOT can be given as fallow:

$$V(\lambda) = V_0(\lambda)\, d^2 \exp[-\tau(\lambda)_{TOT} * m]\ \ t_y \qquad [Eq. 2.1]$$

Given equation is based on the spectral extinction of direct beam radiation according to the Beer-Lambert-Bouguer law where V is digital voltage measured at λ wavelength by the instrument at the surface, V_o is extraterrestrial voltage at λ wavelength measured at Mauna Loa Observatory in Hawaii, d is the ratio of the average to the actual Earth-Sun distance, m is the optical mass, t_y is transmission of absorbing gases and $\tau(\lambda)_{TOT}$ is the total optical thickness (Holben *et al*., 1998). $\tau(\lambda)_{TOT}$ includes optical thickness that results from aerosol, WV, trace gases (O_3, NO_2, CO_2, CH_4) and molecular scattering. In order to obtain AOT(λ), optical thickness of other atmospheric constituents must be subtracted from $\tau(\lambda)_{TOT}$. AOT at 500 nm is decomposed into fine and coarse mode AOT according to the Spectral De-convolution Algorithm by O'Neill *et al.*, 2001; 2003. The **A**ngstrom **E**xponent (AE or α) is defined by the logarithms of AOT and wavelength (see equation 2.2) and it is calculated for the all wavelengths varing from 440 to 870 nm employing a lean fit between AOT and λ (Holben *et al.*, 1991; 2001). The value approaching zero denotes dominance of coarse particles whereas; the value larger than 1 implies the preeminence of fine aerosol (Kaufman *et al.*, 1994, Eck *et al.*, 1999).

$$AE = -d\ ln\ [AOT\ (\lambda)]/d\ ln(\lambda) \qquad \text{[Eq. 2.2]}$$

SSA is the ratio of scattering to extinction (scattering plus absorption). The values of SSA ranges from 0 to 1. A low value of SSA means that the aerosol predominantly absorbs the sunlight whilst a high value of SSA suggests that the aerosol predominantly scatter the incident sunlight. Knowledge of SSA allows **A**bsorption **A**erosol **O**ptical **T**hickness (AAOT) to be calculated. Then, **A**bsorption **A**ngstrom **E**xponent (AAE), the wavelength dependence of the AAOT, can also be derived.

$$SSA = \frac{Scattering}{Scattering + Absortion} \qquad \text{[Eq. 2.3]}$$

$$AAOT = (1 - SSA) * AOT \qquad [Eq. 2.4]$$

$$AAE = -d\ ln \frac{[AAOT\ (\lambda)]}{d} ln(\lambda) \qquad [Eq. 2.5]$$

The instrument also performs hourly sky radiance measurements in almucantar geometry at 440, 675, 870 and 1020 nm. These sky radiance measurements in conjunction with corresponding direct sun measurements are then used in inversion algorithms to derive particle size distribution (PSD), real (n) and imaginary (k) refractive indices and single scattering albedo (Dubovik and King 2000; Dubovik *et al.*, 2006). The retrieval error in PSD is estimated to be 15%-35% for the intermediate particle size range ($0.1 \leq r \leq 0.7$ μm). However, the error in PSD for small ($0.05 \leq r$

≤0.1 μm) and large (7 ≤ r ≤ 15 μm) particle size interval may reach 80%. Uncertainty of SSA, n and k shows variability depending on aerosol type and loading. For instance, SSA, n and k are expected for desert dust loading with an AOT (440 nm) > 0.5 to have an uncertainty of 0.03, 0.04 and 40 %, respectively. On the other hand, at dust loading with AOT (440 nm) < 0.2, the uncertainty of SSA, n and k increases up to 0.05-0.07, 0.05 and 80-100 %, respectively (Dubovik *et al*., 2000). Therefore, the accuracy of AERONET retrievals, especially imaginary part of refractive index (aerosol absorption), diminishes with decreasing AOTs. The almucantar retrievals for AOT at 440 nm larger than 0.4 have been used in this study in order to obtain more reliable results.

The AERONET sun photometer was installed at the Institute of Marine Science, Middle Technical University Campus in December 1999 and the instrument has been operating since then. The sampling site is called IMS-METU-ERDEMLİ (here after Erdemli) in the AERONET program. The instrument installed at Erdemli site has only 440, 500 (after 2004), 675, 870 and 1020 channels for AOT measurements. The 15-year long Level 2.0 quality-assured daily data set from January 2000 to December 2015 at Erdemli were obtained from Version 2 AERONET. The percent of observational coverage of direct measurements (AOT, AE and WV) per year is illustrated in Figure 2.3. The mean observational coverage of AOT, AE and WV was around 50 % (n = 2712). There is no data available for 2002. The missing values were as a result of quality control issues and technical malfunction of the sun photometer instrument. Regarding Version 2 (Level 2.0), particle size distribution was attained for 1414 days whilst SSA and Refractive index were only derived for 413 days (see Table 2.1).

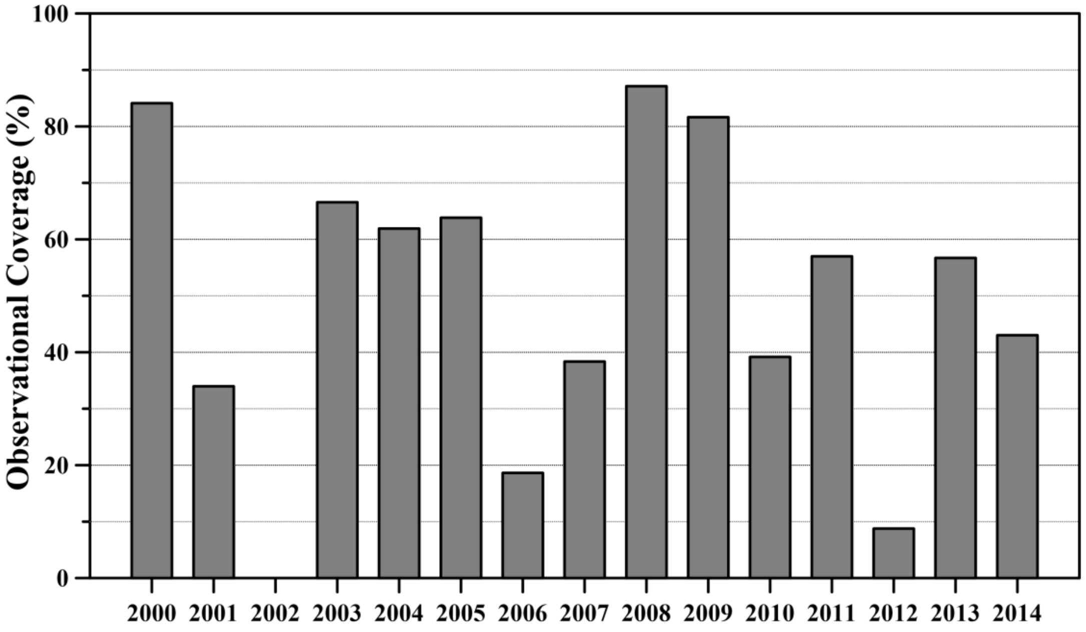

Figure 2.3 Percent coverage of 2000-2014 years for AERONET direct measurements.

Table 2.1 The number of observation between 2000-2014 years for AERONET measurements.

	AOT, AE, WV	PSD	SSA, RR, RI
2000	307	181	41
2001	124	59	8
2002	-	-	-
2003	243	47	8
2004	235	152	46
2005	231	173	51
2006	68	22	5
2007	140	57	10
2008	324	206	76
2009	293	196	38
2010	143	79	34
2011	208	130	48
2012	32	1	-
2013	207	35	10
2014	157	76	38
Total	2712	1414	413

2.3 Calculation of the 5 day Air Mass Back Trajectories

Five-day back-trajectories were calculated by running the HYSPLIT Dispersion Model, (HybridSingle Particle Langrangian Integrated Trajectory; Draxler, 1999; Stein *et al*., 2015). The HYSPLIT model, a hybrid system computing air mass trajectories and dispersion of atmospheric pollutants, performs calculation methods based on the Lagrangian and Eulerian approaches (for more information, http://www.arl.noaa.gov/HYSPLIT_info.php). The meteorological data of the NCEP/NCAR Reanalysis Project was used as input for trajectory calculations, which was gridded to 2.5°X2.5° in latitude and longitude with 18 vertical levels. The air masses arriving at Erdemli at 1, 2, 3 and 4 km above sea level for each day (06:00 UTC) was computed during the period between January 2000 and December 2014 (99.9 % coverage). 5-day backward trajectories were selected since it extends far enough to represent the synoptic scale flow. The vertical motion of air masses was calculated using three-dimensional vertical velocity field.

2.3.1. Potential Source Contribution Function

Possible source regions of atmospheric aerosol or gases having high concentration at a receptor site was determined using the spatial probability distribution of pathways of air parcels that arrived at the receptor site over a time period. When the material is emitted into the air parcel from a source, it can be transported to the receptor site throughout the trajectory of the air parcel. If the endpoint of a trajectory stays at a cell of address (i,j), it is assumed that the trajectory collects the emissions from the cell. The total number of endpoints that are located in the cell is n_{ij} and there exists m_{ij} points for which the measured parameter rises above a criterion value defined for this parameter, then, potential source contribution function (PSCF) is calculated using the following formula (Polissar *et al*., 2001).

$$PSCF_{ij} = m_{ij}/n_{ij} \qquad [Eq. 2.5]$$

Taking into account α, AOT categorized into four groups: (i) $\alpha_{440\text{-}870} < 0.5$, (ii) $0.5 < \alpha_{440\text{-}870} < 1$, and (iii) $1 < \alpha_{440\text{-}870}$. Then, PSCF was applied to identify potential source regions of the largest 10% of AOT (440 nm) values in the groups. Air masses back trajectories arriving at 1 km and 4 km altitudes were utilized to define source areas, by dividing the region into 2°X2° grids (910 cells) between 20°W-50°E and 20°N-70°N. The small number of endpoints in a grid may generate high PSCF values with high uncertainties. For this reason, a binomial test was applied to check the statistical significance of the PSCF values for every grid (Vasconcelos *et al*., 1996; Salvador *et al*., 2004). Therefore, only PSCF values statistically significant at the 95% confidence interval have been considered in the analysis.

2.4 Ambient Ion Monitor Ion Chromatography (AIM-IC) Measurements

Ambient **I**on **M**onitor **I**on **C**hromatography (AIM-IC, see Figure 2.5) consists of two major components: (i) the sampling unit for the simultaneous collecting of aerosols in $PM_{2.5}$ and their precursor gases (AIM 9000D, URG Corp., Chapel Hill, NC, see Figure 2.6) and (ii) the sample analysis unit, ion chromatography (ICS-5000, Thermo-Dionex) for the determination of anionic and cationic ions in the collected aqueous solution.

The online sample collection is carried out by drawing ambient air at 3 L min^{-1} through a pre-impaction (cyclone) assembly which intercepts the atmospheric particles that are bigger than 2.5 μm equivalent aerodynamic diameter. Therefore, only the atmospheric particles smaller than 2.5 μm are directed into the parallel-plate wet denuder. The parallel-plate wet denuder consists of two cellulose membranes (one for per plate) that are continuously supplied with 5 mM of ultrapure hydrogen peroxide (H_2O_2) solution at 10 mL hr^{-1}. As the ambient air passes between the plates, soluble precursor gases are separated from the atmospheric particles by diffusion and dissolution into the denuder solution. The resultant solution from the denuder having dissolved gases is splinted into two 5 mL syringes for the detection of anionic and cationic species in the liquid. The air free of precursor gases, then flows into the particle supersaturation chamber, comprising of (i) a steam generator (ii) mixing/condensation chamber and (iii) a cyclone. In the supersaturation chamber, the particles are activated by steam in order to initiate hygroscopic growth in the mixing/condensation chamber. The cyclone remove large and heavily solvated particles from the bulk air flow. The resultant solution from supersaturation chamber is splinted into two 5 mL syringes for the determination of anionic and cationic species in the liquid. Before reaching the diaphragm pump, the remaining humidified air passes through Vigreux to eliminate water from the flowing air. After the sampling, the solutions are automatically injected into ion chromatography instrument.

Chromatography is a separation method, distributing the analyte in the sample between stationary and mobile phases. Some species adhere to the stationary phase more than the other species as the eluent flows (mobile phase). Thus, the separation of the ion species from each other is achieved as the eluent passes through the column (stationary phase). The apparatus and the conditions of the ion chromatography are illustrated in Table 2.2. Near real time measurements of water-soluble anionic/cationic species in $PM_{2.5}$ and precursor gases were carried out under identical conditions by using an ICS-5000 ion chromatography instrument. Water-soluble anions (Cl^-, SO_4^{2-}, NO_3^-) and gases (HCl, HNO_3, HNO_2, and SO_2) were determined by applying AS11-HC separation column, KOH (gradient from 18 to 59 mM) eluent and AERS-500 (4 mm) suppressor whereas water-soluble cations (Na^+, NH_4^+, K^+, Mg^{2+}, Ca^{2+}) and precursor gas (NH_3) were detected electrochemically by using a CS12-A separation column, MSA (20 mM) eluent and CSRS-300 (4 mm) suppressor (Product Manual for Dionex IonPac AS11-HC-4m, IonPac CS12A Manual).

Near real-time hourly measurements were performed using the AIM-IC during the winter period between January 27 and February 3 and the summer period between August 19 and September 2, 2015. From time to time, the measurements were temporarily interrupted for technical reasons during the online sampling campaigns. 127 and 307 measurements were attained in the winter period and the summer period, respectively. In order to compare results from online measurements, offline $PM_{2.5}$ samples were simultaneously collected during the sampling campaign. Offline $PM_{2.5}$ samples were collected on 47 mm Teflon filters (0.8 μm pore size) by using Thermo-Scientific 2025i Partisol Sequential Air Sampler with a flow rate of 16.7 L min-1. Offline aerosol sampling campaign commenced on 21 August 2015 and ended on 02 September 2015. The samples were stored at deep-freezer (-20 ˚C) directly after collection until analysis. In order to determine concentrations of major water-soluble ions in aerosol, one quarter of the filter was extracted for 45 minutes in 20 mL of ultra-pure water (18.2 Ω) by mechanic shaker. The extraction was treated with about 100 µL chloroform to prevent biological activity (Bardouki *et al*., 2003, Koçak *et al*., 2007). The water-soluble ions concentrations were measured by using the ICS-5000 ion chromatography instrument with the configuration in Table 2.2. The detection limit for water-soluble ions was <1 ppb while the blank contributions were smaller than 10 %.

Figure 2.4 Ambient Ion Monitor Ion Chromatography (the sample analysis unit: ICS-5000, Thermo-Dionex, the sampling unit for the simultaneous collecting of $PM_{2.5}$ and their precursor gases: AIM 9000D, URG Corp., Chapel Hill, NC)

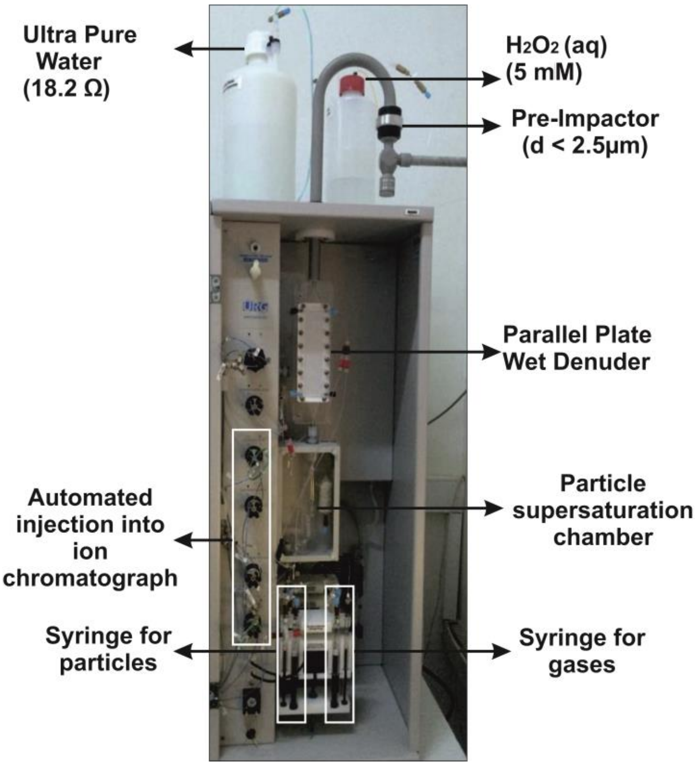

Figure 2.5 Typical setup for Ambient Ion Monitor (URG9000D).

Table 2.2 A summary of ion chromatography applications for water-soluble anions and cations.

Ion Chromatography	**Anion, Gases (Cl^-, NO_3^-, SO_4^{2-}, HCl, HNO_2, HNO_3,SO_2)**	**Cation, Gases (Na^+, NH_4^+, K^+, Mg^{2+}, Ca^{2+}, NH_3)**
Pre-column Separator column	AG11-HC AS11-HC	CG12A CS12A
Loop	150 μL	15 μL
Membrane-Suppressor	ASRS (4 mm)	CSRS (4mm)
Eluent Solution (Concentration) (Flow Rate)	KOH (gradient from 18 to 59 mM) (1.5 mL/min)	MSA (20 mM) (1.5 mL/min)
Detector	Conductivity	Conductivity

CHAPTER III

3. Climatology of Air Masses Back Trajectories for Erdemli during 2000-2014.

3.1. Meteorology

The monthly average of atmospheric temperature and rainfall between 2000 and 2014 is presented in Figure 3.1. Both atmospheric and rainfall exhibited a strong seasonal cycle. Local ambient temperature exhibited winter minimum and summer maximum. The temperature denoted gradual increase from January (~ 9 °C) to January and reached its maximum in August (~25.8 °C). Then from August to December continuously decreased back to its winter value. In contrast to temperature, local rainfall indicated a sharp decrease from January to August (reaching a couple of mm) then it showed a dramatic increase from August to December, attaining its maximum with a value of 120 mm. Local rainfall illustrated that the sampling site was predominantly influenced by rain in winter (JFD), whereas during the summer (JJA) the site received negligible amount of rain yet it received important amount of rain in fall (SON).

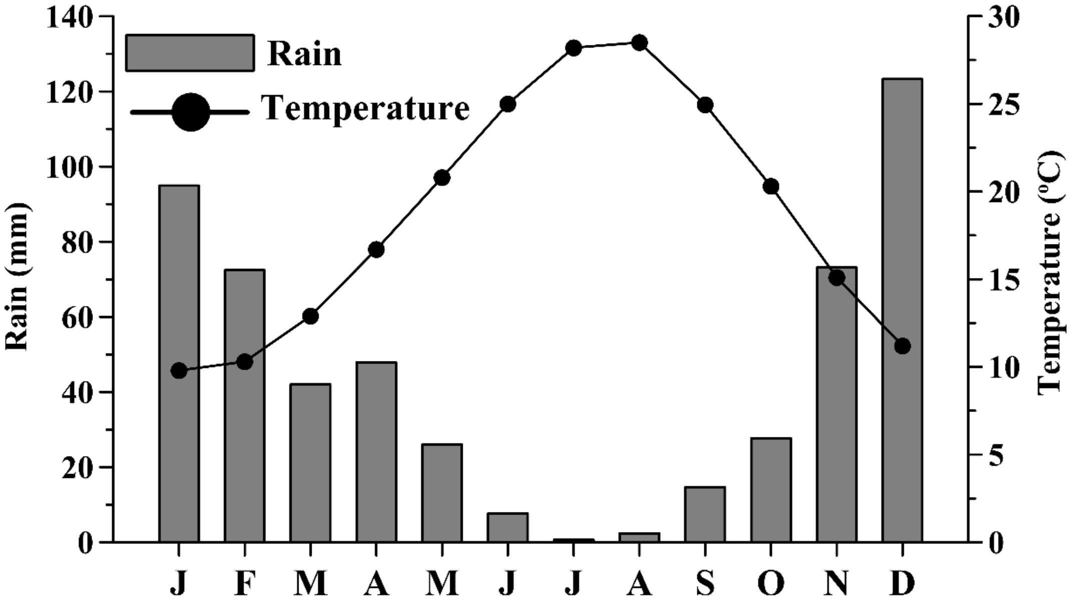

Figure 3.1 The monthly average of atmospheric temperature and rainfall between 2000 and 2014

3.2 Climatology for Air Flow at Erdemli

Based on the approach by Koçak *et al*. (2005, 2012), five day back trajectories arriving to Erdemli at the height of 1 km and 4 km were classified into six sectors: (i) Western Europe (WE), (ii) Eastern Europe (EE), (iii) Turkey (TUR), (iv) Middle East (MID), (v) Saharan (SAH) and (vi) Mediterranean Sea (MED) in order to evaluate the impact of airflow on aerosol optical properties (Figure 3.2). Table 3.1(a) and (b) presents air mass back trajectory climatology for aerosol optical data along with whole trajectories climatology at Erdemli expressed as % influence of air flow from each of the defined sectors between January 2000 and December 2014 for 1 km and 4 km, respectively.

If we compare air flow climatology for AOT data set with air flow climatology, it can be asserted that both altitudes for data set were more (less) influenced by northerly (southerly) air masses. However, it should be noted that air flow for data set were representative of air masses influencing study site within ± 5 % for each defined air masses sector.

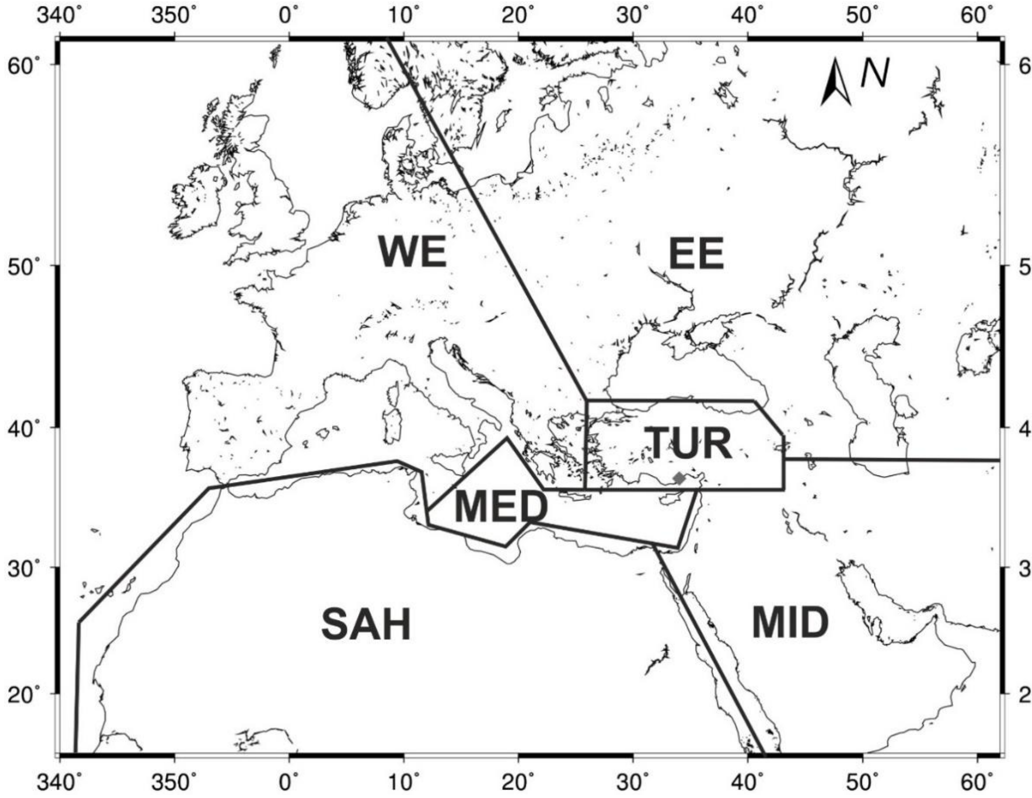

Figure 3.2 Classification of 5-day back trajectories arriving at Erdemli. Airflow sectors are presented as WE (Western Europe), EE (Eastern Europe), TUR (Turkey), SAH (Saharan), MID (Middle East) and MED (Mediterranean Sea).

Table 3.1 Air masses back trajectories climatology for aerosol optical data along with whole trajectories climatology for 1 km **(a)** and 4 km **(b)**.

a)	**Air Flow Climatology (%)**	**Air Flow Climatology for AOT data (%)**
WE	13.3	12.1
EE	32.9	37.9
TUR	28.2	28.4
MID	7.4	5.4
SAH	8.7	7.2
MED	9.5	9.0

b)	**Air Flow Climatology (%)**	**Air Flow Climatology for AOT data (%)**
WE	52.8	55.9
EE	10.4	12.0
TUR	10.2	10.1
MID	2.7	3.0
SAH	23.9	18.9
MED	-	-

Correspondingly, Table 3.2.a and b illustrate seasonal air flow for 1 km and 4 km arriving at Erdemli expressed as % influence of air masses back trajectory from each of the cluster. Air masses back trajectories exhibited distinct differences between seasons. These differences may be summarized as follows:

Regarding 1 km, higher air flows from EE and TUR were observed for four seasons. Largest transport from the EE and TUR were observed in summer, being 49.7 % and 30.8 %, respectively. However, lowest air masses emerged from SAH (2.2 %) and MID (0.4 %) were monitored in summer. Highest air flow from MED (12 %) was detected in spring. Lowest air masses originated from Turkey were found in winter (23.3%). As for results for 4 km, almost % 50 of air flows originated from WE during all seasons. Similar to those of the 1 km, the highest (lowest) transport from TUR (SAH) were found in summer, being % 14.0 (% 13.6). On the other hand, air flows from MID in summer were at least 3 % than those observed for winter, spring and fall. There was no assigned air masses to MED sector for 4 km level.

Table 3.2 Seasonal air flow for 1 km **(a)** and 4 km **(b)** arriving at Erdemli.

a)	**Winter**	**Spring**	**Summer**	**Fall**
WE	16.5	17.4	9.2	10.2
EE	25.5	28.3	49.7	27.8
TUR	23.3	25.5	30.8	33.0
MID	12.8	5.6	0.4	11.0
SAH	12.5	11.2	2.2	8.8
MED	9.4	12.0	7.6	9.2

Table 3.2 continue …

b)	**Winter**	**Spring**	**Summer**	**Fall**
WE	55.1	47.9	59.7	48.6
EE	13.0	9.8	7.5	11.5
TUR	5.9	10.2	14.0	10.6
MID	1.0	2.1	5.2	2.4
SAH	25.0	29.9	13.6	26.9
MED	-	-	-	-

3.3 Anomalies of air flow at Erdemli.

Anomaly is a term describing the deviation from the expected value. The expected value can be mean or a model prediction. In this study, annual air flow anomalies of each sector were derived using the yearly percent of air masses back trajectories in the defined sectors for 1 and 4 km. The annual anomalies presented for a given year were calculated by subtracting the mean value from the annual value. The mean value of a sector was the arithmetic mean of annual air masses percent of the sector over the 2000-2014 period. Moreover, a least-squares fit was applied to air flow anomalies in order to acquire the slope coefficient of the linear regression that denotes annual trend.

(a) Anomalies of air masses backward trajectories at 1km: Time series and linear trends of annual back trajectories anomalies from 2000 to 2014 for 1 km are presented in Figure 3.3. The anomalies mostly had temporal variability and different magnitude compared to the mean values. Generally, it can be stated that the negative trend was observed in northerly air flows whereas positive trend was captured in southerly flow. Specifically, air flow anomalies of sectors can be evaluated as follow:

i) *EE and WE (Figure 3.3a, g):* Calculated air flow anomalies for EE and WE denoted a negative trend from 2000 to 2014. The calculated decrease was significant, being 0.18 % per year. The positive anomalies were dominant until 2006, on the other hand, negative anomalies were pronounced after the aforementioned year.

ii) *MED and MID (Figure 3.3b, c):* Air flow anomalies for MED and MID exhibited a negative trend from 2010 to 2014. However, the calculated decrease was relatively insignificant, being 0.06 % and % 0.04 per year for MED and MID, respectively.

iii) *SAH and TUR (Figure 3.3d, e):* Air flow anomalies for SAH and TUR showed a positive trend throughout the study period. The significant increase of 0.15 % and 0.29 % per year were found for SAH and TUR, respectively. The negative anomalies were prevailing until 2008, however, positive and relatively weak negative anomalies were calculated after 2008.

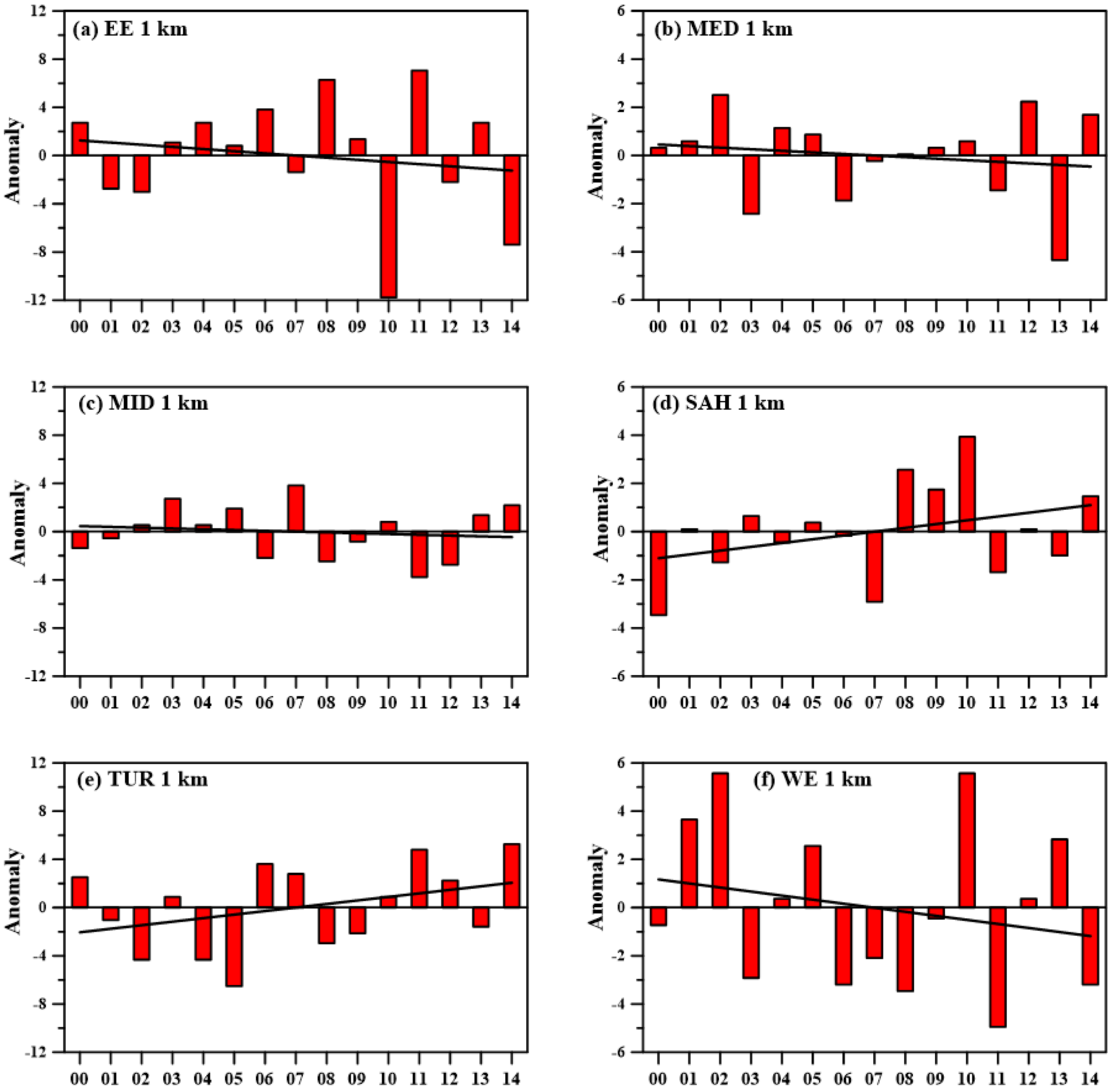

Figure 3.3 Anomalies (%) of air masses backward trajectories in EE **(a)**, MED **(b)**, MID **(c)**, SAH **(d)**, TUR **(e)** and WE **(f)** at 1 km level.

(b) Anomalies of air masses backward trajectories at 4 km: Time series and linear trends of annual back trajectories anomalies from 2000 to 2014 for 4 km are illustrated in Figure 3.4. Similar to 1 km, it can be reported that the negative trend was observed for northerly air flows while, positive trend was detected in southerly flow anomalies. Specifically, anomalies of back trajectories of each cluster might be evaluated as follow:

i) *EE and WE (Figure 3.4a, g):* Air masses anomalies for EE and WE indicated a negative trend from 2000 to 2014. The calculated decrease for EE and WE was significant, being 0.22 % and 0.39 % per year, respectively. The positive anomalies were prevailing until 2006 nevertheless, the negative anomalies were pronounced after the aforementioned year.

ii) *MID (Figure 3.4c):* Air masses anomalies for MID demonstrated a negative trend between 2010 and 2014. Nonetheless, the calculated decline for MID was relatively insignificant, being 0.05 % per year.

iii) *SAH and TUR (Figure 3.4d, e):* Air masses anomalies for SAH and TUR revealed a positive trend over the period 2000-2014. Correspondingly, the significant increase of 0.40 % and 0.15 % per year were observed for SAH and TUR, respectively. The negative anomalies were obvious until 2007, however, positive and relatively weak negative anomalies for SAH and successive positive anomalies for TUR were calculated after 2006.

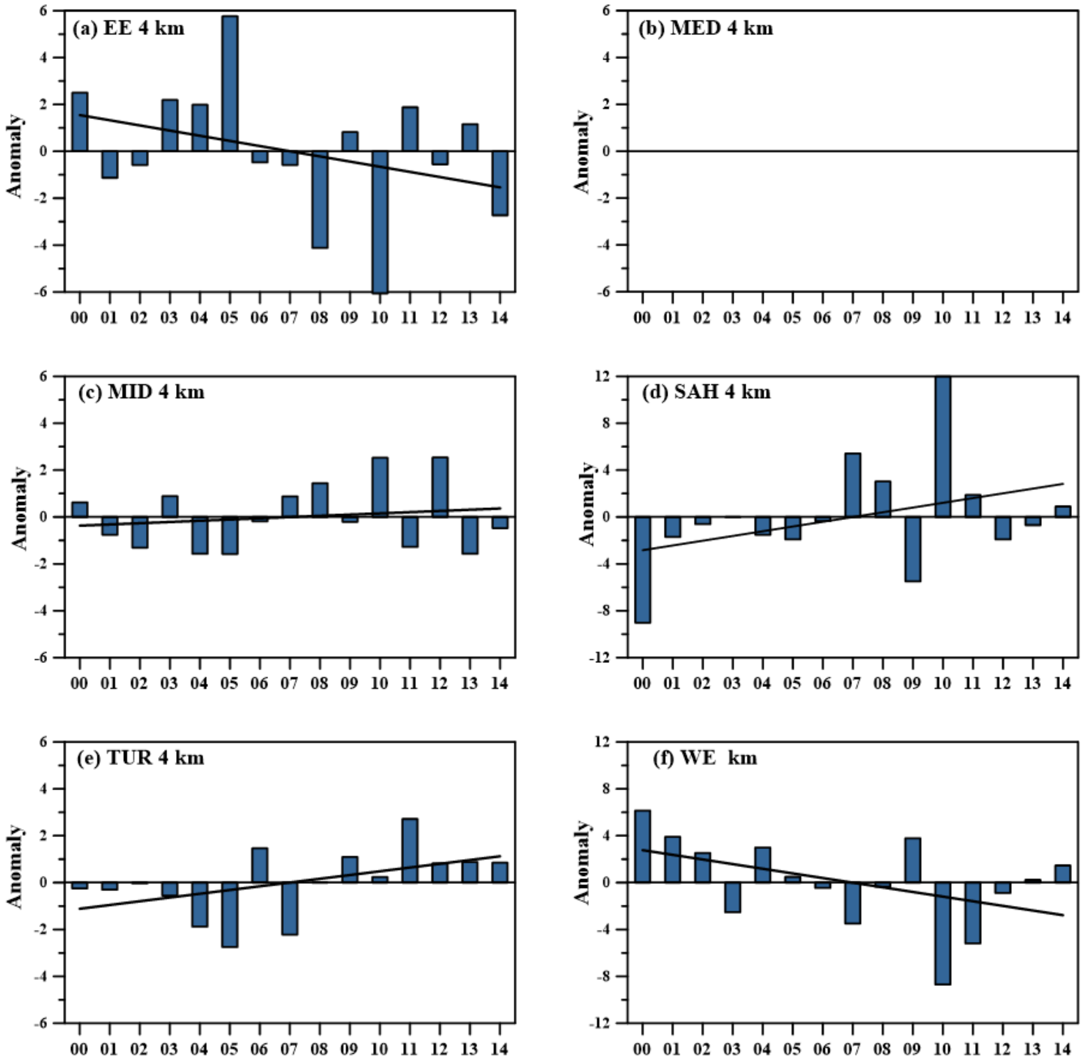

Figure 3.4 Anomalies (%) of air masses backward trajectories in EE **(a)**, MED **(b)**, MID **(c)**, SAH **(d)**, TR **(e)** and WE **(f)** at 4 km level.

CHAPTER IV

4. Long-term Measurements of Aerosol Optical and Physical Properties over the Eastern Mediterranean: Hygroscopic state and Source Region.

4.1. General Characteristics of AOT, Angstrom Exponent, WV and Size Distribution at Erdemli

Before discussing aerosol optical properties and size distribution, it is worth mentioning the probability distribution of aerosol optical thickness (AOT) measured at Erdemli from January 2000 to December 2014. Kolmogorov-Smirnov test (at 95 % confidence interval) demonstrated that AOT at 440 nm distribution was lognormal (Fig. 4.1). Therefore, it should be highlighted that the AOT is best represented by geometric mean value. O’Neill *et al.* (2000) have also been shown similar distribution for AOT. Since there is a lack of such values in the literature and therefore arithmetic mean values will be applied when comparing the current values obtained and those from previous studies.

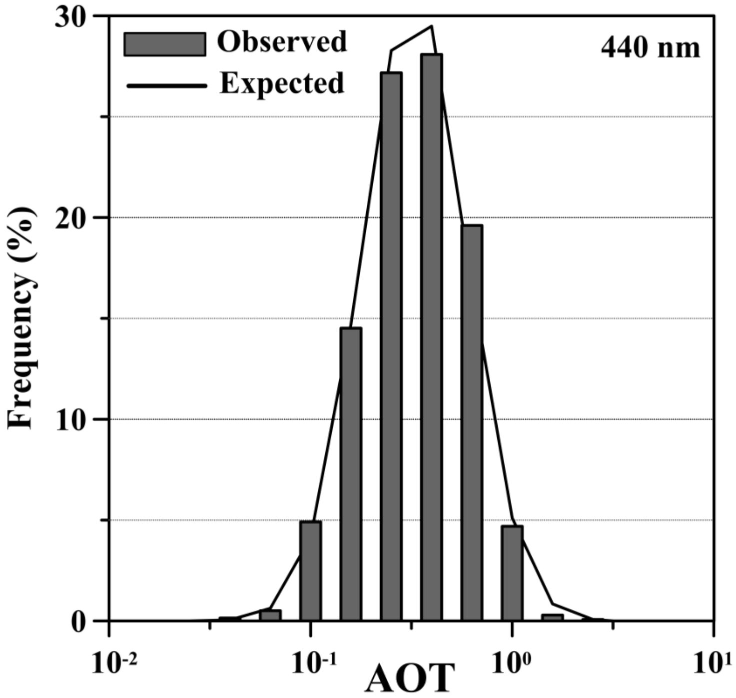

Figure 4.1 Frequency histogram of the log-transferred columnar AOT_{440} and its expected distribution at Erdemli.

Table 4.1 illustrates statistical summary for AOT and Angstrom Exponent (α) obtained between January 2000 and December 2014 at the Erdemli site**.** Figure 4.2 also shows corresponding mean aerosol volume size concentration throughout the study period. As can be seen from the Table 4.1, AOT exhibited a remarkable increase from 1020 nm (0.12) to 440 nm (0.30) and this reduction might be attributed to the dominance of fine particles. The arithmetic mean of AOT (440 nm) was 0.30±0.18 with values ranging between 0.03 and 1.96. Geometric mean and median were identical with a value of 0.26, being 1.15 times less than that of arithmetic mean. Angstrom exponent was found to be varied between 0.03 and 2.23 with an arithmetic mean value of 1.22±0.37. WV ranged from 0.19 cm to 4.54 cm with an arithmetic mean of 2.04 cm. Mean aerosol volume size concentration demonstrated bimodal distribution. The first peak was ascribed to fine particles, majority being between 0.1 μm and 0.3 μm whilst the second peak was attributed to coarse particles, chiefly existing between 1.5 μm and 6.0 μm.

Table 4.1 Statistical summary for aerosol optical thickness (AOT: 440, 500, 675, 870, 1020 nm), angstrom exponent ($\alpha_{440-870}$) and WV (cm) at Erdemli between January 2000 and December 2014

Parameter	**Arithmetic Mean (±δ)**	**Geometric Mean**	**Median**	**Minimum**	**Maximum**
AOT_{1020}	0.12±0.11	0.10	0.10	0.01	1.85
AOT_{870}	0.14±0.11	0.11	0.12	0.01	1.87
AOT_{675}	0.18±0.13	0.15	0.15	0.01	1.90
AOT_{500}	0.26±0.16	0.22	0.22	0.01	1.94
AOT_{440}	0.30±0.18	0.26	0.26	0.03	1.96
$\alpha_{440-870}$	1.22±0.37	1.14	1.30	0.03	2.23
WV	2.04±0.91	1.82	1.90	0.19	4.54

δ refers to standard deviation

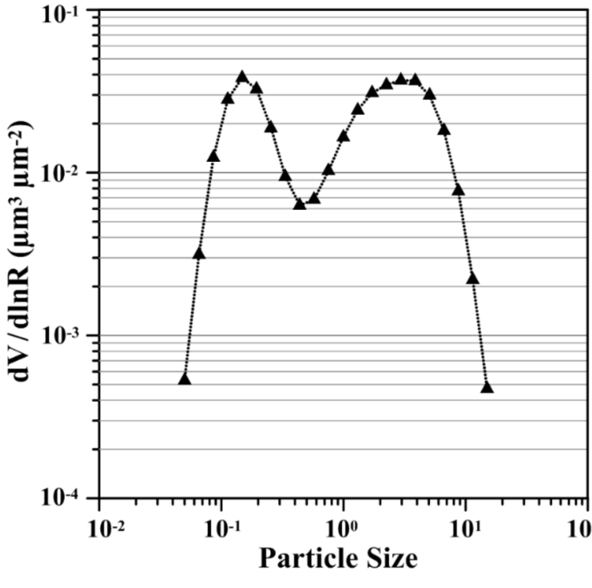

Figure 4.2 Average volume size distributions from Erdemli station throughout the study period (2000-2014).

The relationship between AOT_{440} and water vapor is shown in Figure 4.3. The relationships between these two variables were investigated for three different α classes specifically: (i) $\alpha_{440-870} < 0.5$, (ii) $0.5 < \alpha_{440-870} < 1.0$ and (iii) $1.0 < \alpha_{440-870} < 2.0$. The first group was dominated by coarse particles, accounting of 75 % of AOT_{440} whilst the second group was equally influenced by coarse (~ 51 %) and fine (~ 49 %) particles. In contrast, the third class was dominated by fine particles, elucidating 80 % of the observed AOT_{440}. The logarithmic fit was found to explain much more of the variance between AOT_{440} and water vapor compared to linear fit. In general, AOT_{440} increased with increasing water vapor, however; the degree of relationship between AOT_{440} and water vapor for each group was different. The residual correlation coefficient between two variables was found to increase with enhancing α. The relationship for the first group was weak ($R^2 = 0.13$, Figure 4.3a), suggesting that the particles in this group exhibited non-hygroscopic behavior. Since sea salt has a high hygroscopicity (Petters and Kreidenweis, 2007), it is seem that the aerosols in the first group was mainly dominated by mineral dust with a low hygroscopicity (Koehler *et al.*, 2009). The relationship for the second group was moderate ($R^2 = 0.36$, Figure 4.3b) and this moderate hygroscopic property of this group might be ascribed to mixing of different type aerosols such as mineral dust and anthropogenic sulfates, nitrates and/or organic acids (Koçak *et al.*, 2007, 2012). The residual correlation coefficient ($R^2 = 0.60$, Figure 4.3c) for the last group was strong with a value of 0.60, stating that this class had a hygroscopic characteristic. As stated above, the third category was chiefly associated with hygroscopic fine particles, which may include ammonium sulfate and ammonium nitrate (Tang and Munkelwitz, 1994). Simirnov *et al.* (2002) have shown similar relationship between AOT_{500} and water vapor for coarse ($R^2 = 0.2$, $\alpha_{440-870} < 0.7$) and fine ($R^2 = 0.67$, $\alpha_{440-870} > 0.7$) mode at Bahrain/Arabian Gulf. The increasing trend of AOT_{500} as augmenting water vapor has been reported for a low humid site in Hamim/Arabian Gulf, nonetheless, the relationship between these two variables was found to be independent of aerosol type ($R^2 \sim 0.30$ for both coarse and fine mode, Eck *et al.*, 2008).

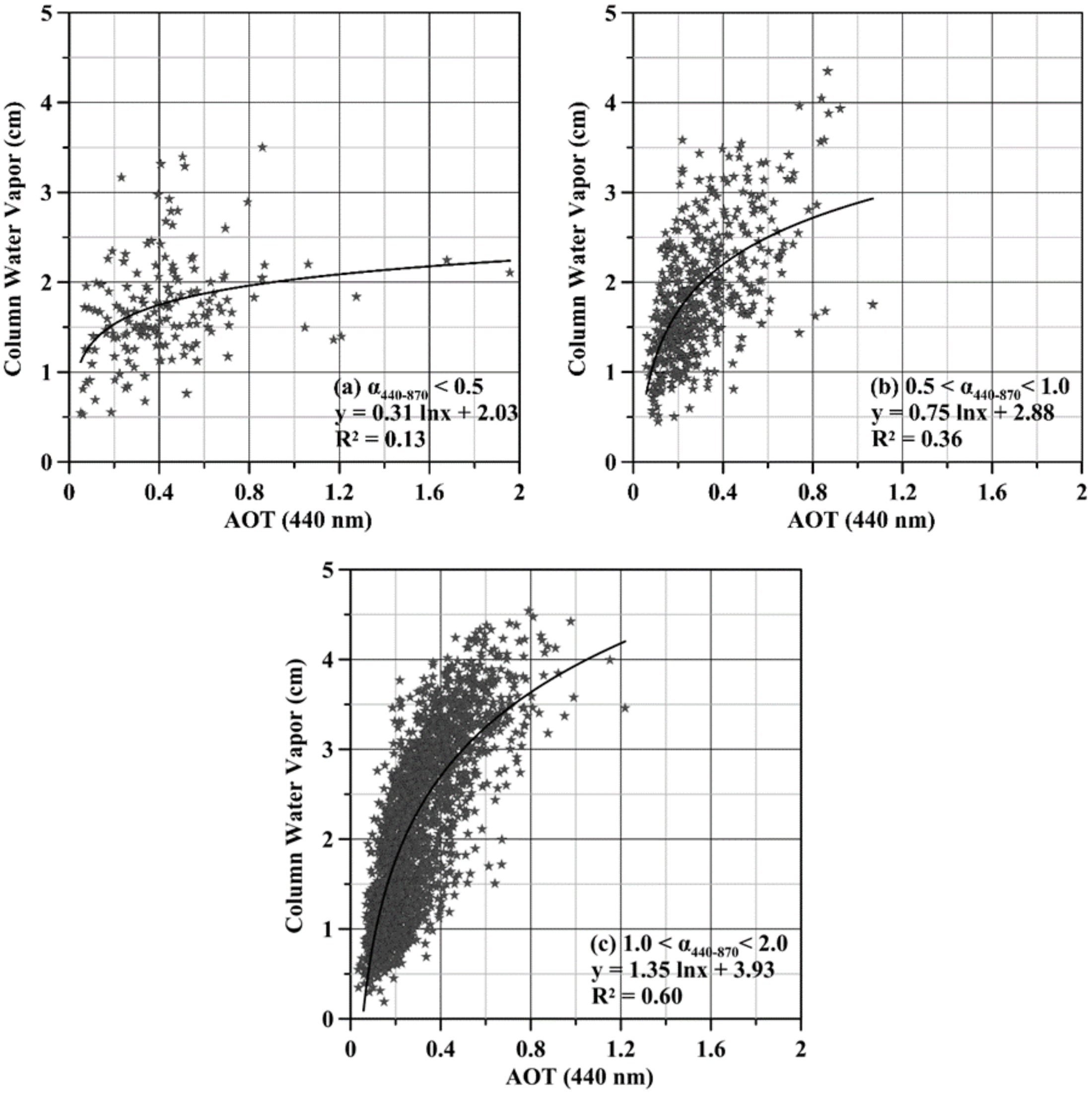

Figure 4.3 Aerosol optical thickness versus water vapor with regression analysis for the values of $\alpha_{440\text{-}870} < 0.5$ **(a)**, $0.5 < \alpha_{440\text{-}870} < 1.0$ **(b)**, and $1.0 < \alpha_{440\text{-}870} < 2.0$ **(c)**

The AOT and α values from different geographical regions of the world including free troposphere, natural, rural and urban sites were used in order to assess spatial variability (Fig. 4.4). Figure 4.5 presents mean AOT_{440} and $\alpha_{440\text{-}870}$ for each site together with their regions and characters. Mauna-Lao (Yoon *et al.,* 2012) had the lowest AOT (0.02) since the site is above the planetary boundary layer (altitude of 3397 m). Corresponding α was 1.2, indicating contribution of stratospheric aerosols to the columnar AOT over the site. Despite Lampedusa and Forth CRETE (Mallet *et al.*, 2013) are characterized as natural backgrounds, AOT (~ 0.2) and α (~ 1.1) values at these sites were comparable to those of rural sites such as Erdemli/Turkey (this study), Blida/Algeria (Mallet *et al*., 2013) and Kaashidoo/Maldives (Holben *et al*., 2001). This peculiarity might chiefly be attributed to the influence of anthropic aerosols on AOT and α when airflow originated from industrialized and semi-industrialized countries located at the northern border of the Mediterranean Sea. On the other hand, AOT and α at San Nicolas (Holben *et al*., 2001) were respectively 0.05 and 1.2, exhibiting the natural background character of the site. Being a natural site, AOT (0.4) and α (0.3) values at Capoverde/Sal Island were remarkably similar to those observed for Dakar (rural coastal), Banizoumbou (rural/semi-arid) and Solar Village (rural). It might be argued that AOT and α values at Sal Island, Dakar and Banizoumbou were heavily modified by mineral dust transport from North Africa and the Middle East (Holben *et al.*, 2001, Yoon *et al*., 2012, Gama *et al*., 2015). Considering rural sites, AOT (~ 0.5) and α (~ 0.3) at Dakar, Banizoumbou and Solar Village were distinctly different than those of the remaining sites, demonstrating the significant effect of mineral dust particles on columnar AOT and α. The highest AOT values were observed over the urban sites in Asia, namely, Taihu (~ 0.9, Xia *et al*., 2007) and Beijing (~ 0.7, Yoon *et al.*, 2012). It has been reported that these two Asian sites were under the heavy pressure of regional pollution (Xin *et al*., 2007). Except for Ilorin (urban semi-arid), the remaining urban stations had relatively high α values ranging from 1.12 to 1.68, denoting predominance of fine particles.

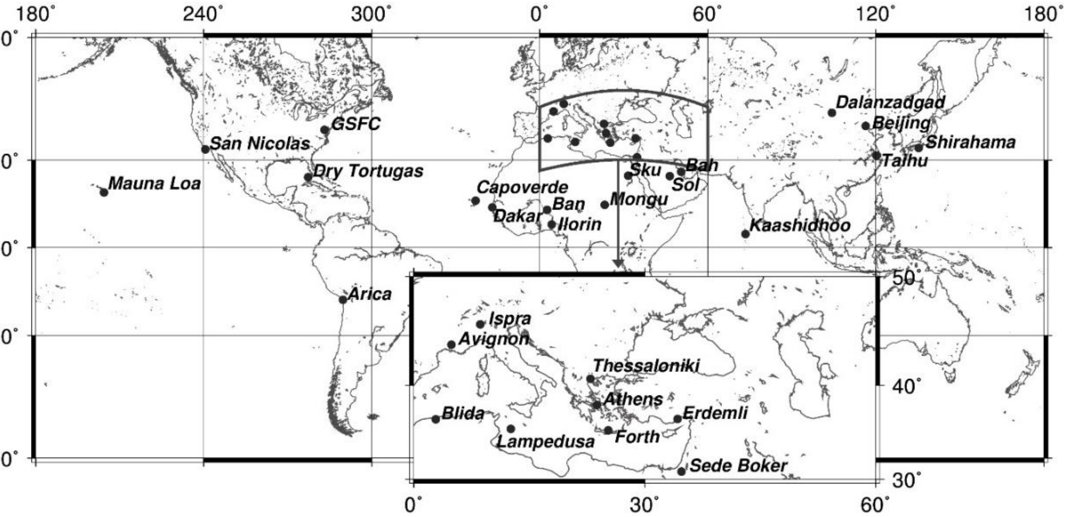

Figure 4.4 Locations of AERONET sites in Mediterranean, Middle East, Africa, Asia, and America.

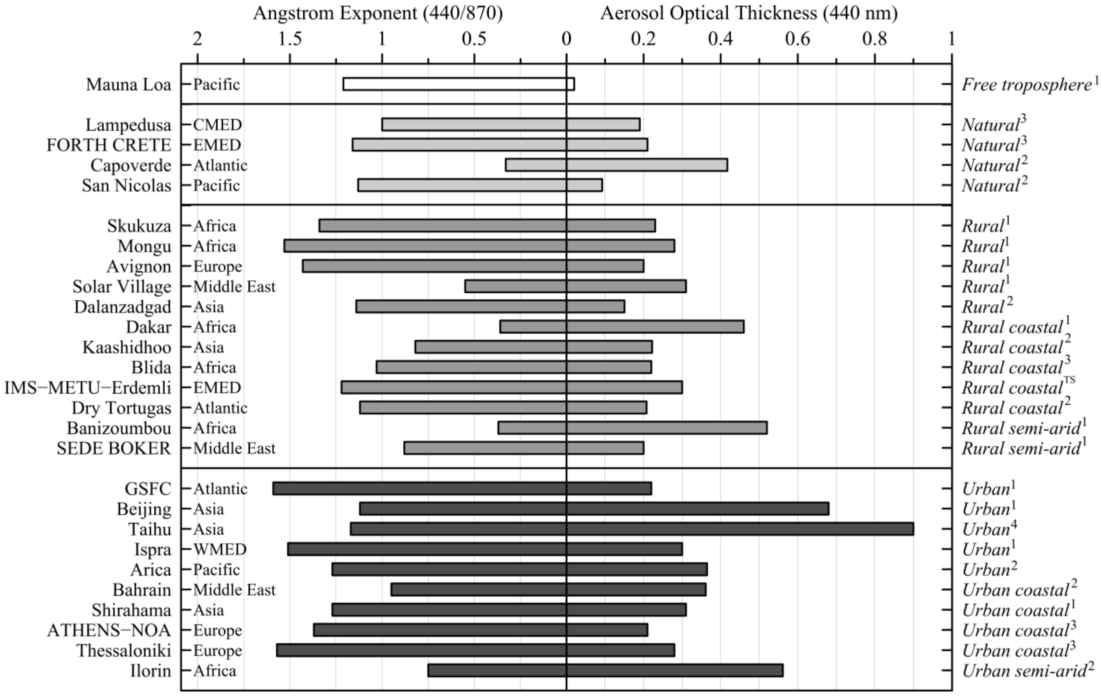

Figure 4.5 Average values of AOT (440 nm) and α (440/870) at the AERONET stations ([TS] This Study; [1] Yoon *et al.*, 2012, [2] Holben *et al.*, 2001; [3] Mallet *et al.*, 2013, [4] Xia *et al*., 2007).

4.2. Daily variability in Aerosol Optical Thickness and Angstrom Exponent

Figure 4.6 exhibits daily variability in aerosol optical thickness and angstrom exponent together with corresponding rainfall amount for Erdemli site between January 2000 and December 2014. As can be deduced from the figure, the lowest AOT values was generally associated with rain or the day after these events since wet deposition removes aerosol particles from the atmospheric compartment efficiently (Cadle and Dasch, 1988). For instance, one of the lowest AOT was observed on 19th of January 2000 with a value of 0.03. Corresponding rainfall for the same day was 15.1 mm. On 19th of January 2000 Angstrom exponent was 1.79, indicating the dominance of submicron particles. In winter, AOT$_{440}$ values seldom reached up to 1.0, the highest being observed on 25th of February 2007.

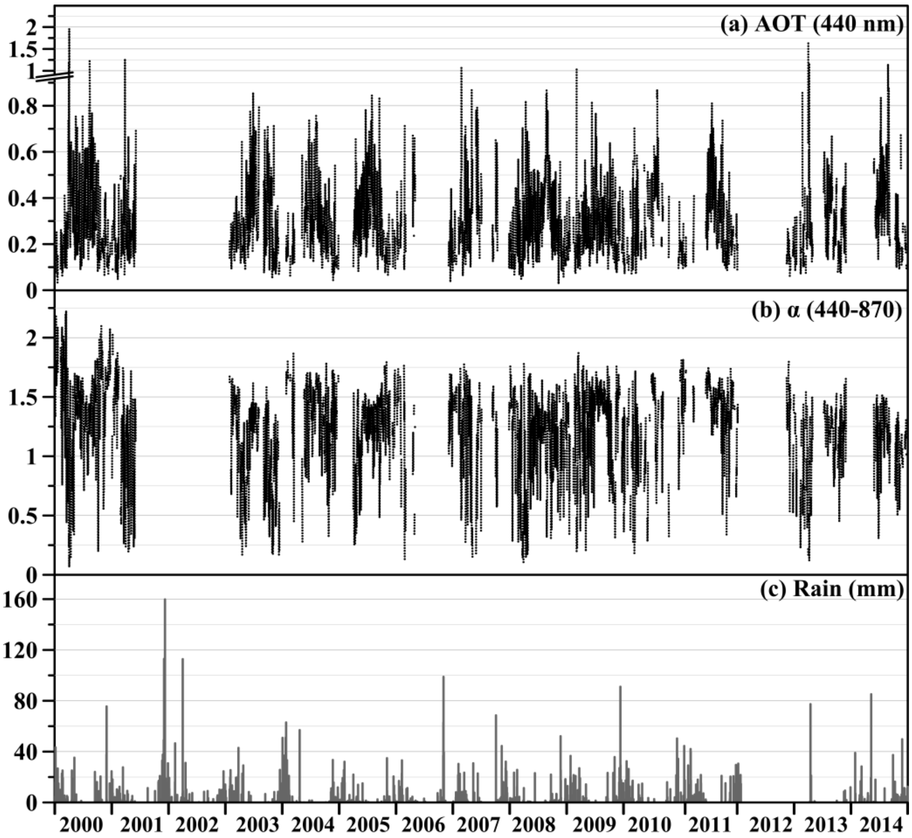

Figure 4.6 Time series of daily Aerosol Optical Thickness **(a),** Angstrom Exponent **(b)** and amount of rain **(c)** from January 2000 to December 2014.

Elevated AOT_{440} values were identified in spring and summer however, their corresponding $\alpha_{440-870}$ were distinctly different. Higher AOT_{440} and lower $\alpha_{440-870}$ were particularly detected during spring months (March, April and May) when the air masses back trajectories originated from deserts situated at North Africa and the Middle East. Studies have clearly shown that aerosol population in the Eastern Mediterranean is considerably affected by sporadic mineral dust pulses mainly occurring in transitional seasons (Kubilay and Saydam, 1995; Kubilay *et al.*, 2000, 2003). Enhanced AOT_{440} and $\alpha_{440-870}$ were identified throughout summer owing to prevailing weather conditions. Higher gas to particle conversion, sluggish airflow and lack of rain allow accumulation of aerosol particles in the atmosphere over the Eastern Mediterranean (Koçak *et al.*, 2007, Dayan *et al.*, 2017 and references therein). Consequently, higher values of AOT might be categorized into three main classes: (a) dust dominated, (b) mixed (dust/pollution) events and (c) pollution dominated. Corresponding examples for each event are presented in Figures 4.7a, b and c.

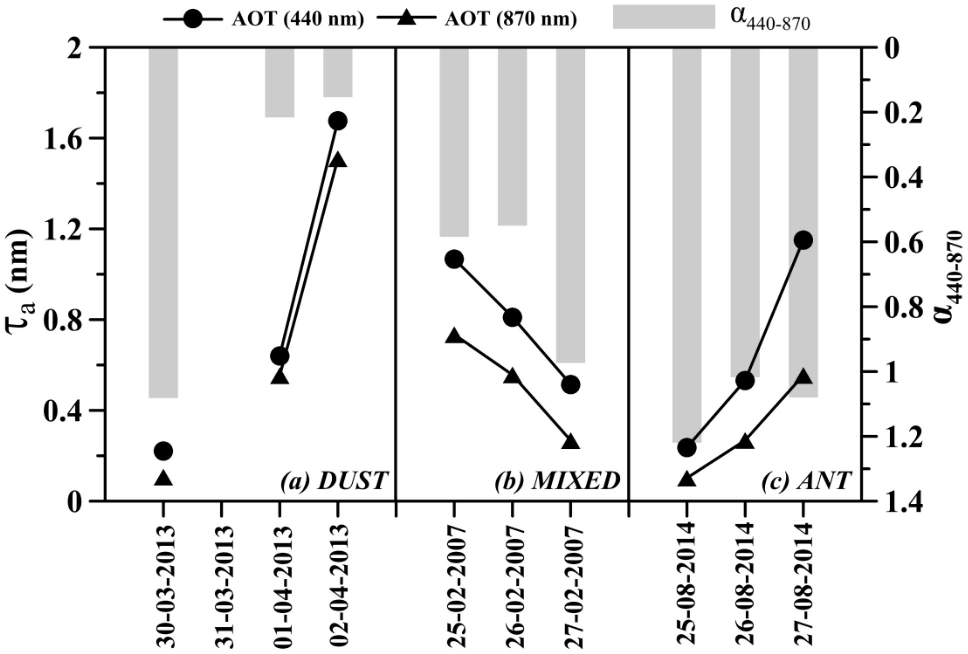

Figure 4.7 Variability in Aerosol Optical Thickness and Angstrom Exponent (α) during dust **(a)**, mixed **(b)** and pollution events **(c)** at Erdemli.

(a) Dust dominated: One of the highest AOT was observed on 2nd of April 2013 with a value of 1.67 (Figure 4.7a). On March 30, AOT (440 nm) and α were respectively found to be 0.22 and 1.08. From March 30 to April 1, AOT (440 nm) tripled over the Erdemli in contrast, α value decreased five times. The initial signal of this dust event was clearly detected by the sun photometer on April 1. During the next day, AOT (α) incremented (reduced) 2.6 (1.5) times compared to former day, demonstrating intensification of the dust episode over the site. Ozone Mapping Instrument Aerosol Index (OMI-AI) satellite image for April 1 (Figure 4.8a) demonstrated dense dust cloud over the Levantine basin however; the thickness of dust was less over the Northeastern Levantine. During this day OMI-AI values reached up to 4 between coordinates 30˚N−37˚N and 27˚E−30˚E. Within a day (Figure 4.8), the dust cloud became less apparent over the South Levantine Basin whilst the intensity of the dust cloud enhanced in the atmosphere over the Northeastern Levantine, especially at Turkish coastline. For instance, AI on April 2 over Erdemli site doubled compared to that of observed on April 1. Five-day back trajectories also supported mineral dust transport from deserts located at the Middle East and North Africa. On April 1 (Figure 4.8a), trajectories at 1, 2 and 3 km denoted that Erdemli site was under the influence of airflow from the Middle East whereas; trajectory at 4 km showed air mass transport from North Africa. Next day, lower layer trajectories (1 and 2 km, Figure 4.8b) demonstrated that site was still affected by airflow from south east. Therefore, prevailing air mass transport mainly from the Middle East and lesser extent from North Africa as well as lack of rain allow accumulation of dust particles over the Erdemli site.

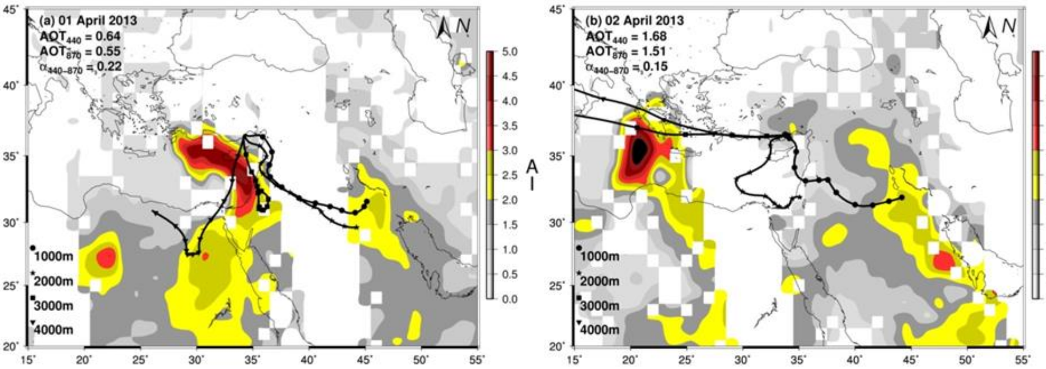

Figure 4.8 Five day back trajectories of air masses reaching at 1000m (black circle), 2000m (black star), 3000m (black square) and 4000m (black triangle) on 1st of April 2014 **(a)** and 2nd of April 2014 **(b)** with corresponding Aerosol Index (AI) from OMI (Ozone Mapping Instrument) for Erdemli.

(b) Mixed Event: Mixed dust event was characterized from February 25th to 27th, 2007 (Figure 4.7b). On 25th February, the influence of the mineral dust first detected by sun photometer with an AOT_{440} (α) value of 1.06 (0.58). The following day AOT_{440} was found to decrease to 0.81, together with a slight reduction in α value. On 27th February, AOT_{440} continued to decreased, attaining value of 0.52 with a twofold decrement compared to the initial AOT_{440} value of the case nonetheless, α value increased 1.9 times compared to the previous days, reaching value of 0.97. OMI-AI satellite image for 25th February indicated a large dust plume over the Eastern Mediterranean extending from 32˚N−38˚N to 25˚E−35˚E, AI values ranging from 2.0 to 3.0 (Figure 4.9). During the next day, the dust plume became less intense and on 27th February dust cloud disappeared over the region. Considering the back trajectories (Figure 4.9), air masses originated from North Africa (passing over Egypt) arrived to the site at 2, 3 and 4 km altitudes on 25th February, whilst the back trajectory for 1 km altitude indicated airflow from Turkey. During the next day, air flow for 1 km altitude showed a transport from region located over Ukraine, the middle Black Sea and Turkey whereas air masses at upper levels (3 and 4 km) advected to the site from North Africa.

Back trajectories for 27th February indicated air flow at upper levels from North Africa terminated and started to come from northwest.

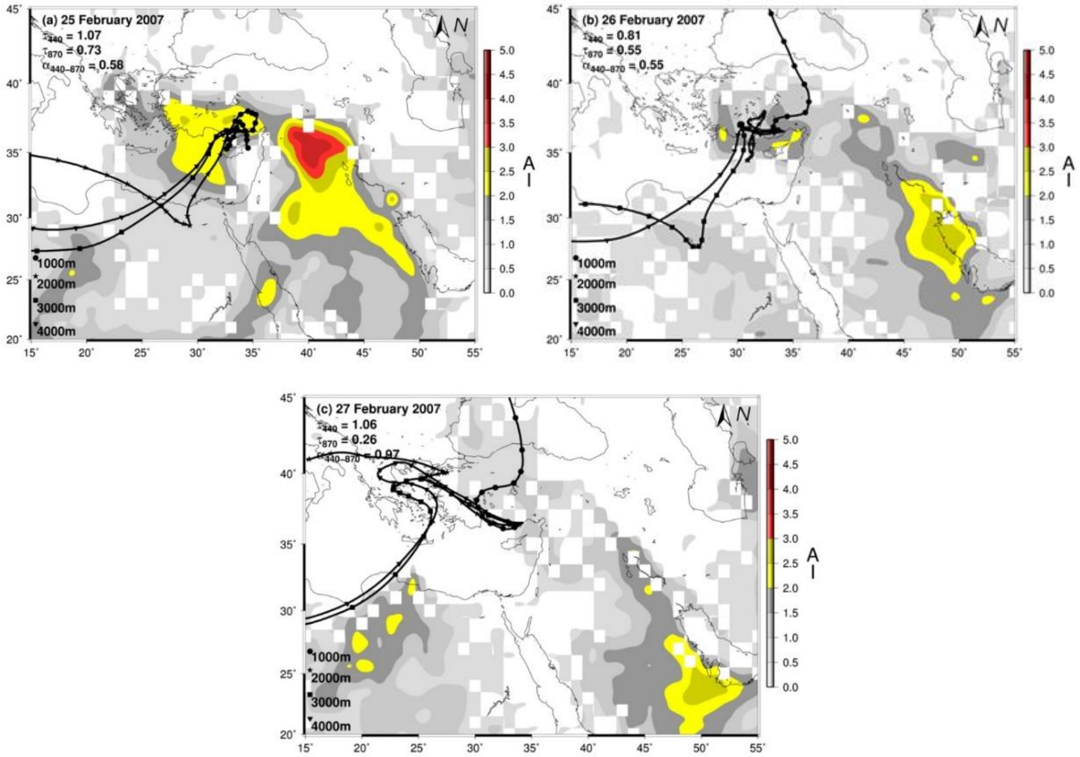

Figure 4.9 Five day back trajectories of air masses reaching at 1000m (black circle), 2000m (black star), 3000m (black square) and 4000m (black triangle) on 25th of February 2007 **(a)**, 26th of February 2007 **(b)**, and 27th of February 2007 **(c)** with corresponding Aerosol Index (AI) from OMI (Ozone Mapping Instrument) for Erdemli.

(c) Pollution Dominated Event: The pollution event was described from August 25th to 27th, 2014 (Figure 4.7c). On 25th August, AOT_{440} and α were respectively found to be 0.24 and 1.21. Next day, AOT_{440} almost doubled over the Erdemli whereas α decreased about 10 %, reaching the value of 1.07. On 27th August, AOT reached the highest value of the event with a fivefold increment, attaining value of 1.15. Nonetheless, α was found to be 1.08 and the change in Angstrom Exponent from 25 August to 27 August was only about 10 %, all values being higher than 1. MODIS-Terra (Moderate Resolution Imaging Spectrometer) AOD satellite image for 25th August indicated low thickness over site (Figure 4.10). Then, next day it started to increase and on 27th August, attained the value of 0.8 with a four-fold increase from 25 August. Corresponding five-day back trajectories exhibited that air masses arrived to the site at all altitudes from north and northwest on 25th August (Figure 4.10). Next day, lower layers (1 and 2 km) back trajectories was related to air flows coming from northern sector whereas, upper layers (3 and 4 km) back trajectories were associated with air mass transport from south. On 27th August, trajectory at 1 km indicated the site still remained under influence of air mass transport from the region located over eastern Black Sea and Turkey. On the other hand, trajectory at 2, 3 and 4 km pointed the air mass transport from southwest. It should be noted that on 26 and 27 August, air masses reached the site at 3 and 4 km, descending vertically from further height levels nonetheless, the trajectory at 1 km on 26 August and trajectories at 1 and 2 km on 27 August indicated that air masses arrived to the site at corresponding heights, ascending vertically from ground levels (Figure 4.11).

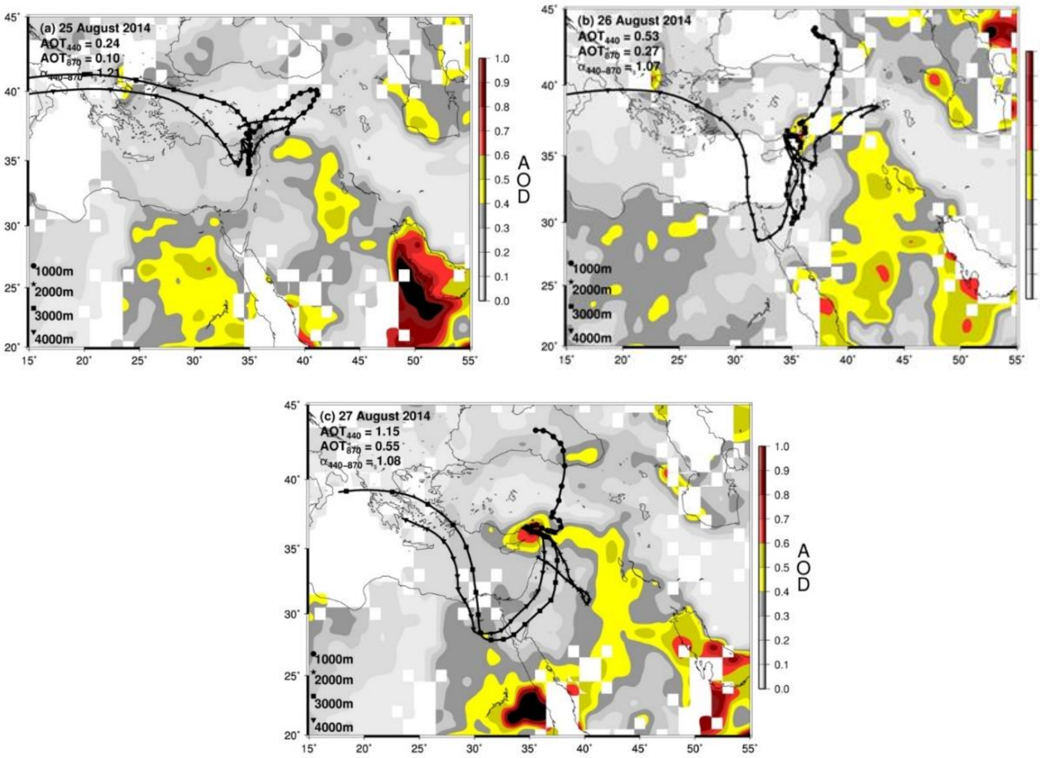

Figure 4.10 Five day back trajectories of air masses reaching at 1000m (black circle), 2000m (black star), 3000m (black square) and 4000m (black triangle) on 25th of August 2014 **(a)**, 26th of August 2014 **(b)** and 27th of August 2014 **(c)** with corresponding AOD from MODIS Terra for Erdemli.

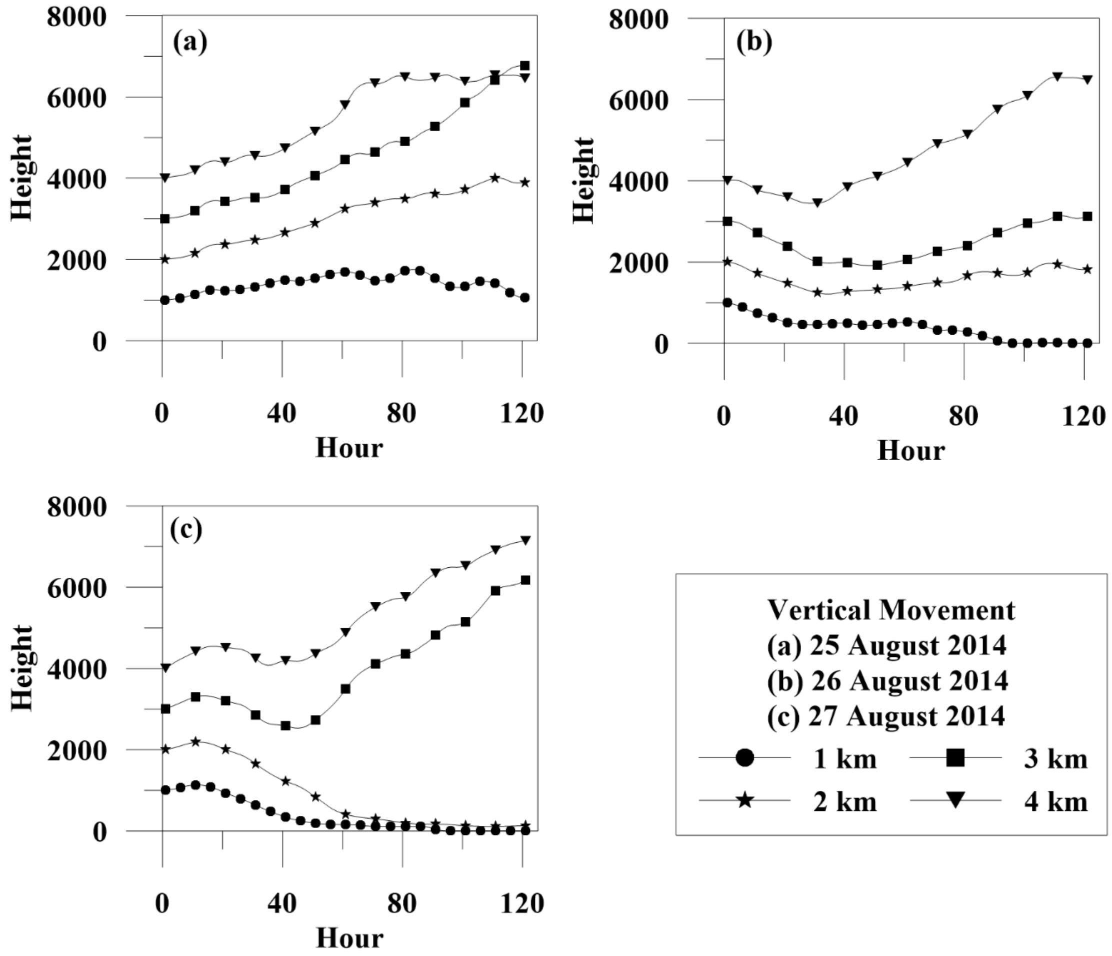

Figure 4.11 Vertical movement of five day back trajectories of air masses reaching at 1000m (black circle), 2000m (black star), 3000m (black square) and 4000m (black triangle) on 25th of August 2014 **(a)**, 26th of August 2014 **(b)** and 27th of August 2014 **(c)**.

4.3. Seasonal variability in Aerosol Optical Thickness and Angstrom Exponent.

Monthly arithmetic mean and standard deviations for aerosol optical thickness (440 and 870nm, coarse and fine at 500 nm), angstrom exponent, water vapor together with local rain amount and temperature are presented in Figure 4.12. The lowest values of AOT (440, 870 nm, fine and coarse) were found in winter. The minimum in winter might be ascribed to four main processes namely (a) efficient removal of aerosol burden from the atmospheric compartment by rain, (b) reduced gas to particle conversion due to cloud cover and incoming solar flux, and (c) less frequent dust transport from the Middle East and North Africa (d) emission strength of sources (Bergametti *et al.*, 1989; Güllü *et al.*, 1998; Kubilay *et al.*, 2000). Notwithstanding, there was a distinct difference in the seasonal cycle of AOT$_{440}$, AOT$_{870}$, AOT$_{coarse}$ and

AOT_{fine}. To begin with AOT_{870} (AOT_{coarse}), monthly arithmetic mean gradually increased from January to March and reached its maximum in April with a value of 0.22 (0.17). Arithmetic mean of AOT_{870} (AOT_{coarse}) then reduced 40 % (60 %) from April to June. AOT_{870} (AOT_{coarse}) demonstrated 20 % (only 5 %) enhancement from June to August. Mean AOT_{870} (AOT_{coarse}) abruptly declined from 0.18 (0.09) to 0.08 (0.05) between August and December On the whole, arithmetic mean of AOT_{440} (AOT_{fine}) illustrated piecemeal augmentation from January to August, attaining its maximum with a value of 0.44 (0.27). After that, mean AOT_{440} (AOT_{fine}) began to decrease and achieved its winter values in December (AOT_{440} ~ 0.18, AOT_{fine} ~ 0.10). Monthly mean of $\alpha_{440\text{-}870}$ denoted steady decrease from 1.40 to 0.94 between January and April. Then $\alpha_{440\text{-}870}$, raised about 40 %, reaching value of 1.30 in June whilst $\alpha_{440\text{-}870}$ did not point out remarkable change from June to December. The seasonal cycle of water vapor, on the other hand, was similar to that of observed for AOT_{fine}. Monthly mean water vapor exhibited substantial increase from January (1.0 cm) to August (3.2 cm) and later its monthly values drastically dropped to 1.1 cm towards end of the year.

Seasonal scatter diagrams for AOT_{440} versus $\alpha_{440\text{-}870}$ together with the frequency of occurrence of these two parameters are depicted in Figure 4.13. As can be deduced from scatter plots, winter (DJF) and spring (MAM) showed a strong trend of increase in AOT_{440} values as $\alpha_{440\text{-}870}$ decreases, though, summer (JJA) and fall (SON) exhibited a very weak trend of reduction in AOT_{440} values with decreasing $\alpha_{440\text{-}870}$. Seasonal histograms for AOT_{440} and α_{440}-870 also denoted distinct difference. The frequency of occurrence histogram of AOT_{440} showed gradual shift toward higher values from winter to summer and it decreased from summer to fall. In winter, spring and fall, the AOT_{440} probability distributions exhibited peak values of 0.1-0.2 (51 %) 0.2-0.3 (35 %) and 0.1-0.2 (32 %), respectively, whereas AOT_{440} illustrated peak value of 0.3-0.4 (25 %) in summer. The AOT_{440} frequency distributions clearly showed that the atmosphere over the Eastern Mediterranean was more turbid in summer than those observed for the remaining seasons. As stated before, this might be result of higher gas to particle conversion, sluggish airflow and lack of rain. The frequency of occurrences histogram for $\alpha_{440\text{-}870}$ displayed relatively narrow peak from 1.1 to 1.6 in summer (77 %) and fall (56 %) on the other hand, only few percent had values less than 0.5 (summer: 1.2 %, fall: 3.5 %), showing that fine particles were dominant. Unlike summer and fall, the $\alpha_{440\text{-}870}$ probability distribution was rather broader (wide range particle size) in spring, 16 % being lower than 0.5. About 50 % of $\alpha_{440-870}$ < 0.5 values had AOT_{440} larger than 0.4, implying the transport of mineral dust from North Africa and Middle East deserts (Koçak *et al.*, 2004). The remaining episodes might be attributed to weak dust events and/or sea salt (Smirnov *et al.*, 2002; Fotiadi *et al.*, 2006). Furthermore, more than 16 % of the $\alpha_{440-870}$ in winter, spring and fall ranged from 0.5 to 1.0, suggesting mixed mineral dust and anthropic particles (Eck *et al.*, 1999; Holben *et al.*, 2001; Smirnov *et al.*, 2002) Therefore, it might be argued that the aerosol population was comparatively more diverse in spring compared to winter, summer and fall.

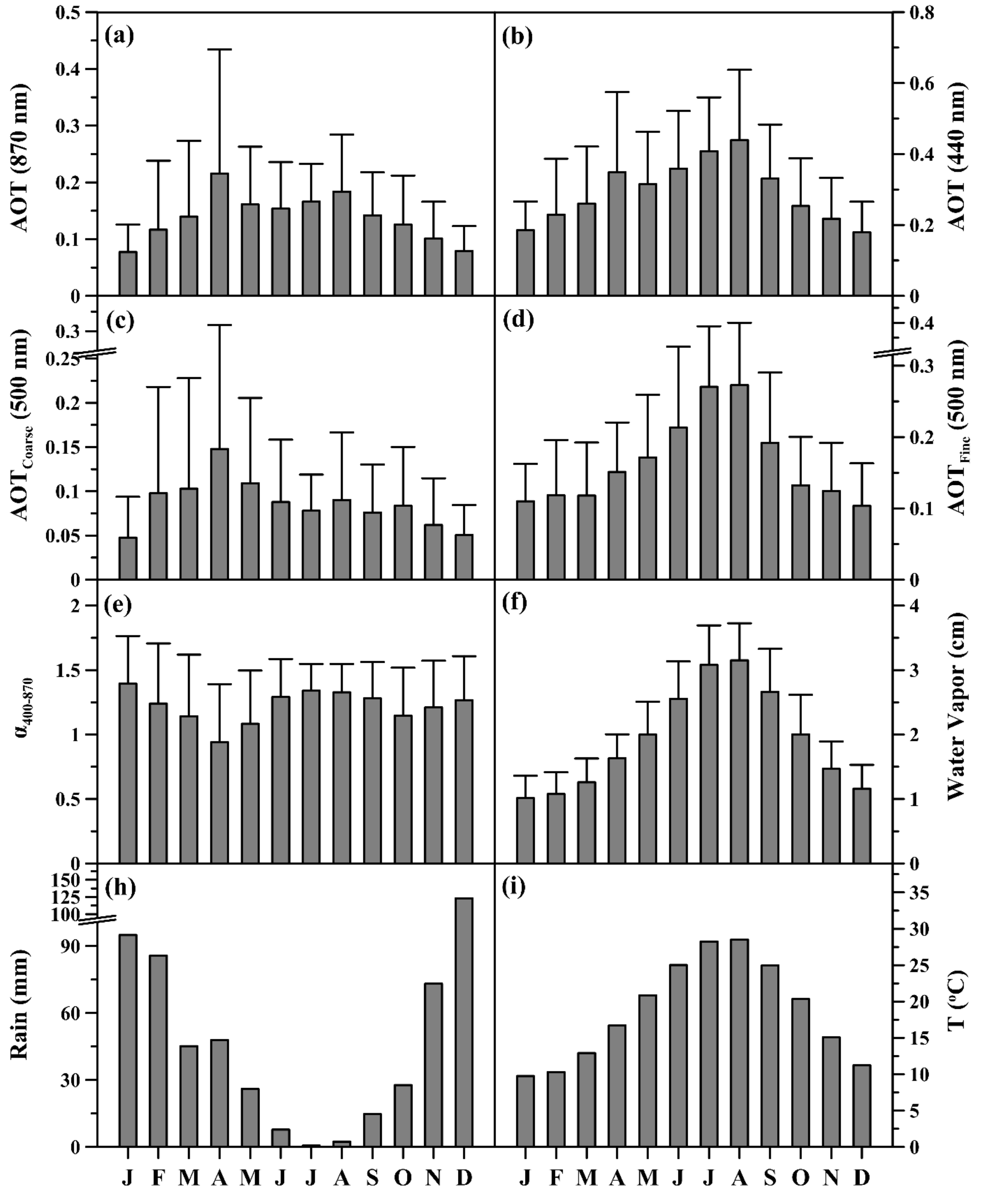

Figure 4.12 Mean monthly values of AOT_{440} **(a)**, AOT_{870} **(b)**, coarse mode AOT **(c)** and fine mode AOT **(d)** at 500 nm, $\alpha_{440-870}$ **(e)**, water vapor **(f),** rain **(h)** and temperatures **(i).** The bars represent standard deviations.

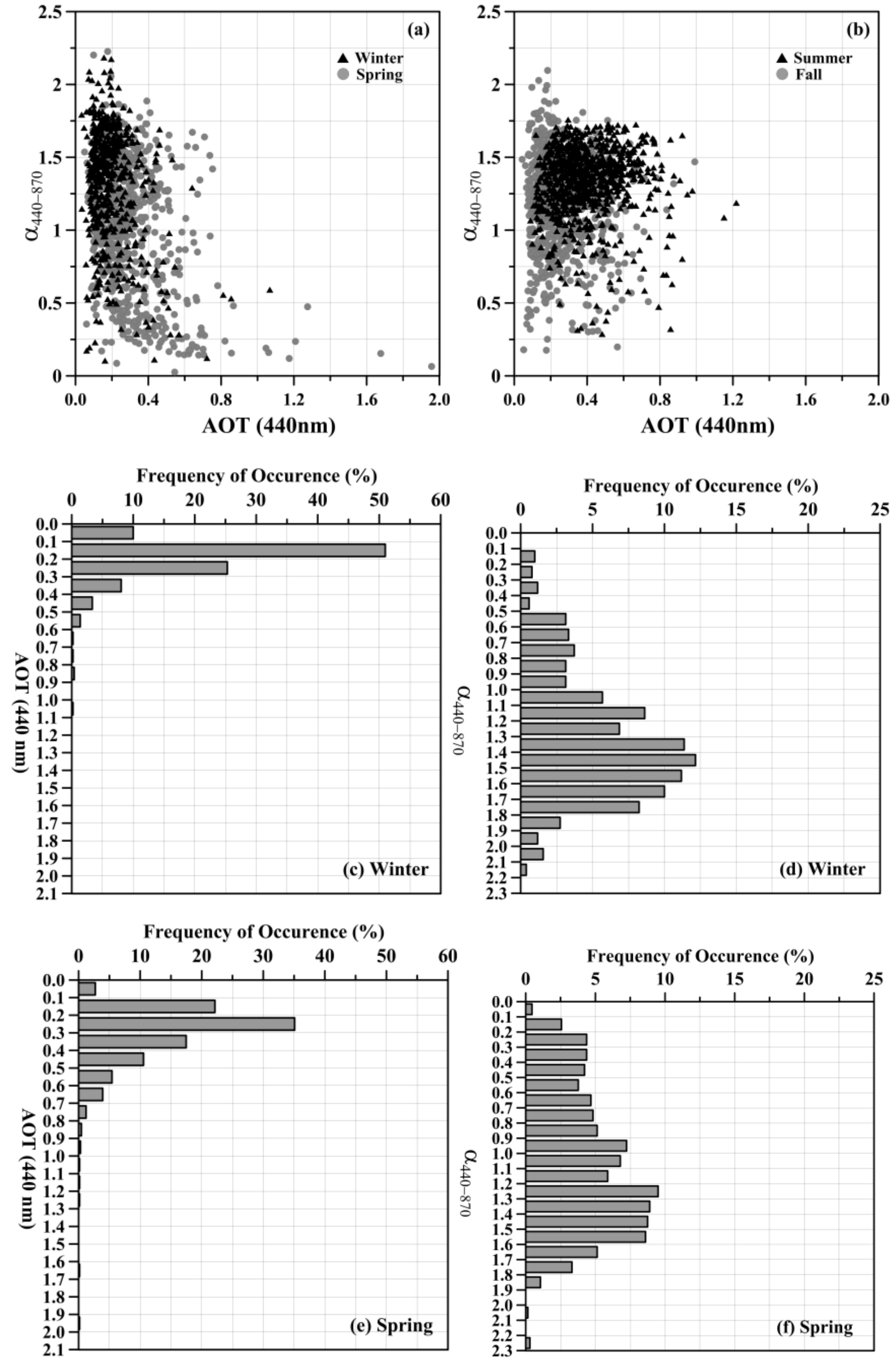

Figure 4.13 Seasonal scatter plot of AOT$_{440}$ versus $\alpha_{440-870}$ **(a-b)** and frequency of occurrence of AOT$_{440}$ and $\alpha_{440-870}$ for winter **(c-d)**, spring **(e-f)**, summer **(g-h)**, and fall **(i-j)**.

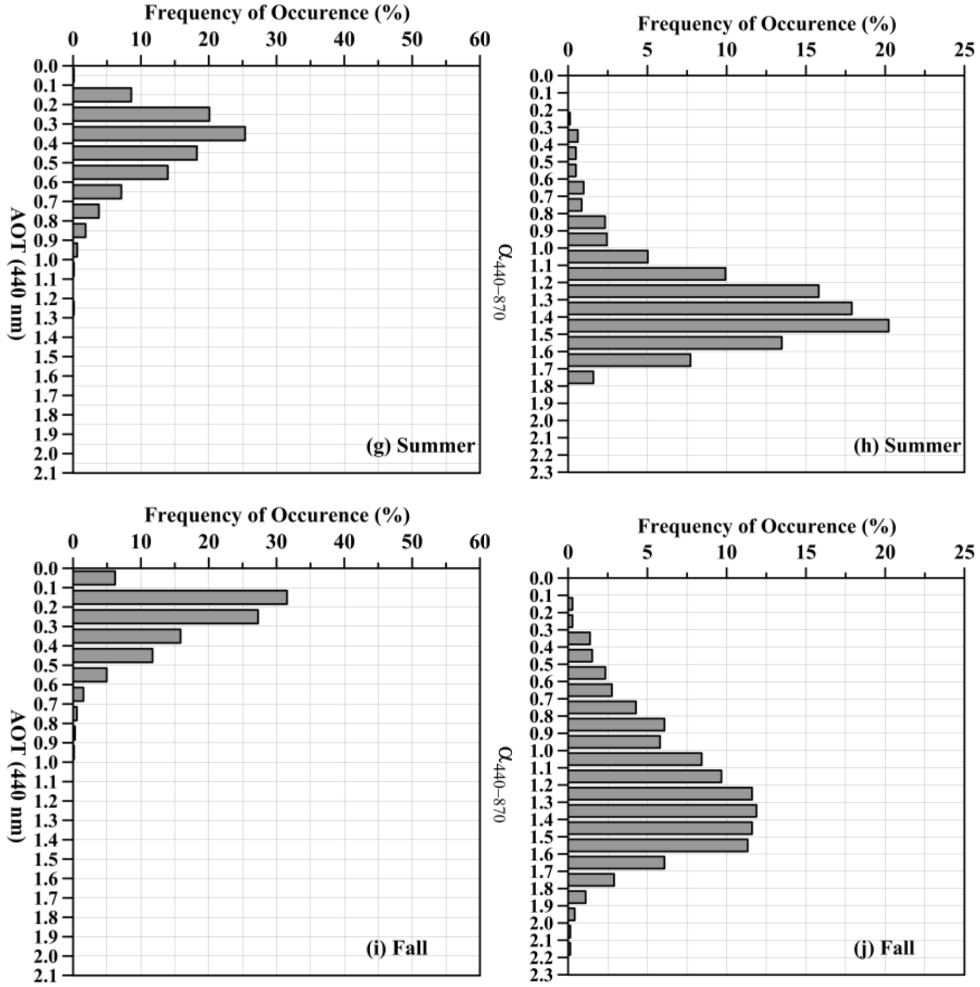

Figure 4.13 continue ...

Correlations between variables illustrate the degree to which they together. In order to clarify monthly relationship between AOT, $\alpha_{440\text{-}870}$, water vapor and local meteorological parameters, namely temperature and rain were used. The correlation coefficients between aforementioned variables are given in Table 4.2. The obtained correlation coefficients indicated that water vapor, temperature and total rain amount significantly modified the seasonality of aerosol physics in the atmosphere over the Erdemli. Except for $\text{AOT}_{\text{coarse}}$, there were negative correlation between rain amount and AOT_{870}, AOT_{440} and AOT_{fine}. However, the correlation coefficients were statistically significant (c.l. 95 %, n = 12) for AOT_{440} (r = -0.59) and AOT_{fine} (r = -0.77). In addition, AOT_{440} (r = 0.79) and AOT_{fine} (r=0.83) showed significant correlation coefficients with temperature. Therefore, during winter month's AOT_{440} and AOT_{fine} decreased not only due to the removal of particles from atmospheric compartment but also because of less efficient gas to particle conversion (e.g. cloudy days, inferior incoming solar influx). Influence of rain on AOT$_{870}$ and AOT$_{coarse}$ was not significant and hence this might be ascribed to the mechanical formation of coarse particles and their source strength. For example, atmospheric sea salt production especially increases in rainy winter months owing to more active and frequent storms (Marks, 1990; O'Dowd and Smith, 1993). Furthermore, in spite of considerable rain, the mineral dust transport from desert sources to the receptor site has primarily been determined in spring (March, April and May) when the prevailing conditions are more favorable for the Saharan cyclones (Kubilay *et al.*, 2000). Angstrom Exponent indicated strong negative correlation with AOT$_{coarse}$ (-0.80) although it showed moderate negative correlation coefficient with AOT$_{870}$ (-0.49). Considering these relationship, it might be note that the seasonality of $\alpha_{440\text{-}870}$ was mainly controlled by the existence of coarse particles.

Table 4.2 Matrix correlation of the monthly AOT (440 nm), AOT (870 nm), fine and coarse AOT, α (440/870), water vapor (WV), temperature (T), rain (R). Marked correlations (in bold and italic) are significant at $p < 0.05$.

	AOT$_{870}$	**AOT$_{440}$**	**AOT$_{coarse}$**	**AOT$_{fine}$**	**$\alpha_{440\text{-}870}$**	**WV**	**T**	**R**
AOT$_{870}$	1.00							
AOT$_{440}$	**0.87**	1.00						
AOT$_{coarse}$	**0.83**	0.47	1.00					
AOT$_{fine}$	*0.64*	**0.94**	0.15	1.00				
$\alpha_{440\text{-}870}$	-0.49	-0.01	**-0.80**	0.30	1.00			
WV	*0.60*	**0.90**	0.11	**0.96**	0.25	1.00		
T	*0.64*	**0.89**	0.17	**0.91**	0.13	**0.99**	1.00	
R	-0.47	*-0.77*	0.02	**-0.88**	-0.31	**-0.87**	**-0.83**	1.00

4.4 Influence of Air Flow on Aerosol Optical Properties

To assess the influence of air flow on aerosol optical properties the categorization of trajectories were utilized (see Chapter III). The Kruskal-Wallis (K-W) test was applied to test for the presence of significant differences in aerosol optical properties namely aerosol optical thickness at 440, 675, 870 as well as 1020 nm, angstrom exponent and fine fraction (%) classified according to air masses. Table 4.3 statistical summary of the AOT, AE and FF (%) for each air flow sector at 1 km and 4 km.

Air flow reaching at altitude of 1 km: Table 4.3a and Figure 4.14 illustrate statistical summary of the AOT, AE and FF (%) for each air flow sector at 1 km. Application of

Kruskal-Wallis test exhibited that aerosol optical thicknesses at 440 nm for MID, SAH and TR were not statistically different. Likewise, AOT for MED, EE and WE were found to be comparable and they were statistically not different. AOT for MID, SAH and TR was at least 15 % larger than those observed for MED, EE and WE. On the other hand, mean AOT for air flow showed dramatic difference with increasing wavelength. For MID and SAH air flow, AOT exhibited slight decrease from 440 nm to 1020 nm, indicating dominance of coarse particle. Angstrom exponent and the percent contribution of fine fraction in these air masses were also support the above statement, former and later being around 0.75 and 47 %, respectively. Conversely, AOT for MED, EE, WE and TR denoted almost 65 % decrease between 440 nm and 1020 nm since aerosols arising from these air flow sectors were mainly associated with fine mode (AE > 1.1 and FF > 62 %, see Table 4.3 and Figure 4.14). Results from K-W test demonstrated statistically significant difference for AOT between MID, SAH and MED, EE, WE as well as TR at 675 nm, 870 nm and 1020 nm, first two sectors being approximately 2 times higher than the remaining air flows. Furthermore, angstrom exponent and the percent contribution of fine fraction were remarkably lower for MID and SAH compared to air flow originated from MED, EE, WE and TR.

Table 4.3 Arithmetic means and standard deviations for AOT, AE and fine mode fraction as a function of air flow for 1 km **(a)** and 4 km **(b).**

a)	WE (n=327) Mean±Std	EE (n=1028) Mean±Std	TR (n=771) Mean±Std	MID (n=147) Mean±Std	SAH (n=194) Mean±Std	MED (n=244) Mean±Std
AOT_{440}	0.27 ± 0.15	0.28 ± 0.16	0.34 ± 0.18	0.36 ± 0.25	0.35 ± 0.20	0.29 ± 0.15
AOT_{675}	0.17 ± 0.11	0.15 ± 0.09	0.20 ± 0.11	0.28 ± 0.24	0.26 ± 0.19	0.17 ± 0.09
AOT_{870}	0.13 ± 0.09	0.11 ± 0.07	0.15 ± 0.09	0.25 ± 0.24	0.23 ± 0.18	0.13 ± 0.07
AOT_{1020}	0.12 ± 0.09	0.09 ± 0.06	0.12 ± 0.08	0.23 ± 0.24	0.21 ± 0.17	0.11 ± 0.06
$\alpha_{440-870}$	1.1 ± 0.4	1.3 ± 0.3	1.3 ± 0.3	0.8 ± 0.4	0.8 ± 0.4	1.3 ± 0.3
FF	0.62 ± 0.17	0.73 ± 0.11	0.71 ± 0.14	0.49 ± 0.19	0.47 ± 0.19	0.68 ± 0.13

FF, std denotes fine mode fraction at 500 nm and standard deviation, respectively.

b)	WE (n=1508) Mean±Std	EE (n=325) Mean±Std	TR (n=273) Mean±Std	MID (n=81) Mean±Std	SAH (n=511) Mean±Std
AOT_{440}	0.30 ± 0.16	0.21 ± 0.11	0.33 ± 0.17	0.46 ± 0.26	0.37 ± 0.20
AOT_{675}	0.17 ± 0.11	0.11 ± 0.06	0.18 ± 0.10	0.30 ± 0.18	0.26 ± 0.17
AOT_{870}	0.13 ± 0.09	0.08 ± 0.04	0.13 ± 0.08	0.24 ± 0.15	0.22 ± 0.16
AOT_{1020}	0.11 ± 0.08	0.07 ± 0.03	0.11 ± 0.07	0.21 ± 0.14	0.20 ± 0.15
$\alpha_{440-870}$	1.3 ± 0.3	1.4 ± 0.3	1.4 ± 0.3	1.1 ± 0.4	0.9 ± 0.4
FF	0.70 ± 0.14	0.73 ± 0.12	0.74 ± 0.12	0.62 ± 0.17	0.55 ± 0.20

FF, std denotes fine mode fraction at 500 nm and standard deviation, respectively.

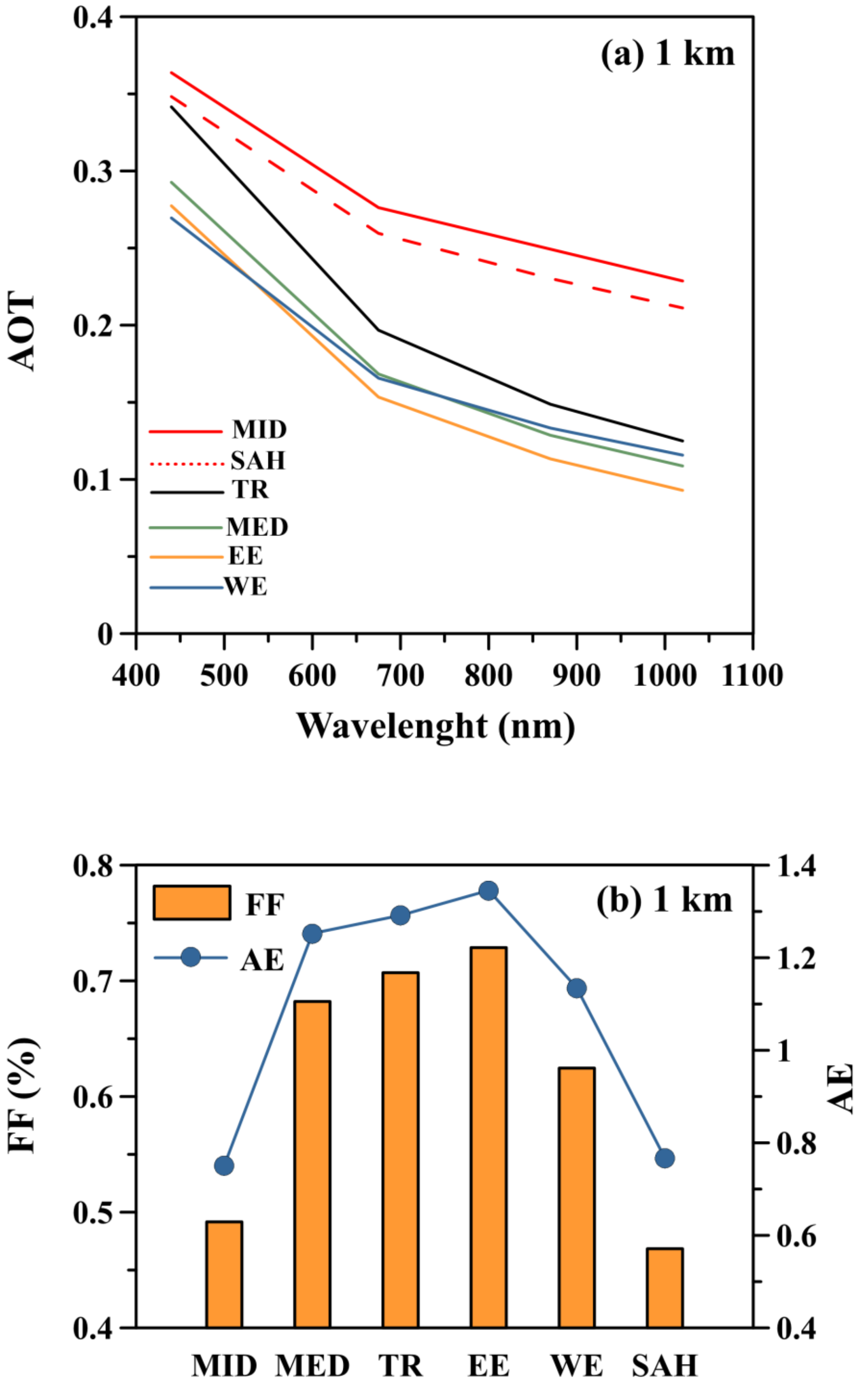

Figure 4.14 Variability in aerosol optical thickness **(a)**, fine fraction and angstrom exponent **(b)** according to the clusters at 1 km.

Air flow reaching at altitude of 4 km: The results from K-W test for 4 km air flow was less dramatic relative to 1 km, suggesting influence of different air masses in the atmospheric column at the same time. For example, the air flow reaching at 4 km altitude from SAH sector exhibited diverse air masses transport at 1 km. Correspondingly, 18, 5, 17, 21, 27 and 12 % of trajectories at 1 km altitude were associated with air flow from EE, MED, MID, SAH, TR and WE when air masses arriving at 4 km altitude from SAH. Figure 4.15a and b show AOT at 1020 nm and angstrom exponent according to air masses transport from EE, MED, MID, SAH, TR and WE for SAH air flow at 4 km altitude. As expected, K-W test exhibited dramatic difference for air masses categories. For AOT at 1020 nm, air masses back trajectories arising from SAH and MID was remarkably larger (at least 30 %) than those observed for the remaining air flow sectors. Angstrom exponent of MID and SAH was also statistically different than the other sectors, the former group being less than 0.62 and the latter group being higher than 0.86. Therefore, it might be suggested that the impact of mineral dust transport was less obvious in the atmospheric column when the air flows originated from industrialized and populated areas due to the dilution effect of anthropic aerosols.

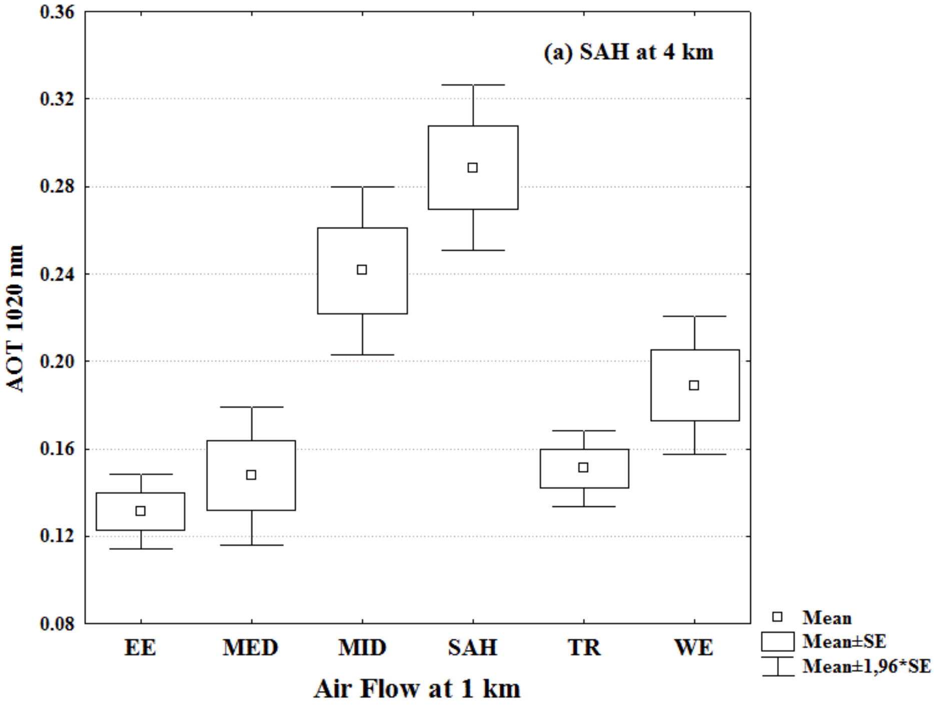

Figure 4.15 Bow-whisker plot of AOT at 1020 nm **(a)** and angstrom exponent **(b)** according to air masses transport from EE, MED, MID, SAH, TR and WE at 1 km when air masses arriving at 4 km altitude from SAH.

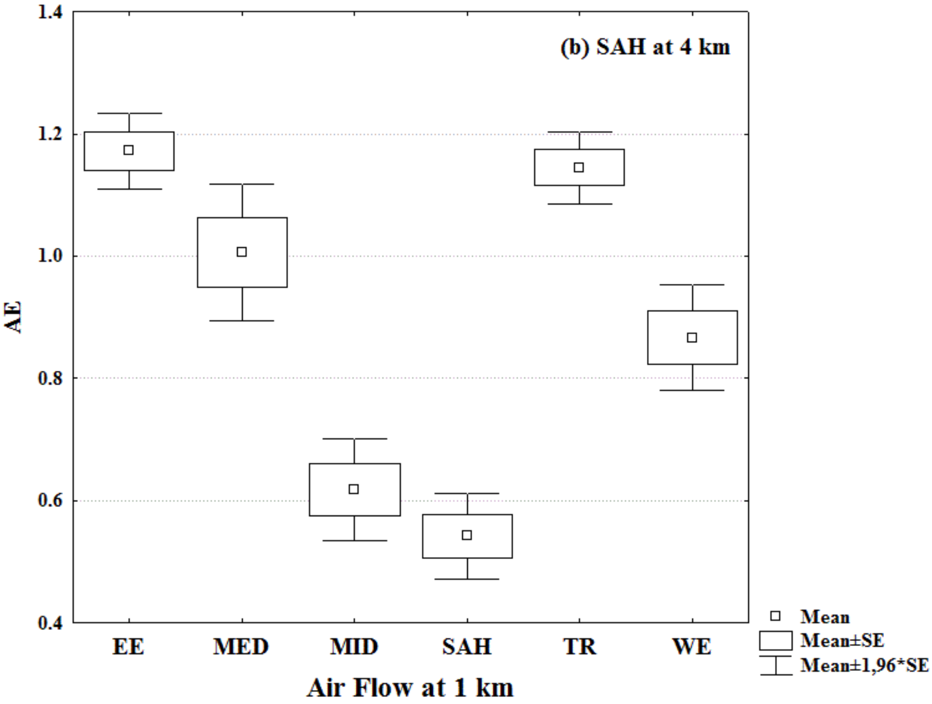

Figure 4.15 continue …

4.4. PSCF Analysis.

The PSCF analysis have been applied to three α groups: (i) $\alpha_{440\text{-}870} < 0.5$, (ii) $0.5 < \alpha_{440\text{-}870} < 1.0$ and (iii) $1.0 < \alpha_{440\text{-}870}$ and the result of PSCF analysis are presented in the maps with a color scale (Figure 4.14). Calculated PSCF values were divided into three parts: (a) weak (0.0–0.4), (b) intermediate (0.4–0.6) and (c) strong (0.6–1.0).

1st group ($\alpha_{440\text{-}870} < 0.5$, Figure 4.14a-b): The PSCF map for 1 km level indicates the presence of intermediate and strong PSCF valued grid cells in North Africa and the Middle East between coordinates 22˚N−34˚N and 8˚E−48˚E (Fig. 4.14a). Particularly, the strong potential probabilities were located at regions covering patches of Southern Tunisia, Western Libya, Libya/Chad border, southern Egypt in North Africa and areas extending from Iraq to eastern Saudi Arabia in the Middle East. On the other hand, the map for 4 km level only shows the major source regions located on North Africa (Fig. 4.14b). It could be interpreted that mineral dust transported to the region at high altitudes, which was characterized by low angstrom exponent, originated mainly from North Africa. The intermediate and strong PSCF valued cells for 4 km level took place between 16˚N-30˚N and 10˚W-30˚E. The map identifies northeastern Mauritania and part of north Mali, southern Algerian Northwestern Niger as strong potential source locations (Fig. 4.14b). Identified source regions in North African and Middle East are in correspondence with previous studies (Washigngton *et al.*, 2003, Ginoux *et al.*, 2012, Gherboudj *et al.*, 2017). For instance, Gherboudj *et al.* (2017) highlighted Chott el-Jerid (Southern Tunisia), Aljafra plain/ Nafusa mountains slopes (Tunisia/Libya), Tibesti mountains slopes (Libya-Chad border), river drainage basin of the Aiir (southern Algerian), Erg of Bilma (Northwestern Niger) and Nubian desert (Sudan/Egypt) as important dust emission source areas, which was related to the source regions identified in this study.

2nd group (0.5 <$\alpha_{440-870}$ <1.0, Figure 4.14c-d): The PSCF map for 1 km level identifies similar region as the map of 1 km level for $\alpha_{440-870} < 0.5$. However, a wide area of Western Europe going from Spain to Italy and other small areas in France and Germany appeared to be potential source locations (Fig. 4.14c). These results show that air masses belonging to this group was influenced by both anthropogenic and natural aerosols before reaching to Erdemli (Koçak *et al.*, 2007). As for the PSCF map for 4 km level, region stretching from Northeastern Sudan to Syria was also identified as possible source locations compared to first group's 4 km level PSCF map.

3rd group 1.0 < $\alpha_{440-870}$, Figure 4.14e-f): The PSCF map for 1.0 < $\alpha_{440-870}$ doesn't clearly show any significant source regions. This may mainly point to the local sources formed under summer conditions. Similar PSCF patterns have been demonstrated for secondary aerosols measured in Erdemli (Kocak *et al.*, 2009).

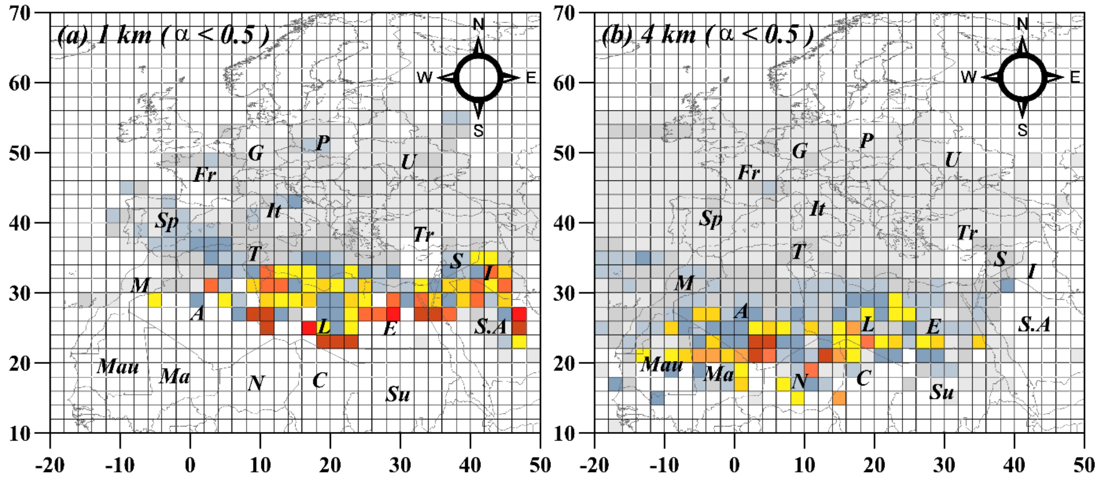

Figure 4.16 Distribution of PSCF values at 1km and 4km for the values of $\alpha_{440-870} < 0.5$ **(a-b)**, $0.5<\alpha_{440-870} < 1.0$ **(c-d)**, $1.0<\alpha_{440-870}$ **(e-f)**. Explanation of abbreviation: Spain (Sp), France (Fr), Germany (G), Poland (P), Ukraine (U), Turkey (Tr), Syria (S), Iraq (I), Saudi Arabia (S.A), Egypt (E), Libya (L),Tunisia (T), Algeria (A), Morocco (M), Mauritania (Mau), Mali (Ma), Niger (N), Chad (C) and Sudan (Su).

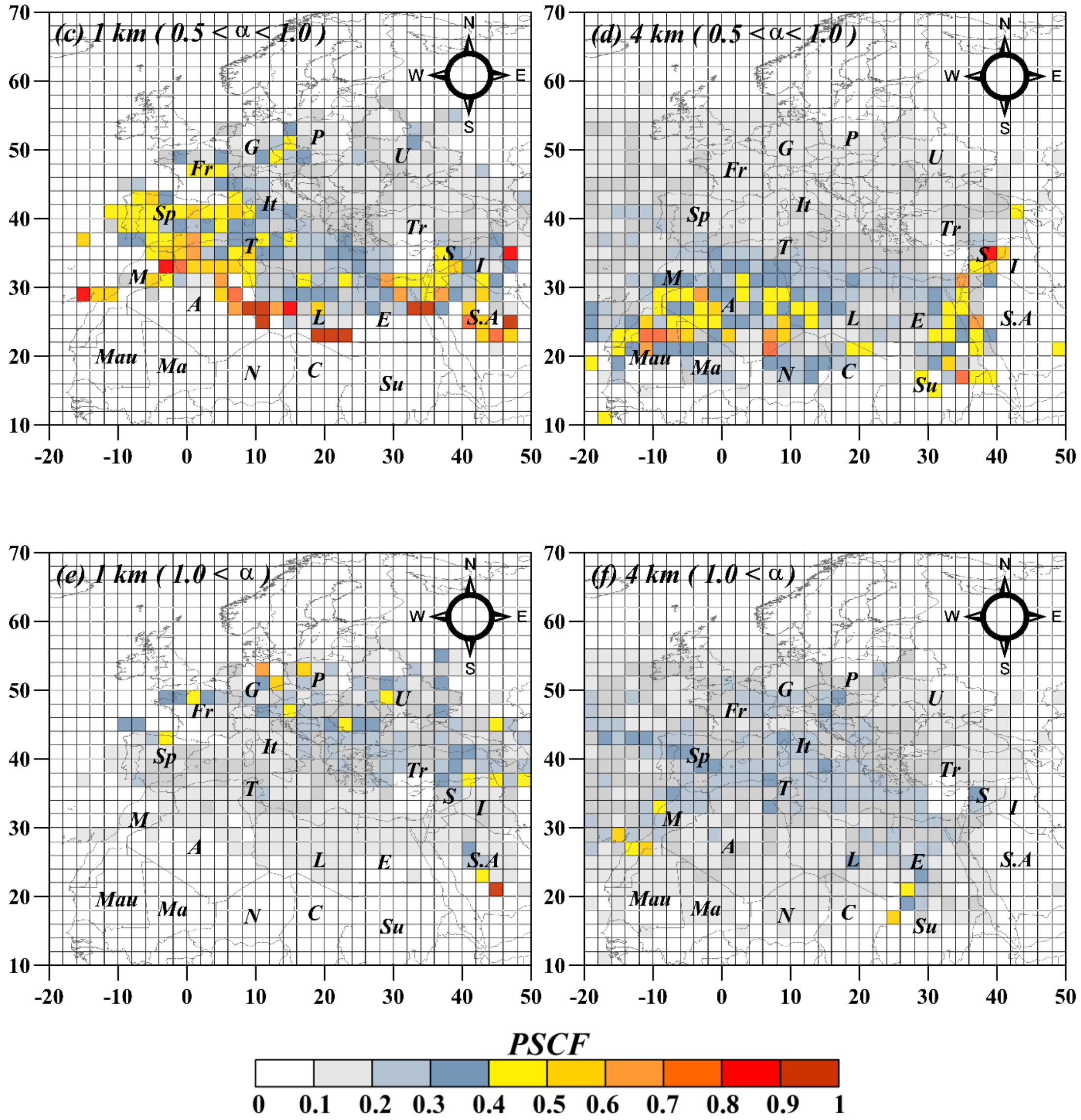

Figure 4.16 continue …

CHAPTER V

5. Climatology of Aerosol Optical Properties and Classification of Aerosol Type over Eastern Mediterranean.

5.1. Daily Variations in the Aerosol Optical and Microphysical Properties

The daily variations in the aerosol optical and microphysical properties from January 2002 to December 2014 together with the particles size distribution for each period are illustrated in Figure 5.1. As can be deduced from the figure, aerosol optical and microphysical properties exhibited a great variability, with the individual properties varying up to couple of fold from day to day during the study period. Similar variability in these properties has been previously reported by several authors (Kubilay *et al*., 2003; Byrant *et al*., 2005; Fotiadi *et al*., 2006; Pandolfi *et al*., 2011; Mallet *et al*., 2013; Lyamani *et al*., 2015) for the Mediterranean region. Imaginary part of the refractive index (I-REF) at 440 nm ranged between 0.0005 and 0.044 whilst Single Scattering Albedo (SSA) at 440 nm fluctuated from 0.72 to 0.93. Absorption Angstrom Exponent (AAE) ranged from 0.08 to 2.97 whereas Absorption Aerosol Optical Thickness (AAOT) varied between 0.004 and 0.26. Fine Fraction also denoted variability with percent contribution fluctuating from 10 % to 96 %.

As stated previously, the daily variability in aerosol optical thickness and angstrom exponent in the Mediterranean region was mainly found to be influenced by rain, temperature, water vapor and aerosol type namely, (a) dust dominated, (b) mixed (dust/pollution) as well as (c) pollution dominated. Therefore, three cases for each aerosol type will be used in order to assess the effect of dust, mixed and pollution episodes on the aerosol optical and physical properties.

(a) Dust Dominated: The mineral dust dominated event was characterized on 24th of March 2008 by AOT and AAOT value of 0.7 and 0.13 at 440 nm, respectively. 5-day air masses back trajectories for 1, 2, 3 and 4 km altitude arriving at Erdemli site together with Ozone Mapping Instrument Aerosol Index (OMI-AI) is given in Figure 5.2 for 24th of March 2008. On 24th of March 2008, the air masses back trajectories at four levels exhibited that the receptor site was under the influence of air flow from North Africa (particularly from Eastern Sahara). OMI-AI satellite image also clearly demonstrated the presence of the dust cloud over the Eastern Mediterranean. The dense dust cloud was specifically obvious between coordinates 33˚N−36˚N and 27˚E−35˚E, AI reaching up to 4 whilst AI values ranged between 2 to 3 over the sampling region.

(b) Mixed Event: During the mixed event (3rd of April 2000) AOT and AAOT at 440 nm were respectively at around 2 and 0.25. Correspondingly, the values of AOT and AAOT for the mixed event were 2.8 and 2.0 times higher than those observed for dust event (for more details see below). 5-day air masses back trajectories arriving at 1 and 2 km altitude showed air flow from the Middle East whereas, the trajectories reaching at 3 and 4 km demonstrated transport from North Africa (see Figure 5.3). On the one hand, TOMS-AI supported mineral dust event, AI values exceeding 3 (see Figure 5.3), on the other hand, the true color satellite image exhibited a brownish gold instead of yellowish color between coordinates 33˚N−36˚N and 32˚E−35˚E which suggests the influence of pollution on this event (see Figure 5.4).

(c) Pollution Event: Corresponding AOT and AAOT at 440 nm for pollution event (27th of July 2014) were 0.55 and 0.027. The observed low AAOT value suggested that the pollution event was likely due mainly to secondary aerosols. Air mass trajectory arriving at 1 km altitude exhibited air flow reaching at Erdemli from the North East of the Black Sea after sweeping Central Anatolia, while trajectory arriving at 2 km altitude showed transport from Mediterranean Sea after passing through the Antalya and Konya region of the Turkey (see Figure 5.5). Trajectories reaching at 3 and 4 km demonstrated transport originating from Iberian Peninsula after travelling over the Mediterranean Sea. MODIS-Terra (Moderate Resolution Imaging Spectrometer) AOD and EAE satellite images (see Figure 5.5 and 5.6) for 27th of 07 2014 respectively denoted values around 0.4 and 1.6 over the Turkey, proving the pollution event.

Figure 5.7 shows I-REF, SSA, AAOT, AAE and PSD for dust, mixed and pollution events. As can be deduced from the figure, aerosol optical and micro-physical properties indicated a significant difference for dust, mixed and pollution events. The imaginary part of the refractive index decreased with increasing wavelength for dust and mixed events, on contrary, it showed slight increase for pollution event. Patterson *et al*. (1977) have been reported the spectral dependence of the I-REF by using two Saharan dust events obtained from Tenerife and Barbados. These authors showed that the imaginary part of the refractive index for Saharan dust samples decreased from about 0.025 at 300 nm to 0.0038 between 600 and 700 nm. About three decades later, Saharan Mineral Dust Experiments (SAMUM-1 and SAMUM-2) were carried out in order to clarify aerosol optical and micro-physical properties about Saharan Dust (Heintzenberg, 2009; Müller *et al.*, 2009, 2010, 2011; Kandler *et al.*, 2009, 2011). Similar spectral dependence for the mineral dust events has been observed by these researchers imaginary part of the refractive decreasing from 0.035 at 320 nm to 0.003 at 650 nm and being around 0.002 for wavelengths higher than 650 nm (Müller *et al.*, 2011). The imaginary part of refractive index for dust event ranged from 2.5 x 10^{-3} to 2.0 x 10^{-3} between 870 and 1020 nm and for wavelengths between 675 nm and 440 nm the imaginary part of refractive index increased from 4.3 x 10^{-3} to 11.0 x 10^{-3}. Although similar spectral behavior was observed, the imaginary part of the refractive index at 440 nm for mixed event was 2.2 times smaller than that of mineral dust event. For pollution event, the imaginary part of refractive index slightly increased from 5.0 x 10^{-3} at 440 nm to 6.3 x 10^{-3} at 1020 nm. SSA for dust and mixed events increased with increasing wavelength (Dubovik *et al.*, 2002; Meloni *et al.*, 2006), however, the absorption character of the dust event was higher at 440 and 675 nm than that of mixed event. Smaller absorption and imaginary refractive index for mixed event might be attributed to ‘shield’ or encapsulate of iron oxides by secondary aerosol such as sulfate and nitrate when the dust particles arrived at the receptor sites after passing through populated and industrialized urban areas (Koçak *et al.*, 2012). As expected, SSA decreased from 0.95 at 440 nm to 0.91 and 1020 nm which is typical for Industrial/Urban aerosol (Dubovik *et al.*, 2002). Decrease in AAOT for dust event (from 0.13 to 0.018 between 440 and 1020 nm) was a sharper than those observed for mixed (from 0.25 to 0.068 between 440 and 1020 nm) and pollution (from 0.027 to 0.017 between 440 and 1020 nm) events. AAE also supported decrease in AAOT, with values decreasing order dust (2.3) > mixed (1.5) > pollution (0.6). The scatter diagram of AAE versus EAE is also presented in Figure 5.7e along with values from literature (Russell *et al.*, 2010). Considering the literature values reported for aerosol types, it might be argued that such plots are not capable enough to differentiate dust dominated event from mixed event but useful for separating pollution event from dust and mixed events.

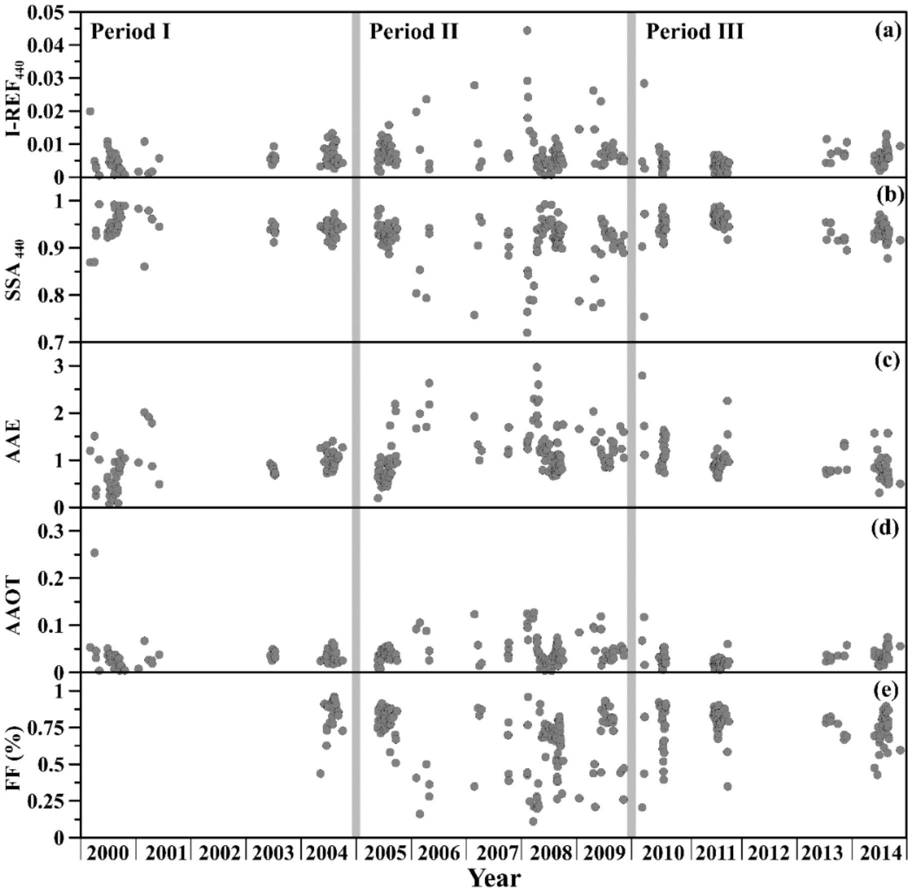

Figure 5.1 Daily variability in aerosol optical and micro-physical properties. **(a)** Imaginary part of the refractive index (I-REF), **(b)** single scattering albedo (SSA), **(c)** absorption angstrom exponent (AAE), **(d)** aerosol absorption optical thickness and **(e)** contribution of fine fraction in percent (FF).

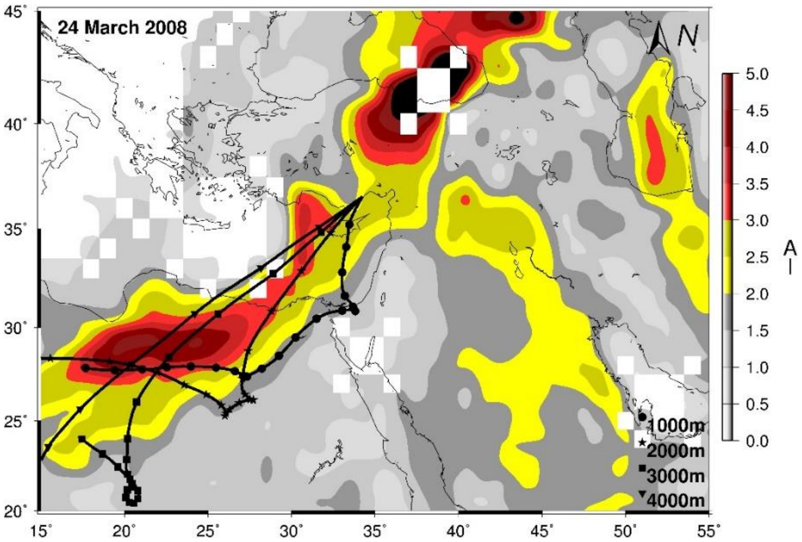

Figure 5.2 Five day back trajectories of air masses reaching at 1000m (black circle), 2000m (black star), 3000m (black square) and 4000m (black triangle) on 24th of March 2008 with corresponding Aerosol Index (AI) from OMI (Ozone Mapping Instrument) for Erdemli.

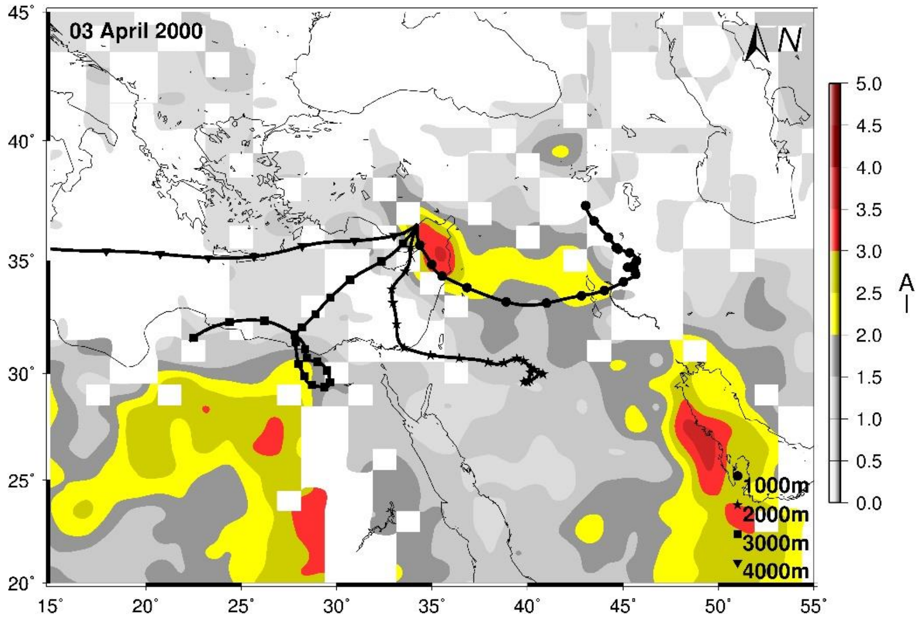

Figure 5.3 Five day back trajectories of air masses reaching at 1000m (black circle), 2000m (black star), 3000m (black square) and 4000m (black triangle) on 3rd of April 2008 with corresponding Aerosol Index (AI) from OMI (Ozone Mapping Instrument) for Erdemli.

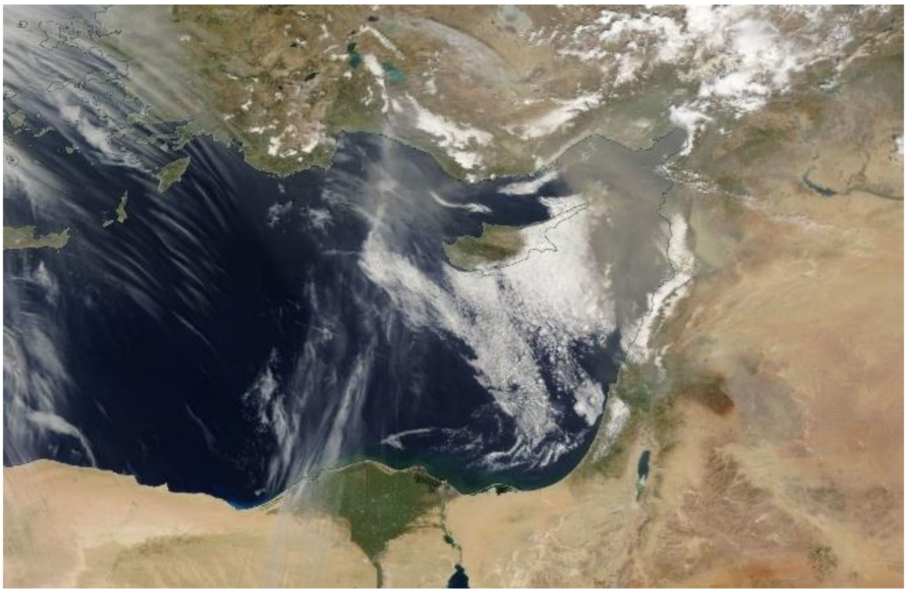

Figure 5.4 True color Moderate Resolution Imaging Spectrometer (MODIS) exhibits a large dust plume mixed with pollution over the Eastern Mediterranean on 03 April 2000.

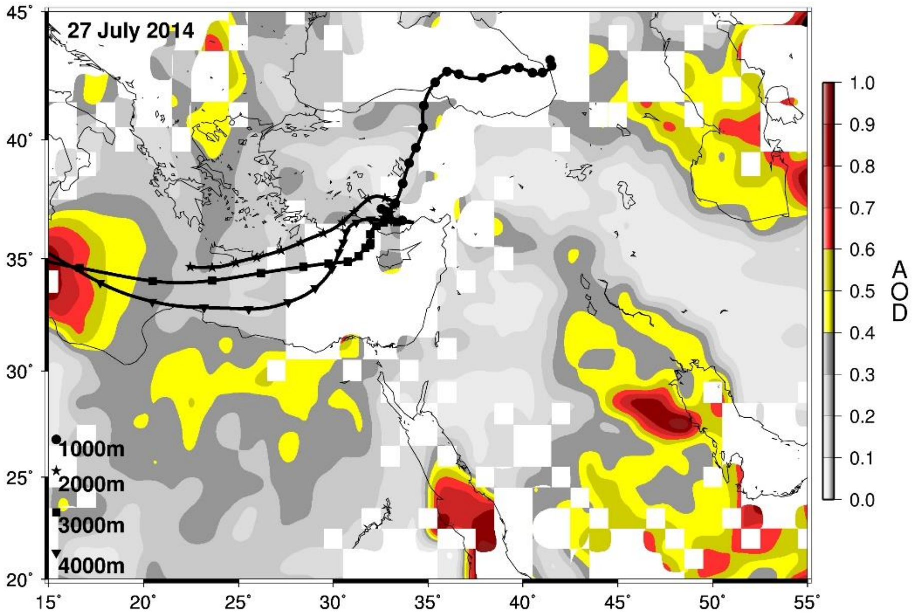

Figure 5.5 Five day back trajectories of air masses reaching at 1000m (black circle), 2000m (black star), 3000m (black square) and 4000m (black triangle) on 27th of July 2014 with corresponding AOD from MODIS Terra for Erdemli.

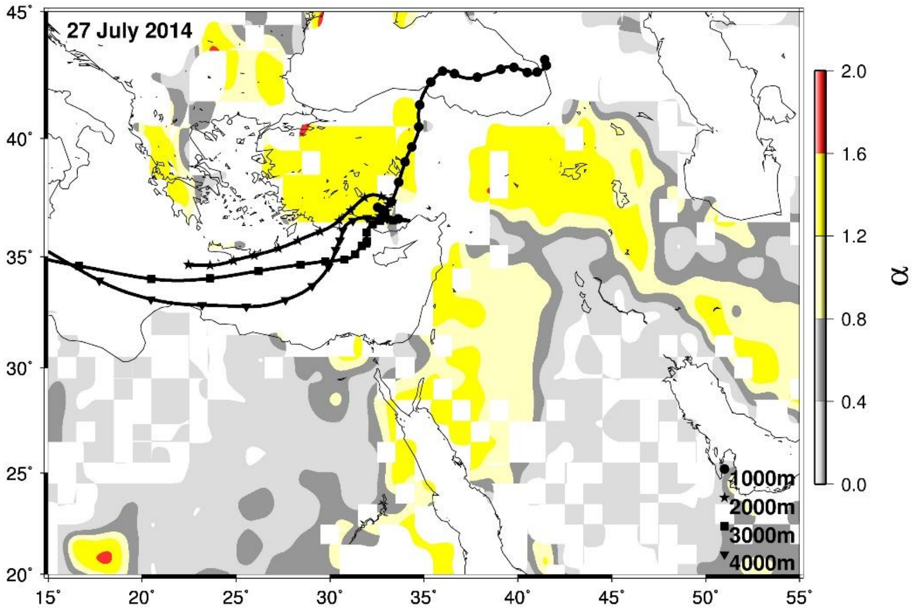

Figure 5.6 Five day back trajectories of air masses reaching at 1000m (black circle), 2000m (black star), 3000m (black square) and 4000m (black triangle) on 27th of July 2014 with corresponding Angstrom Exponent from MODIS Terra for Erdemli.

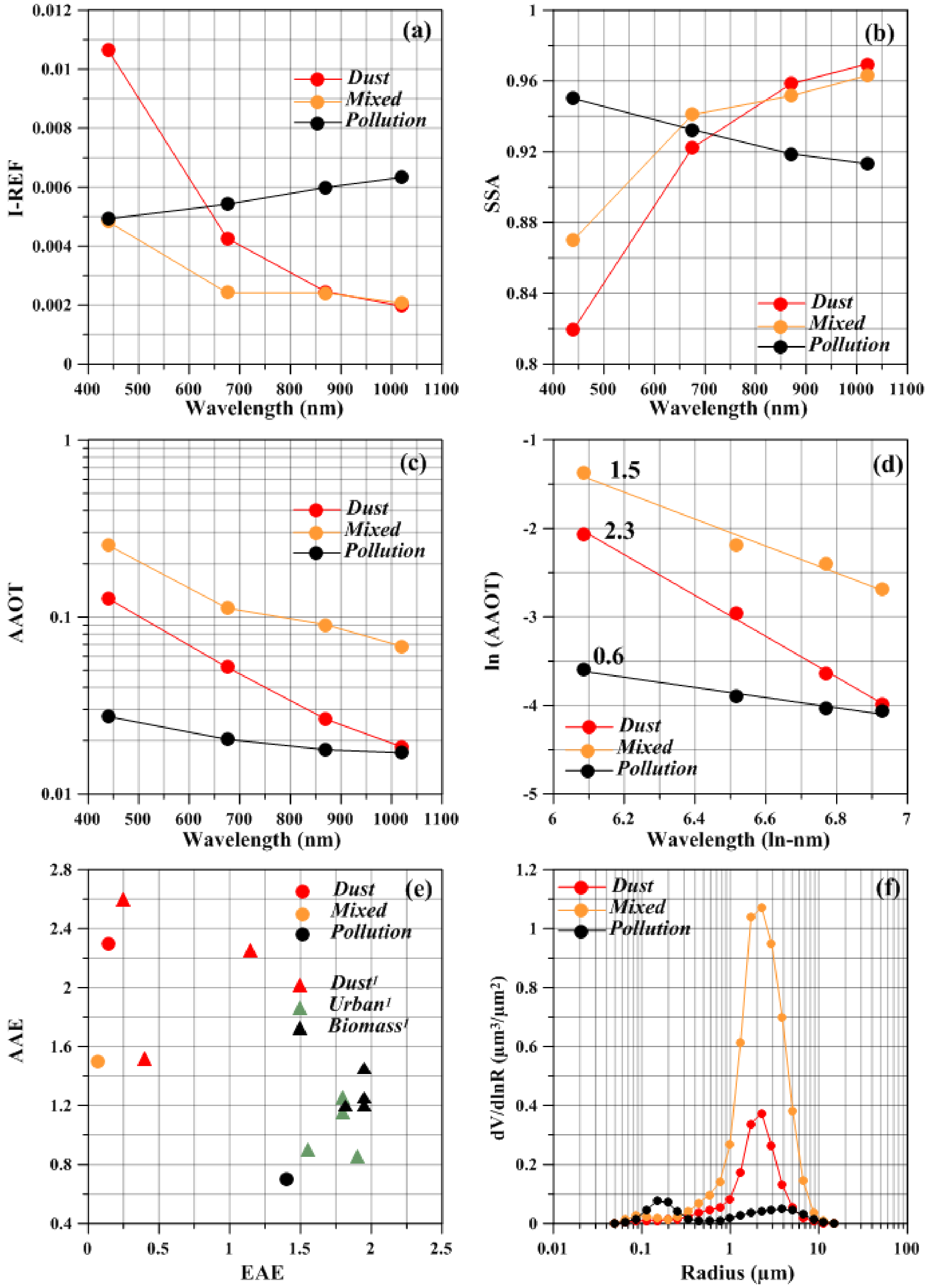

Figure 5.7 Aerosol optical and micro-physical properties for dust, mixed and pollution events. **(a)** Imaginary part of the refractive index (I-REF), **(b)** single scattering albedo (SSA), **(c)** aerosol absorption optical thickness, **(d)** absorption angstrom exponent (AAE), **(e)** scatter plot between AAE and EAE and **(f)** particle size distribution. ^{1}Russel *et al*., 2010.

5.2. Seasonal Variations in the Aerosol Optical and Microphysical Properties

Table 5.1 exhibits statistical summary, including arithmetic mean, standard deviation, minimum and maximum of optical and microphysical properties for spring (MAM), summer (JJA) and fall (SON) between January 2002 and December 2014. Correspondingly, the seasonal percent observational coverage were 3.4 %, 13.1 %, 65.2 % and 18.3 % for winter (DJN), spring, summer and fall. It is apparent that the seasonal percent observational coverage was not evenly distributed. On the one hand, since the winter only presented about 3 % observational coverage, it will be omitted for seasonal comparison, on the other hand, the spring and fall will be used for the aforementioned purpose because they showed observational coverage larger than 10 %. The highest % observational coverage (65.2 %) was observed for summer due mainly to relatively less could coverage under the prevailing meteorological conditions.

Figure 5.8 shows I-REF, SSA, AAOT, AAE and PSD for spring, summer and fall. As can be seen from the diagrams there was a significant difference for spring, summer and fall periods. The spectral dependence of the I-REF and SSA exhibited distinct variation from one season to another. For spring season, the imaginary part of refractive index denoted decrease with increasing wavelength whereas, the imaginary part of refractive index was almost similar for all wavelengths during summer and fall. The imaginary part of refractive index for spring ranged from 4.4 x 10^{-3} to 3.8 x 10^{-3} between 675 and 1020 nm and for wavelengths smaller than 675 nm the imaginary part of refractive index increased with decreasing wavelength, being 7.0 x 10^{-3} at 440 nm. This type of spectral dependence might be ascribed to the frequent occurrence of mineral dust episodes in the spring (Kubilay *et al.*, 2000; Fotiadi *et al*., 2006). Although, the imaginary part of refractive index did not show significant change for summer and fall, the former was at least 1.15 times higher than of later for all wavelengths. The difference between summer and fall was likely owing to the anthropic aerosol type, such as black carbon and secondary aerosol, with varying contribution. SSA for spring exhibited increase with increasing wavelength, showing absorbance of iron oxides that associated with mineral dust near the blue wavelength. For summer and fall, however; SSA demonstrated reduction while wavelength increase, suggesting the dominance of man-made particles. It is worth mentioning that the former showed relatively steeper decrease compared to later and this implies the aerosol burden in the summer had more absorbing character in the near-infrared wavelength due possible to black carbon originated from biomass burning (Sciare *et al.*, 2008). As expected, AAOT for spring (from 0.050 to 0.014 between 440 and 1020 nm) indicated a sharper decrease than those observed for summer (from 0.034 to 0.016 between 440 and 1020 nm) and fall (from 0.033 to 0.014 between 440 and 1020 nm). This difference was likely because of the particles size distribution of the mineral dust which is associated with coarse mode (see Figure 5.7f). Absorption angstrom exponent (see Figure 5.7d) for spring (1.5) was substantially larger than those of summer (0.9) and fall (1.0). The scatter diagram of AAE versus EAE did differentiate spring from summer and fall, but, did not show remarkable difference for summer and fall.

Table 5.1 Statistical summary of optical and microphysical properties for spring, summer and fall between January 2002 and December 2014.

	Spring(n=39)				Summer (n=210)				Fall (n=59)			
	Mean	Std	Min	Max	Mean	Std	Min	Max	Mean	Std	Min	Max
AOT_{440}	0.59	0.27	0.41	1.96	0.57	0.13	0.40	1.15	0.52	0.12	0.40	0.99
AOT_{675}	0.45	0.30	0.19	1.90	0.32	0.09	0.20	0.74	0.31	0.09	0.21	0.62
AOT_{870}	0.40	0.31	0.12	1.87	0.24	0.08	0.13	0.70	0.23	0.09	0.14	0.58
AOT_{1020}	0.37	0.31	0.10	1.85	0.20	0.08	0.10	0.68	0.20	0.09	0.11	0.55
$\alpha_{440-870}$	0.79	0.57	0.03	1.81	1.34	0.25	0.32	1.72	1.25	0.35	0.31	1.67
FMF	54	27	11	91	77	13	26	96	69	16	26	88
AAE	1.42	0.67	0.20	2.97	0.89	0.29	0.08	1.74	1.07	0.41	0.09	2.26
$AAOT_{440}$	0.05	0.05	0.00	0.25	0.03	0.02	0.00	0.12	0.03	0.01	0.00	0.06
$AAOT_{675}$	0.02	0.02	0.00	0.11	0.02	0.01	0.00	0.07	0.02	0.01	0.00	0.05
$AAOT_{870}$	0.02	0.02	0.00	0.09	0.02	0.01	0.00	0.05	0.02	0.01	0.00	0.04
$AAOT_{1020}$	0.01	0.01	0.00	0.07	0.02	0.01	0.00	0.06	0.01	0.01	0.00	0.04
SSA_{440}	0.92	0.06	0.75	0.99	0.94	0.02	0.78	0.99	0.94	0.02	0.88	0.99
SSA_{675}	0.94	0.04	0.83	0.99	0.92	0.03	0.78	0.99	0.93	0.03	0.88	0.99
SSA_{870}	0.94	0.04	0.80	0.99	0.92	0.04	0.77	0.99	0.93	0.03	0.87	0.99
SSA_{1020}	0.95	0.04	0.79	0.99	0.91	0.04	0.78	0.99	0.93	0.03	0.86	0.99
$REFI_{440}$	.0065	.0063	.0005	.0284	.0061	.0030	.0007	.0229	.0054	.0022	.0008	.0106
$REFI_{675}$	.0044	.0038	.0005	.0183	.0067	.0036	.0006	.0204	.0052	.0025	.0007	.0124
$REFI_{870}$	.0040	.0034	.0005	.0179	.0066	.0037	.0006	.0196	.0050	.0026	.0006	.0122
$REFI_{1020}$	.0038	.0033	.0005	.0177	.0065	.0037	.0006	.0190	.0049	.0027	.0006	.0138

Std, Min and Max refer to standard deviation, minimum and maximum, respectively. FMF stands for Fine Mode Fraction in percent.

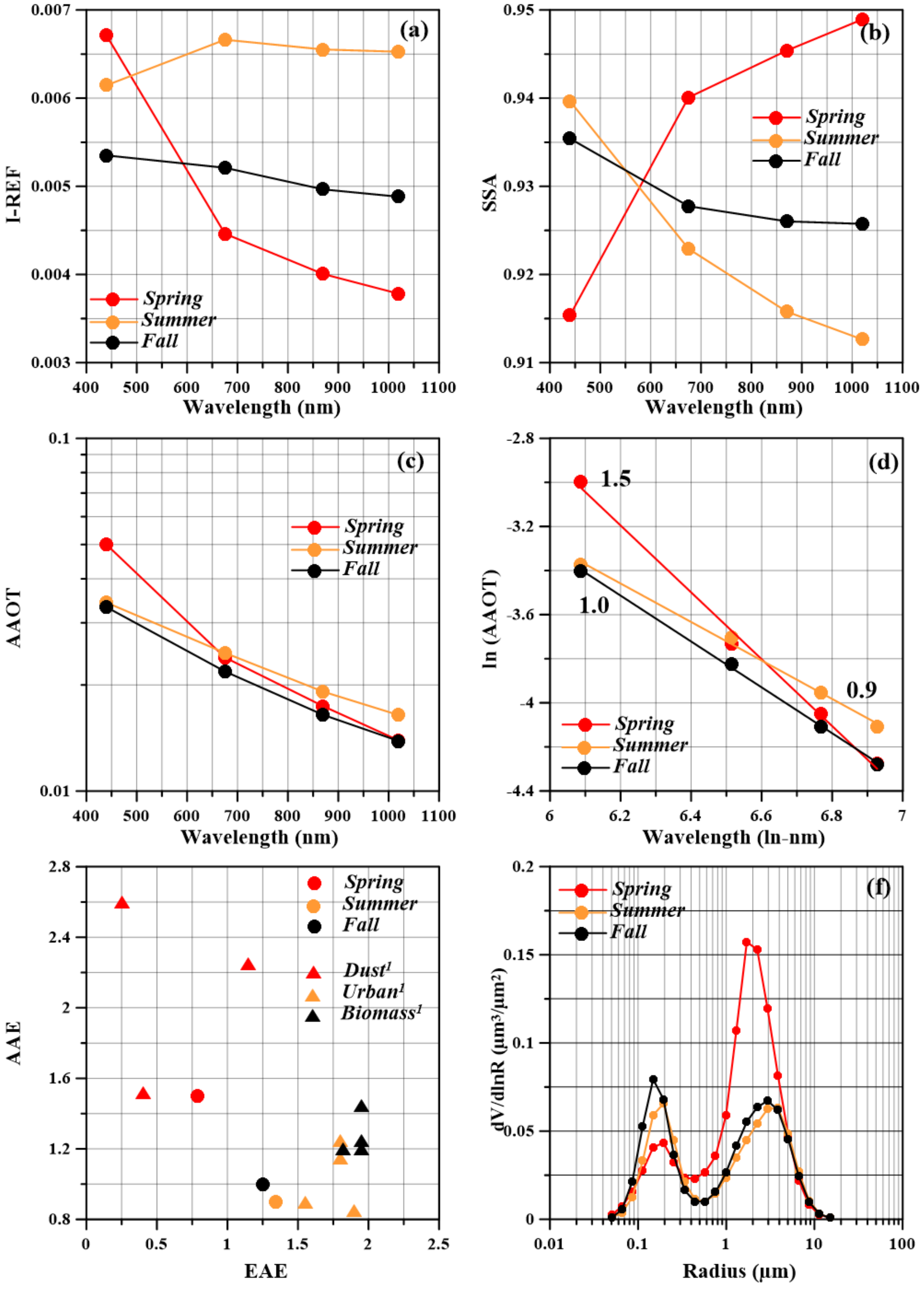

Figure 5.8 Aerosol optical and micro-physical properties for spring, summer and fall. **(a)** Imaginary part of the refractive index (I-REF), **(b)** single scattering albedo (SSA), **(c)** aerosol absorption optical thickness, **(d)** absorption angstrom exponent (AAE), **(e)** scatter plot between AAE and EAE and **(f)** particle size distribution. ^{1}Russel *et al.*, 2010.

5.3. Influence of Dust, Mixed and Pollution events on Aerosol Optical and Microphysical Properties

As it is well documented the, the aerosol burden in the atmosphere over the Mediterranean region is affected by large quantities of mineral dust when air mass transport originated from North Africa and the Middle East (Bergametti *et al.*, 1989; Dayan *et al.*, 1991; Moulin *et al.*, 1998; Hamonou *et al.*, 1999; Kubilay *et al.*, 2000; Gobbi *et al.*, 2000). The studies have also demonstrated the influence of pollutants associated with air mass transport from the Western/Eastern Europe, Asia and a lesser extent from North America (Lelieveld *et al.*, 2002; Metzger *et al.*, 2006; Lyamani *et al.*, 2015). The mixing of the dust dominated and anthropic aerosol has been documented in the Mediterranean when the dust particles arrived at the receptor sites after passing through populated and industrialized urban areas (Koçak *et al.*, 2012). In order to categorize events into (i) dust, (ii) mixed and (ii) pollution, Extinction Angstrom Exponent (EAE) had respectively been divided into three groups considering the percent contribution of coarse/fine particles: (a) EAE < 0.5, (b) 0.5 < EAE < 1.0 and (c) 1.0 < EAE. The Kruskal-Wallis (K-W) test was used with a 95 % confidence interval in order to assess the differences in the aerosol optical and microphysical properties for dust (n = 23), mixed (n = 42) and pollution (n = 257) events. As expected, 78 % of the dust events were observed in spring season while 4%, 9% and 9 % were respectively categorized in summer, fall and winter. The seasonal frequency of mixed events were found in decreasing in the order summer (48 %) > spring (24 %) > fall (19 %) > winter (9 %). The seasonal frequency of the pollution events, on the other hand, was calculated in increasing in the order winter (1 %) < spring (6%) < fall (19%) < summer (74 %).

Table 5.2 and Figure 5.9 presents arithmetic mean of AOT, I-REF, SSA, AAOT, AAE and PSD together with corresponding standard deviations, minimum and maximum for dust, mixed and pollution events. AOT for dust and mixed events were comparable however, they were statistically higher than that observed for pollution events at all wavelengths. The imaginary part of the refractive index did not show statistically significant difference at 440 nm among the events whereas, the imaginary part of the refractive index for pollution event at 675, 870 and 1020 nm were higher than those observed for dust and mixed events. SSA particularly at 440 nm was smaller for dust and mixed (absorption by iron oxides) events than that observed for pollution events. On contrary, SSA at 1020 nm for pollution events was remarkably less relative to dust and mixed events, former likely showing absorbing character due to black carbon. AAOT at 440 nm for dust and mixed events was at least 1.7 ($p = 0.05$) times larger compared to pollution events, because chiefly of the absorption by iron oxides near blue light. Nonetheless, AAOT did not exhibit any statistically significant difference at wavelength larger than 440 nm. Absorption Angstrom Exponent was found to be similar for dust and mixed events whilst AAE for pollution events was statistically smaller compared dust and mixed events. As stated before, scatter diagrams between AAE and EAE are not capable enough to differentiate dust dominated events from mixed events but useful for separating pollution events from dust and mixed events.

Table 5.2 Statistical summary for Dust, Mixed and Pollution groups classified according to Extinction Aerosol Exponent.

	Dust (n=23)				Mixed (n=42)				Pollution (n=257)			
	Mean	Std	Min	Max	Mean	Std	Min	Max	Mean	Std	Min	Max
AOT_{440}	0.68	0.34	0.40	1.96	0.57	0.13	0.41	0.87	0.55	0.12	0.40	1.15
AOT_{675}	0.62	0.32	0.34	1.90	0.41	0.10	0.27	0.66	0.30	0.07	0.19	0.72
AOT_{870}	0.59	0.31	0.32	1.87	0.35	0.09	0.21	0.58	0.21	0.06	0.12	0.55
AOT_{1020}	0.57	0.31	0.31	1.85	0.32	0.08	0.19	0.55	0.18	0.05	0.10	0.51
$\alpha_{440\text{-}870}$	0.24	0.12	0.03	0.47	0.73	0.14	0.50	0.96	1.40	0.17	1.00	1.81
FMF	24	5	11	35	47	7	35	66	80	8	58	96
AAE	1.86	0.63	0.38	2.97	1.36	0.46	0.17	2.18	0.89	0.29	0.08	2.26
$AAOT_{440}$	0.07	0.05	0.02	0.25	0.05	0.03	0.00	0.13	0.03	0.01	0.00	0.12
$AAOT_{675}$	0.03	0.02	0.01	0.11	0.03	0.01	0.00	0.07	0.02	0.01	0.00	0.07
$AAOT_{870}$	0.02	0.02	0.00	0.09	0.02	0.01	0.00	0.05	0.02	0.01	0.00	0.05
$AAOT_{1020}$	0.02	0.01	0.00	0.07	0.02	0.01	0.00	0.04	0.02	0.01	0.00	0.06
SSA_{440}	0.89	0.06	0.76	0.98	0.90	0.06	0.72	0.99	0.94	0.03	0.78	0.99
SSA_{675}	0.94	0.04	0.86	0.99	0.92	0.05	0.77	0.99	0.92	0.03	0.78	0.99
SSA_{870}	0.96	0.03	0.91	0.99	0.94	0.04	0.82	0.99	0.92	0.04	0.77	0.99
SSA_{1020}	0.97	0.02	0.93	0.99	0.94	0.03	0.85	0.99	0.91	0.04	0.78	0.99
$REFI_{440}$	.0066	.0060	.0011	.0278	.0085	.0091	.0005	.0444	.0062	.0034	.0007	.0243
$REFI_{675}$	.0030	.0024	.0006	.0106	.0053	.0045	.0005	.0227	.0067	.0037	.0006	.0204
$REFI_{870}$	.0024	.0016	.0005	.0067	.0043	.0030	.0005	.0142	.0066	.0037	.0006	.0196
$REFI_{1020}$	.0021	.0013	.0005	.0051	.0039	.0025	.0005	.0112	.0065	.0037	.0006	.0190

Std, Min and Max refer to standard deviation, minimum and maximum, respectively. FMF stands for Fine Mode Fraction in percent.

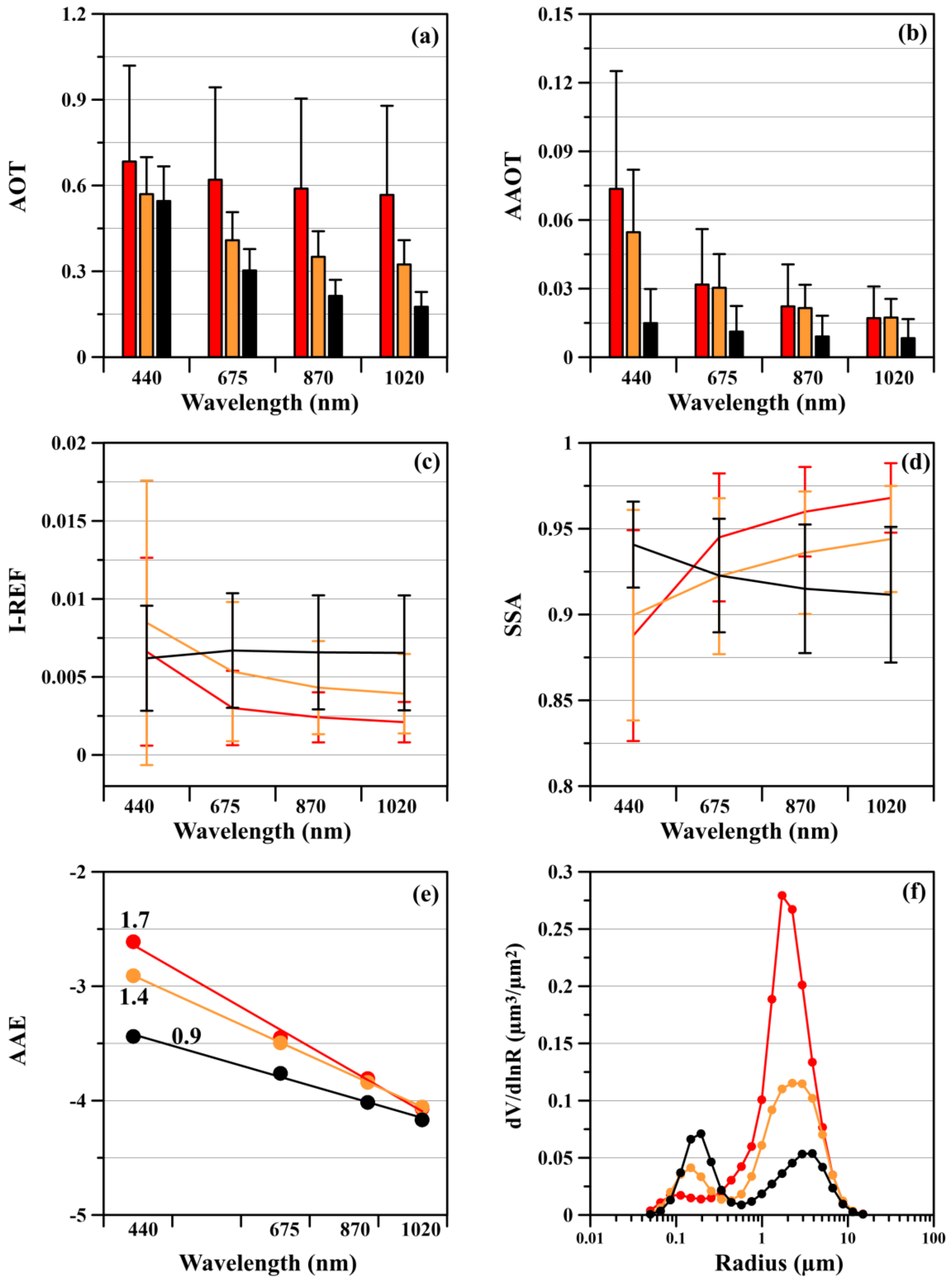

Figure 5.9 Aerosol optical and micro-physical properties for dust (red), mixed (orange) and pollution (black) events. **(a)** Aerosol Optical Thickness (AOT), **(b)** Aerosol Absorption Optical Thickness (AAOT), **(c)** Imaginary part of the refractive index (I-REF), **(d)** single scattering albedo (SSA), **(e)** absorption angstrom exponent (AAE) and **(f)** particle size distribution.

Aerosol optical and micro-physical properties of the each cases for dust, mixed and pollution are respectively illustrated in Figure 5.10, 11 and 12. These diagrams are presented in order to assess the capability of the classification of the dust, mixed and pollution events according to Extinction Angstrom Exponent (EAE). Imaginary part of the refractive index single scattering albedo as well as Aerosol Absorption Optical Thickness for dust events (see Figure 10.a, b and c) were found to deviate from the spectral dependence of the mineral dust aerosol type. There were, for example, a number of cases that did not exhibit change with increasing wavelength from 440 nm to 1020 nm. AAE also demonstrated great variability which is not typical for mineral dust events, being less than 1 whereas generally particle size distribution showed the dominance of coarse particles. Similarly, imaginary part of the refractive index single scattering albedo and Aerosol Absorption Optical Thickness for mixed events (see Figure 11.a, b and c) indicated departure from the spectral dependence of the mixed (dust + pollution) aerosol type. A number of cases were found to act as secondary aerosol, for example, showing almost pure scattering character. AAE values, on the other hand, larger than 2 implied that these events were likely dust dominated instead of mixed event. In general (or except for few cases see Figure 5.13), aerosol optical and micro-physical properties for pollution events illustrated the spectral dependence for imaginary part of the refractive index, single scattering albedo and Aerosol Absorption Optical Thickness, nonetheless; they exhibited large variability, denoting different types of pollutants over the region. On the other hand, AAE (see Figure 11.e) higher than value of 2 suggests that the origin might be mineral dust rather than pollution. To illustrate, on 28th of September 2011 AAE was 2.3 and close inspection of the particle size distribution showed that the particles were dominated by coarse mode, though EAE was larger than 1. The true color satellite image exhibited a dirty yellowish dust cloud color between coordinates 32˚N−36˚N and 32˚E−37˚E which suggests the influence of dust event originating from the desert located at the Middle East (see Figure 5.13). Consequently, the classification of the aerosol type regarding extinction angstrom exponent was found to be insufficient and this type of categorization should be avoided.

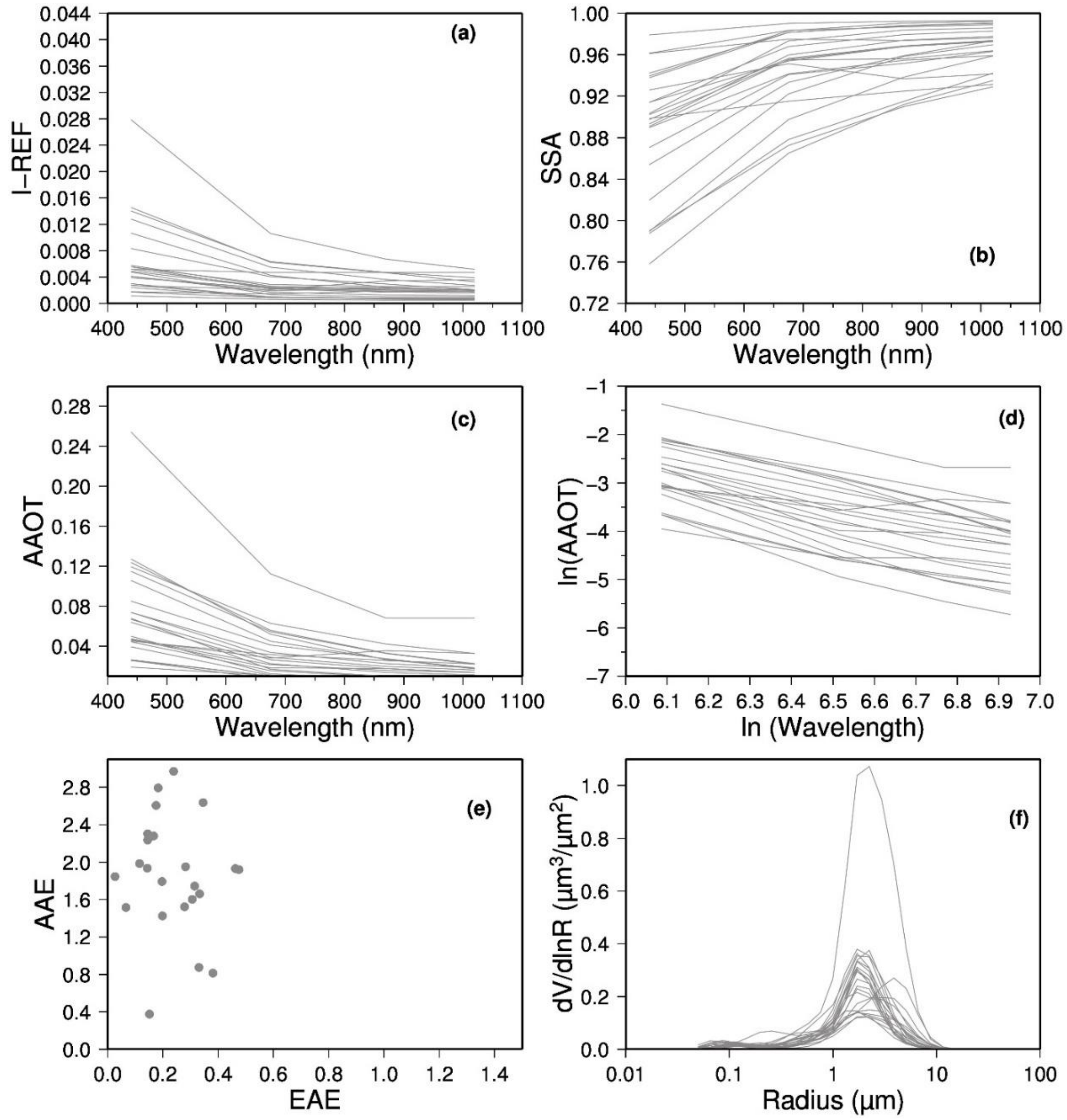

Figure 5.10 Aerosol optical and micro-physical properties of the each case for dust events. **(a)** Imaginary part of the refractive index (I-REF), **(b)** single scattering albedo (SSA), **(c)** aerosol absorption optical thickness, **(d)** absorption angstrom exponent (AAE), **(e)** scatter plot between AAE and EAE and **(f)** particle size distribution.

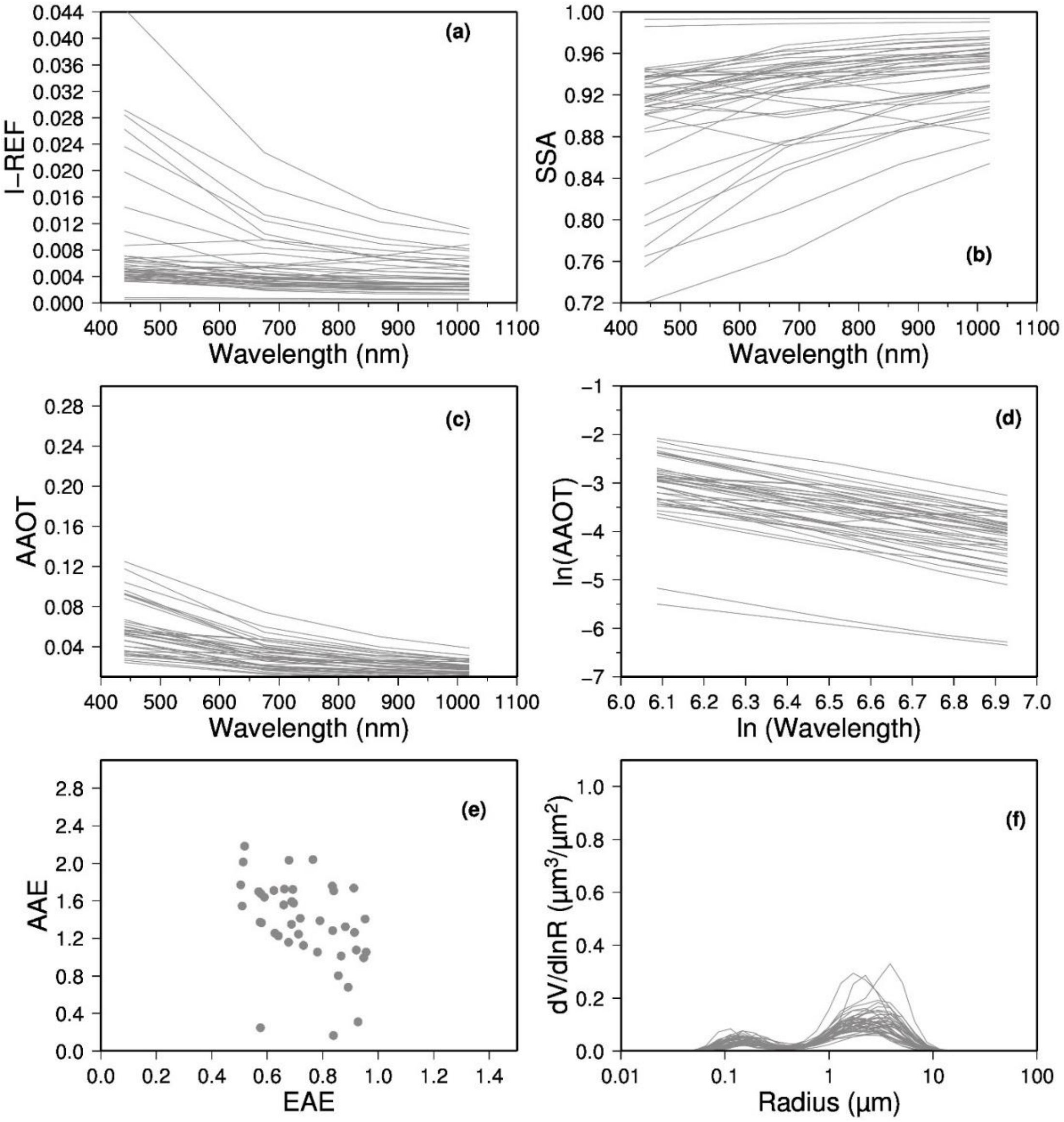

Figure 5.11 Aerosol optical and micro-physical properties of the each case for mixed events. **(a)** Imaginary part of the refractive index (I-REF), **(b)** single scattering albedo (SSA), **(c)** aerosol absorption optical thickness, **(d)** absorption angstrom exponent (AAE), **(e)** scatter plot between AAE and EAE and **(f)** particle size distribution.

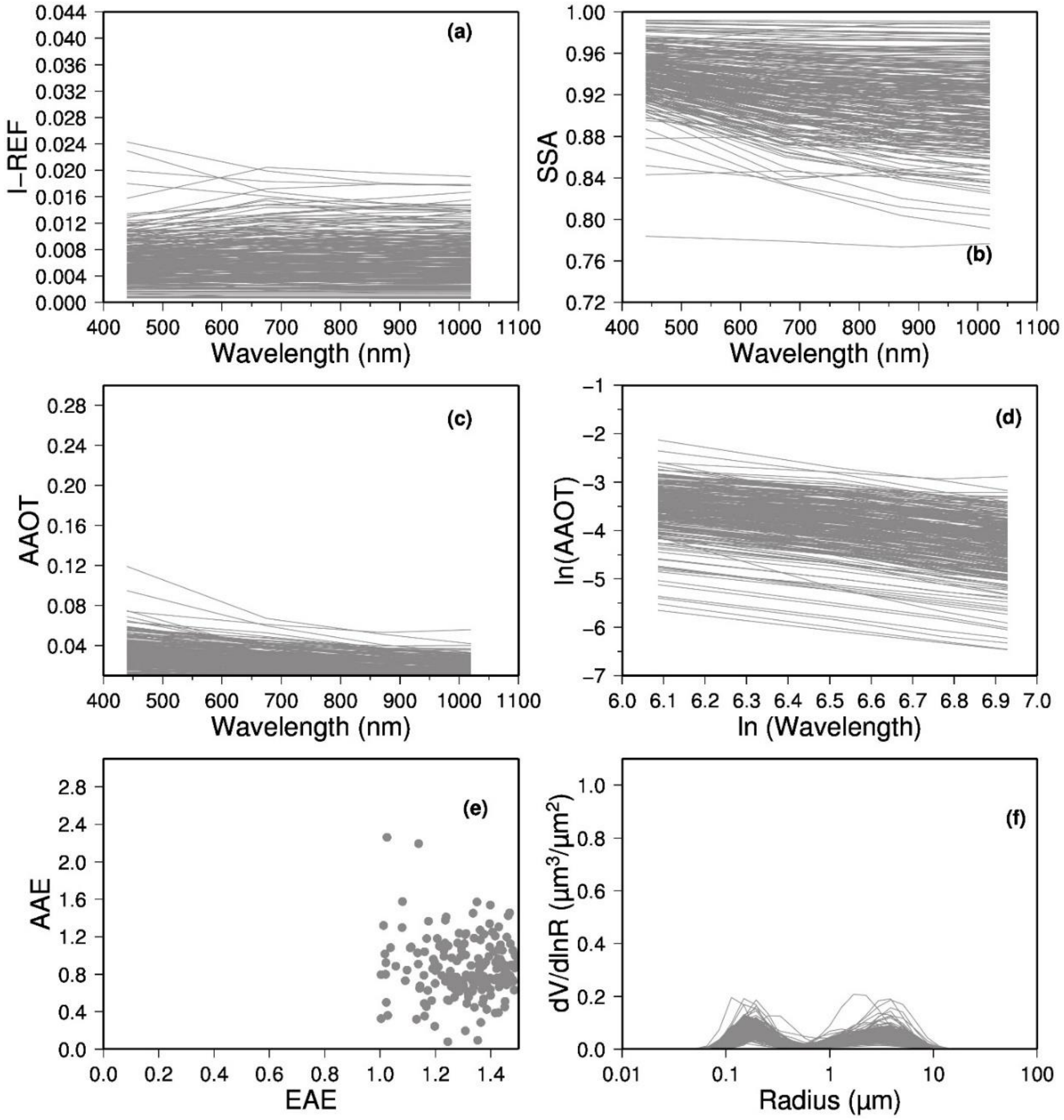

Figure 5.12 Aerosol optical and micro-physical properties of the each case for pollution events. **(a)** Imaginary part of the refractive index (I-REF), **(b)** single scattering albedo (SSA), (c) aerosol absorption optical thickness, **(d)** absorption angstrom exponent (AAE), **(e)** scatter plot between AAE and EAE and **(f)** particle size distribution.

Figure 5.13 True color Moderate Resolution Imaging Spectrometer (MODIS) exhibits a large dust cloud over the Eastern Mediterranean on 28th of September 2011.

5.4. Classification of the Aerosol Type at the Erdemli

A number of studies have been classified aerosol type by using cluster analysis (Kahn *et al*., 2001; Omar *et al*., 2005 and Taylor *et al*., 2015). During the application of cluster analysis, aerosol optical and micro-physical parameter such as AOT, SSA, AAOT, complex refractive index, size distribution, extinction/backscatter ratio and chemical composition fractions have been utilized by researcher in order to define aerosol type.

Aerosol optical and micro-physical properties namely, AOT, EAE, AAOT, SSA, I-REF and AAE were used for the classification of aerosol type at Erdemli. Before applying cluster analysis, each variable was re-scaled to a range between 0 and 1. A total of 322 observation between 2000 and 2014 were included in the analysis, which 4, 12, 65, and 18 % of days were from winter, spring, summer, and fall, respectively. Inspiring by studies involving air mass clustering (Dorling *et al*., 1992, Brankov *et al*., 1998 and Toledano *et al*., 2009), the number of clusters was determined based on the total root mean-square deviation (TRMSD). TRMSD is defined as the sum of the distances of each case to its corresponding cluster centroid. Change in

TRMSD as percentage was calculated along with number of clusters reducing from 10 to 2 (see Figure 5.14). Over % 5 change in TRMSD was assumed to be significantly large for determining the optimal number of cluster. A significant change (% 12) was first observed with the number of clusters reducing from 7 to 6, showing 7 clusters as a result. Since one of cluster had only one member for 7 clusters, they were neglected. Therefore, smaller number of clusters than 7 were closer examined. % 7.5 change in TRMSD while reducing from 5 to 4 cluster were found to be greater than 6 clusters (corresponding change was % 6.1). Consequently, 5 clusters were defined as an optimal number of clusters.

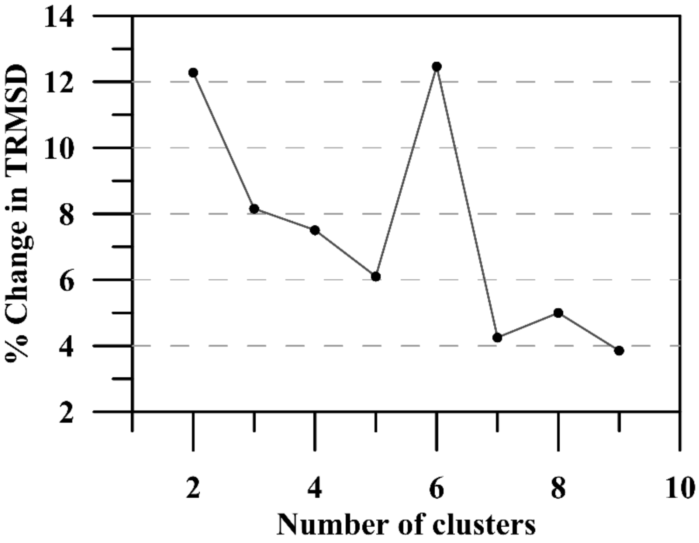

Figure 5.14 The percent change in the total root mean square deviation (TRMSD) as decreasing number of cluster**.**

Regarding the mean of the each clusters, the aerosol type might be classified into five groups: (i) Dust, (ii) Mixed, (iii) Black Carbon, (iv) Black Carbon + Secondary and (v) Secondary. Figure 5.15, 16, 17, 18 and 19 respectively illustrates members of Dust, Mixed, Black Carbon, (iv) Black Carbon + Secondary and (v) Secondary.

The classification for Dust was found to be sufficient. The imaginary part of the refractive index decreased with increasing wavelength while single scattering increased with increasing wavelength from 440 nm to 1020 nm. However, for most of the cases the imaginary part of the refractive index was much higher than expected to be from 670 nm 1020 nm. SSA exhibited increase from 440 nm to 1020 nm. EAE and AAE scatter plot diagram also indicated a large variability, ranging between 0.07-0.9

and 1.2-2.4, respectively. PSD also supported the observed variability of EAE. Similar conclusion can be made for the mixed group as well. For BC group, it clear that I-REF and SSA were not classified as expected since remarkable events exhibited decrease (increase) from 400 nm to 1020 nm for the imaginary part of the refractive index (single scattering albedo). These events might be ascribe to mixed events. On the other hand, the classification for secondary and secondary/black carbon groups seems sufficient because I-REF and SSA showed rather uniform spectral behavior between 440 nm 1020 nm.

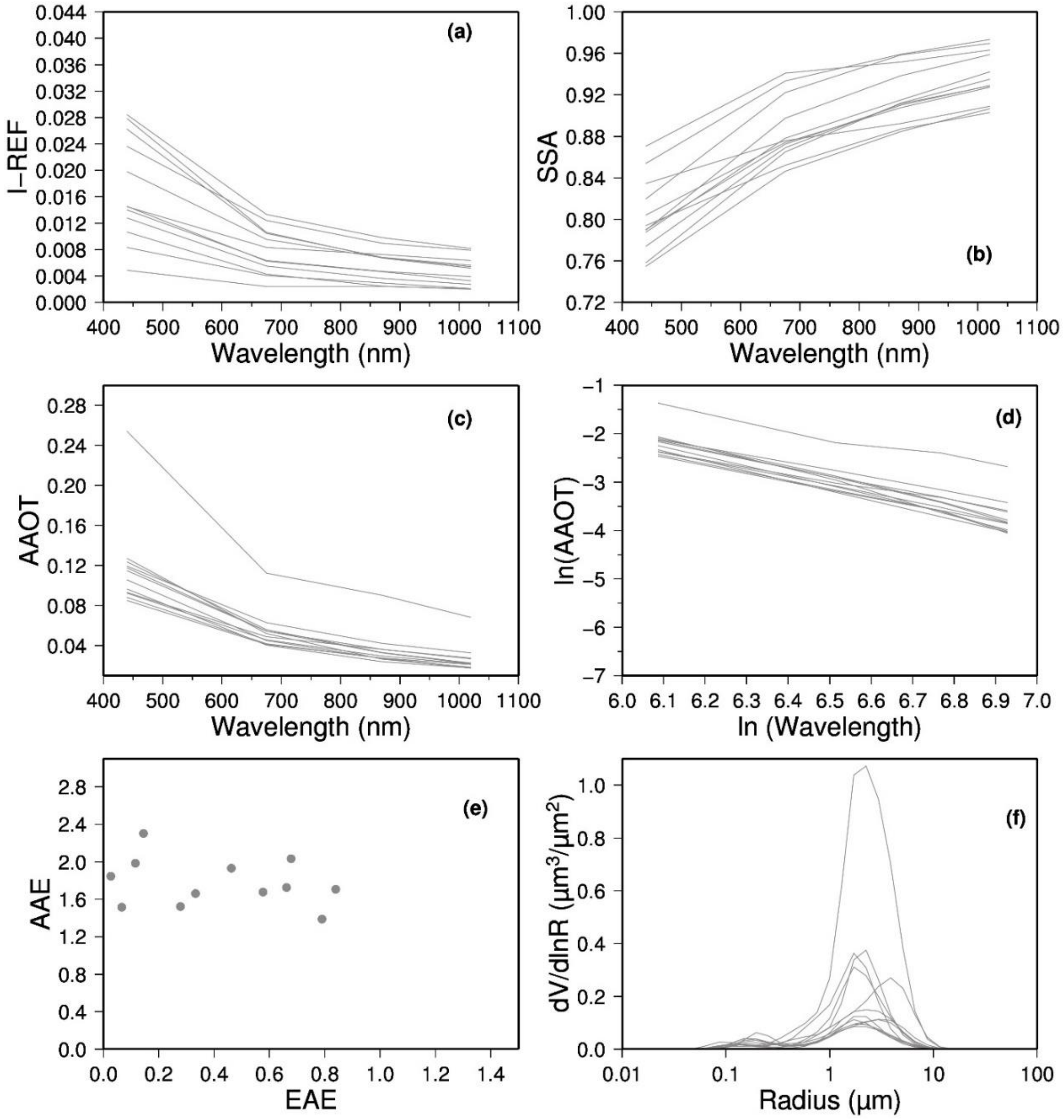

Figure 5.15 Aerosol optical and micro-physical properties of the each case for dust group. **(a)** Imaginary part of the refractive index (I-REF), **(b)** single scattering albedo (SSA), **(c)** aerosol absorption optical thickness, **(d)** absorption angstrom exponent (AAE), **(e)** scatter plot between AAE and EAE and **(f)** particle size distribution.

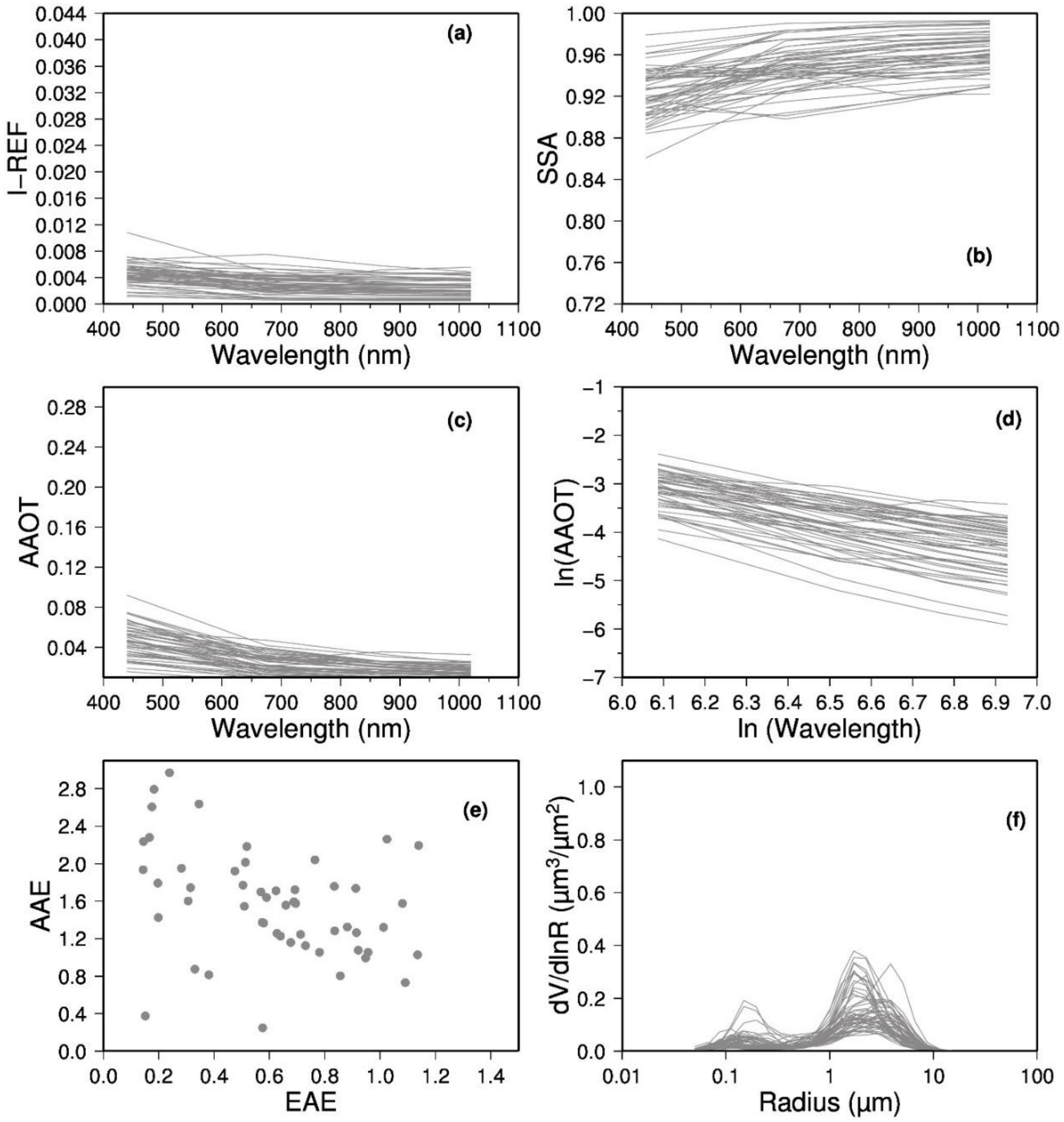

Figure 5.16 Aerosol optical and micro-physical properties of the each case for mixed group. **(a)** Imaginary part of the refractive index (I-REF), **(b)** single scattering albedo (SSA), **(c)** aerosol absorption optical thickness, **(d)** absorption angstrom exponent (AAE), **(e)** scatter plot between AAE and EAE and **(f)** particle size distribution.

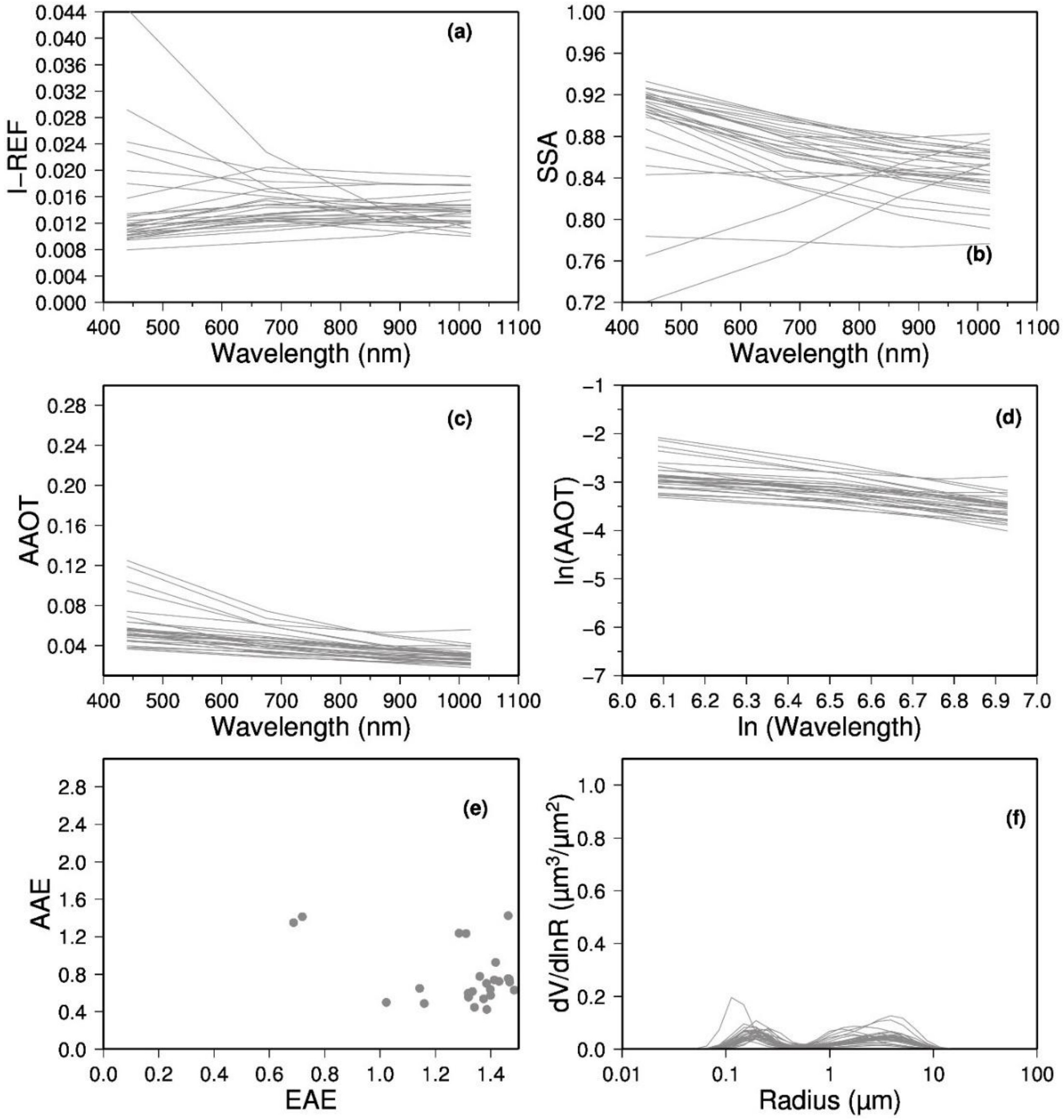

Figure 5.17 Aerosol optical and micro-physical properties of the each case for BC group. **(a)** Imaginary part of the refractive index (I-REF), **(b)** single scattering albedo (SSA), **(c)** aerosol absorption optical thickness, **(d)** absorption angstrom exponent (AAE), **(e)** scatter plot between AAE and EAE and **(f)** particle size distribution.

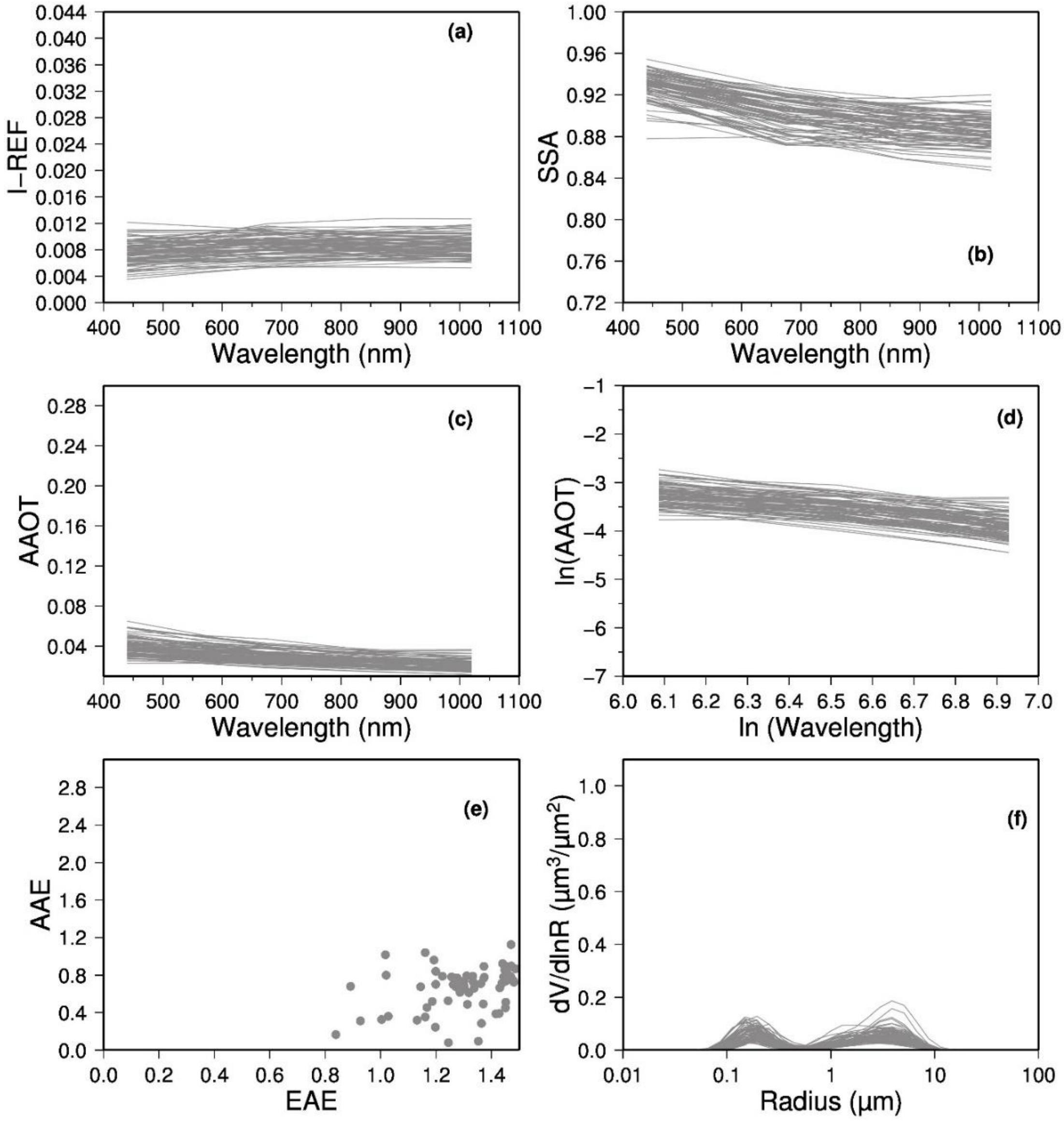

Figure 5.18 Aerosol optical and micro-physical properties of the each case for SEC+BC group. **(a)** Imaginary part of the refractive index (I-REF), **(b)** single scattering albedo (SSA), **(c)** aerosol absorption optical thickness, **(d)** absorption angstrom exponent (AAE), **(e)** scatter plot between AAE and EAE and **(f)** particle size distribution.

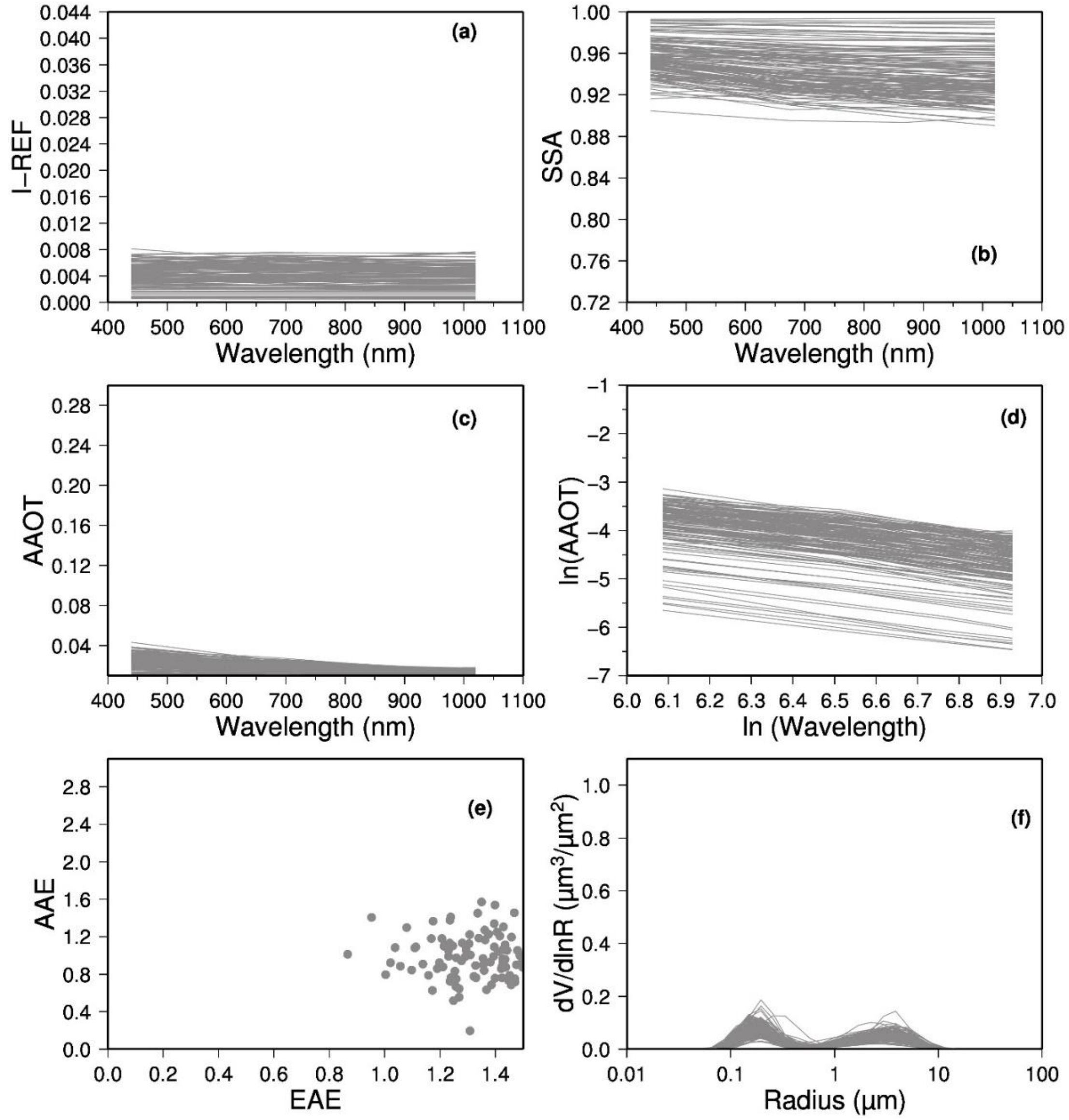

Figure 5.19 Aerosol optical and micro-physical properties of the each case for secondary group. **(a)** Imaginary part of the refractive index (I-REF), **(b)** single scattering albedo (SSA), **(c)** aerosol absorption optical thickness, **(d)** absorption angstrom exponent (AAE), **(e)** scatter plot between AAE and EAE and **(f)** particle size distribution.

5.5. Quinquennial variation in Aerosol Optical and Microphysical Properties

Within the 15 year, the data will be classified into three quinquennial period namely (i) Period I: 2000-2004, (ii) Period II: 2005-2009 and (iii) Period III: 2010-2014 in order to explore long term change in the aerosol optical and microphysical properties as well as clarify the parameters that affect the discrepancy between quinquennial periods. As stated before, out of 2942 samples only 322 samples had aerosol optical and microphysical information, therefore; the aforementioned approach was adopted. The Kruskal-Wallis (K-W) test was applied with a 95 % confidence interval in order to assess the quinquennial differences in the aerosol optical and microphysical properties for three periods.

Box-Whisker diagrams of AAOT, EAE, I-REF, SSA and AAE for Period I, II and III are shown in Figure 5.20. As can be deduced from the Box-Whisker plots there was a statistically difference for aerosol optical and microphysical properties. The results from K-W test also supported the Box-Whisker diagrams. Beginning from the aerosol absorption optical thickness at 440 nm, Period II (0.045) was at least 25 % higher than those observed for Period I (0.035) and II (0.031). Extinction Angstrom Exponent also exhibited a significant difference between Period II (1.1) and Period I/Period III (1.3), suggesting the former period was remarkably influenced by coarse particles compared to the later periods. Imaginary part of the refractive index and sing scattering albedo at 440 nm were also found to be statistically different for Period II and Period I/Period III. Imaginary part of the refractive index was larger for Period II whereas single scattering albedo was lower for the same period relative to Period I and Period III. This difference might be attributed that Period II was considerably affected by mineral dust intrusions from North Africa and the Middle East than those for Period I and Period III. In the same way, Absorption Angstrom Exponent for Period II was statistically higher than Period I and Period III, supporting the larger influence of mineral dust on Period II. Subsequently, it might be argued that the Period II was relatively more influenced by air mass transport originated from dust areas whereas, the Period I and Period III were largely effected by air flow from populated and/or industrialized regions compared to Period II. If this is the case, than one should expect distinct difference in the air mass transport from one period to another. In order to explore such difference, the percent influence and anomaly of the air-masses transport reaching at 1 km and 4 km of the each air flow sector was calculated for Period I, II and III. The percent influence and anomalies of the each air flow arriving at 1 km and 4 km for Period I, Period II and Period III are respectively presented in Figure 5.21, 22, 23, 24. Based on percent influence of air flow sector and air masses anomalies for Period I, Period II and Period III, the following generalizations may be made:

(i) For Period I and Period III, the percent influence of air flow sector at 1 km originated from northerly air masses were respectively found to be higher than 79 % while the northerly air flow for Period II was around 72 %,

(ii) Correspondingly, the percent influence of MID and SAH sector for 1 km were decreasing in the order Period II (9.0 %) < Period III (2.9 %) < Period II (1.4 %) and Period II (8.3 %) < Period II (5.5 %) < Period III (1.9 %), respectively,

(iii) There were respectively positive anomalies for WE/MED and EE/TR air flow reaching at 1 km altitude during Period I and III, whilst Period II had positive anomaly of air masses arriving at 1 km from MID and SAH.

(iv) Similar to 1 km, for 4 km altitude, air masses from the northerly sector of Period II (63.2 %) was considerably lower than those calculated for Period I (75.3 %) and Period III (78.8 %). On contrary, air flow reaching at 4 km from SAH sector for Period II (31.3 %) was larger than Period I (21.9 %) and Period III (9.6 %).

(v) Air masses arriving at 4 km altitude for Period I and Period III were respectively associated with positive anomalies of WE and TR/MID. However, Period II for 4 km altitude demonstrated positive anomaly of air flow SAH sector.

Taking into account the % influence and anomaly for air flow, it might be argued that micro-physical properties, for instance, larger imaginary part of the refractive index and higher absorption at 440 nm, in the Period II was mainly modified by more frequent mineral dust transport both from Sahara and the Middle East compared to Period I and III.

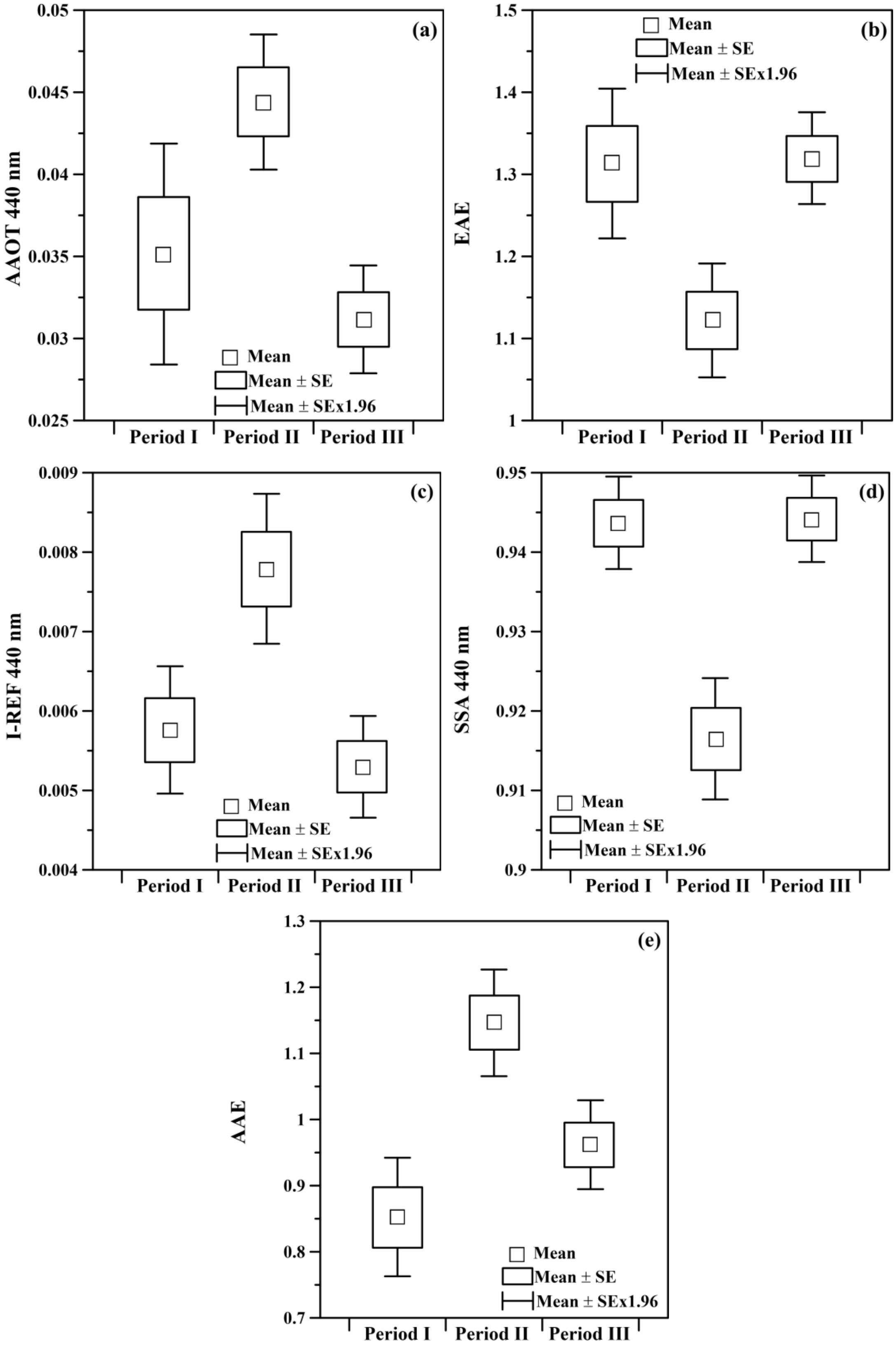

Figure 5.20 Bow-whisker plot of AAOT **(a)**, EAE **(b)**, I-REF **(c)**, SSA **(d)**, AAE **(e)** for Period I, Period II and Period III.

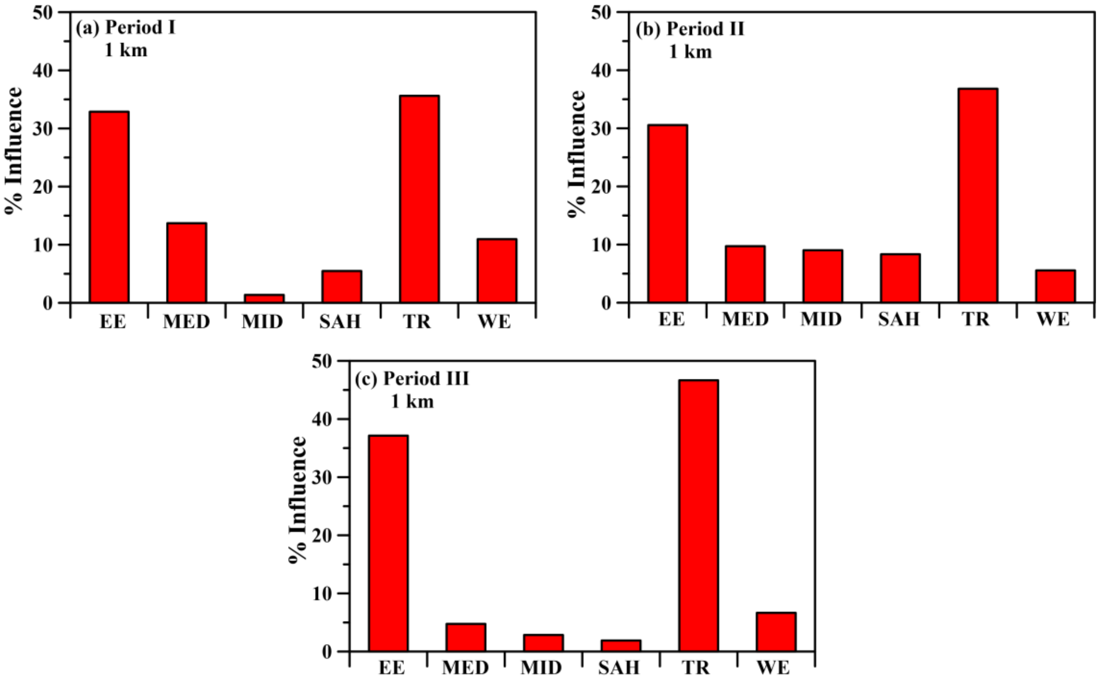

Figure 5.21 Percent of air flow for defined sectors during Period I **(a)**, Period II **(b)** and Period III **(c)** for 1km.

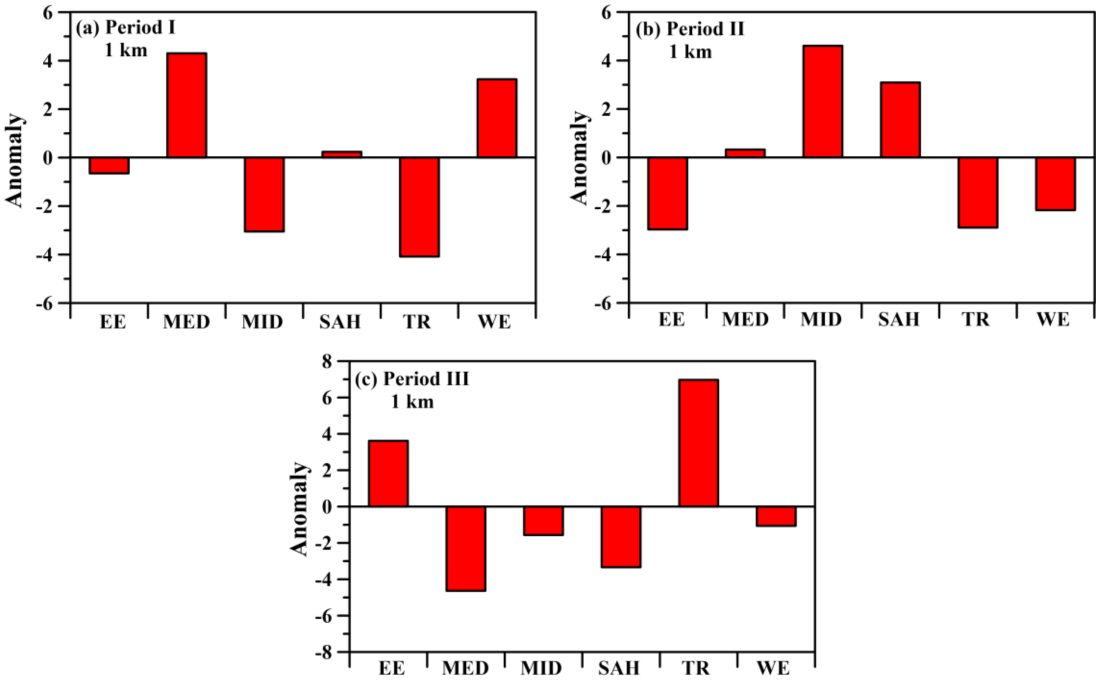

Figure 5.22 Anomalies of air flow according to defined sectors during Period I **(a)**, Period II **(b)** and Period III **(c)** for 1 km.

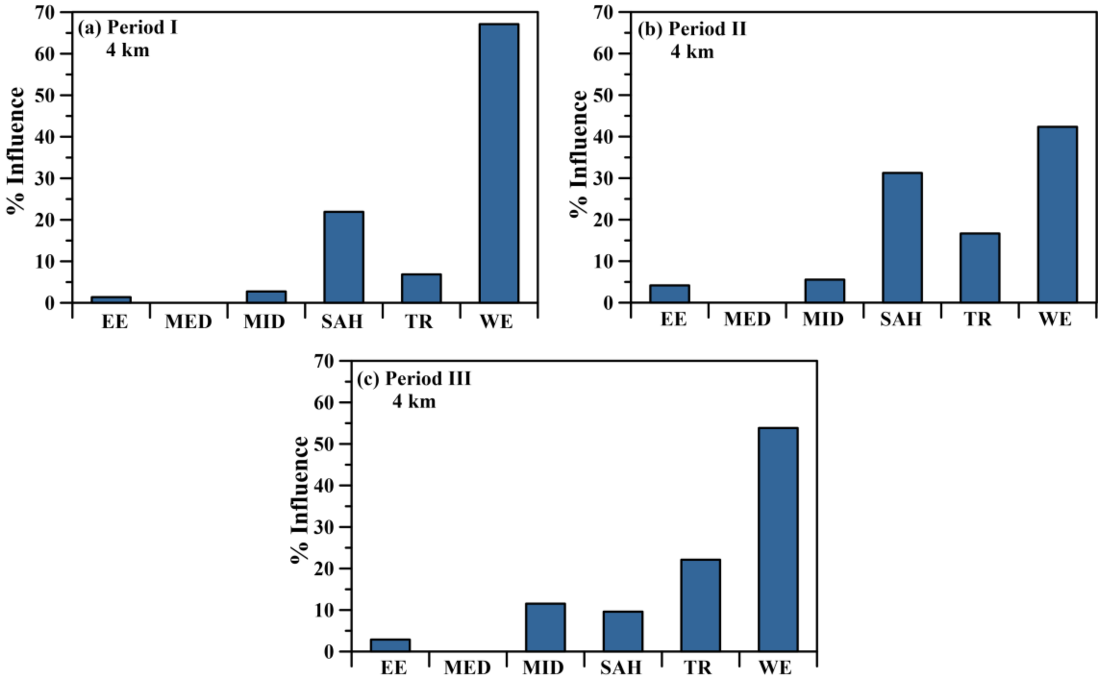

Figure 5.23 Percent of air flow according to defined sectors during Period I **(a)**, Period II **(b)** and Period III **(c)** for 4 km.

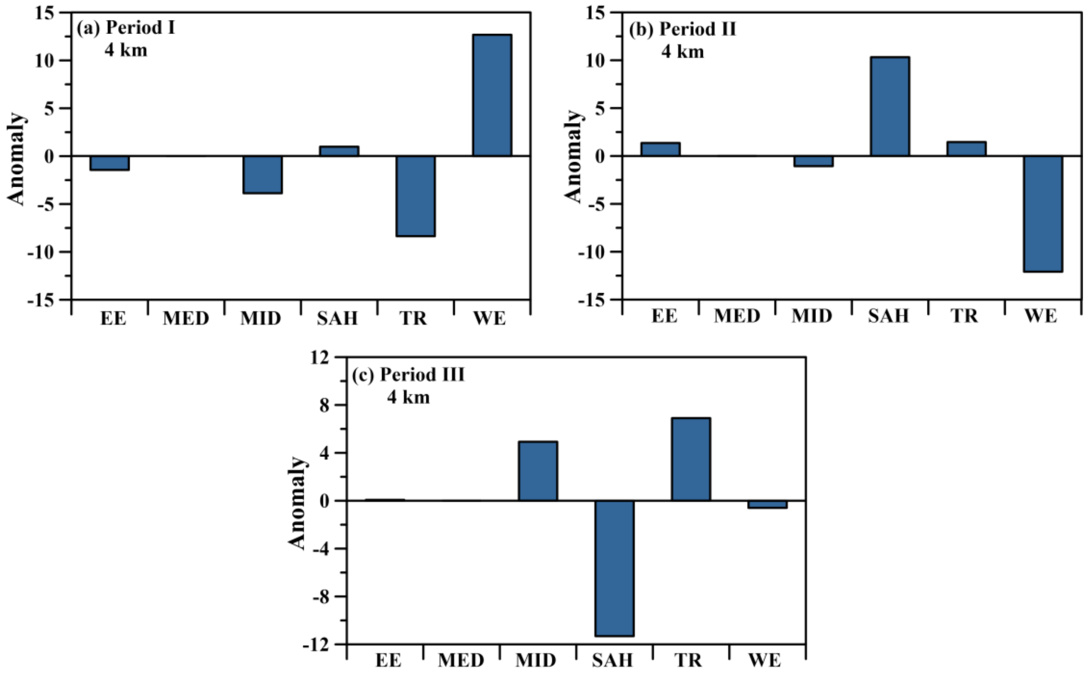

Figure 5.24 Anomalies of air flow according to defined sectors during Period I **(a)**, Period II **(b)** and Period III **(c)** for 4 km.

CHAPTER VI

6. Near Real-Time Measurements of Water-Soluble Ions in $PM_{2.5}$ and their Precursor Gases

6.1. Comparison of online and offline measurements

Before presenting general characteristics of the data set obtained from online (hourly AIM-IC) measurements it is worth mentioning that the sulfate, ammonium and nitrate values were determined by two different measurement techniques namely; (i) hourly online and (ii) daily offline. In order to evaluate and compare the results from online and offline techniques, hourly data obtained from AIM-IC were utilized to calculate the arithmetic means to be comparable with the collection time of the offline samples. The percentage difference for each sample between the online and offline values were calculated (see Eq. 6.1) as suggested by Malaguti *et al*., (2015).

$$\% D = \frac{24\ hrs\ A.Mean\ of\ Online\ - Daily\ Concen.of\ Offline}{Daily\ Concentration\ of\ Offline\ Measurement} x\ 100\ [Eq. 6.1]$$

As it is well documented, offline techniques may lead to positive and negative artefacts during sampling and storage (Lipfert, 1994; Tsai and Perng, 1998; Hering and Cass, 1999; Pakkenen *et al*., 1999; Schaap *et al*., 2002; Schaap *et al*., 2004; Wieprecht *et al*., 2004; Keck and Wittmaack 2005; Chow *et al*., 2008; Vecchi *et al*., 2009; Cheng *et al*., 2012). A number of studies have compared online and offline sulfate, ammonium and nitrate measurements (Drewnick *et al*., 2003; Nie *et al*., 2010; Gao *et al*., 2011; Schaap *et al*., 2011; Xue *et al*., 2011; Makkonen *et al*., 2012; Hu *et al*., 2014; Liu *et al*., 2014; Makkonen *et al*., 2014; Malaguti *et al*., 2015). Offline sampling errors result from gas absorption by sampling material, gas-particle/particle-particle interactions, evaporation of collected aerosol species from filter, meteorological conditions (such as temperature and humidity). Glass-fiber, quartz and cellulose acetate filters have been found to adsorb gaseous SO_2 and HNO_3 (Appel *et al*., 1984; Savoie *et al*., 1992). Acidic gases may also adsorb onto pre-existing alkaline particles such as sea salt and mineral dust. Such errors lead to positive bias. Nitrate volatilization may occur owing to (i) thermal decomposition, particularly when ambient temperature exceeds 20^oC and (ii) chemical reactions between NH_4NO_3 and H_2SO_4 and HCl (Appel *et al*., 1980; Appel and Tokiwa, 1981). Hering and Cass (1999) have reported about 30 % loss of nitrate from Teflon filters and this volatilization have been attributed to either (i) scavenging of nitric acid and ammonia in the sampler inlet or (ii) heating the filter substrate. Schaap *et al*. (2004) have demonstrated that Teflon filters were more prone to evaporation losses than those of quartz filters. Comparison of online and offline measurements has shown that obtained results from the two techniques for sulfate and ammonium were comparable exhibiting good correlation coefficients (Drewnick *et al*., 2003; Nie *et al*., 2010; Xue *et al*., 2011; Makkonen *et al*., 2012; Malaguti *et al*., 2015). In contrast, comparisons of nitrate have indicated poor correlation coefficients with a remarkable difference in attained concentrations from online and offline measurements (Nie *et al*., 2010; Malaguti *et al*., 2015).

Table 6.1 Daily concentrations of SO_4^{2-}, NH_4^+ and NO_3^- (ng m^{-3}) obtained from AIM-IC and Teflon Filters and corresponding % Difference for each sample.

	AIM-IC			**Teflon Filters**			**% Difference**		
Date	**SO_4^{2-}**	**NH_4^+**	**NO_3^-**	**SO_4^{2-}**	**NH_4^+**	**NO_3^-**	**SO_4^{2-}**	**NH_4^+**	**NO_3^-**
21.08.2015	4014	1569	144	5823	2186	157	-31	-28	-9
22.08.2015	8420	2880	152	11713	4118	256	-28	-30	-41
23.08.2015	7570	2549	146	10316	3735	170	-27	-32	-14
24.08.2015	6469	2575	240	7682	2741	66	-16	-6	262
25.08.2015	3926	2457	243	5044	1758	101	-22	40	141
26.08.2015	1561	843	453	2037	705	132	-23	20	243
27.08.2015	1109	866	241	1343	600	121	-17	44	99
28.08.2015	1533	1076	410	1957	622	98	-22	73	319
29.08.2015	1147	902	175	1550	626	106	-26	44	66
30.08.2015	1433	983	183	1729	650	90	-17	51	103
31.08.2015	2201	1255	266	2768	963	132	-20	30	101
01.09.2015	3253	2151	352	3971	1569	53	-18	37	562
Average	3553	1676	250	4661	1690	124	-24	-1	103

Figure 6.1 shows plots of online concentrations against offline concentrations whilst Table 6.1 exhibits the percentage difference for sulfate, ammonium and nitrate achieved from online and offline measurements. As can be deduced from the Figure 6.1, the residual correlation coefficients (R^2) for sulfate and ammonium were considerably better than that attended for nitrate. Correspondingly, the residual correlation coefficients for sulfate and ammonium were 0.99 and 0.91 with an increase in concentrations obtained from both measurements. The slope of the regression lines for sulfate and ammonium were higher than unity, being 1.33 and 1.08, respectively. The residual correlation coefficient for nitrate was 0.63 whereas the slope of the regression was 0.4. The slope of the regressions suggests that positive bias for sulfate

and ammonium and negative bias for nitrate. Negative biases have been reported for offline nitrate as well as ammonium sampling compared to online measurements (Chow *et al*., 2008; Nie *et al*., 2010; Makkonen *et al*., 2014; Malaguti *et al*., 2015).

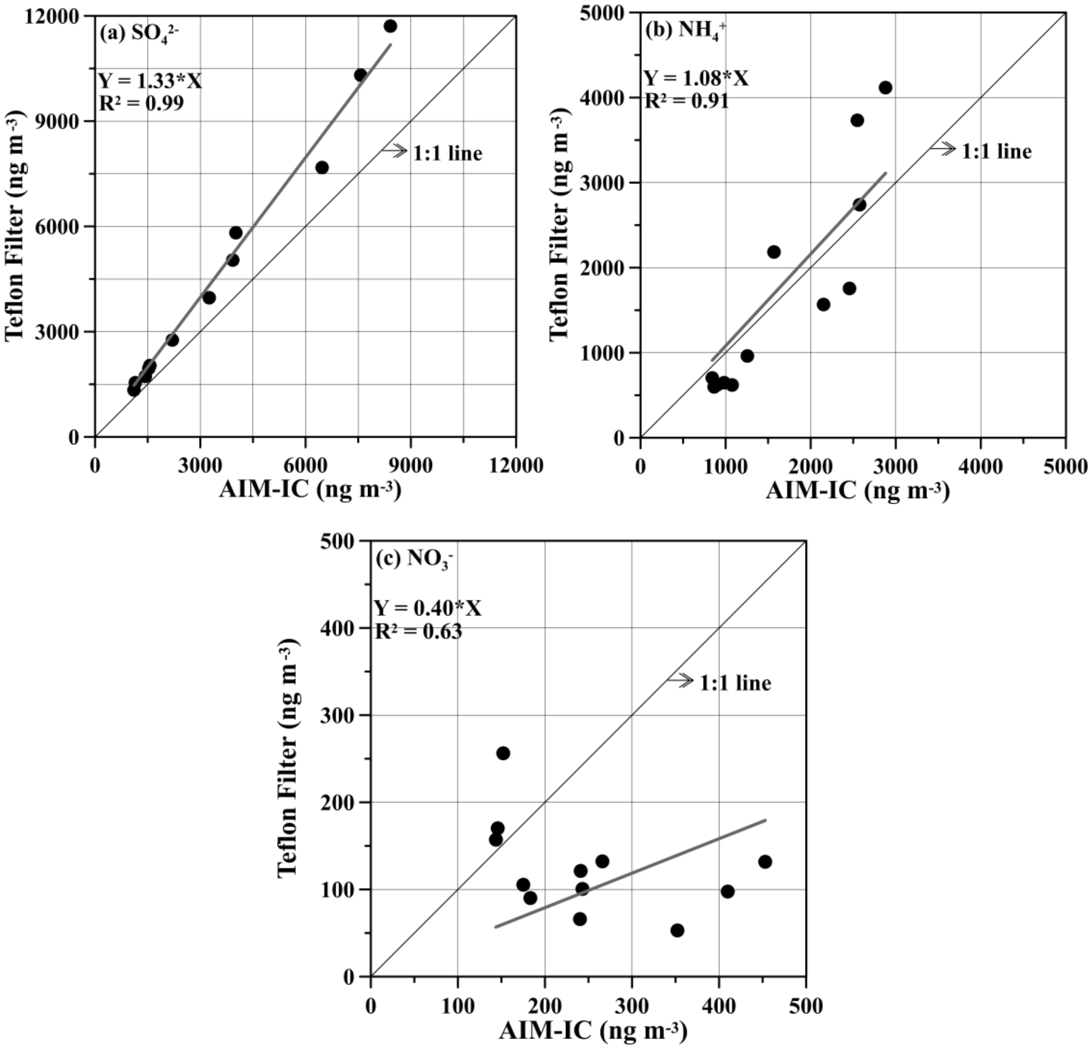

Figure 6.1 Scatter plots of sulfate **(a)**, ammonium **(b)** and nitrate **(c)** obtained from AIM-IC and Teflon Filters.

Regarding Table 6.1, sulfate concentrations from online technique for all measurements were lower than those obtained from offline technique, % difference varying between -16 and -31 %. Nonetheless, the % difference between online and offline measurements for ammonium and nitrate was relatively complex compared to sulfate. At the beginning of the experiment % difference was positive then it was negative until the end of the experiment. Figure 6.2 shows relationship between enhanced non sea salt sulfate (en-nssSO_4^{2-} = offline-nssSO_4^{2-} - onlinen-ssSO_4^{2-}) and offline-Na^+ (indicator of sea salt) in neq m^{-3}. A statistically significant residual correlation coefficient ($R^2 = 0.85$) was found between en-nssSO_4^{2-} and Na^+. Therefore, the difference between offline and online techniques for sulfate might be ascribed to the enhancement of sulfate because of either (i) the reaction between acidic H_2SO_4 and preexisting sea salt particles or (ii) oxidation of SO_2 on the surface of preexisting sea salt particles.

It has been stated that the gas-particle partitioning may promote dissociation of ammonium nitrate (Vecchi *et al.*, 2009). The partial correlations between temperature/relative humidity/particle-to-gas ratio and ammonium/nitrate are given in Table 6.2. As can be deduced from the table, the percent difference for ammonium and nitrate was mainly influenced by partitioning between gas and aerosol phase. % D increased with decreasing ammonium in particle phase for ammonium, whilst % D decreased with increasing nitric acid likely owing to adsorption of nitric acid on alkaline particles. % D for ammonium and nitrate also exhibited statistically important relationship with temperature, suggesting evaporation from the Teflon Filters during off-line sampling. On the other hand, % D of nitrate denoted increase under dry conditions, promoting nitrate evaporation from filter substrate with increasing temperature.

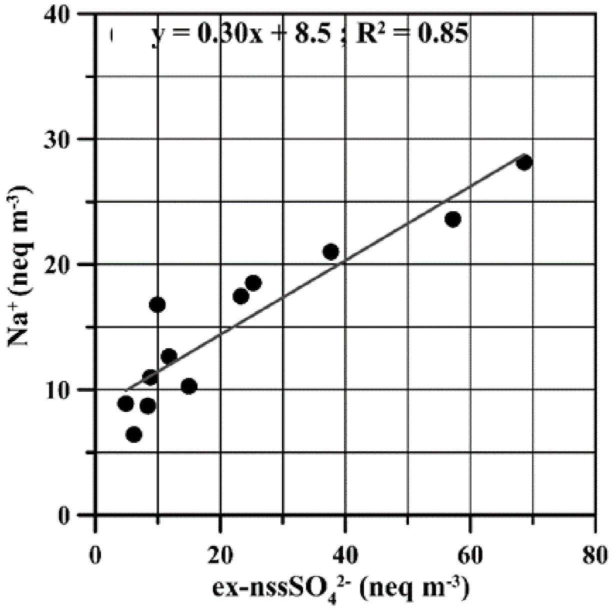

Figure 6.2 Scatter plot of enhanced non sea salt sulfate (en-nssSO_4^{2-} = offline-nssSO_4^{2-} - online-nssSO_4^{2-}) and offline-Na^+.

Table 6.2 Partial correlation between ammonium/nitrate and temperature/relative humidity/ particle-to-gas ratio conversion

% Difference	NH_4^+/NH_3	NO_3^-/HNO_3	T (°C)	RH
NH_4^+	-0.70	-	0.42	0.18
NO_3^-	-	0.90	0.67	-0.49

6.2. Local Meteorological Conditions during Near-Real Time Measurements

Climatology of the meteorological parameters has been presented in section 3.1. As stated before, such parameters play a vital role in the variability of the aerosols and their precursor gases as well as gas to particle conversions. Statistical summary of hourly rain, temperature, relative humidity and pressure in winter and summer during near-real time measurements are illustrated in Table 6.3. As expected, winter was the wettest season and hence rain was particularly intensive from 27th to 31st of the January 2015, which is likely to lead to the removal of aerosols and their precursor gases from the atmosphere by wet deposition. In contrast, there was no rain in the summer during sampling. In winter, the average surface temperature was 11.5 °C, ranging from 5.5 °C to 19.5 °C. The surface temperature was at least 2 times higher in summer compared to winter, varying between 19.1 °C and 33.2 °C with a mean value of 28.2 °C. The sea surface pressure was higher in winter (1016.4 hPa) than that of summer (1007.9 hPa), implying comparatively stable weather conditions in winter. During the winter the average relative humidity was 75.6, fluctuating from 39.0 to 94.0 whilst it ranged between 26.0 and 89.0 with an arithmetic mean of 59.6 during summer. Wind direction/speed and % influence of each wind sector for winter and summer are shown in Figure 6.3. Wind direction and speed exhibited a great difference between winter and summer. The wind speed was higher in summer (1.6 m s^{-1}) than that of observed in winter (1.2 m s^{-1}). During winter most of the winds originated from the north, explaining 82.3 % of the wind direction whilst the highest wind speeds were associated with Easterlies (2.0 m s^{-1}) and East-North-Easterlies (1.6 m s^{-1}). It is worth mentioning there was no southerly winds during the winter sampling. During summer, northerly and southerly winds had almost equal importance, being 45.7 % and 41.4 %, respectively. In general, the northerly winds were more sluggish (varying from 0.7 m s^{-1} to 1.6 m s^{-1}) than those observed for southerly winds (ranging between 1.6 m s^{-1} and 2.6 m s^{-1}).

Table 6.3 Statistical summary of hourly meteorological parameters for winter and summer during the near-real time measurements.

Parameters	Arithmetic Mean	Standard Deviation	Minimum	Maximum
Winter				
Temperature (°C)	11.5	3.2	5.5	19.5
Relative Humidity (%)	75.6	14.1	39.0	94.0
Atmospheric Pressure (hPa)	1016.4	3.0	1010.2	1021.4
Wind Speed (m s^{-1})	1.2	0.5	0.2	2.8
Rain (mm)	29.2*	-	0.2	5.2
Summer				
Temperature (°C)	28.2	3.4	19.1	33.2
Relative Humidity (%)	59.6	14.0	26.0	85.0
Atmospheric Pressure (hPa)	1007.9	2.0	1003.5	1011.6
Wind Speed (m s^{-1})	1.6	1.0	0.1	4.2
Rain (mm)	-	-	-	

*denotes total amount of rain

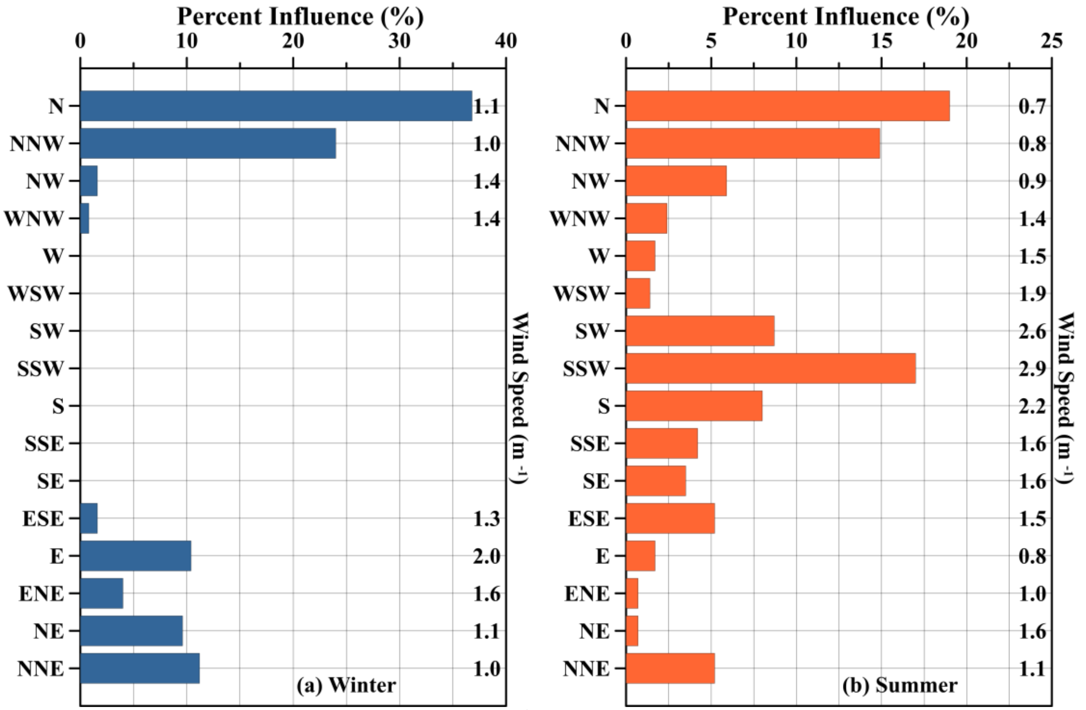

Figure 6.3 Wind direction and speed (m s^{-1}) for winter **(a)** and summer **(b)** 2015 during near-real time measurements.

6.3. General Characteristics of Data Set

At the Erdemli site hourly measurements carried out between 27 January and 03 February 2015 as well as between 19 August and 01 September 2015. Correspondingly, a total of 127 and 310 hourly measurements were achieved in winter and summer. The arithmetic average concentrations of SO_4^{2-}, NH_4^+, NO_3^- (in $PM_{2.5}$), SO_2, NH_3 and HNO_3 along with corresponding standard deviations, median, minimum and maximum, and geometric means is presented in Table 6.3. As can be deduced from the table, the minimum and maximum concentrations as well as the standard deviations exhibit large variability in both period. Such high variability has been reported for semi-continuous SO_4^{2-}, NH_4^+, NO_3^-, SO_2, NH_3 and HNO_3 measurements (Godri *et al.*, 2009; Du *et al.*, 2010; Shi *et al.*, 2014; Tian *et al.*, 2017). The large variability may be ascribed to (i) local meteorological parameter (such as temperature, relative humidity, rain, solar irradiance and wind direction), (ii) type of source, (iii) emission strength of source, (iv) proximity to source, (v) history of air masses and (vi) chemical transformation and removal of species throughout middle and long range of transport.

The arithmetic mean, median and geometric mean values as well as skewness are utilized to assess the distribution type of the interested variable during the study period. The arithmetic mean, median and geometric mean values are identical when the variable denotes a normal distribution. In general, the arithmetic mean, median and geometric mean values for SO_4^{2-}, NH_4^+, NO_3^-, SO_2, NH_3 and HNO_3 showed considerable difference between arithmetic mean concentrations and geometric means/medians, the former being higher than those of later whereas geometric means and medians were comparable. The skewness also supports that the species were not normally distributed. This suggests that the variable is lognormally distributed. Previous studies in the region have been demonstrated that the aerosol species are lognormally distributed (Koçak *et al.*, 2004).

The observed and expected frequency of SO_4^{2-}, NH_4^+, NO_3^-, SO_2, NH_3 and HNO_3 for lognormal distribution is shown in Figure 6.4. The non-parametric Kolmogorov-Smirnov statistical test exhibited that above mentioned species were lognormally distributed within the 90 % confidence level.

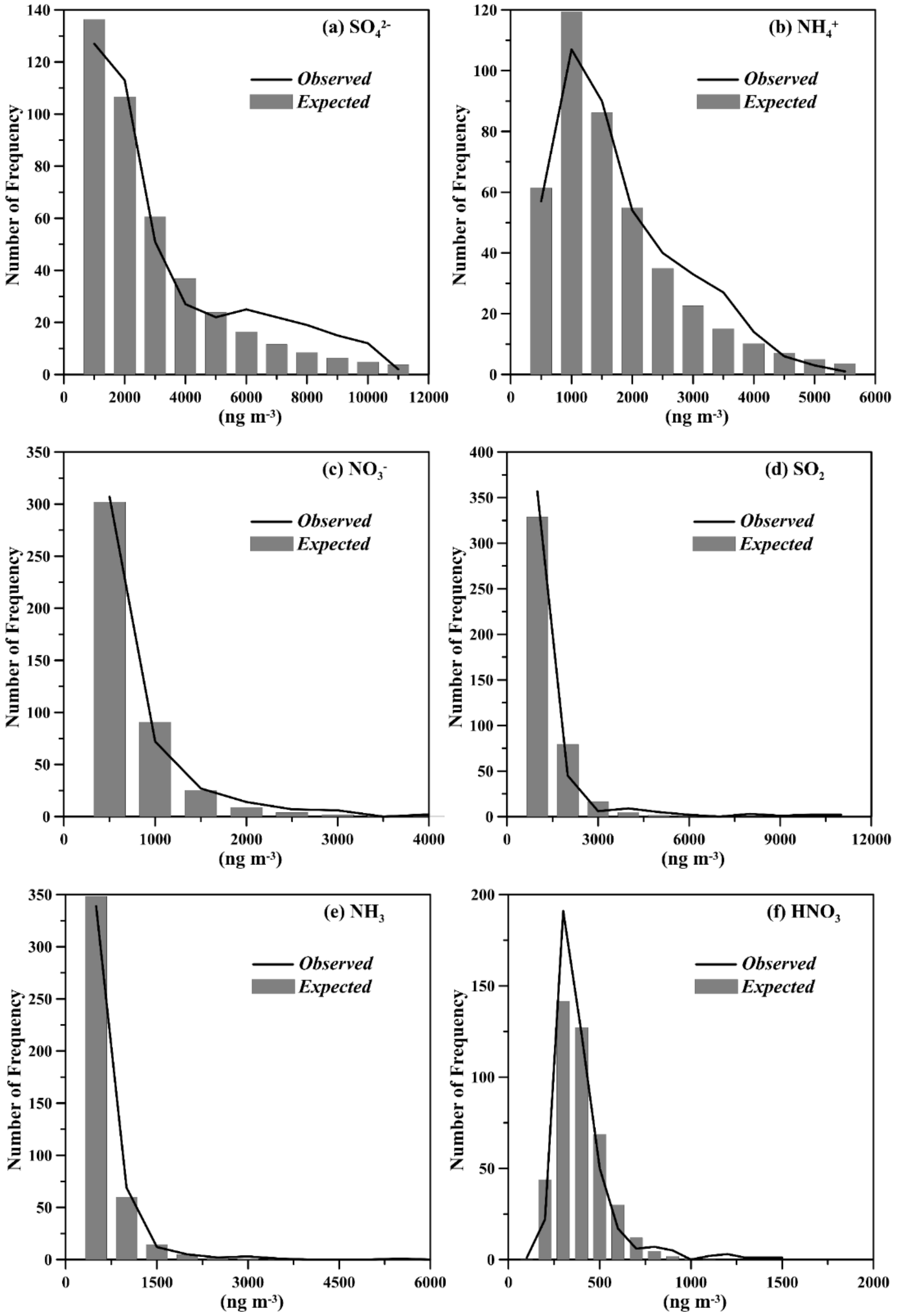

Figure 6.4 Population frequency histogram of sulfate **(a)**, ammonium **(b)**, nitrate **(c)**, sulfur dioxide **(d)**, ammonia **(e)** and nitric acid **(f)**.

Of the water-soluble ions in $PM_{2.5}$, sulfate and ammonium were the dominant species. Arithmetic mean sulfate and ammonium concentrations were 2814 ng m^{-3} and 1371 µg m^{-3}, ranging between 120-10233 ng m^{-3} and 39-4796 ng m^{-3}, respectively. Aerosol nitrate ranged between 64 ng m^{-3} and 3891 ng m^{-3} with an arithmetic mean of 495 ng m^{-3}. Among the precursor gases, ammonia exhibited the highest concentration with a value of 3330 ng m^{-3}, fluctuating between 72 ng m^{-3} and 54927 ng m^{-3}. Sulfur dioxide and nitric acid concentrations varied from 101-10334 ng m^{-3} to 55-1440 ng m^{-3}, with mean concentrations of 879 ng m^{-3} and 346 ng m^{-3}, respectively. Taking into account precursor gases concentrations, it is clear that alkaline ammonia (g) concentration was more than enough to neutralize acidic gases. The arithmetic mean of gas-to-particle ratios for sulfate, ammonium and nitrate were respectively found to be 0.69 ± 0.25, 0.38 ± 0.24 and 0.49 ± 0.17. The gas-to-particle ratios for sulfate, ammonium and nitrate fluctuated from 0.01 to 0.97. It has been argued that the ratio less than 0.3, exhibits local sources. In contrast, the ratio larger than 0.3 denotes aged air masses and the higher values implies the older air masses and/or larger travelling distances. Thus, regarding arithmetic means of gas-to-particle conversion ratios for sulfate, ammonium and nitrate, it might be suggested that the concentrations of these species were mainly influenced by non-local sources.

Table 6.4 Statistical summary for SO_4^{2}; NH_4^+, NO_3^- in $PM_{2.5}$ (ng m^{-3}) and their precursor gases along with gas-to-particle (molar) ratios.

Species	Mean	Standard Deviation	Minimum	Maximum	Median	Geometric Mean	Skewness
SO_4^{2-}	2814	2620	120	10233	1755	1701	1.11
NH_4^+	1371	1016	39	4796	1168	958	0.90
NO_3^-	495	568	64	3891	260	320	2.59
SO_2	879	1329	101	10334	499	574	4.63
NH_3	3330	4896	72	54927	1394	1834	4.66
HNO_3	346	168	55	1440	302	320	3.03
$SO_4^{2-}/SO_4^{2-}+ SO_2$	0.62	0.27	0.02	0.95	0.68	0.53	
$NH_4^+/NH_4^++ NH_3$	0.38	0.24	0.01	0.86	0.35	0.28	
$NO_3^-/NO_3^-+HNO_3$	0.50	0.17	0.09	0.90	0.46	0.47	

6.4. Comparison of the current real-time study with data from Literature

In order to define spatial and long term difference in the concentrations of sulfate, ammonium, nitrate, sulfur dioxide, ammonia and nitric acid two types of data from Literature will be used namely, (i) online and (ii) offline.

(i) Online Data Set

Bari (southern Italy, Lat: 47.15; Long: 16.66; Gilio *et al*., 2015)) site is characterized as an urban back-ground site. Near-real time (online) measurements of water-soluble ions in PM2.5 and their precursor gases were carried out for 20 days (October 2011).

Rural ***Trisaia*** (Italy, 40.09 °N, 16.38 °E; Malaguti *et al*., 2015) is located in the South Italy, about 4 km away from Ionian Sea. Hourly measurements (online) were conducted between 3 May to 30 June 2010.

Shanghai (China, 31.3 °N, 121. °E; Du *et al*., 2010, 2011) site is an urban district since there is an influence of residential, traffic and construction emissions. Hourly measurements (online) were achieved from May 27 to June 16, 2009.

Jinan (China, 36.69 °N, 117.06 °E; Gao *et al*., 2011) is an urban site since it is surrounded by residential and commercial districts. Near-real time (online) measurements were conducted from December 1, 2007-January 3, 2008 to April 1-18, 2008.

Beijing (China, Gao *et al.*, 2016) is the capital of Chania. The site is an urban district because of mixed influence of emissions from residual, traffic and construction. The near-time (online) measurements conducted from July 22 to August 12 in 2014.

Singapore (1.09 °N, 103.36 °E; Behera *et al*., 2013), this site (urban) is situated at the southern tip of the Malayan peninsula. The site is mainly under the influence of pollution originating from fossil fuel burning and traffic. Near-real time campaign was carried out from 14 September to 8 November, 2011.

Megacity ***Seul*** is the capital of Korea. The station is located at Guui-dong of Gwang Jin district (32.40 °N, 127.05 °E; Shon *et al*., 2012) and hourly measurements were conducted between 1 January and 31 December 2010.

Bakersfield (USA, Markovic *et al*., 2014) site is an urban industrial station located in a large agricultural region. Near-real time measurements were carried out between May 5 and June 23, 2010.

(ii) Offline Data Set

Finokalia site (25.6 °N, 35.2 °E; Kouvarakis *et al*., 2001, 2002) is described as a natural back-ground since it has a distance greater than 50 km from the large pollution sources. The sampling was commenced in 1996 and finished in 1999.

Patras (Danalatos and Glavas, 1999), sampling site is located 10 km north east of the center of the city. The samples were collected between November 1995 and September 1996.

Jerusalem (Israel; Luria *et al*., 1996) is a rural site. The sampling was conducted from 1990 to 1991.

The concentrations of sulfate, ammonium, nitrate, sulfur dioxide, ammonia and nitric acid obtained from online measurements along with offline measurements carried out in the Eastern Mediterranean are presented in Table 6.5. Generally, the highest concentrations of sulfate, ammonium, nitrate and ammonia concentrations were found over China (Du *et al*., 2011; Gao *et al*., 2011; Gao *et al*., 2016). Aerosol sulfate (from 14 to 40 µg m^{-3}), ammonium (from 9 to 22 µg m^{-3}), nitrate (from 15 to 33 µg m^{-3}), sulfur dioxide (Beijin: 6.65 µg m^{-3}) and ammonia (Beijing: 24.54 µg m^{-3}), concentrations over China were order of magnitude higher that of observed for Erdemli. As stated, the sampling sites at China were heavily influenced by anthropogenic emissions such as traffic, fossil fuel combustion, man induced biomass burning and construction (Du *et al*., 2011; Gao *et al*., 2011, 2016). Aerosol sulfate, ammonium, nitrate and nitric acid concentrations over Italy (Bari and Trisaia) were comparable to the values obtained at Erdemli. In contrast however, ammonia (3.60 µg m^{-3}) the mean concentration at Erdemli was about two times higher compared to that of Bari (1.57 µg m^{-3}), Italy. However, detected sulfur dioxide (0.88 µg m^{-3}) concentration for Erdemli was half of that of observed for Bari (2.04 µg m^{-3}). This distinct difference might be attributed to the influences at the sampling sites, former being surrounded by cultivated soil and the latter being urban and influenced by the comparatively emissions from heavy traffic. The highest nitric acid concentrations were observed at Seoul (8.71 µg m^{-3}) and Singapore (3.00 µg m^{-3}) being at least nine times that detected at Erdemli (0.35 µg m^{-3}). These high values might be ascribed to the night time production of nitric acid due to NO_x emissions from heavy traffic close to the vicinity. Although ammonia concentration at the Erdemli site is influenced by cultivated soil, the value observed at Bakersfield (13.69 µg m^{-3}) was 4 times higher than that of Erdemli (3.60 µg m^{-3}) since the Bakersfield is located in a huge agricultural region.

Taking into account this study and historic off-line measurements, there was a decreasing trend in the concentrations of sulfate, nitrate and their precursor gases in the Eastern Mediterranean atmosphere. Nitrate, sulfur dioxide and nitric acid were respectively found to show 3.3, 4.6 and 5.3 times decrease compared to results reported by Kouvarakis *et al*. (2001, 2002). Similar, decrease in the concentrations of sulfur dioxide and nitrate has respectively been reported for the Mediterranean (Lelieveld *et al*., 2002) and the Black Sea (Koçak *et al*., 2016). The decrease for sulfate was 1.4

relative to Finokalia, however, sulfate concentration was 4.4 times less than that of Jerusalem. Ammonium and ammonia concentrations at Erdemli were larger than those for Finokalia because the Erdemli site is surrounded by agricultural area. Table 6.6 shows the recent (January 2014-April 2015) and historical (March 2001-April 2002) offline $nssSO_4^{2-}$, NO_3^- and NH_4^+ concentrations at Erdemli. During the thirteen years, the percentanges of decreases for $nssSO_4^{2-}$, NO_3^- and NH_4^+ at Erdemli sampling site in offline measurements were % 55, % 42 and % 51, respectively. These results also indicate the negative trend in the concentrations of sulfate, nitrate and ammonium.

Table 6.5 Arithmetic mean concentrations of sulfate, ammonium, nitrate, sulfur dioxide, ammonia and nitric acid (µg m^{-3}) obtained from online for different sites of the world and offline for the Eastern Mediterranean.

Site	SO_4^{2-}	NH_4^+	NO_3^-	SO_2	NH_3	HNO_3	Reference	Character
ONLINE								
Erdemli, Turkey	2.81	1.37	0.49	0.88	3.33	0.35	This Study	Rural
Bari, Italy	2.43	2.80	0.40	2.04	1.57	0.32	Gilio et al. [2015]	Urban
Trisaia, Italy	1.87	1.03	0.52	-	-	-	Malaguti et al. [2015]	Rural
Shanghai, China	28.71	19.31	32.93	-	-	-	Du et al. [2011]	Urban
Jinan, China	38.33	21.26	15.77	-	-	-	Gao et al. [2011]	Urban
Beijin, China	14.80	8.90	15.18	6.65	24.54	-	Gao et al. [2016]	Urban
Singapore	4.41	1.76	1.29	21.77	2.47	3.00	Behera et al. [2013]	Urban
Seoul, Korea	5.80	3.91	13.78	3.58	4.80	8.71	Shon et al. [2012]	Urban
Bakersfield, USA	0.53	0.46	0.80	1.83	13.69	0.36	Markovic et al. [2014]	Urban
OFFLINE								
Finokalia, Greece	3.94	1.01	1.63	4.00	0.31	1.86	Kouvarakis et al. [2001, 2002]	Natural
Patras, Greece				-	3.20	2.60	Danalatos and Glavas [1999]	Urban
Jerusalem, Israel	12.29	-	-	17.79	-	-	Luria et al. [1996]	Rural

Table 6.6 Recent and historical offline $nssSO_4^{2-}$, NO_3^- and NH_4^+ concentrations at Erdemli.

	Erdemli[1]	**Erdemli**[2]	**Difference**
$nssSO_4^{2-}$	1.88	4.15	-2.27
NO_3^-	1.11	1.86	-0.75
NH_4^+	0.42	0.85	-0.40

[1]Unpublished data, [2]Koçak *et al.*, (2007b).

6.5. Temporal variations of Sulfate, Ammonium, Nitrate in $PM_{2.5}$ and their precursor gases

A number of studies have demonstrated that sulfate, ammonium and nitrate in $PM_{2.5}$ as well as their precursor gases may exhibit large hourly variability in their concentrations (Nie *et al.*, 2010; Makkonen *et al.*, 2012; Markovic *et al.*, 2014; Malaguti *et al.*, 2015). As stated above, such a high variability may arise from (i) local meteorological parameter (such as temperature, relative humidity, rain, solar irradiance and wind direction), (ii) type of source, (iii) emission strength of source, (iv) proximity to source, (v) history of air masses and (vi) chemical transformation and removal of species throughout middle and long range of transport.

Figure 6.5 shows the hourly variations in the concentrations of SO_4^{2-}, NH_4^+, NO_3^-, SO_2, NH_3 and HNO_3 together with corresponding gas-to-particle conversion ratios and local meteorological parameters from 27 January to 03 February 2015 and from 19 August to 01 September 2015 at Erdemli station. It is clear that water-soluble aerosol SO_4^{2-}, NH_4^+, NO_3^- and gases SO_2, NH_3 and HNO_3 exhibit a considerable variability, with the concentrations of the individual species fluctuating up to order of magnitude from one hour to another during the study period. Aerosol sulfate and ammonium in $PM_{2.5}$ showed their lowest concentrations in winter particularly during rain events since these particles efficiently scavenged by wet precipitation. For instance, a rain event started at around 23.00 pm on 29th of January 2015 and lasted 8 hours. Just one hour before the rain started, aerosol sulfate and ammonium (nitrate) concentrations were 913 ng m^{-3} and 1035 ng m^{-3} (3890 ng m^{-3}), respectively. Within a few hours of consequential rain, aerosol sulfate and ammonium (nitrate) denoted an order of magnitude decrease in their concentrations reaching down to 100 ng m^{-3} and 50 ng m^{-3} (280 ng m^{-3}) respectively. In addition to removal of particles by rain, lower gas-to-particle conversion may also contribute to observe lower concentrations of these aerosol species due to inferior solar radiation in winter. Even though, aerosol nitrate concentration was influenced by wet scavenging in winter, it denoted lower concentrations in summer. This might be attributed to evaporation of nitrate due to either elevated temperatures (reaching up to 40 °C during day) and (ii) reaction between H_2SO_4 and NH_4NO_3 (Appel *et al.*, 1980; Appel and Tokiwa, 1981). High concentrations of SO_2 was observed in winter compared to summer. In winter, elevated concentrations of SO_2 might be resulted from (i) residential heating, (ii) enhanced power generation by using high sulfur containing coal combustion for, (iii) inferior gas-to-particle conversion, (iv) lower boundary layer height which prevents dilution of sulfur dioxide. In contrast, gas NH_3 exhibited lower concentrations in winter than that of summer. The soil moisture and temperature have been identified as one of the controlling factors for NH_3 emissions (Roelle and Aneja, 2002). On the one hand, it has been demonstrated that NH_3 flux increase with increasing soil temperature, although, Roelle and Aneja (2002) suggested that rainwater may fill pores of the soil and prevents NH_3 diffusion from the soil to the air. Prevailing meteorological conditions such as rain and temperature may lead to lower NH_3 concentrations in winter. HNO_3 also demonstrated large variability whereas, observed concentrations in winter and summer were comparable. SO_2 and NH_3 concentrations were also influenced by rain events however, the decrease in their concentrations were less remarkable compared to aerosols. During the aforementioned rain events, SO_2 and NH_3 concentrations were respectively found to decrease from 2100 ng m^{-3} to 600 and to 500 ng m^{-3} to 240 ng m^{-3} ng m^{-3}. Gas-to-particle conversion ratios for sulfate, ammonium and nitrate remarkably changed from one hour to another. Except for nitrate, the conversion ratios for summer were higher than that of calculated for winter (see Table 6.7). The arithmetic average concentrations of SO_4^{2-}, NH_4^+, NO_3^- (in $PM_{2.5}$), SO_2, NH_3 and HNO_3 along with corresponding standard deviations, median, minimum and maximum, and geometric means from winter and summer are presented in Tables 6.7. In winter, among the water-soluble species, the mean concentrations of nitrate was higher than those of sulfate and ammonium. The arithmetic mean for nitrate was 1064 ± 740 ng m^{-3}, while concentrations ranged from to 154 - 3891 ng m^{-3}. Correspondingly, the arithmetic mean of ammonium and sulfate were 473 ± 389 ng m^{-3} and 656 ± 557 ng m^{-3}, fluctuating between 39-1728 ng m^{-3} and 120/ 3203 ng m^{-3}. Regarding their precursor gases, the highest arithmetic mean was observed for sulfur dioxide with a value of 1493 ± 2190 ng m^{-3}, varying from 101 to 10334 ng m^{-3}. Gaseous sulfur dioxide followed by ammonia and nitric acid, their corresponding arithmetic mean (minimum and maximum) concentrations being 1033 ± 601 (72 – 3060) ng m^{-3} and (to) 422 ± 215 (55 – 1304) ng m^{-3}. In summer, aerosol sulfate denoted the highest arithmetic mean with a value of 2694 ± 2620 ng m^{-3}, exceeding 10000 ng m^{-3}. The arithmetic mean concentrations for ammonium and nitrate were respectively 1728 ± 966 (from 139 to 4796) ng m^{-3} and 263 ± 215 (from 67 to 1604) ng m^{-3} in summer.

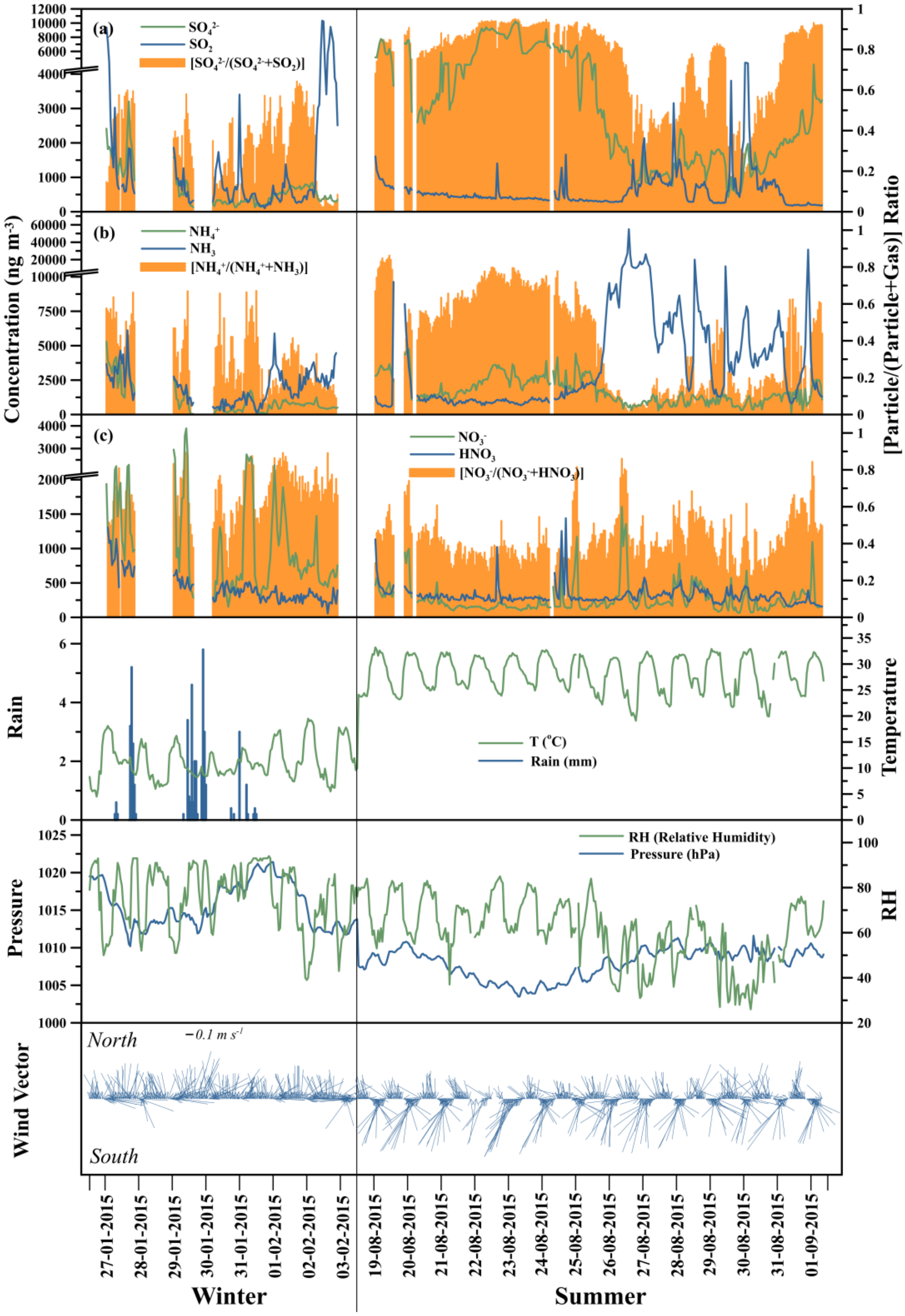

Figure 6.5 Hourly variability of sulfate, ammonium and nitrate in $PM_{2.5}$ and their precursor gases along with gas-to-particle conversion ratios (molar) and meteorological parameters from to 27 January - 03 February 2015 to 19 August - 01 September 2015 at Erdemli station.

Table 6.7 Statistical summary for SO_4^{2}, NH_4^+, NO_3^- and their precursor gases along with gas-to-particle ratios during winter and summer periods.

Species	Arithmetic Mean	Standard Deviation	Minimum	Maximum	Median
Winter					
SO_4^{2-}	656	557	120	3203	471
NH_4^+	473	389	39	1728	360
NO_3^-	1064	740	154	3891	794
SO_2	1493	2190	101	10334	638
NH_3	1033	601	72	3060	989
HNO_3	422	215	55	1304	364
$SO_4^{2-}/SO_4^{2-}+ SO_2$	0.34	0.18	0.02	0.64	0.36
$NH_4^+/NH_4^++ NH_3$	0.30	0.15	0.06	0.67	0.27
$NO_3^-/NO_3^- +HNO_3$	0.68	0.13	0.27	0.90	0.69
Summer					
SO_4^{2-}	3694	2620	431	10233	2895
NH_4^+	1728	966	139	4796	1483
NO_3^-	263	215	64	1604	186
SO_2	629	571	176	4408	441
NH_3	4243	5518	555	54927	2059
HNO_3	316	134	154	1440	286
$SO_4^{2-}/SO_4^{2-}+ SO_2$	0.74	0.21	0.15	0.95	0.83
$NH_4^+/NH_4^++ NH_3$	0.41	0.26	0.01	0.86	0.45
$NO_3^-/NO_3^- +HNO_3$	0.42	0.13	0.09	0.86	0.4

The highest gases concentration was found to be ammonia (4243 ± 5518 ng m-3, varying between 555 and 54927 ng m-3) followed by sulfur dioxide (629 ± 571 ng m-3, varying between 176 and 4408 ng m-3) and nitric acid (316 ± 134 ng m-3, varying between 154 and 1440 ng m-3). Taking into account precursor gases concentrations in winter and summer, it is clear that alkaline ammonia (g) concentration was more than enough to neutralize acidic gases sulfur dioxide and nitric acid.

To illustrate the influence of air mass transport on the temporal variation of the measured concentrations, an event characterized from August 25th to 27th will be discussed. Before the event, on 24th August, air masses originated from the west and southwest sectors reached Erdemli site at 200m, with a daily mean NH_3 concentration of 64 nmol m^3 (Fig. 6.6a). The next day, on 25th August at 07:00am (local time), the airflow shifted to a northerly direction (Fig. 6.6b). During the following hours, NH_3 concentration began to rise steadily and reached 128 nmol m^{-3} at 00:00am on 26th August. Sequent 2-day back trajectories for every hour from 26th to 27th August showed that transport pathway extended over the northeastern Black Sea and Russian and remained prevailing until end of the event (Fig. 6.6c,d). NH_3 continued to increase and reached its highest value at 01:00am on 27th August, attaining 3230 nmol m^{-3}. The second maxima peak in NH_3 concentrations was also observed around 1540 nmol m^{-3} at 13:00pm on 27th August. The arithmetic mean of NH_3 values for the event was 490 nmol m^{-3}. Gas-to-particle conversion ratio for ammonium decreased to 0.10 during the event whilst it was around 0.65 before the event. Since atmospheric NH_3 mostly has a life of 1 day (Seinfeld and Pandis, 1998), emission source might be in the range of one day transport. Meanwhile, NH_4^+ (SO_4^{2-}) was found to be decrease by about 50% (65%), reaching the mean concentration of 55 (20) nmol m^{-3} during the event. On the other hand, SO_2 increased substantially during the event with a time lag of one day to NH_3, reaching 15 nmol m^{-3} levels. In other words, SO_2 hourly variations did not show a similar pattern with NH_3. MODIS-Terra (Moderate Resolution Imaging Spectrometer) AOD satellite images indicated slight decrease in optical thickness over site from 24th to 27th August. Daily concentrations from Teflon filters also supported the same amount of decrease in SO_4^{2-} and NH_4^+. Moreover, nssK obtained from filters and NH_3 correlated well ($r = 0.77$) during summer time indicating their origin from similar sources. Potassium has been used as an inorganic tracer of biomass burning (Ramadan *et al.*, 2000; Ma *et al.*, 2003; Liu *et al.*, 2005; Lee *et al.*, 2008) and high levels of NH_3 are emitted through biomass burning (Hegg *et al.*, 1988, Crutzen and Andreae, 1990). Taking into account air mass histories an active fire spots in Fig. 6.6, this sharp increase in NH3 may be attributed to either man or natural induced biomass burning.

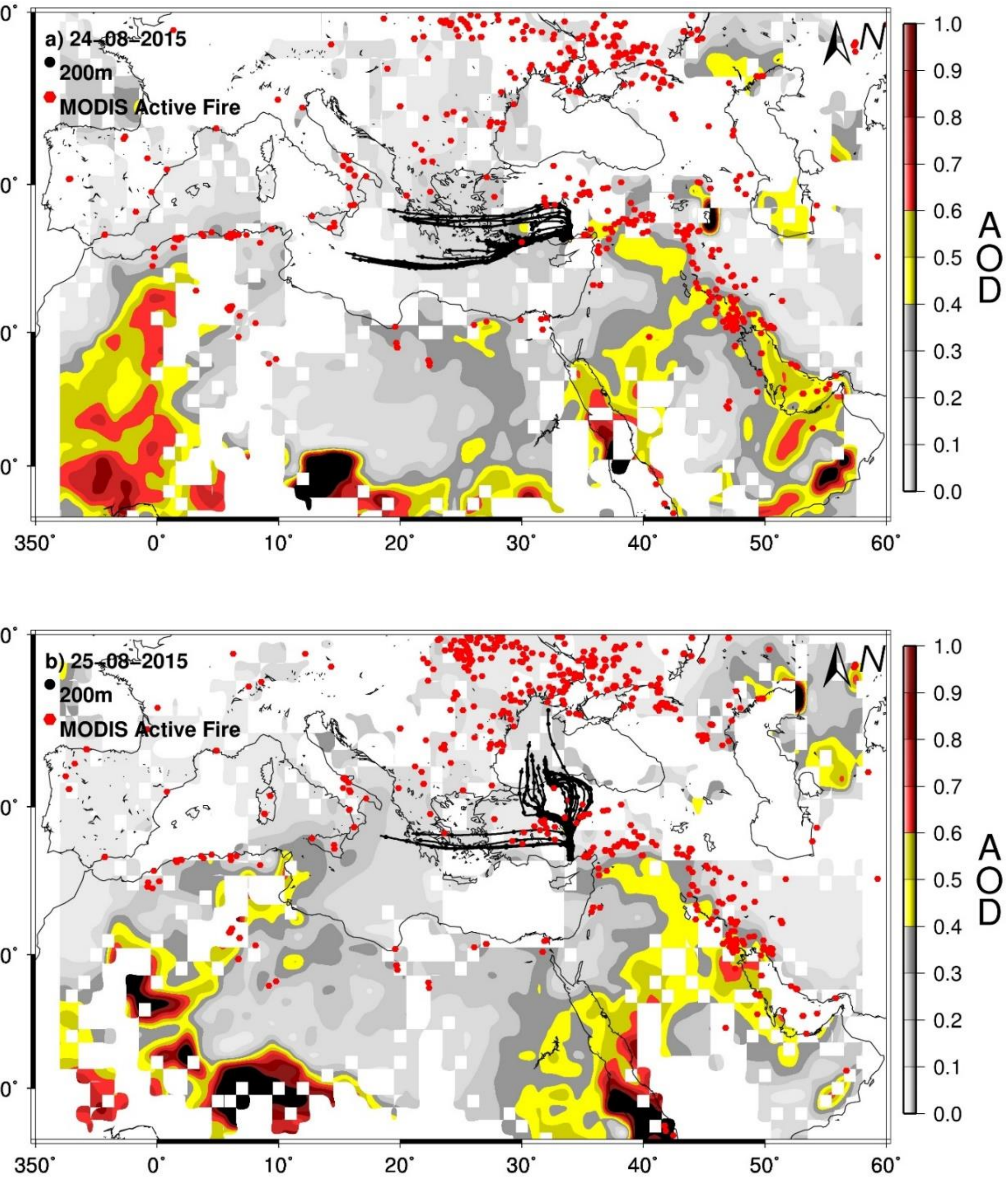

Figure 6.6 Two-day back trajectories demonstrating the transport of air masses to Erdemli for every hour at 200 m and MODIS aerosol optical depth and active fire spots on 24 August 2015 **(a)**, 25 August 2015 **(b)**, 26 August 2015 **(c)**, 27 August 2015 **(d)**.

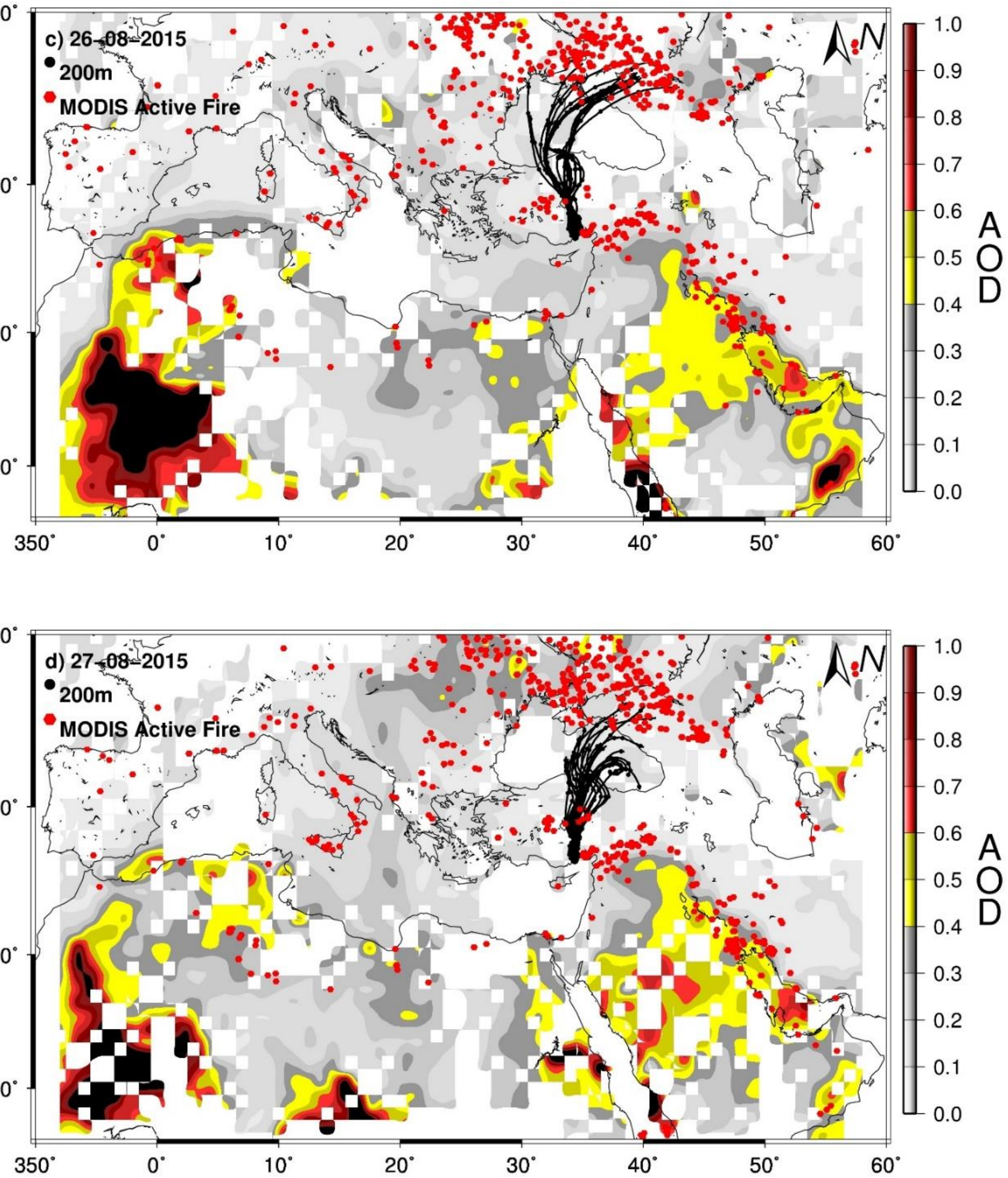

Figure 6.6. continue.

6.6 Correlation between Sulfate, Ammonium, Nitrate in $PM_{2.5}$ and their precursor gases

Correlation between variables shows the degree to which they vary together. The strong correlation coefficients between two species may be because of one or more of the following common processes: (a) similar sources (b) similar generation and/or removal mechanism and/or (c) similar transport patterns. The significance level of the correlation coefficient strictly depends on the number of the sample. As a result, populations with a high number of samples, even a small correlation coefficient can be statistically significant. Thus, five different terms will be used during the interpretation of correlation coefficients derived from the current datasets: (a) no correlation (r=0), (b) weak correlation (r=0-0.4), (c) moderate correlation (0.4-0.7) (d) strong correlation (0.7-1.0) and (d) perfect correlation (r=1.0). Correlation coefficients between variables are illustrated in Table 6.8 [(a) winter and (b) summer].

a) Winter: Ammonium showed strong correlation coefficients with sulfate and nitrate, being 0.90 and 0.71, respectively. At the coastal Eastern Mediterranean, it has been shown that the ammonium levels were enough to neutralize acidic sulfate and nitrate during the winter (Koçak *et al.*, 2007). As well as the documented thermal stability of the NH_4NO_3 increases with decreasing temperature or from hot dry summer towards cold winter (Bennett, D., 1972). In order to clarify the forms of ammonium in the winter multi linear regression analysis (MLR) was applied. Obtained results were statistically significant with $p < 0.00001$. Estimated ammonium concentrations from MRL against measured concentrations of ammonium are illustrated in Figure 6.7. The slope of the regression line was 1.00 with a correlation coefficient value of 0.96, implying acidic species sulfate and nitrate were completely neutralized by alkaline ammonium. Results from MRL also demonstrated that 60 % of the ammonium presented in the form of $(NH_4)_2SO_4$ whilst 40 % was in the form of NH_4NO_3 under the prevailing winter conditions (see Table 6.1). SO_4^{2-} (NO_3^-) and SO_2 (HNO_3) showed weak correlation coefficient with a value of 0.15 (0.36), implying that sulfate (nitrate) was primarily originated from non-local sources. HNO_3 illustrated strong correlations coefficients with sulfate and ammonium, being 0.70 and 0.74, respectively. It might be argued that these species either originated from same source or had similar transport pattern. Gaseous ammonia exhibited moderate correlation coefficients with aerosol ammonium (0.47) and sulfate (0.49). This relationship suggested that the secondary ammonium and sulfate formation was partially influenced by locally emitted ammonia. Moreover, ammonia and temperature denoted moderate correlation coefficient with a value of 0.47 and this might be attributed to (i) release of ammonium from leaf and vegetation surfaces, or (ii) evaporation of dew (Sutton *et al.*, 1993). Whereas ammonia showed moderate negative correlation coefficient with RH (-0.44) most likely due to enhanced formation of NH_4NO_3 under humid conditions (Chang *et al.*, 1986).

b) Summer: As expected, there was a strong correlation coefficient (0.84) between ammonium and sulfate in summer. The slope of the regression line was 0.82 when sulfate plotted against ammonium in neq m^{-3}. The value of 0.82 implies that ammonium levels were also enough to neutralize acidic sulfate in summer. These findings are contradict with the previous results documented for the same site (Koçak *et al.*, 2007). This discrepancy may chiefly ascribed to the enhancement of sulfate particles throughout the off-line sampling campaigns (for more details see section 6.1). Correspondingly, gaseous ammonia/sulfur dioxide and RH exhibited moderate negative and positive correlation coefficients with sulfate (-0.41 and 0.54) and ammonia (-0.41 and 0.50), suggesting influence of RH on gas to particle conversions of ammonium and sulfate during more humid conditions in summer. There was a moderate correlation coefficient between SO_2 and HNO_3 (0.44), denoting that these gaseous species somewhat originated from similar source or air-mass. Sulfate and ammonium respectively indicated strong (-0.77) and moderate (-0.55) negative correlation coefficient with sea surface pressure. Elevated levels of sulfate and ammonium under the unsettled weather conditions might be resulted from either middle or long range transport since these particles relatively longer lifetime in summer (Koçak *et al.*, 2007).

Table 6.8 Correlation coefficient matrix of water-soluble ions in $PM_{2.5}$ and precursor gases along with meteorological parameters at Erdemli in winter **(a)** and summer **(b)**.

a) winter	**SO_4^{2-}**	**NH_4^+**	**NO_3^-**	**SO_2**	**NH_3**	**HHO_3**	**T**	**RH**	**AP**
SO_4^{2-}	1.00								
NH_4^+	**0.90**	1.00							
NO_3^-	*0.44*	**0.70**	1.00						
SO_2	0.15	0.11	-0.10	1.00					
NH_3	*0.49*	*0.47*	0.28	0.27	1.00				
HNO_3	**0.70**	**0.74**	0.36	-0.02	0.19	1.00			
T	0.33	0.28	0.21	-0.18	*0.47*	0.30	1.00		
RH	-0.36	-0.22	-0.04	-0.17	*-0.44*	-0.15	**-0.73**	1.00	
AP	-0.37	-0.31	-0.02	*-0.42*	-0.38	-0.21	0.01	*0.44*	1.00

b) summer	**SO_4^{2-}**	**NH_4^+**	**NO_3^-**	**SO_2**	**NH_3**	**HHO_3**	**T**	**RH**	**AP**
SO_4^{2-}	1.00								
NH_4^+	**0.84**	1.00							
NO_3^-	-0.08	0.06	1.00						
SO_2	-0.24	-0.21	0.17	1.00					
NH_3	*-0.44*	*-0.41*	0.28	0.22	1.00				
HNO_3	0.09	0.12	0.24	*0.44*	0.14	1.00			
T	0.23	0.22	0.04	0.07	-0.13	0.01	1.00		
RH	*0.54*	*0.50*	-0.02	*-0.41*	-0.38	0.00	-0.34	1.00	
AP	**-0.77**	*-0.55*	0.30	0.32	0.36	0.03	0.01	*-0.46*	1.00

GPS: SO_4^{2-} / SO_4^{2-} + SO_2. GPN: NH_4^+ / NH_4^+ + NH_3. GPN: NO_3^-/ NO_3^- + HNO_3. T: Temperature. RH: Relative Humidity. AP: Atmospheric Pressure

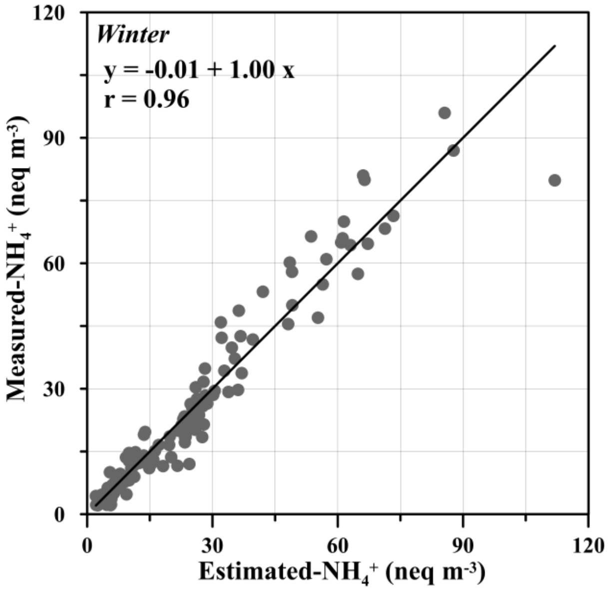

Figure 6.7 Comparison of measured and estimated hourly concentrations from MRL for NH_4^+ in winter.

6.7. Diurnal Variability

Typically, the concentrations of sulfate, ammonium, nitrate and their precursor gases demonstrate large diurnal variability (Gao *et al*., 2011; Shon *et al*., 2013; Hu *et al*., 2014; Makkonen *et al*., 2014; Markovic *et al*., 2014). Sort-term changes in the concentrations of aforementioned species and gas to particle conversions can be very complex and thus arises from a combination of multi factors: (a) meteorological parameters such as temperature, solar influx, relative humidity, rain, wind speed/direction, sea surface pressure, cloud cover and boundary layer height, (ii) chemical reactions, (iii) source strength, (iv) type of the source and (v) history of air masses (Kadowaki 198; Utsunomiya and Wakamatsu 1996; Khoder 2002; Hu *et al*., 2014).

The arithmetic mean diurnal variability of sulfate, ammonium, nitrate and their precursor gases as well as the gas to particle conversions for winter and summer are illustrated in Figure 6.8. Taking into account the diurnal variations for winter and summer, the following general observations may be made:

(a) Winter: SO_4^{2-} and SO_2 (see Figure 6.8a) concentrations did not show dramatic changes from 00.00 to 02.00, demonstrating low values around 5 and 16 nmol m^{-3}, respectively. These low concentrations may chiefly be attributed to removal of both species by wet deposition (see Figure 6.8f) despite of a shallow planetary boundary layer (~ 450 m, see Figure 6.8e). From 02.00 to 03.00 SO_4^{2-} and SO_2 concentrations respectively increased 60 and 40 % and reached the first peak at 04.00 with corresponding values of 10.1 and 37.5 nmol m^{-3}, when rain events ceased between 02.00 and 05.00. After this peak, there was a sharp decrease in the concentrations of SO_4^{2-} and SO_2 until 10.00, reaching correspondingly 4.2 and 14.8 nmol m^{-3}, because of sequential rain events that occurred between 05.00 and 08.00. From 10.00 to 12.00, SO_4^{2-} and SO_2 exhibited a significant increase, attaining their highest concentrations with values of 11.7 and 42.7 nmol m^{-3} when the airflow originated from highly populated City of Mersin. Both species then demonstrated gradual decline in their concentrations until 17.00 in the afternoon particularly under the influence of Easterly winds that may bring relatively less polluted air-masses originating from sea. SO_4^{2-} showed more or less constant concentrations after sunset (from 17.00 to 23.00) however, SO_2 concentrations increased from 10 nmol m^{-3} to 34 nmol m^{-3} between 17.00 and 23.00. The increment in SO_2 after sunset might be ascribed to (i) residential heating due to cold, (ii) decrease in PBL, (iii) change in airflow from Easterly (sea breeze) to Northerly (land breeze) and (iv) relatively a less efficient gas-to particle conversion.

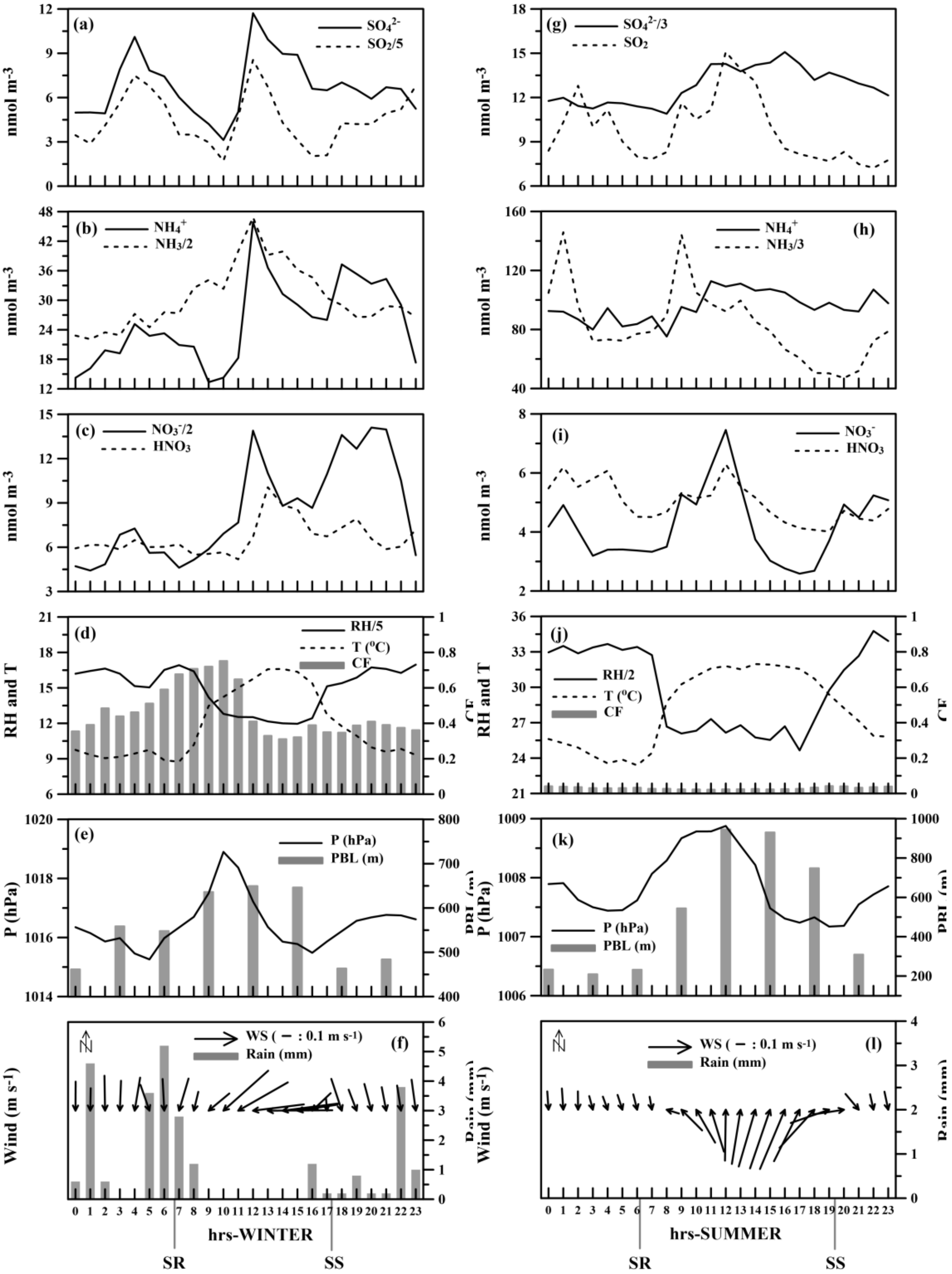

Figure 6.8 Diurnal variability of sulfate, ammonium and nitrate in $PM_{2.5}$ and their precursor gases and meteorological parameters in winter and summer.

Ammonia demonstrated slight enhancement between 00.00 and 07.00 (sun rise about at 06.45), reaching 55.1 nmol m^{-3} with a 20 % increase. From sun rise (07.00) to midday (12.00) there was a considerable raise in the concentration of ammonia, showing maximum at 12.00 with a value of 93.7 nmol m^{-3}. Ammonia concentration gradually decreased from 12.00 to 23.00, retaining to the night time concentrations, being around 50 nmol m^{-3}. As can be seen from Figures 6.8b and d, the diurnal trend of ammonia was coincident with the diurnal cycle of temperature and relative humidity. Correspondingly, the diurnal relationship of ammonia with temperature and RH were positive (r = 0.88) and negative (r = -0.83), suggesting release of ammonia from dew as well as emissions from vegetation under hot and dry conditions or elevated formation of particle ammonium when the temperature is high and the relative humidity is low. Figure 6.9a and b respectively exhibit relationship of ammonia with temperature and RH for hourly measurements obtained during day and night time. During the day time there was a significant correlation coefficient (r = 0.76) between ammonia concentration and temperature, however; this relationship was insignificant during night time. On the other hand, the correlation coefficients between ammonia concentration and relative humidity for day and night time (r= -0.56) and night (r = -0.45) were comparable, the former being slightly higher than that of later. Hence, since ammonia respectively showed strong positive and moderate negative correlation coefficients with temperature and humidity the day time increment might be ascribed to either evaporation of dew or emission from plant stoma whereas the night time decrease was more likely due to uptake of ammonia by plant and/or enhanced particle ammonium formation under low temperature (mean ~ 10 °C) and humid conditions.

Diurnal cycle of NH_4^+ was similar to that of observed for NO_3^-. Both species exhibited low concentrations from 00.00 to 10.00. Within two hours, NH_4^+ and NO_3^- concentrations steeply increased and reached their first maximum at 12.00 with values of 46 nmol m^{-3} and 28 nmol m^{-3}, respectively. Afterwards, their concentrations dropped about 40 % between 12.00 and 17.00, values respectively reaching down to 26.6 nmol m^{-3} and 17.3 nmol m^{-3} when the site was affected by comparatively clean Easterly (sea breeze) winds. NH_4^+ as well as NO_3^- correspondingly showed 40 % and 60 % rise in their concentrations peculiarly after sunset (17.00), illustrating the broader second peak compared to the first peak. The second peak appeared from 17.00 to 22.00 and might be connected with (i) decline in temperature and increase in RH, (ii) decrease in PBL and (iii) airflow from rather polluted air-masses originating from North. Next two hour, the concentrations of NH_4^+ and NO_3^- exhibited remarkable decrease, going down to 17.3 nmol m^{-3} and 10.7 nmol m^{-3} owing primarily to efficient removal of these particles from the atmospheric compartment by wet deposition.

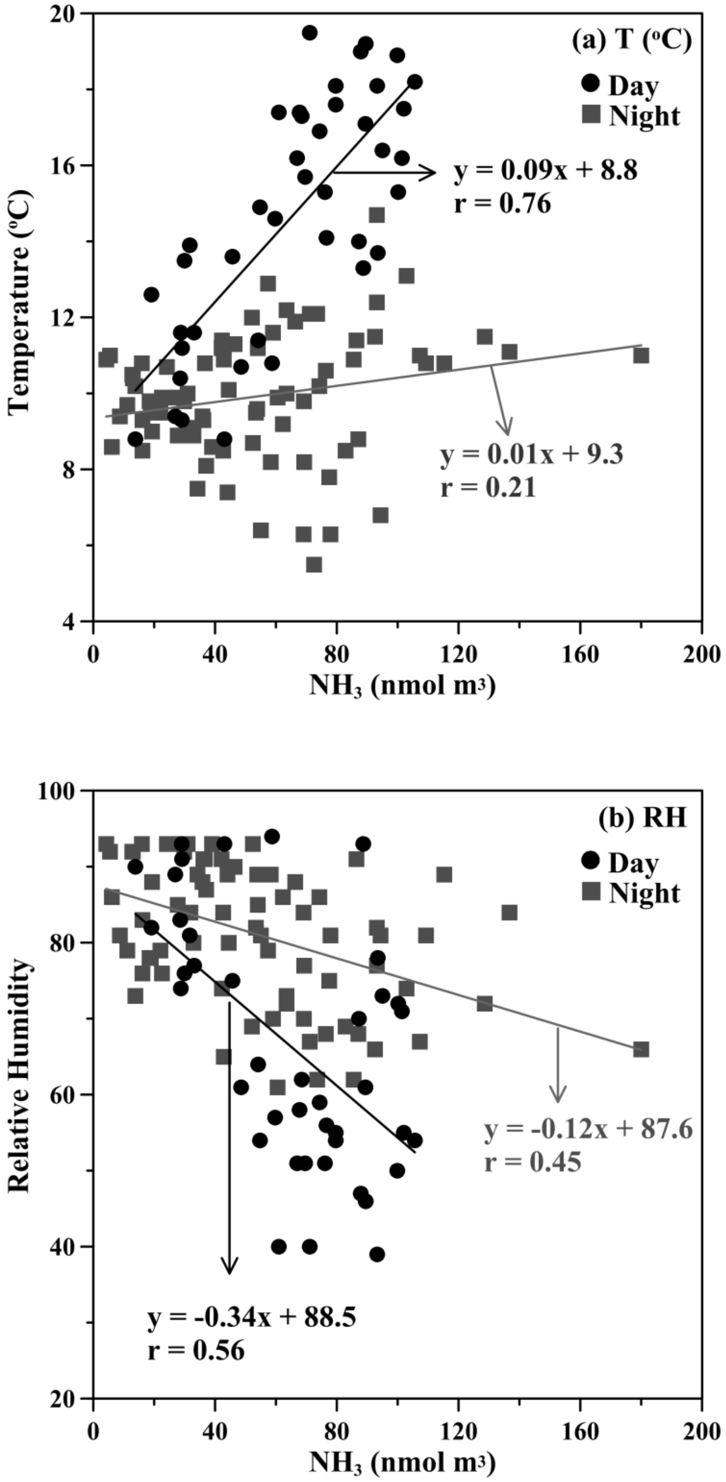

Figure 6.9 The relationship of NH_3 with temperature **(a)** and relative humidity **(b)** in winter.

(b) Summer: From 00.00 to 08.00, sulfate and ammonium (Fig. 6.8g, h) did not exhibit a considerable change in their concentrations, being around 33 and 85 nmol m^{-3}, respectively. These low and constant values may chiefly be attributed to lack of photochemical activities during night time and sluggish northerly airflow associated with low sulfate and ammonium concentrations (see section 6.8). Sulfate and ammonium concentrations increased about 30 % and 45 % respectively between 00.80 and 12.00, demonstrating a broad peak from 09.00 to 20.00 with (i) increasing temperature and planetary boundary layer, (ii) decreasing humidity and (iii) airflow from south (sea breeze). This might chiefly be attributed to enhanced gas to particle conversion in spite of increasing pbl. From 00.00 to 01.00 SO_2 concentration (Fig. 6.8h) augmented 25 % and reached the first peak at 02.00 with the value of 12.8 nmol m^{-3}. After this peak, there was a decreasing tendency in the concentrations of SO_2 until 07.00, reaching 7.8 nmol m^{-3}. From 07.00 to 12.00, SO_2 demonstrated remarkable increase, attaining its highest concentrations with the value of 15.1 nmol m^{-3}. These sharp two peaks might be ascribed to transport of air flow relatively polluted with SO_2 from north. Following that, SO_2 declined steadily until 19.00 in the afternoon, reaching 7.5 nmol m^{-3}. The decrement in SO_2 might be associated with (i) relatively high efficient gas to particle conversion and (ii) increase in PBL. SO_2 then showed more or less similar concentrations from 17.00 to 23.00. NH_3 (Fig 6.8h) concentration reached the first peak at 01.00 with the value of 437.7 nmol m^{-3}. After this peak, there was a 50 % decrease in the concentrations of NH_3 until 03.00, attaining 216.9 nmol m^{-3}. From 03.00 to 08.00, NH_3 did not exhibit a remarkable change in its concentration, being around 230 nmol m^{-3}. Then, NH_3 concentration increased sharply, reaching the second peak at 09.00 with the value of 433 nmol m^{-3}. After this peak, NH_3 continue to decrease from 10.00 to 20.00, reaching the lowest value of 141.4 nmol m^{-3}. This two maxima peaks in NH_3 resulted from biomass burning events that affected the site (for more details see section 6.8). On the other hand, decrease from 10.00 to 20.00 might be linked with i) relatively high efficient gas to particle conversion and (ii) increase in PBL. NO_3^- (Fig 6.8i) exhibited low concentration from 00.00 to 08.00. Afterwards, NO_3^- concentration increased steeply and attained its maximum at 12.00 with values of 7.5 nmol m^{-3}. Within two hours, its concentrations dropped about 50 % when the site was affected by sea breeze winds and again increased with the land breeze from 18.00 to 23.00. The sudden decrease of NO_3^- might be attributed to thermal decomposition of $NO3^-$ with increasing temperature ii) increase in PBL and iii) change in the air flow.

6.8 Influence of air flow on near real-time measurements of water-soluble ions in $PM_{2.5}$ and precursor gases.

To evaluate the impact of air flow on near real-time measurements of water-soluble ions in $PM_{2.5}$ and precursor gases, the classification of 2-day back trajectories for every hour during the sampling period was done. The Kruskal-Wallis (K-W) test was applied to check for the presence of significant differences in SO_4^{2-}, NH_4^+, NO_3^-, SO_2, NH_3, HNO_3 according to classified groups. The classification of 2-day back trajectories for winter didn't yield any statistically significant results. This could be caused by 5 rainy days out of total 8 sampling days in winter, implying local or nearly mesoscale transport rather than long range transport. Therefore, classification for winter was done according to local wind direction. Table 6.9 shows statistical summary of measured species for winter according to local wind direction sectors. On the other hand, Figure 6.11 and Table 6.10 illustrate obtained clusters from 2-day back trajectories at 200 m for every hour during the sampling period in summer and statistical summary of the measured species according to these clusters, respectively.

<u>Winter:</u> Four local wind direction sectors (NW: Northwest, N: North, NE: Northeast and E: East) has been found in winter. Mean concentrations of SO_4^{2-}, NH_4^+, NO_3^-, SO_2, NH_3, HNO_3 and meteorological parameters are given according to the defined four local wind direction sectors in Table 6.9 and 6.10, respectively. K-W test exhibited that SO_4^{2-} in NE, N and NW sectors were not statistically different. However, it demonstrated statistically significant difference for SO_4^{2-} between E sector and other three sectors, mean SO_4^{2-} concertation in E sector being approximately 40% higher than the remaining's (Table 6.9) and also the box-whiskers plot support this statement (Fig 6.10a). This relatively high SO_4^{2-} concertation in E sector may be attributed to plume of Mersin city center and industry areas located on the east of the sampling site and/or no rainfall event in E sector (see Table 6.10). Mean NH_4^+, NO_3^- and SO_2 concertations in sectors found to be similar, not showing a significant difference according to the K-W test. The box-whiskers plot of NH_3 shows that there existed statistically difference between E sector and NW, N and NE sectors (Fig. 6.10b). As expected, K-W test for NH_3 also exhibited significant difference between the aforementioned sectors. NH_3 for the E sector was at least 30 % larger than those calculated for the other 3 sectors. Additionally, high temperature and low humidity in E sector were observed compared to other sectors (see Table 6.10). This high mean value of NH_3 in E sector may result from reasons that were specified in the former section and/or no washout in E sector as well as aforementioned plume of city center and industry areas.

Table 6.9 Statistical summary of SO_4^{2-}, NH_4^+, NO_3^-, SO_2, NH_3, HNO_3 as well as gas to particle conversion ratios for clusters in winter

Winter	NW Mean±Std	N Mean±Std	NE Mean±Std	E Mean±Std
Number	33	46	31	14
SO_4^{2-}	6.4 ± 5.8	6.1 ± 4.2	6.4 ± 6.8	10.4 ± 6.5
NH_4^+	26.1 ± 22.5	22.7 ± 19.0	23.9 ± 21.6	35.9 ± 25.6
NO_3^-	17.0 ± 10.2	15.3 ± 13.2	19.2 ± 12.7	19.6 ± 10.4
SO_2	28.3 ± 31.2	21.4 ± 36.9	11.7 ± 12.2	30.0 ± 44.2
NH_3	51.7 ± 32.0	50.2 ± 32.9	63.1 ± 40.9	91.8 ± 30.7
HNO_3	6.8 ± 3.7	6.0 ± 2.8	6.5 ± 2.5	8.4 ± 5.2

Table 6.10 Statistical summary of meteorological parameters for sectors in winter.

Winter	NW Mean±Std	N Mean±Std	NE Mean±Std	E Mean±Std
Temperature (^oC)	10.5 ± 1.7	9.6 ± 1.8	12.9 ± 2.5	17.4 ± 1.5
Relative Humidity (%)	79.4 ± 9.7	81.3 ± 10.2	72.8 ± 14.8	55.3 ± 11.7
Number of Hourly Rain	12	5	5	-
Rain (mm)	22*	4*	3.2*	-

*denotes total amount of rain.

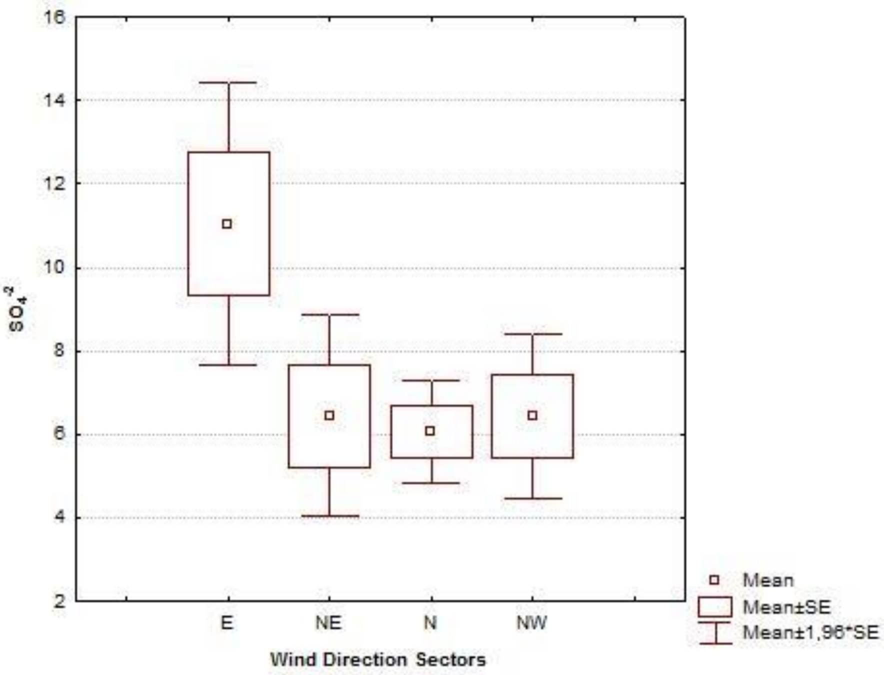

Figure 6.10 Bow-whisker plot of SO_4 **(a)** and NH_3 **(b)** in winter according to local wind direction sectors.

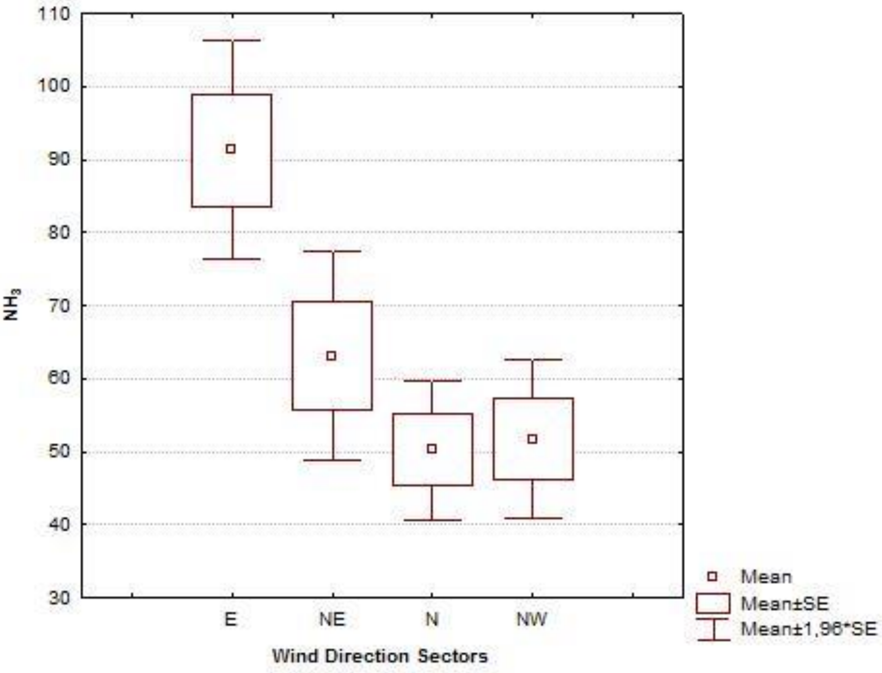

Figure 6.10 continue …

Summer: The results from cluster analysis for summer are illustrated in Fig. 6.11, together with the means of clusters and calculated occurrences for each cluster. Air flows were categorized into 5 groups. Starting from northwest, the first cluster (Northwest:NW) emerges from Greece; then, air flows pass through Aegean Sea and the west region of Turkey before arriving sampling site, explaining 3.2 % of trajectories. The second (North:N) reveal trajectories originating from north Turkey, clarifying 58.2 % of the trajectories. The third cluster (Soutwest-short:SWS) represents short trajectories originating from southwest Turkey; then following coastline of south Turkey before reaching the site, accounting 32.7 % of the trajectories. The fourth cluster (Mediterranean=MED) indicates air flows originated from middle Mediterranean Sea, explain 5.8 % of trajectories.

Mean concentrations of SO_4^{2-}, NH_4^+, NO_3^-, SO_2, NH_3, HNO_3 and meteorological parameters are presented as a function of air flow in Table 6.11 and 6.12, respectively. K-W test exhibited that SO_4^{2-} and NH_4^+ in SWS, MED and NW clusters were not statistically different. Nonetheless, it showed statistically significant difference for SO_4^{2-} and NH_4^+ between N cluster and other three sectors. This difference can be also seen from the box-whiskers plot (Fig 6.12a,b). Mean SO_4^{2-} (44.4 nmol m^{-3}) and NH_4^+ (106.9 nmol m^{-3}) concentration in cluster N were found to be respectively about 39 % and 27 % lower than those of remaining air flow (Table 6.11). Figure 6.13 presents SO_4 surface mass concertation for August 2015 from MERRA-2 which is an atmospheric reanalysis for the satellite era using the Goddard Earth Observing System Model. As can be deduced from Figure 6.13, air flow pathway of SWS, MED and NW clusters accompanied with the areas which had relatively a high concentration of SO_4. Similarly, Koçak *et al.* (2011) showed secondary aerosol transport from Eastern European countries into the atmosphere above the Aegean and Levantine Sea, enhancing in the concentration over İstanbul. K-W test also revealed a significant difference for NH_3 between N cluster and SWS, MED and NW clusters (see also Fig 6.12c for box-whiskers plot of NH_3). Figure 6.14a,b shows black carbon column mass density from MERRA-2 for 19 – 12 August 2015 and 25 August- 01 September 2015, respectively. 2-day air masses back trajectories between 25 August and 01 September 2015 in Fig. 6.13b represent N cluster whereas back trajectories between 19 - 12 August 2015 in Fig. 6.14a belong to clusters SWS, MED and NW clusters. As can been seen from figure, high amount of black carbon was observed at the area surrounding north Black Sea cost between 45˚N-50˚N and 25˚E-40˚E, which was associated with source region of air flow for the period between 25 August and 01 September 2015 and also an small area very close to the site had high BC concertation, implying a local source. The relationship between NH_3 and biomass burning discussed was in section 6.5. Therefore, this high amount of NH_3 in cluster N may mainly ascribed to the man/natural biomass burning.

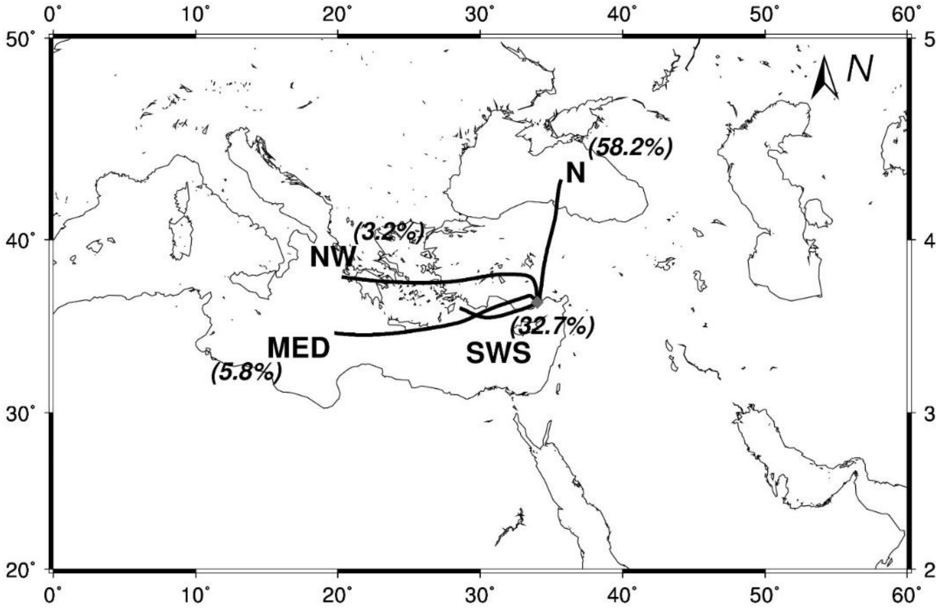

Figure 6.11 Average air mass back trajectory clusters for 200m level during the sampling period in summer. The percentages of each air flow presented in parenthesis.

Table 6.11 Statistical summary of SO_4^{2-}, NH_4^+, NO_3^-, SO_2, NH_3 and HNO_3 for clusters for clusters in summer.

b) Summer	MED Mean±Std	SWS Mean±Std	NW Mean±Std	N Mean±Std
Number	18	99	10	180
SO_4^{2-}	72.6 ± 9.7	61.7 ± 24.7	65.2 ± 3.7	44.4 ± 29.1
NH_4^+	145.8 ± 18.5	130.5 ± 52.4	141.4 ± 41.5	106.9 ± 54.2
NO_3^-	2.6 ± 0.8	3.9 ± 2.8	3.9 ± 3.8	4.1 ± 3.4
SO_2	6.1 ± 0.3	8.3 ± 3.4	10.7 ± 7.0	10.0 ± 10.0
NH_3	60.9 ± 7.4	72.9 ± 77.8	78.9 ± 17.9	222.3 ± 256.8
HNO_3	4.5 ± 0.2	5.2 ± 2.1	10.2 ± 6.4	4.9 ± 1.9

Table 6.12 Statistical summary of meteorological parameters for clusters in summer.

Summer	MED Mean±Std	SWS Mean±Std	NW Mean±Std	N Mean±Std
Temperature (ºC)	28.0 ± 2.3	29.2 ± 2.7	27.0 ± 1.4	27.7 ± 3.8
Relative Humidity (%)	72.4 ± 6.9	67.1 ± 9.3	72.1 ± 2.2	53.3 ± 13.6
Number of Hourly Rain	-	-	-	-
Rain (mm)	-*	-*	-*	-*

*denotes total amount of rain.

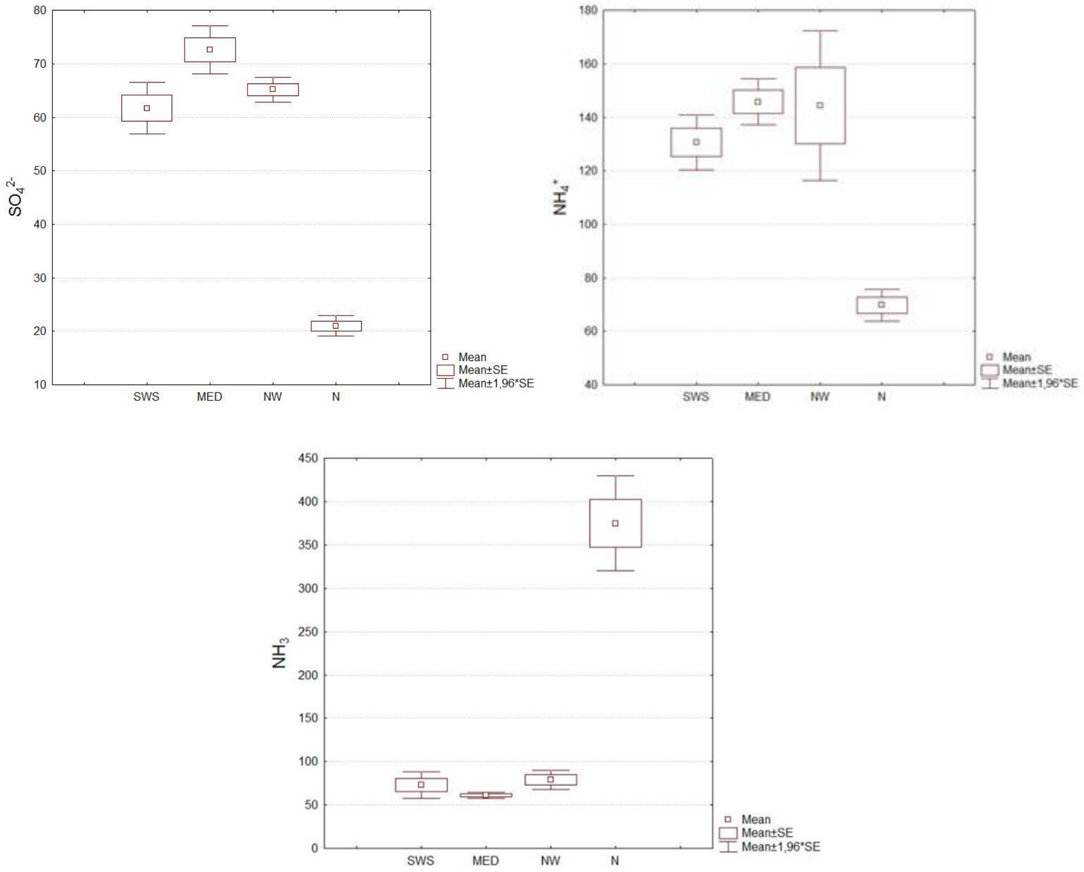

Figure 6.12 Bow-whisker plot of SO_4^{2-} **(a)**, NH_4^+ **(b)** and NH_3 **(c)** in summer according to clusters.

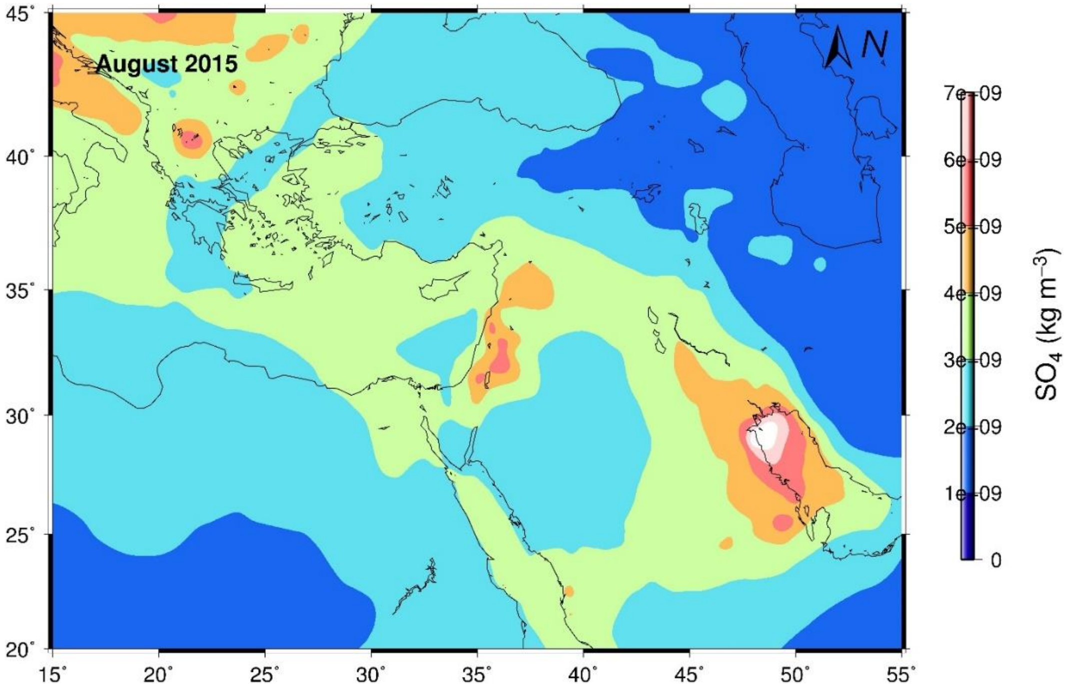

Figure 6.13 SO_4 surface mass concertation for August 2015 from MERRA-2 (atmospheric reanalysis for the satellite era using the Goddard Earth Observing System Model).

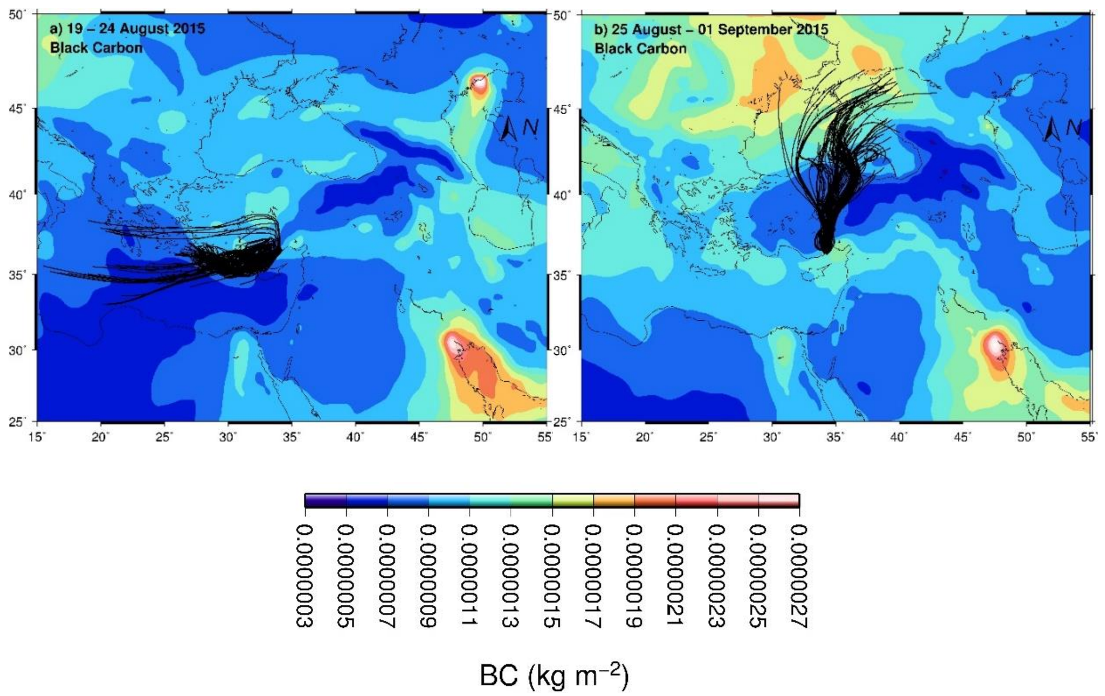

Figure 6.14 Black carbon column mass density for 19 – 12 August 2015 **(a)** and 25 August -01 September 2015 **(b)** from MERRA-2 (atmospheric reanalysis for the satellite era using the Goddard Earth Observing System Model).

CHAPTER VII

7. CONCLUSIONS

A detailed analysis of AERONET aerosol optical and microphysical properties for a fifteen year period (2000-2014) at the Eastern Mediterranean has been made in this study. Being a long term study for the Eastern Mediterranean makes this study unique. The results clearly exhibited the temporal dynamic in aerosol burden and types in the Eastern Mediterranean atmosphere. It has been shown that the site has been affected by both natural and anthropogenic aerosols (e.g. mineral dust, sulfate, nitrate and ammonium). Furthermore, the results of this study indicated that the location of Erdemli site is a characteristic place to monitor both anthropogenic particles from urban/industrial areas and mineral dust particles originated from North Africa and the Middle East deserts.

The degree of the relationship Aerosol Optical Thickness (AOT) with water vapor as a function of angstrom exponent revealed three aerosol groups, namely, non-hygroscopic, moderately hygroscopic and hygroscopic.

Imaginary part of the refractive index, single scattering albedo, absorption angstrom exponent for dust, mixed and pollution events showed distinct difference and also the spectral dependence of the I-REF and SSA exhibited distinct variation from one season to another.

Aerosol type were classified into three groups namely dust, mixed and anthropic according to extinction angstrom exponent. The comparison of the microphysical properties of the three aerosol type exhibited that categorization of the aerosol type based on extinction angstrom exponent was insufficient and this type of categorization should be avoided. The classification of aerosol type by applying cluster analysis to the optical properties exhibited relatively better results.

In addition, concentrations of SO_4^{2-}, NH_4^+, NO_3^- (in $PM_{2.5}$) and their precursor gases (SO_2, NH_3 and HNO_3) were measured with a near real-time Ambient Ion Monitor-Ion Chromatography instrument in winter and summer of 2015. Regarding arithmetic means of gas-to-particle conversion ratios for sulfate, ammonium and nitrate, it might be suggested that the concentrations of these species were mainly influenced by non-local sources. Taking into account this study and historic off-line measurements, there was a decreasing trend for sulfate, nitrate and their precursor gases in the Eastern Mediterranean.

The main results of this study can be summarized as follow:

- The arithmetic mean Aerosol Optical Thickness (AOT) decreased 2.5 times between 440 nm (0.30) and 1020 nm (0.12), demonstrating the dominance of fine particles. Angstrom Exponent (α = 1.22), particle size distribution (bi-modal distribution, majority being between 0.1 µm and 0.3 µm) and fine mode fraction (68 %) contribution also showed that the aerosol burden was chiefly associated with fine particles.
- The lowest AOT values was mainly found in winter during rain or just the day after rain since wet deposition removes aerosol particles from the atmospheric compartment efficiently. Enhanced AOT values at 440 nm was observed in spring with low $\alpha_{440-870}$ owing primarily to sporadic mineral dust intrusions originated from North Africa and the Middle East. High AOT at 440 nm and $\alpha_{440-870}$ were principally characterized in summer because of high gas-to particle conversion, sluggish air masses and absence of rain.
- Seasonal frequency distribution for AOT at 440 nm exhibited that summer was more turbid than those of the remaining seasons. 50 % of the $\alpha_{440-870} < 0.5$ in spring was found to be associated with AOT values higher than 0.4, indicating impact of dust transported from deserts located at North Africa and the Middle East. The seasonality of the aerosol optical and physical properties was remarkably modified by water vapor, temperature and rain events. AOT_{440} and AOT_{fine} showed statistically significant negative and positive correlation with rain and temperature, respectively. Consequently, low values of AOT_{440} and AOT_{fine} in winter was not only owing to the wet deposition but also due to the inferior gas to particle conversion. The relationship between AOT_{870}/AOT_{coarse} and rain was statistically not significant and this discrepancy might be attributed to the mechanical formation of coarse particles and/or their source strength namely: (i) enhanced sea salt production throughout rainy winter months because of more active and frequent storms and (ii) despite of remarkable rain amount, the mineral dust intrusions was mainly observed in spring when prevailing conditions were favorable such as Saharan cyclones.
- Results of air flow categorization for 1 km altitude exhibited that elevated AOT with relatively lower α (0.7) and fine mode fraction (47 %) were observed when the air masses originated from North Africa (SAH) and the Middle East

(MID). Mean AOT also showed slight decrease between 440 nm and 1020 nm for SAH and MID air flows, denoting importance of coarse mode particles, whereas, this decrease was 65 % for air flow from Mediterranean Sea, Eastern Europe, Western Europe and Turkey with comparatively higher α (> 1.1) and fine mode fraction (> 62 %).

- Potential source contribution function (PSCF) maps exhibited that non-hygroscopic particles were associated with mineral dust dominated aerosol population, originating from North Africa (Southern Tunisia, Western Libya, Libya/Chad border, southern Egypt northeastern Mauritania, north Mali, southern Algeria, and Northwestern Niger) and the Middle East (extending from Iraq to eastern Saudi Arabia). Moderately hygroscopic particles, on the other hand, were a mixture of mineral dust and anthropic aerosols due mainly to arrival of the dust after passing through industrialized and populated sites (such as Spain, France and Italy). PSCF maps did not show any particular potential source area for hygroscopic particles, exhibiting nearly mesoscale formation of secondary aerosols under the prevailing summer conditions.
- The imaginary part of refractive index for dust event ranged from 2.5×10^{-3} to 2.0×10^{-3} between 870 and 1020 nm and for wavelengths between 675 nm and 440 nm the imaginary part of refractive index increased from 4.3×10^{-3} to 11.0×10^{-3}. Although similar spectral behavior was observed, the imaginary part of the refractive index at 440 nm for mixed event was 2.2 times smaller than that of mineral dust event. For pollution event, the imaginary part of refractive index slightly increased from 5.0×10^{-3} at 440 nm to 6.3×10^{-3} at 1020 nm. SSA for dust and mixed events increased with increasing wavelength, however, the absorption character of the dust event was higher at 440 and 675 nm than that of mixed event. Smaller absorption and imaginary refractive index for mixed event might be attributed to ‘shield’ or encapsulate of iron oxides by secondary aerosol such as sulfate and nitrate.
- For spring season, the imaginary part of refractive index denoted decrease with increasing wavelength whereas, the imaginary part of refractive index was almost similar for all wavelengths during summer and fall. The imaginary part of refractive index for spring ranged from 4.4×10^{-3} to 3.8×10^{-3} between 675 and 1020 nm and for wavelengths smaller than 675 nm the imaginary part of

refractive index increased with decreasing wavelength, being 7.0 x 10^{-3} at 440 nm. This type of spectral dependence might be ascribed to the frequent occurrence of mineral dust episodes in the spring. SSA for spring exhibited increase with increasing wavelength, showing absorbance of iron oxides that associated with mineral dust near the blue wavelength. For summer and fall, however; SSA demonstrated reduction while wavelength increase, suggesting the dominance of man-made particles.

- The results from multivariate cluster analysis denoted five distinct groups: (i) Dust, (ii) Mixed, (iii) Black Carbon (BC), (iv) Black Carbon + Secondary Aerosols (BC + SEC) and (v) Secondary Aerosols (SEC). The classification for dust was found to be sufficient. The imaginary part of the refractive index decreased with increasing wavelength while single scattering increased with increasing wavelength from 440 nm to 1020 nm. SSA exhibited increase from 440 nm to 1020 nm. EAE and AAE scatter plot diagram also indicated a large variability, ranging between 0.07-0.9 and 1.2-2.4, respectively. PSD also supported the observed variability of EAE. Similar conclusion can be made for the mixed group as well. For BC group, it is clear that I-REF and SSA were not classified as expected since remarkable events exhibited decrease (increase) from 400 nm to 1020 nm for the imaginary part of the refractive index (single scattering albedo). These events might be ascribe to mixed events. On the other hand, the classification for secondary and secondary/black carbon groups seems sufficient because I-REF and SSA showed rather uniform spectral behavior between 440 nm 1020 nm.
- The Kruskal-Wallis (K-W) test showed that there was statistically significant quinquennial difference for aerosol microphysical properties. The aerosol absorption optical thickness at 440 nm, the imaginary part of the refractive index were larger for Period II (2005-2009) compared to Period I (2000-2004) and III (20010-2014) whilst extinction angstrom exponent and single scattering albedo was statistically smaller for Period II than those of Period I and III. This difference was attributed to the higher influence of dust intrusion from desert areas during Period II.
- Of the water-soluble ions in $PM_{2.5}$, sulfate and ammonium were the dominant species. Arithmetic mean sulfate and ammonium concentrations were

respectively 2814 ng m^{-3} and 1371 μg m^{-3}. Aerosol nitrate arithmetic mean was 495 ng m^{-3}. Among the precursor gases, ammonia exhibited the highest concentration with a value of 3330 ng m^{-3}. Sulfur dioxide and nitric acid concentrations were 879 ng m^{-3} and 346 ng m^{-3}, respectively. Taking into account precursor gases concentrations, it is clear that alkaline ammonia (g) concentration was more than enough to neutralize acidic gases. The arithmetic mean of gas-to-particle ratios for sulfate, ammonium and nitrate were respectively found to be 0.69 ± 0.25, 0.38 ± 0.24 and 0.49 ± 0.17.

- Nitrate, sulfur dioxide and nitric acid were respectively found to show 3.3, 4.6 and 5.3 times decrease compared to results reported by Kouvarakis *et al.* (2001, 2002). The decrease for sulfate was 1.4 relative to Finokalia, however, sulfate concentration was 4.4 times less than that of Jerusalem. Ammonium and ammonia concentrations at Erdemli were larger than those for Finokalia because the Erdemli site is surrounded by agricultural area.
- The increment in SO_2 after sunset during winter might be ascribed to (i) residential heating due to cold, (ii) decrease in PBL, (iii) change in airflow from Easterly (sea breeze) to Northerly (land breeze) and (iv) relatively less efficient gas-to particle conversion. In winter, the diurnal relationship of ammonia with temperature and RH were positive ($r = 0.88$) and negative ($r = -0.83$), suggesting release of ammonia from dew and emission from the vegetation under hot and dry conditions or elevated formation of particle ammonium when temperature low and relative humidity high. The classification of 2-day back trajectories for winter didn't yield any statistically significant results. This could be caused by 5 rainy days out of total 8 sampling days in winter, implying local or nearly mesoscale transport rather than long range transport.
- Direct and indirect aerosol forcing tightly depend on geographical distribution, optical properties and types of the aerosols in relation to history of air-masses, aging process, external/internal mixing, interaction with gaseous species, gas-to-particle conversion and removal either by wet or dry deposition The characterization of aerosol properties namely (i) particle size distribution, (ii) hygroscopic nature (iii) scattering (single scattering albedo) and absorption (absorption aerosol optical thickness) and (iv) chemical composition and

mixing state (absorption angstrom exponent, refractive index) is vital to figure out the impact of atmospheric particles on the Earth's radiation budget. In order to enhance information about microphysical properties of aerosol burden over the Eastern Mediterranean, the field samples would be simultaneously obtained and analyzed for refractive index, single scattering albedo, mineralogical and chemical composition with the measurements of Lidar, particle size counter, multi-spectrometer black carbon analyzer. After integrating these scientific knowledge obtained from these measurements, the radiative transfer model would be used to assess direct aerosol radiative forcing with a high accuracy.

REFERENCE

Appel, B. R., Tokiwa, Y., Haik, M. and Kothny, E. L., 1984. Artifact particulate sulfate and nitrate formation on filter media. Atmos. Environ., 18, 409.

Appel, B.R., Tokiwa, Y., 1981. Atmospheric particulate nitrate sampling errors due to reactions with particulate and gaseous strong acids. Atmos. Environ., 15 (6), 1087–1089.

Appel, R., Tokiwa, Y. and Haik, M., 1980. Sampling of nitrates in ambient air. Atmos. Environ., 15, 283-289.

Arimoto, R., 2001. Eolian dust and climate: relationships to sources, tropospheric chemistry, transport and deposition, Earth-Science Reviews, 54, 29–42.

Baker, A.R., Kelly, S.D., Biswas, K.F., Witt, M. and Jickells T.D., 2003. Atmospheric deposition of nutrients to the Atlantic Ocean. Geophysical Research Letters, 30, 24, doi:10.1029/2003GL018518.

Bardouki, H., Liakakou, H., Economou, C., Sciare, J., Smolik, J., Zdimal, V., Eleftheriadis, K., Lazaridis, M., Dye, C., Mihalopoulos, N., 2003. Chemical composition of size resolved atmospheric aerosols in the eastern Mediterranean during summer and winter. Atmos. Environ., 37,195–208.

Barnaba, F., Gobbi, G.P., 2004. Aerosol seasonal variability over the Mediterranean region and relative impact of maritime, continental and Saharan dust particles over the basin from MODIS data in the year 2001. Atmos. Chem. Phys., 4, 2367e2391.

Behera, S.N., Sharma, M., 2010. Investigating the potential role of ammonia in ion chemistry of fine particulate matter formation for an urban environment. Sci. Total Environ. 408, 3569–3575.

Behera, S.N, Betha S., and Balasubramanian, R., 2013. Insights into chemical coupling among acidic gases, ammonia and secondary inorganic aerosols. Aerosol Air Qual. Res. 13: 1282–1296.

Bennett, D., 1972. A study of the thermal decomposition of ammonium nitrate using a gas chromatographic technique. J. Appl. Chem., 22, 973-982.

Bergametti, G., Dutot, A.L., Buat-Menard, P., Losno, R., and Remoudaki, E., 1989. Seasonal variability of the elemental composition of atmospheric aerosol particles over the northwestern Mediterranean, Tellus, 41B, 353-361.

Bergametti, G., Gomes, L., Remoudaki, E., Desbois, M., Martin, D. and co-authors. 1989. Present transport and deposition patterns of African dusts to the north–western Mediterranean. In: Palaeoclimatology and Palaeometeorology: Modern and Past Patterns of Global Atmospheric Transport. 282, (eds. M. Leinen and M. Sarntheim). NATO ASI Series, C, Kluwer Academic Publishers B.V., Dordrecht, The Netherlands, 227–252.

Blanchard, D.C. and Cipriano, R.J., 1983. Sea spray production from bubbles. Science, 220, 1410.

Bond, T. and Bergstrom, R., 2006. Light absorption by carbonaceous particles: An investigative review, Aerosol Sci. Tech., 40, 27–67.

Bouwman, A. F. et al., 1997. A global high-resolution emission inventory for ammonia. Global Biogeochem. Cy. 11, 561–587.

Brankov, E., Rao, S.T. and Porter, P. S., 1998. A trajectory-clustering-correlation methodology for examining the long-range transport of air pollutants. Atmos. Environ., 32, 1525-1534.

Cabada, J.C., Rees, S., Takahama, S., Khlystov, A., Pandis, S.N., Davidson, C.I., and Robinson, A.L., 2004. Mass size distributions and size resolved chemical composition of fine particulate matter at the Pittsburgh supersite. Atmos. Environ., 38(20), 3127–3141, doi:10.1016/j.atmosenv.2004.03.004.

Cadle, S. H. and Dasch, J. M., 1988. Wintertime concentrations and sinks of atmospheric particulate carbon at a rural location in northern Michigan, 1988. Atmos. Environ., 22, 1373–1381.

Charlson, R. J., Schwartz, S. E., Hales, J. M., Cess, R. D., Coakley Jr., J. A., Hansen, J. E., et al., 1992. Climate forcing by anthropogenic aerosol. Science, 255, 423−430.

Chen, Y., Mills, S., Street, J., Golan, D., Post, A., Jacobson, M., Paytan, A., 2007. Estimates of atmospheric dry deposition and associated input of nutrients to Gulf of Aqaba seawater. Journal of Geophysical Research, 112, D04309, doi:10.1029/2006JD00785.

Cheng, Y., Duan, F. K., He, K. B., Du, Z. Y., Zheng, M., and Ma, Y. L., 2012. Intercomparison of thermal-optical method with different temperature protocols: implications from source samples and solvent extraction, Atmos. Environ., 61, 453–462.

Chow, J.C., Doraiswamy, P., Waston, J.G., Chen, L.A., Ho, S.S.H., and Sodeman, D.A., 2008. Advances in integrated and continuous measurements for particle mass and chemical composition, J. Air Waste Manage., 58, 141–163.

Crutzen, P.J., and Andreae, M.O., 1990. Biomass burning in the Tropics: Impact on Atmospheric Chemistry and Biogeochemical Cycles, Science, 250, 1669-1678, doi:10.1126/science.250.4988.1669.

Danalatos, D., and Glavas, S., 1999. Gas phase nitric acid, ammonia and related particulate matter at a Mediterranean coastal site, Patras, Greece. Atmos. Environ., 33, 20, 3417-3425.

Dayan, U., 1986. Climatology of back trajectories from Israel based on synoptic analysis. Journal of Applied Meteorology, 25, 591-595.

Dayan, U., Heffter, J., Miller, J., Gutman, G., 1991. Dust intrusion events into the Mediterranean basin, J. Appl. Meteorol., 30, 1185– 1199.

Dayan, U., Ricaud, P., Zbinden, R., and Dulac, F., 2017. Atmospheric pollution concentrations over the Eastern Mediterranean during summer – A review, Atmos. Chem. Phys. Discuss., doi:10.5194/acp-2017-79.

Dentener, F.J., Carmichael, G.R., Zhang, Y., Lelieveld, J., Crutzen, P.J., 1996. Role of mineral aerosol as a reactive surface in the global troposphere. Journal of Geophysical Research, 101, 22869-22889.

Dobbie, S., Li, J., Harvey, R. and Chylek, P., 2003. Sea-salt optical properties and GCM forcing at solar wavelengths. Atmospheric Research, 65, 211– 233.

Dorling, S.R., Davies, T.D. and Pierce, C.E., 1992. Cluster analysis: A technique for estimating the synoptic meteorological controls on air and precipitation chemistry-Method and applications. Atmos. Environ., 26A, 2575-2581.

Draxler, R.R., 1999. HYSPLIT4 user's guide. NOAA Tech. Memo. ERL ARL-230, NOAA Air Resources Laboratory, Silver Spring, MD.

Drewnick, F., Schwab, J.J., Hogrefe, O., Peters, S., Husain, L., Diamond, D., Weber, R., Demerjian, K.L., 2003. Intercomparison and evaluation of four semi-continuous $PM_{2.5}$ sulfate instruments. Atmos. Environ., 37, 3335e3350.

Du, H.H., Kong L.D., Cheng T., et al., 2010. Insights into ammonium particle-to-gas conversion: Non-sulfate ammonium coupling with nitrate and chloride. Aerosol Air Qual Res, 10, 589–595.

Du, H.H., Kong, L.D., Cheng, T.T., Chen, J.M., Du, J.F., Li, L., Xia, X.G., Leng, C.P., Huang, G.H., 2011. Insights into summertime haze pollution events over Shanghai based on online water-soluble ionic composition of aerosols. Atmos. Environ., 45, 5131e5137.

Dubovik, O. and King, M.D., 2000. A flexible inversion algorithm for retrieval of aerosol optical properties from Sun and sky radiance measurements. J. Geophys. Res., 105, 20673-20 696.

Dubovik, O., A. Sinyuk, T. Lapyonok, B. N. Holben, M. Mishchenko, P. Yang, T. F. Eck, H. Volten, O. Munoz, B. Veihelmann, W. J. van der Zande, J-F Leon, M. Sorokin, and I. Slutsker, 2006. Application of spheroid models to account for aerosol particle nonsphericity in remonte sensing of desert dust. J. Geophys. Res., 111, doi:10.1029/2005JD006619.

Dubovik, O., A. Smirnov, B.N. Holben, M.D. King, Y.J. Kaufman, T.F. Eck, and I. Slutsker, 2000. Accuracy assessments of aerosol optical properties retrieved from AERONET sun and sky-radiance measurements, J. Geophys. Res., 105, 9791-9806.

Dubovik, O., B. Holben, T.F. Eck, A. Smirnov, Y.J. Kaufman, M.D. King, D. Tanre, and I. Slutsker, 2002. Variability of absorption and optical properties of key aerosol types observed in worldwide locations, J. Atmos. Sci., 59, 590–608.

Duce R.A., 1995. Sources, distributions, and fluxes of mineral aerosols and their relationship to climate. In: Charlson RJ, Heintzenberg J (eds) Dahlem Workshop on Aerosol Forcing of Climate. John Wiley, Chichester, pp 43–72.

Dulac, F., Buat-Menard, P., Arnold, M., Ezat, U. and Martin, D., 1987. Atmospheric input of trace metals to the western Mediterranean sea: Factors controlling the variability of atmospheric concentrations. Journal of Geophysical Research, 92, 8437-8453.

Dusek, U., Frank, G. P., Gwaze, P., Iinuma, Y., Zeromskiene, K., Henning, T., Massling, A., Andreae, M. O., Hermann, H., Wiedensohler, A., and Helas, G., 2005. ‘Missing’ cloud condensation nuclei in peat smoke, Geophys. Res. Lett., 32, L11802, doi:10.1029/2005GL022473.

Eck, T.F., B.N. Holben, J.S. Reid, N.T. O’Neill, J.S. Schafer, O. Dubovik, A. Smirnov, M.A. Yamasoe, and P. Artaxo, 2003. High aerosol optical depth biomass burning events: A comparison of optical properties for different source regions, Geophys. Res. Lett., 30(20), 2035, doi:10.1029/2003GL017861.

Eck, T.F., et al. 2008. Spatial and temporal variability of column-integrated aerosol optical properties in the southern Arabian Gulf and United Arab Emirates in summer, J. Geophys. Res., 113, D01204, doi:10.1029/2007JD008944.

Eck, T. F., et al. 2010. Climatological aspects of the optical properties of fine/coarse mode aerosol mixtures, J. Geophys. Res., 115, D19205, doi:10.1029/2010JD014002.

Eck, T.F., B.N.Holben, J.S.Reid, O.Dubovik, A.Smirnov, N.T.O'Neill, I.Slutsker, and S.Kinne, 1999. Wavelength dependence of the optical depth of biomass burning, urban and desert dust aerosols, J. Geophys. Res., 104, 31 333-31 350.

Falkovich, A.H., Schkolnik, G., Ganor, E., Rudich, Y., 2004. Adsorption of organic compounds to urban environment onto mineral dust particles. Journal of Geophysical Research, 109, D02208, doi 10.1029/2003JD003919.

Fine, P.M., Sioutas, C., and Solomon, P.A., 2008. Secondary particulate matter in the United States: Insights from the particulate matter supersites program and related studies, J. Air Waste Manage., 58(2), 234–253, 2008.

Finlayson-Pitts, B.J. and Pitts, J.N, 1999. Chemistry of the upper and lower atmosphere, Academic Press, New York, 1nd Edn.

Fotiadi, A., Hatzianastassiou, N., Drakakis, E., Matsoukas, C., Pavlakis, K.G et al.. 2006. Aerosol physical and optical properties in the Eastern Mediterranean Basin, Crete, from Aerosol Robotic Network data. Atmospheric Chemistry and Physics, European Geosciences Union, 6 (12), pp.5399-5413.

Gama, C., Tchepel, O., Baldasano, J.M., Basart, S., Ferreira, J., Pio, C., Cardoso, J., Borrego, C., 2015. Seasonal patterns of Saharan dust over Cape Verde – a combined approach using observations and modelling. Tellus B: Chemical and Physical Meteorology, 67:1, 24410, DOI: 10.3402/tellusb.v67.24410.

Gao, J., Peng, X., Chen, G., Xu, J., Shi, G., Zhang, Y., Feng, Y., 2016. Insights into the chemical characterization and sources of $PM_{2.5}$ in Beijing at a 1-h time resolution. Sci. Total Environ., 542, 162-171, doi:10.1016/j.scitotenv.2015.10.082.

Gao, X., Yang, L., Cheng, S., Gao, R., Zhou, Y., Xue, L., Shou, Y., Wang, J., Wang, X., Nie, W., Pengju, X. and Wang, W., 2011. Semi-continuous Measurement of Water-soluble Ions in $PM_{2.5}$ in Jinan, China: Temporal Variations and Source Apportionments. Atmos. Environ., 45, 6048–6056.

Gerasopoulos, E., Andreae, M., Zerefos, S.C., Andreae W.T, Balis, D., Formenti, P., Merlet, P., Amiridis, V., Papastefanou, C., 2003. Climatological aspects of aerosol optical properties in Northern Greece. Atmos. Chem. Phys., 3, doi:10.5194/acpd-3-2059-2003.

Gherboudj, I., Beegum, N., Ghedira, H., 2016. Identifying natural dust source regions over the Middle-East and North-Africa: Estimation of dust emission potential. Earth-Science Reviews. 165, 342-355.

Giles, D.M., et al., 2011. Aerosol properties over the Indo-Gangetic Plain: A mesoscale perspective from the TIGERZ experiment. J. Geophys. Res., 116, D18203, doi:10.1029/2011JD015809.

Giles, D.M., Holben, B.N., Eck, T.F., Sinyuk, A., Smirnov, A., Slutsker, I., Dickerson, R.R., Thompson, A.M. and Schafer, J.S., 2012. An Analysis of AERONET Aerosol Absorption Properties and Classifications Representative of Aerosol Source Regions. J. Geophys. Res., 117, D17203.

Gilio, A., de gennaro, G., Dambruoso, P., Ventrella, G., 2015. An integrated approach using high time-resolved tools to study the origin of aerosols. Sci. Total Environ., 530-531C, 28-37. doi:10.1016/j.scitotenv.2015.04.073.

Ginoux, P., Prospero, J.M., Gill, T.E., Hsu, N.C., Zhao, M., 2012. Global scale attribution of anthropogenic and natural dust sources and their emission rates based on MODIS deep blue aerosol products. Rev. Geophys. 50, 3005.

Gobbi, G.P., Barnaba, F., Giorgi, R. and Santacasa, A., 2000. Altituderesolved properties of a Saharan dust event over the Mediterranean. Atmos. Environ., 34, 5119–5127.

Godri, K.J., Evans, G.J., Slowik, J., Knox, A., Abbatt, J., Brook, J., Dann, T., and Dabek-Zlotorzynska, E., 2009. Evaluation and application of a semi-continuous chemical characterization system for water soluble inorganic $PM_{2.5}$ and associated precursor gases. Atmos. Meas. Tech., 2, 65–80, doi:10.5194/amt-2-65-2009.

Güllü, G.H., Ölmez, I., Aygün, S. and Tuncel, G., 1998. Atmospheric trace element concentrations over the Eastern Mediterranean Sea: Factors affecting temporal variability. Journal of Geophysical Research, 103, D17, 21943-21954.

Hansen, J.M., Sato, M., Ruedy, R., Lacis, A., Oinas, V., 2000. Global warming in the twenty-first century: An alternative scenario. Proceedings of the National Academy of Sciences of the United States of America, 97, 9875−9880.

Hamonou, E.P., Chazette, P., Balis, D., Dulac, F., Schneider, X. and coauthors. 1999. Characterization of the vertical structure of Saharan dust export to the Mediterranean basin. J. Geophys. Res. 104, D18, doi:10.1029/1999JD900257.

Haywood, J.M. and Shine, K.P., 1997. Multi-spectral calculations of the radiative forcing of tropospheric sulphate and soot aerosols using a column model. Quart. J. Roy. Meteor. Soc., 123, 1907–1930.

Hegg, D.A., Radke, L.F., Hobbs, P.V., and Riggan, P.J., 1988. Ammonia emissions from biomass burning. Geophys. Res. Lett., 335-337.

Heintzenberg, J. 2009. The SAMUM–1 experiment over Southern Morocco: overview and introduction. Tellus, 61B, 2–11.

Hering S. and Cass G., 1999. The Magnitude of Bias in the Measurement of PM25 Arising from Volatilization of Particulate Nitrate from Teflon Filters, Journal of the Air & Waste Management Association, 49,6, 725-733, DOI: 10.1080/10473289.1999.10463843.

Herut, B., Krom, M.D., Pan, G. and Mortimer, R., 1999. Atmospheric input of nitrogen and phosphorus to the Southeast Mediterranean: sources, fluxes, and possible impact. Limnology and Oceanography, 44, 1683–1692.

Herut, B., Zohary, T., Krom, M.D., Mantoura, R. F. C., Pitta, P., Psarra, S., Rassoulzadegan, F., Tanaka, T. and Thingstad, T. F., 2005. Response of East Mediterranean surface water to Saharan dust: On-board microcosm experiment and field observations. Deep-Sea Research II, 52, 3024–3040.

Hess, M., P. Koepke, and Schult I., 1998. Optical properties of aerosols and clouds: The software package OPAC. Bull. Am. Meteorol. Soc., 79, 831-844.

Holben B.N., Eck, T.F, Slutsker, I., Tanre, D., Buis, J.P., Setzer, A., Vermote, E., Reagan, J.A., Kaufman, Y., Nakajima, T., Lavenu, F., Jankowiak, I., and Smirnov, A., 1998. AERONET - A federated instrument network and data archive for aerosol characterization.Rem. Sens. Environ., 66, 1-16.

Holben, B.N., T.F. Eck, I. Slutsker, A. Smirnov, A Sinyuk, J. Schafer, D. Giles, O. Dubovik, 2006. Aeronet's Version 2.0 quality assurance criteria. Proc. SPIE 6408, Remote Sensing of the Atmosphere and Clouds, 64080Q, doi:10.1117/12.706524.

Holben, B.N., D.Tanre, A.Smirnov, T.F.Eck, I.Slutsker, N.Abuhassan, W.W.Newcomb, J.Schafer, B.Chatenet, F.Lavenue, Y.J.Kaufman, J.Vande Castle, A.Setzer, B.Markham, D.Clark, R.Frouin, R.Halthore, A.Karnieli, N.T.O'Neill, C.Pietras, R.T.Pinker, K.Voss, and G.Zibordi, 2001. An emerging ground-based aerosol climatology: Aerosol Optical Depth from AERONET. J. Geophys. Res., 106, 12 067-12 097.

Hu, G., Zhang, Y., Sun, J., Zhang, L., Shen, X., Lin, W., Yang, Y., 2014. Variability, formation and acidity of water-soluble ions in $PM_{2.5}$ in Beijing based on the semi-continuous observations. Atmospheric Research, 145–146, 1–11, doi:10.1016/j.atmosres.2014.03.014.

Huang, J., Lin, B., Minnis, P., Wang, T., Wang, X., Hu, Y., Yi, Y., and Ayers, J. K., 2006. Satellite-based assessment of possible dust aerosols semidirect effect on cloud water path over East Asia, Geophys. Res. Lett., 33, L19802, doi:10.1029/2006GL026561, 2006.

IPCC, 2013: Climate Change, 2013. The Physical Science Basis. Contribution of Working Group I to the Fifth Assessment Report of the Intergovernmental Panel on Climate Change [Stocker, T.F., D. Qin, G.-K. Plattner, M. Tignor, S.K. Allen, J. Boschung, A. Nauels, Y. Xia, V. Bex and P.M. Midgley (eds.)]. Cambridge University Press, Cambridge, United Kingdom and New York, NY, USA, 1535 pp, doi:10.1017/CBO9781107415324.

Jacobson, M. Z. 2000. A physically-based treatment of elemental carbon optics: Implications for global direct forcing of aerosols. Geophysical Research Letters, 27, 217–220.

Kahn, R., Banerjee, P., McDonald, D., 2001. Sensitivity of multiangle imaging to natural mixtures of aerosols over ocean. J. Geophys. Res. 106, 18219e18238.

Kandler, K., Schütz, L., Deutscher, C., Ebert, M., Hofmann, H. and co-authors. 2009. Size distributions, mass concentration, chemical and mineralogical composition and derived optical parameters of the boundary layer aerosol at Tinfou, Morocco, during SAMUM 2006. Tellus, 61B, 32–50.

Kandler, K., Schütz, L., Jackel, S., Lieke, K., Emmel, C. and co-authors. 2011. Ground-based off-line aerosol measurements at Praia, Cape Verde, during the Saharan Mineral Dust Experiment: microphysical properties and mineralogy. Tellus, 63B, 4.

Kaufman, Y.J., Tanre, D., Dubovik, O., Karnieli, A., and Remer, L.A., 2001. Absorption of sunlight by dust as inferred from satellite and ground-based measurements. Geophys. Res. Lett., 28, 1479 – 1482, 2001.

Kaufman, Y., Gitelson, A., Karnieli, A., Ganor, E., Fraser, R., Nakajima, T., Mattoo, S., and Holben, B.N., 1994. Size distribution and scattering phase function of aerosol particles retrieved from sky brightness measurements. J. Geophys. Res., 99 (D5), 10,341-356.

Keck, L., and Wittmaack, K., 2005. Effect of filter type and temperature on volatilisation losses from ammonium salts in aerosol matter. Atmos. Environ., 39, 4093-4100. 10.1016/j.atmosenv.2005.03.029.

Khatri, P., T. Takamura, A. Shimizu, and N. Sugimoto, 2014. Observation of low single scattering albedo of aerosols in the downwind of the East Asian desert and urban areas during the inflow of dust aerosols, J. Geophys. Res. Atmos., 119, 787–802, doi:10.1002/2013JD019961.

Kim, E., Hopke, P.K., 2006. Characterization of fine particle sources in the Great Smoky Mountains area. Sci. Total Environ., 368, 781e794.

Klockow, D., Niessner, R., Malejczyk, M., Kiendl, H., vom Berg, B., Keuken, M.P., Wayers-Ypelaan, A., Slanina, J., 1989. Determination of nitric acid and ammonium nitrate by means of a computer-controlled thermo-denuder system. Atmos. Environ., 23, 1131-1138.

Koçak, M. , Mihalopoulos, N., Tutsak, E., Violaki, K., Theodosi, C., Zarmpas, P., Kalegeri, P., 2016. Atmospheric deposition of macronutrients (dissolved inorganic nitrogen and phosphorous) onto the Black Sea and implications on marine productivity. Journal of the Atmospheric Sciences, Volume 73, Issue 4, 1727-1739.

Koçak, M., Theodosi, C., Zarmpas, P., Im, U., Bougiatioti, A., Yenigun ,O., Mihalopoulos, N., 2011. Particulate matter (PM_{10}) in Istanbul: Origin, source areas and potential impact on surrounding regions. Atmos. Environ., 45, 6891-6900.

Koçak, M., Kubilay, N. and Mihalopoulos, N., 2004. Ionic composition of lower tropospheric aerosols at a Northeastern Mediterranean site: implications regarding sources and long-range transport. Atmos. Environ., 38, 2067-2077.

Koçak, M., Kubilay, N., Herut, B. and Nimmo, M., 2005. Dry atmospheric fluxes of trace metals (Al, Fe, Mn, Pb, Cd, Zn, Cu) over the Levantine Basin: A refined assessment. Atmos. Environ., 39, 7330-7341.

Koçak, M., Mihalopoulos, N., and Kubilay, N., 2007. Chemical composition of the fine and coarse fraction of aerosols in the northeastern Mediterranean. Atmos. Environ., 41 7351–7368.

Koçak, M., Mihalopoulos, N., and Kubilay, N., 2009. Origin and source regions of PM_{10} in the eastern Mediterranean atmosphere. Atmospheric Research, 92, 464-474.

Koçak, M., Theodosi, C., Zarmpas, P., Séguret, M.J.M., Herut, B., Kallos, G., Mihalopoulos, N., Kubilay, N., Nimmo M., 2012. Influence of mineral dust transport on the chemical composition and physical properties of the Eastern Mediterranean aerosol. Atmos. Environ., 57, 266-277.

Koehler, K.A., S.M. Kreidenweis, P.J. DeMott, M.D. Petters, A.J. Prenni, and C.M. Carrico 2009. Hygroscopicity and cloud droplet activation of mineral dust aerosol. Geophys. Res. Lett., 36, L08805, doi:10.1029/2009GL037348.

Koulouri, E., Saarikoski, S., Theodosi, C., Markaki, Z., Gerasopoulos, E., Kouvarakis, G., Makela, T., Hillamo, R., and Mihalopoulos, N., 2008. Chemical composition and sources of fine and coarse aerosol particles in the Eastern Mediterranean. Atmos. Environ., 42, 6542–6550, doi:10.1016/j.atmosenv.2008.04.010.

Koutrakis P., Sioustas C., Ferguson S., Wolfson J. M., Mulik J. D. and Burton R. M., 1993. Development and evaluation of a glass honeycomb denuder/filter pack system to collect atmospheric gases and particles. Envir. Sci. Technol., 27, 2497-2501.

Kouvarakis, G. and Mihalopoulos, N., 2002. Seasonal variation of dimethylsulfide in the gas phase and of methanesulfonate and non-sea-salt sulfate in the aerosols phase in the Eastern Mediterranean atmosphere. Atmos. Environ., 36, 929-938.

Kouvarakis, G., Bardouki H., Mihalopoulos, N., 2002. Sulfur budget above the Eastern Mediterranean: relative contribution of anthropogenic and biogenic sources, Tellus B: Chemical and Physical Meteorology, 54:3, 201-212, DOI: 10.3402/tellusb.v54i3.16661.

Kouvarakis, G., Mihalopoulos, N., Tselepides, T., Stavrakakis, S., 2001. On the importance of atmospheric nitrogen inputs on the productivity of Eastern Mediterranean. Global Biogeochem. Cycles, 15, 805-818.

Krueger, B.J., Grassian, V.H., Cowin, J.P., Laskin, A., 2004. Heterogeneous chemistry of individual mineral dust particles from different dust source regions: the importance of particle mineralogy. Atmos. Environ., 38, 6253e6261.

Kubilay, N. and Saydam, C., 1995. Trace elements in atmospheric particulates over the Eastern Mediterranean: concentration, sources and temporal variability. Atmos. Environ., 29, 2289-2300.

Kubilay N., Nickovic S., Moulin C. and Dulac F., 2000. An illustration of the transport and deposition of mineral dust onto the eastern Mediterranean. Atmos. Environ., 34, 1293-1303.
Kubilay, N., Çokacar, T. and Oguz, T., 2003. Optical properties of mineral dust outbreaks over the northeastern Mediterranean. Journal of Geophysical Research, 108(D21), 4666, doi:10.1029/2003JD003798.

Kubilay, N., Koçak, M., Çokacar, T. and Oguz, T., 2002. Influence of Black Sea and local biogenic activity on the seasonal variation of aerosol sulfur species in the eastern Mediterranean atmosphere. Global Biogeochemical Cycles, 16, NO. 4,1079, doi:10.1029/2002GB001880.

Kubilay, N., Oguz, T. and Koçak, M., 2005. Ground-based assessment of Total Ozone Mapping Spectrometer (TOMS) data for dust transport over the northeastern Mediterranean. Global Biogeochemical Cycles, 19, GB1022, doi:10.1029/2004GB002370.

Lee, S., Liu, W., Wang, Y.H., Russell, A.G., and Edgerton, E.S. 2008. Source apportionment of $PM_{2.5}$: Comparing PMF and CMB results for four ambient monitoring sites in the southeastern United States. Atmos. Environ., 42(18), 4126–4137.

Lelieveld, J., et al., 2002. Global air pollution crossroads over the Mediterranean. Science, 298, 794–798.

Levin, Z., Teller, A., Ganor, E., and Yin, Y., 2005. On the interactions of mineral dust, sea salt particles and clouds – Measurements and modeling study from the MEIDEX campaign. J. Geophys. Res, 110, D20202, doi:10.1029/2005JD005810.

Lionello, P., Malanotte-Rizzoli, P., Boscolo, R., et al., 2006. The Mediterranean Climate: An overview of the main characteristics and issues, Mediterranean Climate Variability, Elsevier B. V., 1–26..

Lipfert, F., 1994. Filter artifacts associated with particulate measurements: Recent evidence and effects on statistical relationships. Atmos. Environ., 28, 3233-3249, 10.1016/1352-2310(94)00167-J.

Liu, C., Lin, S., Awasthi, A., Tsai, C., Wu, Y., Chen, C., 2014. Sampling and conditioning artifacts of $PM_{2.5}$ in filter-based samplers. Atmos. Environ., 85, 48–53, 10.1016/j.atmosenv.2013.11.075.

Liu, W., Wang, Y.H., Russell, A., and Edgerton, E.S., 2005.Atmospheric aerosol over two urban-rural pairs in the southeastern United States: Chemical composition and possible sources. Atmos. Environ., 39(25), 4453–4470.

Lohmann, U. and Feichter, J., 2005. Global indirect aerosol effects: A review. Atmos. Chem. Phys. 5, 715–737.

Luria, M., M. Peleg, G. Sharf, D.S. Tov-Alper, N. Spitz, Y. Ben Ami, Z. Gawii, B. Lifschitz, A. Yitzchaki and I. Seter, 1996. Atmospheric sulfur over the east Mediterranean region. Journal of Geophysical Research, 101, 25917-25930.

Lyamani, H., Valenzuela, A., Perez-Ramirez, D., Toledano, C., Granados-Muoz, M. J., Olmo, F. J., and Alados-Arboledas, L., 2015. Aerosol properties over the western Mediterranean basin: temporal and spatial variability. Atmos. Chem. Phys., 15, 2473–2486, doi:10.5194/acp-15-2473-2015.

Ma, Y., Weber, R. J., Lee, Y.-N., Orsini, D.A., Maxwell-Meier,K., Thornton, D.C., Bandy, A. R., Clarke, A.D., Blake, D.R., Sachse, G. W., Fuelberg, H. E., Kiley, C. M., Woo, J.-H., Streets, D.G., and Carmichael, G.R., 2003. Characteristics and influence of biosmoke on the fine-particle ionic composition measured in Asian outflow during the Transport and Chemical Evolution Over the Pacific (TRACE-P) experiment, J. Geophys. Res., 108(D21), 8816, doi:10.1029/2002JD003128.

Makkonen, U., Virkkula, A., Mäntykenttä, J., Hakola, H., Keronen, P., Vakkari, V. and Aalto, P.P., 2012. Semi-continuous Gas and Inorganic Aerosol Measurements at a Finnish Urban Site: Comparisons with Filters, Nitrogen in Aerosol Gas Phases, and Aerosol Acidity. Atmos. Chem. Phys., 12, 5617–5631.

Makkonen, U., Virkkula, A., Hellén, H., Hemmilä, M., Sund, J., Hakola, H., Äijälä, M., Ehn, M.,Junninen, H., Keronen, P., Petäjä, T., Worsnop, R.D., Kulmala, M., 2014. Semi-continuous gas and inorganic aerosol measurements at a boreal forest site: Seasonal and diurnal cycles of NH3, HONO and HNO3. Boreal Environment Research, 19, 311-328.

Malaguti, A., Mircea, M., La Torretta, M. G. T., Telloli, C., Petralia, E., Stracquadanio, M., Berico, M., 2015. Comparison of Online and Offline Methods for Measuring Fine Secondary Inorganic Ions and Carbonaceous Aerosols in the Central Mediterranean Area. Aerosol and Air Quality Research, doi:10.4209/aaqr.2015.04.0240.

Mallet, M., Dubovik, O., Nabat, P., Dulac, F., Kahn, R., Sciare, J., Paronis, D., and Léon, J. F., 2013. Absorption properties of Mediterranean aerosols obtained from multi-year ground-based remote sensing observations. Atmos. Chem. Phys., 13, 9195-9210, doi:10.5194/acp-13-9195-2013.

Mallet, M., Dubovik, O., Nabat, P., Dulac, F., Kahn, R., Sciare, J., Paronis, D., and Léon, J. F.,
Mamane, Y. and Gottlieb, J., 1989. Heterogeneous reactions of minerals with sulfur and nitrogen oxides. Journal of Aerosol Science, 20, 303-311.

Mamane, Y. and Gottlieb, J., 1992. Nitrate formation on sea-salt and mineral particles-a single particle approach. Atmos. Environ., 26A, 1763-1769.

Markovic, M. Z., VandenBoer, T.C., Baker, K.R., Kelly, J.T., and Murphy J.G., 2014. Measurements and modeling of the inorganic chemical composition of fine particulate matter and associated precursor gases in California's San Joaquin Valley during CalNex 2010, J. Geophys. Res. Atmos., 119, 6853–6866, doi:10.1002/2013JD021408..

Marks, R., 1990. Preliminary investigations on the influence of rain on the production, concentration, and vertical distribution of sea salt aerosol. J. Geophys. Res., 95, 22299-22304.

Mehta, M., Singh, R., Singh, A., Singh, N., Anshumali, 2016. Recent global aerosol optical depth variations and trends - A comparative study using MODIS and MISR level 3 datasets. Remote Sensing of Environment, 181. 137-150, doi:10.1016/j.rse.2016.04.004.

Meloni, D., di Sarra A., Pace, G., Monteleone, F., 2006. Aerosol optical properties at Lampedusa (Central Mediterranean). 2. Determination of single scattering albedo at two wavelengths for different aerosol types. Atmos. Chem. Phys., 6, doi:10.5194/acpd-5-4971-2005.

Metzger, S., Mihalopoulos, N., and Lelieveld, J., 2006. Importance of mineral cations and organics in gas-aerosol partitioning of reactive nitrogen compounds: case study based on MINOS results. Atmos. Chem. Phys., 6, 2549–2567, doi:10.5194/acp-6-2549-2006.

Mihalopoulos, N., Stephanou, E., Kanakidou, M., Pilitsidis, S. and Bousquet, P., 1997. Tropospheric aerosol ionic composition in the E. Mediterranean region. Tellus, 49B, 1-13.

Miller, R. L., Tegen, I., 1998. Climate response to soil dust aerosols. J. Climate, 11, 3247–3267.

Moulin, C., Lambert, E., Dayan, U., Masson, V., Ramonet, M., Bousquet, P., Legrand, M., Balkanski, Y. J., Guelle, W., Marticorena, B., Bergametti, G. and Dulac, F., 1998. Satellite climatology of African dust transport in the Mediterranean atmosphere. Journal of Geophysical Research, 103, 13137-13144.

Müller, T., Schladitz, A., Massling, A., Kaaden, N., Kandler, K. and coauthors, 2009. Spectral absorption coefficients and imaginary parts of refractive indices of Saharan dust during SAMUM-1. Tellus 61B, 78–95.

Müller, D., Weinzierl, B., Petzold, A., Kandler, K., Ansmann, A. and co-authors, 2010. Mineral dust observed with AERONET Sun photometer, Raman lidar, and in situ instruments during SAMUM 2006: shape-independent particle properties. J. Geophys. Res., 115, D07202, doi:10.1029/2009JD012520.

Müller, T., Schladitz, A., Kandler, K., and Wiedensohler, A., 2011. Spectral particle absorption coefficients, single scattering albedos, and imaginary parts of refractive indices from ground-based in-situ measurements at Cape Verde Island during SAMUM–2. Tellus, 63B, 4.

Nakajima, T., et al. 2003. Significance of direct and indirect radiative forcings of aerosols in the East China Sea region, J. Geophys. Res., 108(D23), 8658, doi:10.1029/2002JD003261.

Nie, W., Wang, T., Gao, X., Pathak, R.K., Wang, X., Gao, R., Zhang, Q., Yang, L., and Wang, W. X., 2010. Comparison among filter-based, impactor-based and continuous techniques for measuring atmospheric fine sulfate and nitrate. Atmos. Environ., 44, 4396–4403, doi:10.1016/j.atmosenv.2010.07.047.

O’Neill, N.T., Ignatov, A., Holben, B.N., and Eck, T.F., 2000. The lognormal distribution as a reference for reporting aerosol optical depth statistics: Empirical tests using multi-year, multi-site AERONET sunphotometer data. Geophys. Res. Lett., 27, 3333-3336.

O'Dowd C.D. and Smith M.H., 1993. Physicochemical properties of aerosols over the northeast Atlantic: evidence for wind speed related submicron sea-salt aerosol production. J. Geophys. Res. 98, 1137-1149.

Omar, A.H., Won, J.-G., Winker, D.M., Yoon, S.-C., Dubovik, O., McCormick, M.P., 2005. Development of global aerosol models using cluster analysis of Aeronet Robotic Network (AERONET) measurements. J. Geophys. Res., 110, doi:10.1029/2004JD004874.

O'Neill, N.T., Eck, T.F., Smirnov, A., Holben, B.N., Thulasiraman, S., 2003. Spectral discrimination of coarse and fine mode optical depth. J. Geophys. Res., 108 (D17), 4559-4573, doi:10.1029/2002JD002975.

O'Neill, N.T., Dubovik, O., and Eck, T.F., 2001. A modified Angstrom coefficient for the characterization of sub-micron aerosols. Appl. Opt., 40, 15, 2368-2375.

O'Neill, N.T., Eck, T.F., Holben, B.N., Smirnov, A., Dubovik, O., and Royer, A., 2001. Bimodal size distribution influences on the variation of Angstrom derivatives in spectral and optical depth space. J. Geophys. Res., 106, 9787-9806.

Paerl, H. W., 1985. Enhancement of marine primary production by nitrogen enriched acid rain. Nature, 316, 747–749.

Paerl, H.W., Willey, J.D., Go, M., Peierls, B.L., Pinckney, J.L., and Fogel M.L., 1999. Rainfall stimulation of primary production in Western Atlantic Ocean waters: Roles of different nitrogen sources and co-limiting nutrients. Mar. Ecol. Prog. Ser., 176, 205–214.

Pakkanen, T.A., Hillamo, R.E., Aurela, M., Andersen, H.V., Grundahl, L., Ferm, M., Persson, K., Karlsson, V., Reissell, A., Royset, O., Floisand, I., Oyola, P., Ganko, T., 1999. Nordic intercomparison for measurement of major atmospheric nitrogen species. Journal of Aerosol Science 30, 247–263.

Papadimas, C.D., Hatzianastassiou, N., Matsoukas, C., Kanakidou, M., Mihalopoulos, N., and Vardavas, I., 2012. The direct effect of aerosols on solar radiation over the broader Mediterranean basin. Atmos. Chem. Phys., 12, 7165-7185.

Papadimas, C.D., Hatzianastassiou, N., Mihalopoulos, N., Kanakidou, M.,Katsoulis, B.D., Vardavas, I., 2009. Assessment of the MODIS Collections C005 and C004 aerosol optical depth products over the Mediterranean basin. Atmos. Chem. Phys., 9, 2987-2999.

Patterson, E.M., Gillete, D.A., and Stockton, B.H., 1977. Complex index of refraction between 300 and 700 nm for Saharan aerosol. J. Geophys. Res., 82, 3153-3160.

Paulot, F. et al. 2014. Ammonia emissions in the United States, European Union, and China derived by high-resolution inversion of ammonium wet deposition data: Interpretation with a new agricultural emissions inventory (MASAGE_NH3). J. Geophys. Res. Atmos. 119, 4343-4364.

Paytan, A., Mackey, K.R.M., Mackey, Chen, Y., Lima, I.D., Doney, S.C., Mahowald, N., Labiosa, R., Post,A.F., 2009. Toxicity of atmospheric aerosols on marine phytoplankton. Proceedings of the National Academy of Sciences, 106, 4601-4605.

Pearl, H., 1985. Microzone formation: its role in the enhancement of aquatic N2 fixation. Limnol. Oceanogr., 30, 1246-1252.

Pearl, H.W., Willey, J.D., Go, M., Peierls, B.L., Pinckney, J.L., Fogel, N.L., 1999. Rainfall stimulation of primary production in western Atlantic Ocean waters: roles of different nitrogen sources and co-limiting nutrients. Marine Ecology Progress Series 176, 205-214.

Peltier, R.E., Sullivan, A.P., Weber, R.J., Brock, C.A., Wollny, A.G., Holloway, J.S., de Gouw, J.A., and Warneke, C., 2007. Fine aerosol bulk composition measured on WP-3D research aircraft in vicinity of the northeastern United States—Results from NEAQS, Atmos. Chem. Phys.,7(12), 3231–3247, doi:10.5194/acp-7-3231-2007.

Peng J, et al., 2016. Markedly enhanced absorption and direct radiative forcing of black carbon under polluted urban environments. Proc Natl Acad Sci USA 113(16):4266–4271.

Petters, M.D. and Kreidenweis, S.M, 2007. A single parameter representation of hygroscopic growth and cloud condensation nucleus activity. Atmos. Chem. Phys., 7, 1961–1971.

Polissar, A.V., Hopke, P.K., Harris, J.M., 2001. Source regions for atmospheric aerosol measured at Barrow, Alaska. Environmental Science and Technology, 35, 4214-4226.

Prospero, J.M., Barret, K., Church, T., Dentener, F., Duce, R.A., Galloway, J.N., Levy, H., Moody, J. and Quin, P., 1996. Atmospheric deposition of nutrients to the North Atlantic Basin. Biogeochemistry, 25, 27-73.

Prospero, J.M., Ginoux, P., Torres, O., Nicholson, S.E. and Gill, T.E., 2002. Environmental characterization of global sources of atmospheric soil dust identified with the NIMBUS-7 total ozone mapping spectrometer. Reviews of Geophysics, 40, 1, 1-31.

Ramadan, Z., Song, X. H., and Hopke, P.K., 2000. Identification of sources of Phoenix aerosol by positive matrix factorization. J. Air Waste Manage. Assoc., 50(8), 1308–1320.

Ramanathan, V., Crutzen, P.J., Lelieveld, J., Mitra, A.P., Althausen, D., Anderson, J., et al., 2001. Indian Ocean experiment: An integrated analysis of the climate forcing and effects of the great Indo-Asian haze. Journal of Geophysical Research, 106, 28,371−28, 398.

Rodriguez, S., Querol, X., Alastuey, A. and Plana, F., 2002. Sources and processes affecting levels and composition of atmospheric aerosol in the western Mediterranean. Journal of Geophysical Research, 107, NO. D24, 4777, doi:10.1029/2001JD001488.

Rodriguez, S., Querol, X., Alastuey, A. Kallos, G. and Kakaliagou, O., 2001. Saharan dust contributions to PM10 and TSP levels in Southern and Eastern Spain. Atmos. Environ., 35, 2433-2447.

Roelle, A.P and Aneja, V., 2002. Characterization of ammonia emissions from soils in the upper coastal plain, North Carolina. Atmos. Environ., 36, 1087-1097.

Rosenfeld, D., et al., 2008. Flood or drought: How do aerosols affect precipitation?, Science, 321, 1309–1313, doi:10.1126/science.1160606.

Russell, P., Bergstrom, R., Shinozuka, Y., Clarke, A., DeCarlo, P., Jimenez, J., Livingston, J., Redemann, J., Dubovik, O., and Strawa, A., 2010. Absorption Angstrom Exponent in AERONET and related data as an indicator of aerosol composition. Atmos. Chem. Phys., 10, 1155–1169.

Saltzman, E.S., Savoie, D.L., Prospero, J.M. and Zika, R.G., 1986. Methanesulfonic acid and non sea salt sulfate in Pacific air: Regional and seasonal variations. Journal of Atmospheric Chemistry, 4, 227-240.

Salvador, P., Artinano, B., Alonso, D.G., Querol, X., Alastuey, A., 2004. Identification and characterization of sources of PM_{10} in Madrid (Spain) by statistical methods. Atmos. Environ., 38, 435–447.

Sander, S.P., Seinfeld, J.H., 1976. Chemical kinetics of homogeneous atmospheric oxidation of sulfur dioxide. Environ. Sci. Technol., 10 (12), 1114–1123.

Savoie, D.L., Prospero, J.M., Arimoto, R. and Duce, R.A., 1994. Non sea salt sulfate and methanesulfonate at American Samoa. Journal of Geophysical Research, 99, No.D2, 3587-3596.

Savoie, D.L., Prospero, J.M., Oltmans, S.J., Graustein, W.C., Turekian, K.K., Merrill, J.T., Levy, H., 1992. Sources of nitrate and ozone in the marine boundary layer of the tropical north Atlantic. Journal of Geophysical Research, 97 (D11), 11575–11589.

Schaap, M., Mueller, K., and ten Brink, H. M., 2002. Constructing the European aerosol nitrate concentration field from quality analysed data. Atmos. Environ., 36, 1323–1335.

Schaap, M., Otjes, R.P., and Weijers, E.P., 2011. Illustrating the benefit of using hourly monitoring data on secondary inorganic aerosol and its precursors for model evaluation. Atmos. Chem. Phys., 11, 11041–11053, doi:10.5194/acp-11-11041-2011.

Schaap, M., Spindler, G., Schulz, M., Acker, K., Maenhaut, W., Berner, A., Wieprecht, W., Streit, N., Muller, K., Bruggemann, E., Chi, X., Putaud, J.P., Hitzenberger, R., Puxbaum, H., Baltensperger, U. and ten Brink, H., 2004. Artefacts in the Sampling of Nitrate Studied in the “INTERCOMP” Campaigns of EUROTRAC-AEROSOL. Atmos. Environ., 38, 6487–6496.

Schafer, J. S., et al., 2014. Intercomparison of aerosol single-scattering albedo derived from AERONET surface radiometers and LARGE in situ aircraft profiles during the 2011 DRAGON-MD and DISCOVER-AQ experiments. J. Geophys. Res. Atmos., 119, 7439–7452, doi:10.1002/2013JD021166.

Schafer, J. S., Eck, T.F., Holben, B.N., Artaxo, P., and Duarte, A.F. 2008. Characterization of the optical properties of atmospheric aerosols in Amazônia from long-term AERONET monitoring (1993–1995 and 1999–2006). J. Geophys. Res., 113, D04204, doi:10.1029/2007JD009319.

Schafer, J. S., Eck, T.F., Holben, B.N., Artaxo, P., Yamasoe, M.A., and Procopio, A.S., 2002. Observed reductions of total solar irradiance by biomass-burning aerosols in the Brazilian Amazon and Zambian Savanna. Geophys. Res. Lett., 20, 1823.

Sciare, J., Oikonomou, K., Favez, O., Liakakou, E., Markaki, Z., Cachier, H., and Mihalopoulos, N., 2008. Long-term measurements of carbonaceous aerosols in the

Eastern Mediterranean: evidence of long-range transport of biomass burning, Atmos. Chem. Phys., 8, 5551-5563, doi:10.5194/acp-8-5551-2008.

Seinfeld, J.H. and Pandis, S.N., 1998. Atmospheric Chemistry and Physics: From Air Pollution to Climate Change, J. Wiley, New York.

Seinfeld, J.H. and Pandis, S.N., 2006. Atmospheric Chemistry and Physics: From Air Pollution to Climate Change, 2nd ed, John Wiley, New York, 1203 pp.

Seitzinger, S.P., and Sander, R.W., 1999. Atmospheric inputs of dissolved organic nitrogen stimulate estuarine bacteria and phytoplankton, Limnol. Oceanogr., 44, 721–730.

Shao, Y., Wyrwoll, K.H., Chappell, A., Huang, J., Lin, Z., McTainsh, G.H., Mikami, M., Tanaka, T.Y., Wang, X., Yoon, S., 2011. Dust cycle: An emerging core theme in Earth system science. Aeolian Research, 2, 4, 181-204.

Shaw R. W. Jr., Stevens R.K., Bowermaster J.,Tesch J. W. and Tew E., 1982. Measurements of atmospheric nitrate and nitric acid: the denuder difference experiment. Atmos. Environ., 16, 845-853.

Shi, Y., Chen, J., Hu, D., Wang, L., Yang, X., and Wang, X., 2014. Airborne submicron particulate (PM_1) pollution in Shanghai, China: Chemical variability, formation/dissociation of associated semivolatile components and the impacts on visibility, Sci. Total Environ., 473, 199–206.

Shon Z.H, Kim K.H, Song S.K, Jung K, Kim N.J, Lee J.B, 2012. Relationship between water-soluble ions in $PM_{2.5}$ and their precursor gases in Seoul megacity. Atmos. Environ., 59, 540-550, doi: 10.1016/j.atmosenv.2012.04.033.

Shon, Z.H., Ghosh, S., Kim, K.-H., Song, S.K., Jung, K., Kim, N.J., 2013. Analysis of water-soluble ions and their precursor gases over diurnal cycle. Atmos. Res. 132, 309–321.

Smirnov, A., Holben, B. N., Kaufman, Y. J., Dubovik, O., Eck, T.F., Slutsker, I., Pietras, C., Halthore, R.N., 2002. Optical properties of atmospheric aerosol in maritime environments. J. Atmos. Sci., 59, 501–523.

Smirnov, A., Villevalde, Y., O'Neill, N.T., Royer, A., and Tarussov, A., 1995. Aerosol optical depth over the oceans: Analysis in terms of synoptic air mass types. J. Geophys. Res., 100(D8), 16639–16650, doi:10.1029/95JD01265.

Smith, S. J., Aardenne, van J., Klimont, Z., Andres, R.J., Volke, A. and Delgado, Arias S., 2011. Anthropogenic sulfur dioxide emissions: 1850-2005. Atmos. Chem. Phys., 11, 1101-1116.

Sokolik, I. N., and Toon O.B., 1996. Direct radiative forcing by anthropogenic airborne mineral aerosols, Nature, 381, 681-683, doi:10.1038/381681a0.

Stein, A.F., Draxler, R.R, Rolph, G.D., Stunder, B.J.B., Cohen, M.D., and Ngan, F., 2015. NOAA's HYSPLIT atmospheric transport and dispersion modeling system. Bull. Amer. Meteor. Soc., 96, 2059-2077, doi:10.1175/BAMS-D-14-00110.1.

Tang, I.N. and Munkelwitz, H.R., 1994. Water activities, densities, and refractive indices of aqueous sulfates and sodium nitrate droplets of atmospheric importance. J. Geophys. Res. 99, 18,801-18,808.

Taylor, M., Kazadzis, S., Amiridis, V., Kahn, R.A., 2015. Global aerosol mixtures and their multiyear and seasonal characteristics. Atmos. Environ. 116, 112-129.

Tegen, I., and A.A. Lacis, 1996. Modeling of particle size distribution and its influence on the radiative properties of mineral dust aerosol. J. Geophys. Res., 101, 19,237-19,244.

Tegen, I., Lacis, A.A., Fung, I., 1996. The influence of climate forcing of mineral aerosol from disturbed soils. Nature, 380, 419−422.

Tian, M., Wang, H.B., Chen, Y., Zhang, L.M., Shi, G.M., Liu, Y., Yu, J. Y., Zhai, C.Z., Wang, J., and Yang, F.M., 2017. Highly time-resolved characterization of water-soluble inorganic ions in $PM_{2.5}$ in a humid and acidic mega city in Sichuan Basin, China. Sci. Total Environ., 580, 224–234, doi:10.1016/j.scitotenv.2016.12.048.

Toledano, C., Cachorro, V.E., de Frutos, A.M., Torres, B., Berjon, A., Sorribas, M., and Stone, R. S., 2009. Airmass Classification and Analysis of Aerosol Types at El Arenosillo (Spain), J. Appl. Meteorol. Clim., 48(5), 962–981.

Tsai, C., and Perng, S., 1998. Artifacts of ionic species for hi-vol PM_{10} and PM_{10} dichotomous samplers. Atmos. Environ., 32, 1605–1613, doi:10.1016/S1352-2310(97)00387-7.

Ullah, S., Takeuchi, M., Dasgupta, P., 2006. Versatile Gas/Particle Ion Chromatograph. Environmental Science and Technology, 40, 962-8, doi:10.1021/es051722z.

Updyke, K.M., Nguyen, T.B., Nizkorodov, S. A., 2012. Formation of brown carbon via reactions of ammonia with secondary organic aerosols from biogenic and anthropogenic precursors. Atmos. Environ., 63, 22–31.

Usher, C.R., Michel, A.E. and Grassin, V.H., 2003a. Reactions on mineral dust. Chemical Reviews, 103, 4883-4939.

Usher, C.R., Michel, A.E., Stec, D. and Grassian, V.H., 2003b. Laboratory studies of ozone uptake on processed mineral dust. Atmos. Environ., 37, 5337–5347.
Ussher, S.J., Achterberg, E.P. and Worsfold, P.J., 2004. Marine Biogeochemistry of iron. Environmental Chemistry, 1, 76-80.

Van Damme, M. et al., 2014. Global distributions, time series and error characterization of atmospheric ammonia (NH_3) from IASI satellite observations. Atmos. Chem. Phys., 14, 2905–2922.

Vasconcelos, L., Kahl, J., Liu, D., Macias, E., White,W., 1996. A tracer calibration of back trajectory analysis at the Grand Canyon. Journal of Geophysical Research 101 (D14), 19329–19335.

Vecchi, R., Valli, G., Fermo, P., D'Alessandro, A., Piazzalunga, A., and Bernardoni, V., 2009. Organic and inorganic sampling artefacts assessment. Atmos. Environ., 43, 1713–1720, doi:10.1016/j.atmosenv.2008.12.016.

Vrekoussis, M., Liakakou, E., Koçak, M., Kubilay, N., Oikonomou, K., Sciare, J. and Mihalopoulos, N., 2005. Seasonal variability of optical properties of aerosols in the Eastern Mediterranean. Atmos. Environ., 39, 7083-7094.

Washington, R., Todd, M., Middleton, N.J. and Andrew S. Goudie, A.S., 2003. Dust-storm source areas determined by the Total Ozone Monitoring Spectrometer and surface observations. Annals of the Association of American Geographers, 93, 2, 297–313.

Weber, R. J., Orsini, D., Daun, Y., Lee, Y. N., Klotz, P. J. and Brechtel, F. J., 2001. A Particle-Into-Liquid Collector for Rapid Measurement of Aerosol Bulk Chemical Composition. Aerosol Sci. Technol, 35, 718–727.

Whelpdale, D.M., Ayers, G., Dovland, H., Galloway, J.N., Miller, J.M., Summers, P.W., 1996. Global acid deposition assessment. In: Whelpdale, D.M., Kaiser, M.S. (Eds.), Global Atmospheric Watch Report No. 106. World Meteorological Organization, Geneva.

Wieprecht, W., Acker, K., Müller, K., Spindler, G., Brüggemann, E., Maenhaut, W., Chi, X., Hitzenberger, R., Bauer, H., and ten Brink, H., 2004. INTERCOMP2000: Ionic Constitution and Comparison of Filter and Impactor. Atmos. Environ., 38, 6477–6486.

Xia, X.A., Li, Z.Q., Holben, B., Wang, P.C., Eck, T., Chen, H.B., Cribb, M., and Zhao, Y.X., 2007, Aerosol optical properties and radiative effects in the Yangtze Delta region of China, J. Geophys. Res., 112, D22S12, doi:10.1029/2007JD008859.

Xin, J., et al., 2007. Aerosol optical depth (AOD) and Angstrom exponent of aerosols observed by the Chinese Sun Hazemeter Network from August 2004 to September 2005. J. Geophys. Res., 112, D05203, doi:10.1029/2006JD007075.

Xue, J., Lau, A.K., Yu, J.Z., 2011. A study of acidity on $PM_{2.5}$ in Hong Kong using online ionic chemical composition measurements. Atmospheric Environment, 45(39), 7081–7088.

Yoon, J., Hoyningen-Huene, W., Kokhanovsky, A.A, Vountas, M., Burrows, PJ., 2012. Trend analysis of aerosol optical thickness and Angstrom exponent derived from the global AERONET spectral observations. Atmospheric Measurement Techniques, 5, 1271-1299. doi:10.5194/amt-5-1271-2012.

CURRICULUM VITAE

PERSONAL INFORMATION

Surname, Name: Tutsak, Ersin

email: ersin@ims.metu.edu.tr

EDUCATION

- B.S. Mathematics, Çanakkale Onsekiz Mart University, 2007
- M.S. Physical Oceanography, Middle East Technical University, 2012
- Ph.D. Oceanography, Middle East Technical University, 2018

WORK EXPERIENCE

- METU-IMS, National project, Dredging Applications and Environmental Management of Dredge Material, 2015-2016.
- METU-IMS, National project, Chemical Characterization and Speciation of atmospheric particles, dry and wet deposition modes in Eastern Mediterranean: Origin, Source Areas, Bio-availability and Impact of Atmospheric Inputs on Marine Productivity, 2014-2015
- METU-IMS, Turkish-Germany Bilateral Cooperation, High Reynolds number turbulent mixing in Bosphorus strait, 2012-2014.
- METU-IMS, EU MyOcean Project, 2011-2012.
- METU-IMS, EU SESAME Project (Southern European Seas: Assessing and Modelling Ecosystem change) under FP6 of EC, 2008-2011.
- METU-IMS, EU SeaDataNet Project, 2007-2008

PUBLICATIONS

Journal Papers:

- Kioroglou, Sotiris; Tragou, Elina; Zervakis, Vassilis; Georgopoulos, Dimitris; Herut,Barak; Gertman, Isaak; Kovacevic, Vedrana; Özsoy, Emin; Tutsak, Ersin, Vertical diffusion processes in the Eastern Mediterranean - Black Sea System, 2014, Journal of Marine Systems, 135, 53-63.
- Kocak, Mustafa ; Mihalopoulos, Nikolaos; Tutsak, Ersin; Violaki, Kalliopi; Theodosi, Christina; Zarmpas, Pavlos; Kalegeri, Pınar, PM_{10} and $PM_{2.5}$ composition over the Central Black Sea: origin and seasonal variability, 2015, Environmental Science and Pollution Research, 22, 18076-18092.
- Kocak, Mustafa ;Mihalopoulos, Nikolaos; Tutsak, Ersin; Violaki, Kalliopi; Theodosi, Christina; Zarmpas, Pavlos; Kalegeri, Pınar, Atmospheric Deposition of Macro Nutrients (DIN and DIP) onto the Black Sea and Implications on Marine Productivity, 2016. Journal of the Atmospheric Sciences, 13, 1727-1739, doi:10.1175/JAS-D-15-0039.1.

- Gündüz, Murat; Sözer, Adil ; Tutsak, Ersin; Özsoy, Emin, Water transport variability in the Aegean Sea and its connection with North Sea Caspian Pattern (NCP)., 2015, Ordu Univ. J. Sci. Tech., 5, 1-8.
- Gündüz, Murat; Tutsak, Ersin; Sözer, Adil ; Özsoy, Emin, Connections between climate indices and sea surface temperature over the Caspian Sea, 2015, Ordu Univ. J. Sci. Tech., 5, 29-36.

Book Chapters:

- Özsoy, E., Sofianos S., Gertman, I., Mantziafou, A., Aydogdu, A., Georgiou, S., Tutsak, E., Alex Lascaratos,A., Hecht, A., and Latif, M.A. The Mediterranean Sea: Temporal Variability and Spatial Patterns, Deep-Water Variability and Interbasin Interactions in the Eastern Mediterranean Sea, ISBN: 9781118847343, American Geophysical Union, 2014.
- Tutsak, E., Gündüz, M., and Özsoy E,. “Sea Level and Fixed ADCP Measurements from Turkish Straits System during 2008-2011”. The Sea of Marmara: Marine Biodiversity, fisheries, conservation and governance ,Özsoy E., Çağatay M.N., Balkıs N., Öztürk B., Ed., Turkish Marine Research Foundation (TUDAV), İstanbul, ISBN:978-975-8825-34-9, 2016.

Conference Papers:

- Sözer, A., Gürses, Ö., Tutsak, E. and E. Özsoy . Assembling the fine resolution bathymetry of the Turkish Straits System, TURQUA 2016- The Quaternary Symposium of Turkey, İstanbul, 8-11 May 2016.
- Sözer, A., Gürses, Ö., Aydoğdu, A., Gündüz, M., Tutsak, E. and E. Özsoy. Turkish Straits System: the crucible of Black Sea - Mediterranean exchange, TURQUA 2016- The Quaternary Symposium of Turkey, İstanbul, 8-11 May 2016.
- Tutsak, E., and Koçak, M. The Assessment of the Accuracy of the Clustering Methods for Air Masses Back Trajectories and their Influence on the Aerosol Chemical Composition and the Optical Properties in the Atmosphere over the Eastern Mediterranean. Turkish Marine Sciences Conference, Ankara, Turkey, 31 May - 3 June 2016.
- Koçak M., Mihalopoulos N., Tutsak E., Violaki K., Theodosi C., Zarmpas P., Kalegeri P. Atmospheric Deposition Of Macro Nutrients Onto The Black Sea and Implications on Marine Productivity. Turkish Marine Sciences Conference, Ankara, Turkey, 31 May - 3 June 2016.
- Özsoy, E., Gürses, Ö. and E. Tutsak. Turkish Straits System and Southern Black Sea: Exchange. Mixing and Shelf / Canyon Interactions, EGU General Assembly 2015, Vienna, Geophysical Research Abstracts, Vol. 17, 2015.

- Özsoy, E., Sofianos S., Gertman, I., Mantziafou, A., Aydogdu, A., Georgiou, S., Tutsak, E., Alex Lascaratos,A., Hecht, A., and Latif, M.A. Deep-Water Variability and Interbasin Interactions in the Eastern Mediterranean Sea. Workshop on "The Mediterranean Sea mass and heat budget: Understanding its forcing, uncertainties and time evolution." Palma de Mallorca, Spain, 2014.
- Tuğrul, S., Yücel, N., Uysal, Z., Gürses, Ö, Tutsak E., Yüksek, A., Öztürk, D., and Kıdeys, A. MAREX: Marmara Sea and Turkish Straits Experiments in June 2013. MARES2020 International Conference, Varna, Bulgaria, 2013.
- Özsoy, E., Sofianos S., Gertman, I., Mantziafou, A., Aydogdu, A., Georgiou, S., Tutsak, E., Alex Lascaratos,A., Hecht, A., and Latif, M.A. Deep-water variability and inter-basin interactions in the Eastern Mediterranean Sea, EGU 2013, Vienna, Austria, 2013
- Aydoğdu, A., Tutsak, E., and Özsoy, E. Performance of the Northern Levantine Circulation Model (NLEV), sea-level calibration and applications, COS-TT GODAE Oceanview Workshop, Lecce, Italy, 2013.
- Tutsak, E., Sözer, A., Gürses, Ö., Özsoy, E. Turkish Strait Systems: Observations and Modelling Forecast Systems, Marmara Sea 2010 Symposium, Istanbul, 2010.
- Tutsak, E., Özsoy, E., and Hüsrevoğlu, S. Time-series Analyses of Atmospheric and Marine Observations along the Turkish Coast. 39th CIESM Congresses, Venice, Italy, 2010
- Tutsak, E., and Özsoy, E. Time-Series Analyses of Measurements from Monitoring Stations along the Turkish Coast. 3rd ESF MedCLIVAR Workshop - Understanding the mechanisms responsible for the changes in the Mediterranean Sea circulation and sea level trends. Rhodes, Greece, 2008.

Summer Schools/Courses:

- Summer School of Earth System Modeling 2016. Istanbul Technical University, 5-7 September 2016, Istanbul, Turkey.
- Advanced School on Ocean Climate Modelling: Physical and Biogeochemical Dynamics of Semi- Enclosed Seas Organized by The Abdus Salam International Centre for Theoretical Physics (ICTP). Ankara, 2015.
- 2nd ESA Advanced Atmospheric Training Course. Organized by The European Space Agency (ESA). Forschungszentrum Jülich, Germany, 2014.
- 2011 Coastal Dynamics Modeling Summer School. Organized by University of Toulon. La Londe, France, 2011.
- NCL Workshop, Istanbul Technical University, 3-7 March 2008, Istanbul.